Atomic Scale Simulation of Irradiated Nuclear Fuel

Michael William Donald Cooper

March 27, 2015

Department of Materials Science and Engineering
Imperial College London

submitted in part fulfilment of the requirements for the degree of
Doctor of Philosophy in Materials Science and Engineering
of Imperial College London
and the diploma of Imperial College London

Declaration of originality - The work presented in this thesis is my own and that all else is appropriately referenced.

The copyright of this thesis rests with the author and is made available under a Creative Commons Attribution Non-Commercial No Derivatives licence. Researchers are free to copy, distribute or transmit the thesis on the condition that they attribute it, that they do not use it for commercial purposes and that they do not alter, transform or build upon it. For any reuse or redistribution, researchers must make clear to others the licence terms of this work.

©M.W.D. Cooper

Abstract

Atomic scale simulations have been performed investigating various phenomena governing nuclear fuel performance during reactor operation and during post irradiation storage or disposal.

Following a review of some of the key features of irradiated nuclear fuel, such as fission product distribution, two key factors were identified as the focus for this investigation: i) the role of uranium dioxide non-stoichiometry and ii) the effect of temperature. The former has been carried out using a previous pair potential model, whilst a new many-body potential was developed to enable temperature effects to be studied over the full range of temperatures of interest.

Secondary oxide precipitates are known to exist in irradiated nuclear fuel with Ba, Sr and Zr precipitating to form the perovskite (Ba,Sr)ZrO_3 grey phase. The binary BaO, SrO and ZrO_2 may also be formed. The precipitation enthalpies of these oxides were predicted as a function of hyper-stoichiometry. Additionally, $CrUO_4$ can also precipitate from Cr-doped UO_{2+x}. The possibility of fission product segregation to the phases from UO_2 or UO_{2+x} was also investigated with a broad range of species preferring segregation from stoichiometric UO_2.

The role of defect cluster configuration on vacancy mediated uranium migration was investigated for UO_2 and UO_{2+x}. In both cases the lowest enthalpy migration pathway involved reconfiguration of the cluster to a metastable configuration. Furthermore, there were a very

large number of alternative pathways that had similar migration enthalpies, especially for UO_{2+x}.

A new potential model was developed that uses a novel approach to include many-body interactions in the description of the actinide oxide series. This represents a significant improvement on previous models in the ability to describe the thermal expansion, specific heat capacity and elastic properties of CeO_2, ThO_2, UO_2, NpO_2, PuO_2, AmO_2 and CmO_2 from 300 to 3000 K.

Using the new model the thermal expansion, specific heat capacity, oxygen diffusivity and thermal conductivity of the mixed oxides $(U_xTh_{1-x})O_2$ and $(U_xPu_{1-x})O_2$ were predicted. Enhanced oxygen diffusion and a degradation in thermal conductivity were predicted in terms of the non-uniform cation sublattice.

Acknowledgements

First and foremost I would like to thank all my friends and family for their support throughout. Particular gratitude must go to my parents and Eri for putting up with my continued moaning throughout the writing up stages. A number of my colleagues at the centre for nuclear engineering deserve credit for their assistance but I would like to especially thank Robin Grimes, Michael Rushton and Simon Middleburgh for their invaluable advice, technical support and proof reading, without which this body of work would not have been possible.

Additionally, I acknowledge the NDA for contributing financially to the project and all other members of the UK spent nuclear fuel consortium for their useful guidance.

Contents

1 Introduction **22**

1.1 Outline 22

1.2 Nuclear fission 25

1.3 The fuel cycle 28

1.4 Nuclear reactors 32

1.5 Key features of spent nuclear fuel 35

1.5.1 Macroscopic damage 36

1.5.2 Fission product distribution 37

1.6 Defects in crystals 41

1.7 Thesis objectives 43

2 Methodology **46**

2.1 Static methods 46

2.1.1 Static energy minimisation 46

2.1.2 Defect calculations within the Mott-Littleton approach 48

2.1.3 Rational functional optimisation within Mott-Littleon 50

2.1.4 Defects in supercell statics 51

2.2 Molecular dynamics simulation 53

2.3 Empirical potential description of crystalline solids 55

2.3.1 Pairwise potentials 55

2.3.2 The shell model 57

2.3.3 Embedded atom method potentials 59

3 Comparison of uranium dioxide potentials 61

3.1 MO_2 phases 61

3.2 Thermal expansion 64

3.3 Elastic properties 65

4 Fission product segregation to secondary oxide phases 68

4.1 Introduction 68

4.2 Calculation details 71

4.3 Precipitation energies for the secondary oxide phases 73

4.4 Segregation between uranium dioxide and the grey phase 75

4.4.1 Partition energies of tetravalent cations into (Ba,Sr)ZrO_3 75

4.4.2 Change in lattice volumes due to tetravalent cation segregation 78

4.4.3 Partition energies of trivalent cations into (Ba,Sr)ZrO_3 79

4.4.4 Change in lattice volumes due to trivalent cation segregation 87

4.4.5 Effect of Cr-doping on segregation to the grey phase 89

4.4.6 Effect of excess Cr on swelling due to trivalent cation segregation . . 90

4.5 Segregation between uranium dioxide and zirconia 92

4.5.1 Partition energies of tetravalent cations into ZrO_2 92

4.5.2 Partition energies of trivalent cations into ZrO_2 92

4.6 Segregation between UO_{2+x} and $CrUO_4$ 97

4.6.1 Partition energies of tetravalent cations 97

4.6.2 Partition energies of trivalent cations 98

4.7 Conclusions and further discussion 99

4.7.1 Tetravalent species 99

4.7.2 Trivalent species 100

5 Uranium vacancy migration in UO_2 and UO_{2+x} 102

5.1 Introduction 102

5.2 Calculation details 105

5.3 Isolated uranium vacancy migration . . . 107
5.4 Uranium vacancy migration in stoichiometric UO_2 . . . 108
5.5 Uranium vacancy migration in hyper-stoichiometric UO_{2+x} . . . 112
5.6 Conclusions . . . 114

6 A many-body potential for the description of actinide oxides 116
6.1 Introduction . . . 117
6.2 Calculation details . . . 119
6.2.1 Description of the potential form . . . 119
6.2.2 Fitting procedure . . . 121
6.2.3 Defect calculation details . . . 125
6.2.4 Thermophysical properties validation . . . 126
6.3 Results and discussion . . . 130
6.3.1 Agreement of model with fitting data . . . 130
6.3.2 Validation of model against other experimental data . . . 131
6.3.3 Prediction of defect energies and comparison with DFT . . . 137
6.4 Conclusions . . . 139

7 Modelling the behaviour of mixed oxides 142
7.1 Introduction . . . 143
7.2 Calculation details . . . 145
7.3 Thermophysical and oxygen diffusivity properties . . . 149
7.3.1 $(U_xTh_{1-x})O_2$ . . . 149
7.3.2 $(U_xPu_{1-x})O_2$ . . . 158
7.4 Degradation of fuel thermal conductivity . . . 166
7.4.1 $(U_xTh_{1-x})O_2$ . . . 166
7.4.2 $(U_xPu_{1-x})O_2$ . . . 174
7.4.3 Degradation of UO_2 due to oxygen Frenkel pairs . . . 178
7.5 Conclusions . . . 180

8 Future work 185

8.1 Fission product distribution 185
8.2 Uranium vacancy migration 187
8.3 EAM Potential 188
8.4 Mixed oxides 189

9 Summary **191**
9.1 Non-stoichiometry 192
9.1.1 Fission product distribution 192
9.1.2 Uranium vacancy migration 195
9.2 Temperature effects 196

A Preliminary fitting results for ZrO_2 and $BaZrO_2$ **215**
A.1 Fitting ZrO_2 215
A.1.1 Parameter set 216
A.1.2 Agreement with DFT 216
A.1.3 Agreement with experiment 217

List of Figures

1.1 Schematic diagram of an example nuclear power station. The nuclear island (left) is separated from the conventional island (right) by the containment building. The secondary loop extracts heat from the primary loop, which is connected to the reactor core, via a heat exchange. Steam generated in the heat exchange is passed over the steam turbines to power an electrical generator. Using water from the cooling tower the steam is condensed and returns to the heat exchange. 23

1.2 The binding energy per nucleon for a range of isotopes [1]. 26

1.3 Neutron absorption by a U^{235} nucleus creating an excited and unstable U^{236} nucleus. Here this short lived isotope fissions to form two fission products (e.g. Kr^{92} and Ba^{141}) and several high velocity neutrons. For a chain reaction to occur one of these neutrons must fission a second U^{235} nucleus. 27

1.4 The fission product yield for a PWR fuel rod after 2.9 % burn-up. Those fission products with particularly high yields are identified [2]. 27

1.5 Illustration of the key processes in the nuclear fuel cycle. The open cycle is identified with black arrows, whilst grey arrows are used to shown reprocessing aimed at closing the fuel cycle. 28

1.6 a) Schematic illustration of a MAGNOX reactor and b) of an AGR reactor based on the description of [3]. The MAGNOX uses a two loop coolant system, similar to the PWR design but with a CO_2 coolant rather than water, whilst an internal steam generator is used in the AGR design. 33

1.7 a) Ceramographic cross section of UO_2 pellets showing macroscopic cracks and pores following irradiation in a BWR and a subsequent temperature ramp test [4]. b) The macroscopic changes undergone by (Np,Am,Pu,U)O_2 MOX fuel after irradiation in a fast breeder reactor for up to 24 hours [5]. 36

1.8 Schematic illustration of the key features (1-6) of irradiated UO_2 (left). The grain structure has been mapped onto an undoped SIMFuel micrograph (right) of Hiezl *et al.* [6]. 1) Soluble fission products remain in solution in the grain. 2) Volatile rare gases migrate to form either a) intragranular bubbles or b) intergranular bubbles that grow and eventually interlink (c). Other insoluble fission products precipitate out to form 3) metallic or 4) oxide particles. Extended defects such as 5) dislocations and 6) voids are generated due to radiation damage. 37

1.9 a) Micrograph showing the association of bubbles with (white) metallic precipitates at grain boundaries in irradiated UO_2. The early stages of bubble interlinking can also be seen (taken from [7]). b) The formation of small (100-300 Å bubbles) in the UO_2 matrix (green arrow) and larger bubbles at dislocation lines (red arrow). Association of the bubble with solid precipitates is also observed in this example (purple arrow) [8]. 40

1.10 a) TEM micrograph and SAED pattern from a grain boundary in SIMFuel showing small perovskite precipitates [9]. b) TEM micrograph of fission gas bubble (red arrow) association with a $BaZrO_3$ precipitate (green arrow) in LWR fuel at 4.5% burnup [10]. 41

2.1 Schematic of the Mott-Littleton regions centred around a defect [11]. 49

2.2 Representation of the periodic boundary conditions of the supercell method. The atomistic configuration of the primary cell is repeated to infinity in all directions [11]. 52

2.3 Representation of the shell model for a positively charged ionic core attached to a negatively charged shell with a spring of stiffness, k. 58

3.1 Timeline of the UO_2 interatomic potentials through the last four decades taken from Murphy *et al.* [12]. CRG refers to the potential developed in Chapter 6. 62

3.2 Thermal expansion of uranium dioxide as predicted by a range of empirical pair potentials [2, 13–23]. The experimental data of Fink *et al.* [24] is included for comparison. 64

3.3 Bulk modulus as a function temperature of uranium dioxide as predicted by a range of empirical pair potentials [2, 13–23, 25–34]. The experimental data of Hutchings *et al.* [35] is included for comparison. 65

4.1 Convergence of the zirconium vacancy, V''''_{Zr}, defect energy as function of region I radius. The selection of 13.0 Å for the region IIa radius ensures that the V''''_{Zr} defect energy is converged to within 0.1 eV. 72

4.2 Convergence of the zirconium vacancy, V''''_{Zr}, defect energy as function of region IIa radius. The selection of 34.0 Å for the region IIa radius ensures that the V''''_{Zr} defect energy is converged to within 0.01 eV. For all calculations in this figure the region I radius is fixed at 13.0 Å. 72

4.3 Partition enthalpies for tetravalent cations into a) $BaZrO_3$ and b) $SrZrO_4$ from uranium dioxide as a function of ionic radius by substitution at the Zr^{4+} site (reaction 4.7) and substitution at the Ba^{2+} site with charge compensation by an oxygen interstitial (reaction 4.8), an antisite (reaction 4.9), a Ba^{2+} vacancy (reaction 4.10) or a Zr^{4+} vacancy (reaction 4.11). 77

4.4 Change in lattice volume of $BaZrO_3$ and $SrZrO_3$ for tetravalent cation accommodation on the Zr^{4+} site as a function of ionic radius. 78

4.5 Combined change in lattice volume of both the gray phase and the uranium dioxide phases for tetravalent cation segregation by isovalent accommodation at the Zr^{4+} site. 79

4.6 The cubic perovskite structure of the grey phase. The A site species, Ba^{2+} or Sr^{2+}, are represented by green spheres, whilst the blue sphere indicate the positions of the B site species, Zr^{4+}, with O^{2-} shown in red. The 4 nearest positions of a divalent cation are identified with respect to a Zr^{4+} ion in the lower cube. 81

4.7 The lowest energy configuration for the $\{2T'_{Zr} : V^{\bullet\bullet}_{O}\}^{\times}$ cluster. The A site species, Ba^{2+} and Sr^{2+}, are represented by green spheres, whilst the yellow spheres indicate the positions of the substitutional trivalent cations occupying B sites, T'_{Zr}, with O^{2-} shown in red and the semi-transparent red cube indicating an oxygen vacancy, $V^{\bullet\bullet}_{O}$. 81

4.8 Partition enthalpies for trivalent cations into a) $BaZrO_3$ and b) $SrZrO_3$ from stoichiometric UO_2 as a function of ionic radius by reactions 4.12-4.22. Full and open symbols indicate mechanisms that occur via the Zr^{4+} and A^{2+} sites respectively, whilst half symbols identify reactions with accommodation at both $AZrO_3$ cation sites. 83

4.9 The lowest energy configuration for the $\{2T^{\bullet}_{A} : O''_{i}\}^{\times}$ cluster. The A site species, Ba^{2+} and Sr^{2+}, are represented by green spheres, whilst the yellow spheres indicate the positions of the substitutional trivalent cations at A sites, $T^{\bullet}_{A}$. Blue spheres indicate the B site species, Zr^{4+}, with O^{2-} shown in red and the semi-transparent red cube indicating an oxygen vacancy, $V^{\bullet\bullet}_{O}$. The interstitial oxygen forms a $\langle 110 \rangle$ split interstitial with another oxygen ion. 85

4.10 Partition enthalpies for trivalent cations into a) $BaZrO_3$ and b) $SrZrO_3$ from hyper-stoichiometric UO_{2+x} as a function of ionic radius by reactions 4.23-4.33. Full and open symbols indicate mechanisms that occur via the Zr^{4+} and A^{2+} sites respectively, whilst half symbols identify reactions with accommodation at both $AZrO_3$ cation sites. 86

4.11 Change in lattice volume of $BaZrO_3$ and $SrZrO_3$ as a function of ionic radius for trivalent cations on the Zr^{4+} site with charge compensation by oxygen vacancies for Cr^{3+} and Fe^{3+} and by self charge compensation via accommodation at both cation sites for In^{3+}, Lu^{3+}, Er^{3+}, Y^{3+}, Dy^{3+}, Gd^{3+}, Sm^{3+}, Nd^{3+}, Pr^{3+} and La^{3+}. 88

4.12 Combined lattice volume changes of both the grey phase and the uranium dioxide phase, as function of ionic radius [36], for trivalent cation segregation to the Zr^{4+} site with charge compensation by oxygen vacancies for Cr^{3+} and Fe^{3+} (reaction 4.13) and by self charge compensation via accommodation at both cation sites for In^{3+}, Lu^{3+}, Er^{3+}, Y^{3+}, Dy^{3+}, Gd^{3+}, Sm^{3+}, Nd^{3+}, Pr^{3+} and La^{3+} (reaction 4.14). 88

4.13 Partition enthalpies for trivalent cations into $BaZrO_3$ or $SrZrO_3$ from Cr-doped stoichiometric UO_2 and hyper-stoichiometric UO_{2+x} as a function of ionic radius by accommodation at the Ba site, $T^{\bullet}_{Ba}$, with charge compensation by Cr^{3+} substitution at the Zr^{4+} site, Cr'_{Zr}. 90

4.14 Change in lattice volume of $BaZrO_3$ and $SrZrO_3$, as a function of ionic radius, for trivalent cations on the Ba^{2+} site with charge compensation by Cr^{3+} substitution at the Zr^{4+} site. The defects occupy first nearest neighbour sites with respect to each other. 91

4.15 Combined change in lattice volume of both the grey phase and the uranium dioxide phase, as a function of ionic radius, for the segregation of trivalent cations at the Ba^{2+} site with charge compensation by Cr^{3+} substitution at the Zr^{4+} site. The defects occupy first nearest neighbour sites with respect to each other. 91

4.16 Partition enthalpies for tetravalent cation segregation into ZrO_2 from uranium dioxide as a function of ionic radius by isovalent substitution at the Zr^{4+} site. 93

4.17 The lowest energy configuration of the $\{2T_{Zr} : V_O^{\bullet\bullet}\}^{\times}$ cluster associated with the Cr^{3+} and Fe^{3+} trivalent cations. Blue and red spheres indicate the intrinsic Zr^{4+} and O^{2-} species respectively, with the semi-transparent cube identifying the oxygen vacancy, $V_O^{\bullet\bullet}$. Substitutional trivalent cations at Zr^{4+} sites, T'_{Zr}, are shown by yellow spheres. 94

4.18 The lowest energy configuration of the $\{2T_{Zr} : V_O^{\bullet\bullet}\}^{\times}$ cluster associated with the In^{3+}, Lu^{3+}, Er^{3+}, Y^{3+}, Dy^{3+}, Gd^{3+} and Sm^{3+} trivalent cations. Blue and red spheres indicate the intrinsic Zr^{4+} and O^{2-} species respectively, with the semi-transparent cube identifying the oxygen vacancy, $V_O^{\bullet\bullet}$. Substitutional trivalent cations at Zr^{4+} sites, T'_{Zr}, are shown by yellow spheres. 94

4.19 The lowest energy configuration of the $\{2T_{Zr} : V_O^{\bullet\bullet}\}^{\times}$ cluster associated with the Nd^{3+}, Pr^{3+} and La^{3+} trivalent cations. Blue and red spheres indicate the intrinsic Zr^{4+} and O^{2-} species respectively, with the semi-transparent cube identifying the oxygen vacancy, $V_O^{\bullet\bullet}$. Substitutional trivalent cations at Zr^{4+} sites, T'_{Zr}, are shown by yellow spheres. 95

4.20 Partition enthalpies for trivalent cations into ZrO_2 from stoichiometric UO_2, as a function of ionic radius, by accommodation at the Zr^{4+} site with charge compensation by oxygen vacancies (reactions 4.38 and 4.39) or by self-interstitials (reactions 4.40 and 4.41). 95

4.21 Partition enthalpies for trivalent cations into ZrO_2 from hyper-stoichiometric UO_{2+x} as a function of ionic radius by accommodation at the Zr^{4+} site with charge compensation by oxygen vacancies (reactions 4.42 and 4.43) or by self-interstitials (reactions 4.44 and 4.45). 96

4.22 Partition enthalpies for tetravalent cations into $CrUO_4$ from hyper-stoichiometric UO_{2+x} as a function of ionic radius by substitution, at least partly, at either Cr^{3+} or U^{5+} via reactions 4.46-4.54. 98

4.23 Partition enthalpies for trivalent cations into $CrUO_4$ from hyper-stoichiometric UO_{2+x} as a function of ionic radius by isovalent substitution at Cr^{3+} sites (reaction 4.55) or substitution at the U^{5+} (reactions 4.56-4.59). 99

5.1 a) Schematic illustration of the fluorite structure of UO_2 projected in the ⟨100⟩ direction. Uranium and oxygen ions are indicated by green and red spheres respectively. Note that uranium cations are located on two parallel planes. The fluorite unit cell is identified by the orange box. ⟨100⟩-type and ⟨110⟩-type uranium vacancy mediated uranium migration mechanisms are shown by purple and orange arrows respectively. Uranium-oxygen bonds are shown in light grey. b) The enthalpy barriers without charge compensating defects for ⟨100⟩-type and ⟨110⟩-type U^{4+} migration as well as ⟨110⟩-type migration for U^{3+} and U^{5+}. 107

5.2 Uranium vacancy migration enthalpy as a function of metastable cluster enthalpy relative to the most stable cluster $\{V_U'''' : 2V_O^{\bullet\bullet}\}^\times$ cluster. Green triangles represent configurations of the $\{V_U'''' : 2V_O^{\bullet\bullet}\}^\times$ cluster where both charge compensating oxygen vacancies are within 9.5 Å of the migrating uranium vacancy. Configurations where only one oxygen vacancy is bound are shown by red circles. The migration when all constituent defects are in the dilute limit is shown by the black square. The blue horizontal line represents the migration enthalpy for the most stable $\{V_U'''' : 2V_O^{\bullet\bullet}\}^\times$ cluster configuration (6.60 eV). The cluster with the lowest total migration enthalpy (6.41 eV) is circled. . . . 110

5.3 a) The most stable and b) lowest total migration enthalpy configurations of the $\{V_U'''' : 2V_O^{\bullet\bullet}\}^\times$ cluster for stoichiometric UO_2. U^{4+} and O^{2-} ions are represented by green and red spheres respectively. Similarly, uranium and oxygen vacancies are indicated by green and red semi-transparent cubes respectively. The migration pathway of the U^{4+} cation into the the uranium vacancy is shown by the black arrow. 111

5.4 Uranium vacancy migration enthalpy as a function of metastable cluster enthalpy relative to the most stable $\{V_U'''' : 4U_U^\bullet\}^\times$ cluster. Green diamonds represent configurations of the $\{V_U'''' : 4U_U^\bullet\}^\times$ cluster where all U^{5+} ions are within 9.5 Å of the migrating uranium vacancy. Configurations where one, two or three U^{5+} ions are bound are represented by pink triangles, blue triangles and red circles respectively. Finally, the case where all constituent defects are in the dilute limit is shown by the black square. The blue horizontal line represents the migration enthalpy for the most stable $\{V_U'''' : 4U_U^\bullet\}^\times$ cluster (7.23 eV). The configuration with the lowest total migration enthalpy (6.82 eV) is circled. 113

5.5 a) The most stable and b) lowest total migration enthalpy configurations of the $\{V_U'''' : 4U_U^\bullet\}^\times$ cluster for hyperstoichiometric UO_{2+x}. U^{4+} and U^{5+} cations are represented by green and blue spheres respectively. For clarity the oxygen sublattice is omitted. The migration pathway of the U^{4+} cation into the the uranium vacancy is shown by the black arrow. 114

6.1 Scaling of cation-cation ρ terms as a function of cation radius (coordination number VIII) [36]. The value of $\rho_{UU} = 0.275$, from Grimes *et al.* [2], is the reference point. 124

6.2 Example a) oxygen density and b) uranium embedding functions derived using the new potential. Red lines indicate the effect of embedding a uranium cation potential within the densities of one, two and three oxygen densities at 2 Å. The interaction per uranium-oxygen pair is sequentially less negative (i.e. less favourable) as the coordination of uranium increases. 127

6.3 a) The potential energy between an actinide cation and one, two or three equidistant oxygen anions as a function of separation per actinide-oxygen pair. The difference in potential shape depends on the coordination environment of the actinide cation and demonstrates the many-body nature of this potential set. b) The interactomic forces as given by the first derivative of potential energy (a) with respect to separation. 128

6.4 Comparison of experimental data (solid lines) for CeO_2 [37], ThO_2 [38], UO_2[39], NpO_2 [40], PuO_2 [40], AmO_2 [41] and CmO_2 [42] with the data points from MD simulations using the new potential. 130

6.5 Comparison of the new many-body potential potential with experimental data for the temperature dependence of bulk modulus for UO_2 [35]. Figure 3.3 is included for comparison with previous pair potentials (see Chapter 3). 133

6.6 Bulk modulus as a function of temperature calculated using the new potential for CeO_2, ThO_2, UO_2, NpO_2, PuO_2, AmO_2 and CmO_2. Although not plotted here, equation 6.9 has been fitted to these data with the coefficients B_0 and ϵ summarized in table 6.6. 133

6.7 Change in enthalpy relative to 300 K as a function of temperature, calculated using the new potential with polynomial fitting for PuO_2 (equation 6.12), ThO_2 (equation 6.11) and UO_2 (equation 6.10) shown in green, purple and red, respectively. The specific heat is calculated from the derivative of these fitted polynomials and reported alongside experimental results shown by a solid black line [39, 43]. 135

6.8 The superposition of atomic positions sample every 1 fs over 200 fs during the moving interface method for UO_2 at 3000 K. Uranium and oxygen positions are represented by red and blue dots respectively. 136

6.9 The different configurations of the Schottky defect investigated using the EAM model. The oxygen vacancies (red cubes) are in a first nearest neighbour configuration with respect to the actinide vacancy (green cube). The oxygen vacancies are occupy first (SD1), second (SD2) or third (SD3) nearest neighbour sites with respect to each other. Actinide and oxygen ions are represented by green and red spheres respectively. 138

6.10 The variation of Schottky defect energy for different cluster configurations as a function of supercell size in UO_2 [44]. 139

7.1 A schematic illustration of the NEQM used here to study the thermal conductivity in MD. Uranium and oxygen atoms are shown by green and red spheres respectively. 147

7.2 a) The variation of lattice parameter as a function of temperature for UO_2, ThO_2 and three $(U_xTh_{1-x})O_2$ compositions. Experimental data has been included for UO_2 [24], ThO_2 [38] and $(U_{55}Th_{45})O_2$ [45]. b) The deviation of the MD lattice parameter calculated from that predicted by Vegard's Law. 150

7.3 The variation of the linear thermal expansion coefficient as a function of temperature for UO_2, ThO_2 and three $(U_xTh_{1-x})O_2$ compositions. 151

7.4 The variation of the enthalpy increment as a function of temperature for UO_2, ThO_2 and three $(U_xTh_{1-x})O_2$ compositions. 152

7.5 The variation of the specific heat capacity at constant pressure as a function of temperature for UO_2, ThO_2 and three $(U_xTh_{1-x})O_2$ compositions. Experimental data for UO_2 is included for comparison [39]. 153

7.6 The variation of oxygen diffusivity as a function of a) temperature and b) composition for UO_2, ThO_2 and three $(U_xTh_{1-x})O_2$ compositions. 154

7.7 The variation of oxygen activation enthalpy as a function of temperature for UO_2, ThO_2 and three $(U_xTh_{1-x})O_2$ compositions. 155

7.8 The fraction of oxygen sites that lie within 0.005 eV of the corresponding oxygen vacancy formation enthalpy for UO_2, ThO_2 and three $(U_xTh_{1-x})O_2$ compositions. From left to right, the peaks correspond to sites coordinated by 4, 3, 2, 1 and 0 uranium cations (or 0, 1, 2, 3 and 4 thorium cations). There is only one value for UO_2 and ThO_2 as represented by vertical lines. 156

7.9 The fraction of oxygen interstitial sites that lie within 0.005 eV of the corresponding oxygen interstitial formation enthalpy for UO_2, ThO_2 and three $(U_xTh_{1-x})O_2$ compositions. There is only one value for UO_2 and ThO_2 as represented by vertical lines. 157

7.10 a) The variation of lattice parameter as a function of temperature for UO_2, PuO_2 and three $(U_xPu_{1-x})O_2$ compositions. Experimental data has been included for UO_2 [24], PuO_2 [40]. b) The deviation of the MD lattice parameter calculated from that predicted by Vegard's Law. 158
7.11 The variation of the linear thermal expansion coefficient as a function of temperature for UO_2, PuO_2 and three $(U_xPu_{1-x})O_2$ compositions. 159
7.12 The variation of the enthalpy increment as a function of temperature for UO_2, PuO_2 and three $(U_xPu_{1-x})O_2$ compositions. 160
7.13 The variation of the specific heat capacity at constant pressure as a function of temperature for UO_2, PuO_2 and three $(U_xPu_{1-x})O_2$ compositions. 161
7.14 The variation of oxygen diffusivity as a function of a) temperature and b) composition for UO_2, PuO_2 and three $(U_xPu_{1-x})O_2$ compositions. 162
7.15 The variation of oxygen activation enthalpy as a function of temperature for UO_2, PuO_2 and three $(U_xPu_{1-x})O_2$ compositions. 163
7.16 The fraction of oxygen sites that lie within 0.005 eV of the corresponding oxygen vacancy formation enthalpy for UO_2, PuO_2 and three $(U_xPu_{1-x})O_2$ compositions. From left to right, the peaks correspond to sites coordinated by 4, 3, 2, 1 and 0 plutonium cations (or 0, 1, 2, 3 and 4 uranium cations). There is only one value for UO_2 and PuO_2 as represented by vertical lines. . 165
7.17 The fraction of oxygen interstitial sites that lie within 0.005 eV of the corresponding oxygen interstitial formation enthalpy for UO_2, PuO_2 and three $(U_xPu_{1-x})O_2$ compositions. There is only one value for UO_2 and PuO_2 as represented by vertical lines. 165
7.18 a) The variation of the reciprocal of thermal conductivity as a function of the reciprocal of supercell length for perfect UO_2 at a range of temperatures. The y-intercepts indicate the reciprocal of bulk thermal conductivity. b) Shows the bulk values as a function of temperature for unirradiated UO_2 with comparison to the phonon contribution to thermal conductivity of Wiesenack *et al.* [46] as recommended by the IAEA [39]. 168

7.19 The effect of the addition of thorium to UO_2 up to the $(U_{50}Th_{50})O_2$ solid solution composition, as predicted using the non-equilibrium method. Equation 7.13 has been fitted to the data points from MD and is shown using solid lines. 169

7.20 The degradation of ThO_2 thermal conductivity by the addition of uranium at thorium sites, as predicted using the non-equilibrium method. Equation 7.13 has been fitted to the data points from MD and is shown using solid lines. . . 170

7.21 The variation of thermal conductivity as a function of uranium composition for the $(U_xTh_{1-x})O_2$ solid solution for a range of temperatures. This data is based on the fitting of equation 7.13 to the MD data in Figures 7.19 and 7.20. 171

7.22 Schematic of a slab of area A and thickness dx cut through a medium containing scattering defects with cross sectional area σ. 172

7.23 The variation of thermal conductivity as a function of uranium composition and temperature for the $(U_xTh_{1-x})O_2$ solid solution. MD data are shown with black spheres whilst the result of fitting equation 7.21 to this data is indicated by the surface. 173

7.24 The effect of the addition of uranium to PuO_2 up to the $(U_{75}Pu_{25})O_2$ solid solution composition, as predicted using the non-equilibrium method. Equation 7.13 has been fitted to the data points from MD and is shown using solid lines. 175

7.25 The effect of the addition of plutonium to UO_2 up to the $(U_{50}Pu_{50})O_2$ solid solution composition, as predicted using the non-equilibrium method. Equation 7.13 has been fitted to the data points from MD and is shown using solid lines. 176

7.26 The variation of thermal conductivity as a function of uranium composition for the $(U_xPu_{1-x})O_2$ solid solution for a range of temperatures. This data is based on the fitting of equation 7.13 to the MD data in Figures 7.24 and 7.25. 177

7.27 The variation of thermal conductivity as a function of uranium composition and temperature for the $(U_xPu_{1-x})O_2$ solid solution. MD data are shown with black spheres whilst the result of fitting equation 7.21 to this data is indicated by the surface. 178

7.28 The variation of thermal conductivity as a function of oxygen defect concentration and temperature for a 5×5×200 UO_2 supercell. MD data are shown with black spheres whilst the result of fitting equation 7.19 to this data is indicated by the surface. 179

7.29 The variation of oxygen diffusivity as a function of uranium composition, x, for $(U_xPu_{1-x})O_2$ (left) and $(U_xTh_{1-x})O_2$ (right). 181

7.30 The fraction of defect sites that lie within 0.005 eV of a given defect enthalpy. The distribution of a) vacancy and b) interstitial enthalpies for $(U_{0.5}Th_{0.5})O_2$ compared to $(U_{0.5}Pu_{0.5})O_2$. The distribution of isolated oxygen Frenkel enthalpies is shown in c) by combining every possible combination vacancy-interstitial pair. For the end member systems there are only single values as represented by vertical lines. 183

7.31 The thermal conductivity of $(U_xPu_{1-x})O_2$ (left) and $(U_xTh_{1-x})O_2$ (right) at a number of temperatures as a function of uranium composition, x. 184

A.1 The variation of the a and b lattice parameters of tetragonal ZrO_2 as a function of temperature using the new potential with comparison to experimental data [47–49]. 218

A.2 The variation of the c lattice parameter of tetragonal ZrO_2 as a function of temperature using the new potential with comparison to experimental data [47–49]. 219

A.3 The variation of the a:c ratio of tetragonal ZrO_2 as a function of temperature using the new potential with comparison to experimental data [47–49]. When $\frac{a}{c} = 0.7071$ the tetragonal structure has changed to the fluorite structure (i.e. above 2000 K). 219

Chapter 1

Introduction

1.1 Outline

In many forms of energy production a source of potential energy is identified and converted into useful kinetic or easily accessible stored energy. The combustion of conventional fossil fuel converts chemical potential energy, that is stored by interatomic bonds, into kinetic energy by releasing it as heat during the oxidation of hydrogen and carbon. Alternatively, hydroelectricity makes use of the gravitational potential energy of bodies of water located above sea level. Nuclear power releases energy stored within the nucleus of an atom, contributing to a rise in reactor temperature that can be utilised in much the same way as in any conventional power plant. A basic schematic of an example nuclear power plant is presented in Figure 1.1. Heat generated by fission is removed from the reactor by coolant in the primary loop then used to generate steam in the secondary loop. This ensures the reactor core is fully isolated from the secondary loop, limiting the risk of radioactive material being carried out of the containment building to the conventional island. Notable exceptions to this are boiling water reactors (BWRs) that directly utilise steam generation within the reactor core dispensing with the distinction between the primary and secondary loops. The electrical generator is powered by the steam turbines. The majority of reactors must be lo-

cated close to a source of cool water (e.g. sea or a river) so that the steam can be condensed and returned to the secondary loop (note that some designs use air cooling).

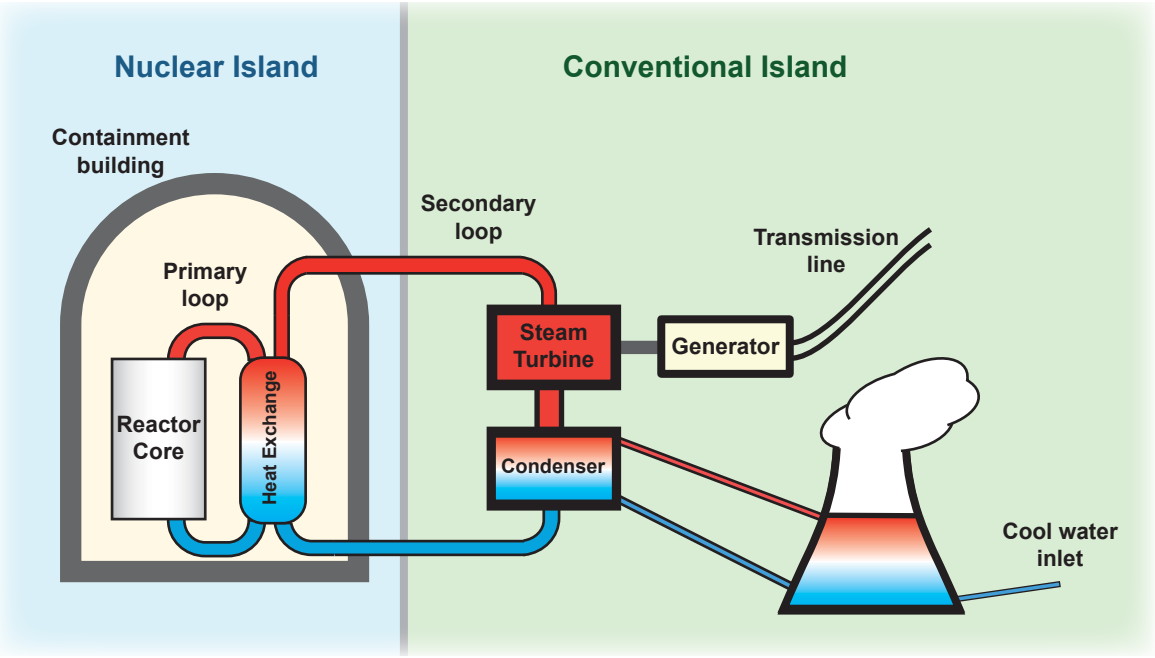


Figure 1.1: Schematic diagram of an example nuclear power station. The nuclear island (left) is separated from the conventional island (right) by the containment building. The secondary loop extracts heat from the primary loop, which is connected to the reactor core, via a heat exchange. Steam generated in the heat exchange is passed over the steam turbines to power an electrical generator. Using water from the cooling tower the steam is condensed and returns to the heat exchange.

During use in a nuclear reactor the fuel properties are altered significantly due to fission and reactor conditions. This underpins the fuel performance and effectively limits the amount of energy that can be extracted before it must be removed from the reactor: this is referred to as burnup and is measured in gigawatt-days per tonne of heavy metal (GWd/tHM). Alternatively, it can be measured as the percentage of heavy metal ions that have undergone fission (where 1 % $\approx$ 10 GWd/tHM). This chapter will discuss the various factors that affect fuel performance during the fuel cycle and the way atomic scale simulations can give insight into the underlying mechanisms. Some useful definitions and concepts follow:

- **Nuclear fission** - Discussion of how nuclear fission enables the release of the nuclear binding energy by the conversion of a large nucleus to two (or more) smaller, more stable nuclei (fission products). This is the most important concept as maintaining a stable fission reaction underpins the selection of suitable reactor materials. Furthermore, the generation of a wide variety of high velocity fission products alters the chemical composition of the fuel, whilst causing radiation damage.

- **The fuel cycle** - Nuclear fuel experiences a wide range of conditions and changes throughout the fuel cycle. This involves the extraction of uranium ore from the ground, the manufacturing of nuclear fuel, irradiation within a reactor, storage of spent nuclear fuel (SNF), reprocessing and eventual disposal. The work of this thesis focuses on factors that govern the performance of fuel throughout irradiation within a nuclear reactor, however, it is important to understand the other stages of the fuel cycle.

- **Nuclear reactor designs** - A broad range of nuclear reactor designs have been developed over 60 years of operations. The selection of appropriate reactor materials, that enable a stable fission reaction, will be discussed in terms of the conditions exhibited by different designs. To understand the key features of SNF it is important to understand the different conditions fuel is expected to perform under.

- **Key features of nuclear fuel** - The macroscopic and microscopic changes in the fuel during reactor operation will be discussed. A particularly strong focus will be given to the accommodation of fission products in their various forms throughout the fuel. The wide variety of elements produced during fission (from inert gases to metals) provides a broad set of challenges that affect fission product distribution and the degradation of fuel performance.

- **Defects in crystals** - Both the host fuel and the precipitates that form during operation exhibit crystalline structures. Fission products dissolved in these phases are accommodated as impurity defects. By understanding the energetics involved in creating these defects, or in defect transport, one can gain insight to the factors determining

fission product distribution and release from the fuel. Alternatively, defects also alter many thermophyical properties of a crystal, such as thermal conductivity and specific heat.

- **Thesis objectives** - In the context of the sections listed above the key research objectives of this thesis will be discussed. More specifically, this involves the application of atomistic simulation techniques to problems involved in fission product distribution, migration of gases and the evolution of thermophysical properties over a broad temperature range.

1.2 Nuclear fission

Nuclear energy makes use of the variation in binding energy of nuclei across the periodic table. Nuclear binding is governed by the attractive strong nuclear force acting between nucleons and the repulsive proton-proton Coulombic interactions. The release of this binding energy during a nuclear reaction gives rise to a very high kinetic energy for the reaction products. The binding energy per nucleon is shown in Figure 1.2, demonstrating that any nuclear process that moves towards the most stable isotope, Fe^{56}, is exothermic. This is achieved by making massive nuclei less massive (fission) or by making tiny nuclei more massive (fusion).

Although fission can occur spontaneously, the probability of fission is greatly increased through the transmutation of a large nucleus through neutron capture. The resultant isotope is in an excited state and, rather than simply relaxing through gamma emission, it undergoes fission; splitting into two smaller isotopes, or fission products. As shown in Figure 1.2, fission product nucleons are more tightly bound than in the fissile species, thus, contributing to a large release of energy. The combined rest mass of the fission products is less than that of the fissile species and this mass deficit is equated to the binding energy through Einstein's mass-energy equivalence relationship [50]. Importantly, several neutrons are also released, one of which (on average) must go on to trigger another fission event in

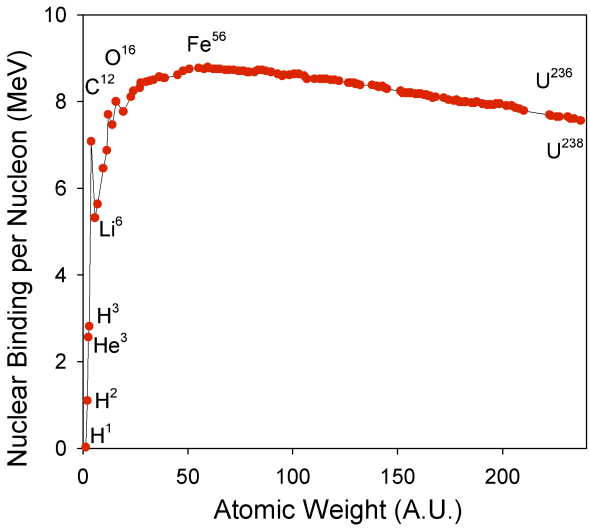


Figure 1.2: The binding energy per nucleon for a range of isotopes [1].

order to create a chain reaction. Figure 1.3 shows the fission of U^{235}, which is by far the most common fissile isotope in fresh nuclear fuel, to form the fission products Kr^{92} and Ba^{141}. During reactor operation there is significant transmutation of the non-fissile U^{238} to other actinides [51, 52]. In particular, neutron capture by U^{238} and two subsequent beta decays generates significant quantities of the fissile isotope Pu^{239}. Fission of Pu^{239} contributes more and more to energy generation within the fuel as burnup proceeds. As will be discussed further in section 1.4, reactor materials interact with neutrons and must be selected carefully to ensure a continuous and stable nuclear reaction.

Typically each fission event creates two fission products. However, there are multiple ways of splitting a large nucleus into two (or more) constituent parts and certain pairs of fission products have an associated probability of being generated [2]. Consequently, there are a wide range of possible fission products each with an associated yield that is proportional to their likelihood of being generated. This is governed by the neutron flux and the available fissile isotopes, therefore, it is reactor and burnup dependent. Figure 1.4 shows the number of fission products generated per 100 fission events as a function of atomic number for pressurised water reactor (PWR) fuel at 2.9 % burnup [2]. The accommodation and distribution of such species in the fuel varies between reactors.

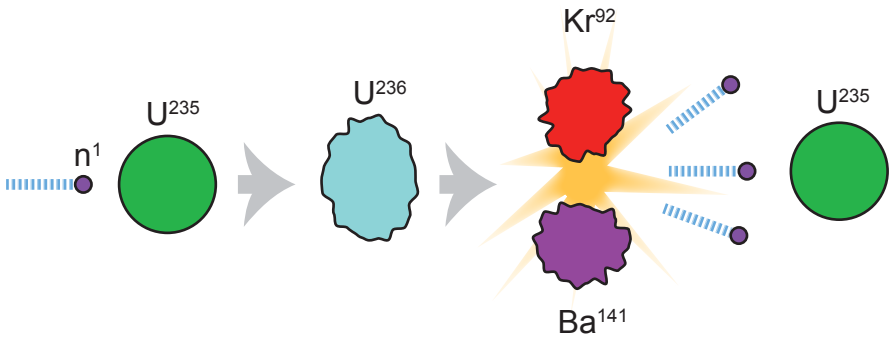


Figure 1.3: Neutron absorption by a U^{235} nucleus creating an excited and unstable U^{236} nucleus. Here this short lived isotope fissions to form two fission products (e.g. Kr^{92} and Ba^{141}) and several high velocity neutrons. For a chain reaction to occur one of these neutrons must fission a second U^{235} nucleus.

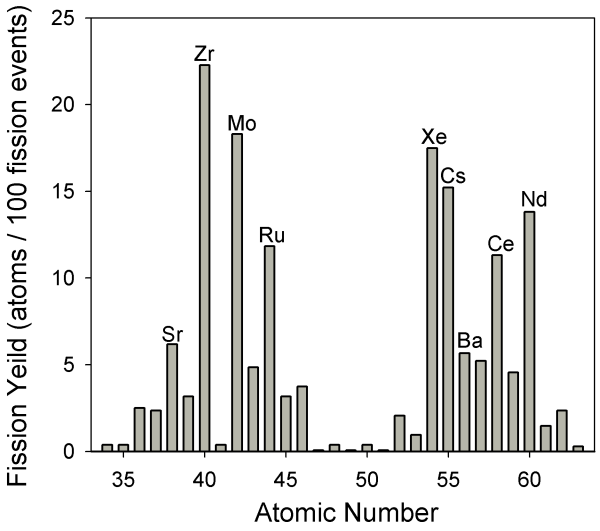


Figure 1.4: The fission product yield for a PWR fuel rod after 2.9 % burn-up. Those fission products with particularly high yields are identified [2].

1.3 The fuel cycle

Nuclear fuel undergoes significant changes throughout its life, from its initial form as uranium ore in the ground to its role in a nuclear reactor (typically as uranium dioxide) where its composition is altered significantly through the generation of a wide range of fission products. Nuclear decay then further alters the composition of SNF during the storage and disposal phases of the nuclear fuel cycle. In addition to the compositional changes experienced due to these nuclear processes, the wide variety of reactor designs and conditions create SNFs that each behave differently. An overview of the nuclear fuel cycle is presented in Figure 1.5.

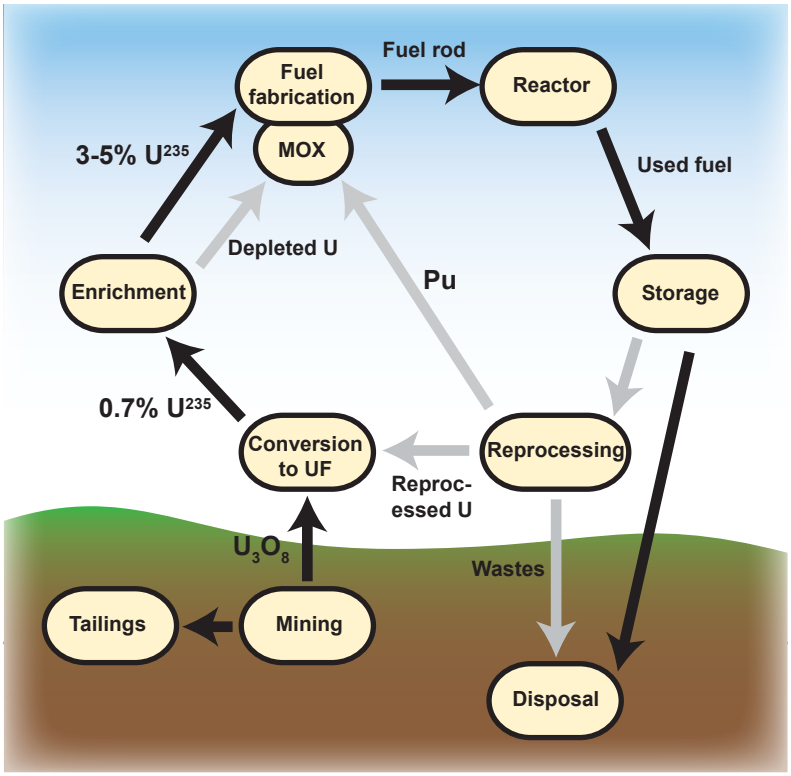


Figure 1.5: Illustration of the key processes in the nuclear fuel cycle. The open cycle is identified with black arrows, whilst grey arrows are used to shown reprocessing aimed at closing the fuel cycle.

Uranium ore is mined and converted to its most stable form, U_3O_8 (yellow cake), for transport to an enrichment facility [52]. Natural uranium contains around 0.7 % of the fissile

uranium isotope U^{235}. For most reactor designs (see section 1.4) this level is not sufficient to achieve a chain reaction, so U_3O_8 is converted to the gaseous UF_6 which can undergo enrichment, for example in a centrifuge [53]. Typically 1.5-3.5 % enriched UO_2 is required for most commercial nuclear reactors operating today [3]. Notable exceptions are the MAGNOX [54, 55] and CANDU [55] designs, which use natural uranium (see section 1.4). Depleted uranium containing less than 0.7 % U^{235} is produced as a waste product.

Enriched UF_6 is converted to UO_2 and is then pressed and sintered into ceramic pellets with a typical grain size of 5-30 μm, however, dopants such as Cr [4] are sometimes used to increase the grain size with some beneficial results for fuel performance. Alternatively, Gd can be used as a burnable poison (that absorbs neutrons to limit the beginning of life reactivity), although this results in significant degradation of the thermal conductivity [56] due to the introduction of phonon scattering centres and may increase the centreline pellet operating temperature. The pellets are bound in a metallic cladding to create the fuel pin. The primary role of the cladding is to prevent fission product release into the coolant and to maintain the structural integrity of the fuel. The fuel pins are arranged into a fuel assembly that can be introduced into the reactor core. The details of the fuel assembly and fuel pin are precisely controlled for any particular reactor design to ensure safe and efficient operation.

The change in temperature across the fuel pellet (<1000 K over ~3 mm [57]) and very high radiation damage throughout operation cause the nature of the fuel to change significantly. The SNF microstructure is outlined in more detail in the next section but some key features will be mentioned here in the context of the fuel cycle. Highly radioactive species are created either through the transmutation of U^{238} to minor actinides or by the creation of radioactive fission product isotopes. Additionally, ramping the temperature up and down during normal operation cycles induces significant macroscopic cracks and pores [4]. Microscopic damage, such as dislocations and voids, are introduced through radiation damage due to fission fragments and the later decay of unstable fission products. Eventually these mechanisms degrade the fuel performance to such an extent that it must be removed from

the reactor before all heavy metal isotopes are fissioned.

Even after the fuel is removed from the reactor and fission has ceased, it continues to generate heat through the decay of the radioactive transuranic and fission product species. As such, the fuel must be stored whilst the decay heat is reduced sufficiently so that reprocessing or disposal can proceed [58]. Two storage methods exist: i) spent fuel ponds or ii) dry cask storage. The water pool option involves packing fuel assemblies into racks and submersing them in about 6 m of water to ensure sufficient gamma shielding. The high neutron absorption cross section (particularly when boronated) enables water to provide neutron shielding, as well as heat removal through natural convection. High density neutron absorbing racks are being considered to increase spent fuel pond capacity, whilst minimising the risk of a criticality accident [58]. After storage in a spent fuel pond for at least one year the fuel can be transferred to dry storage. Typically this consists of a steel cylinder that is welded or bolted shut and surrounded by additional steel or concrete to provide further shielding. Although the decay heat is significantly reduced during the initial year in a spent fuel pond, further cooling must be provided by natural air convection through slots at the top and bottom of the outer case [58].

Once the fuel has cooled sufficiently it can undergo reprocessing through, for example, the PUREX process to separate Pu and U from the fission products. Subsequently, (U,Pu)O_2 mixed oxide (MOX) fuel can be produced for use in conventional thermal reactors. This contributes to a partial closure of the fuel cycle that helps increase the energy extracted per tonne of uranium. Additionally, the quantity of long lived radiological actinides in waste is reduced [59]. If reprocessing techniques can be developed to enable the efficient extraction of minor actinides and these can be fabricated into transuranic containing fuel for use in fast breeder reactors, the fuel cycle can be fully closed with very significant benefits for waste disposal [59]. (U,Th)O_2 is also considered as a major candidate MOX fuel in order to utilise the highly abundant global thorium deposits [60].

The long-term disposal of nuclear waste requires a waste form that is highly stable over geological timescales to prevent the release of radioactive isotopes in the distant future. The

waste stream from the reprocessing facility can be fed with glass into a furnace. The melt is poured into a steel canister resulting in a vitrified waste form, where the fission products and minor actinides are immobilised in the glass. Currently there are no disposal facilities in operation and the waste is stored either in its vitrified form or as SNF in ponds and canisters. The most likely disposal route will be a deep repository within a stable geological environment. The deep geological repository (DGR) concept is based on a multi-barrier approach, whereby, the geological surroundings, the engineered containment and the wasteform all limit the release of radioactive isotopes to the environment.

Countries that are considering a once through, or open, fuel cycle must validate the direct disposal of SNF. This is of particular concern for the UK given the decision to close the thermal oxide reprocessing plant (THORP) in 2018 [61]. Understanding the stability of UK SNF over geological timescales is crucial in order to justify any safety case for a DGR. Key factors that will determine the release of fission products from SNF in a DGR are the distribution and mobility of fission products in the fuel as well as the dissolution rate of the host UO_2 matrix. A detailed discussion of typical SNF characteristics is given in section 1.5. As this varies from reactor to reactor it has the potential to create particular challenges for the direct disposal of UK SNF, given the unique reactor designs (see section 1.4).

Alternative fuel cycles are being studied based on other combinations, notably with ThO_2 since the rate of higher actinide breeding is much lower and due to its relative abundance ($\approx$4 times that of uranium) [62]. The higher actinides are problematic for waste forms as they often have long half lives, therefore, the incorporation of minor actinides such as AmO_2, CmO_2 and NpO_2 with UO_2 or ThO_2 is desirable so that these species can undergo transmutation in a reactor [63] or accelerator driven system [64, 65]. The long term sustainability of nuclear energy could be enhanced if such a range of fuel types could be incorporated into the fuel cycle [66].

1.4 Nuclear reactors

As mentioned previously, in order for significant proportions of energy to be released from uranium it is necessary to initiate a chain reaction. In other words, every fission event must trigger at least one further fission. The fission of U^{235} creates 2 or 3 neutrons on average [67]. There are several possible outcomes for these neutrons: a) absorption and fission of U^{235}, b) absorption and transmutation of U^{238} or other reactor materials (e.g. Fe^{58}) and c) leakage from the reactor. Clearly a) is favourable if one wishes to initiate a chain reaction. There are several ways in which conventional reactor designs ensure a bias towards fission of U^{235}. Moderators are used to slow down (thermalise) the very high energy (fast) neutrons to velocities that are more likely to cause fission of U^{235} (or Pu^{239}). The enrichment of uranium increases the ratio of U^{235} to U^{238} and, therefore, increases the chance of neutron-U^{235} collisions. Typically, reactor materials that are transparent to neutrons, such as Zircalloy (for fuel cladding), are selected to minimise parasitic neutron losses. Neutron reflectors are also used at the reactor boundaries to minimise neutron leakage to the environment. A generalised schematic of the two most prominent UK designs is presented in Figure 1.6a.

The following discussion will deal with the selection of appropriate reactor materials in terms of their thermal and neutronic properties according to the operating conditions of a particular design. A balance is made in all cases to select materials with high radiation damage tolerance, high thermal conductivity, neutron moderating abilities and neutron transparency but materials that can also operate at high temperatures to promote thermal efficiency. Maintaining these properties throughout the fuel lifetime is a critical factor in maximising the energy extracted from the fuel. Even in modern reactors the burnup is limited to 6 % of heavy metal atoms (i.e. 60 GWd/t) [68].

During 60 years of nuclear operations around the world, a wide range of nuclear reactors have been developed. Commonly, early non-commercial reactor programs, such as Windscale [69], were developed in the aftermath of world war two as countries hurried to breed

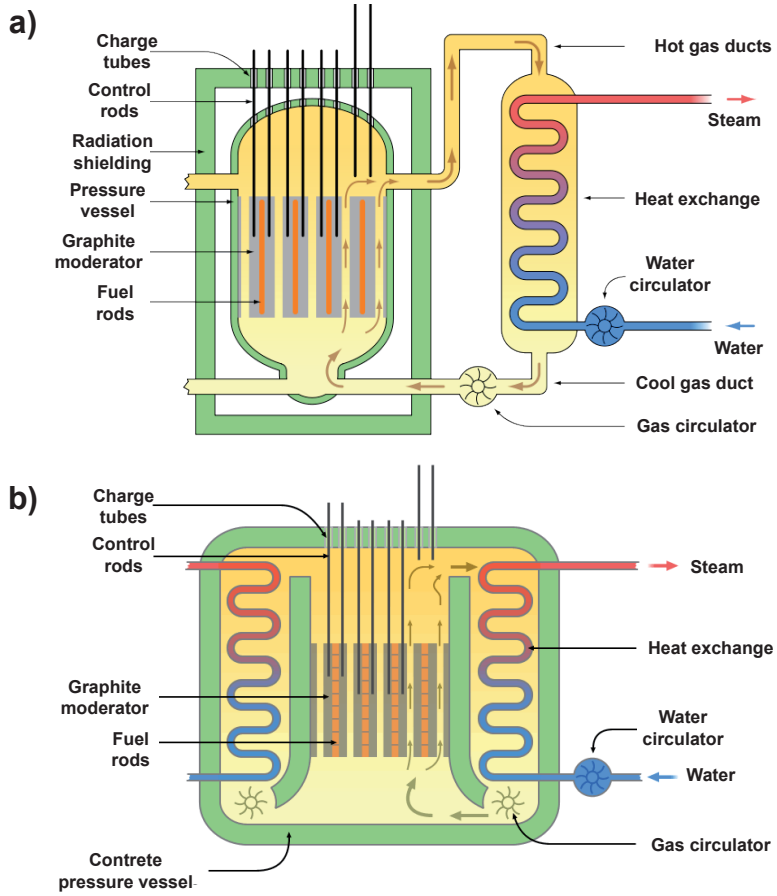


Figure 1.6: a) Schematic illustration of a MAGNOX reactor and b) of an AGR reactor based on the description of [3]. The MAGNOX uses a two loop coolant system, similar to the PWR design but with a CO_2 coolant rather than water, whilst an internal steam generator is used in the AGR design.

Pu for their own nuclear weapons programs. Metal uranium fuel was frequently used for ease of Pu extraction after irradiation. The work presented here is not concerned with the production of nuclear weapon materials, however, the early UK commercial MAGNOX reactors used metal uranium even as the generation of electricity became an end in itself. The natural uranium metal was bound in a cladding made of magnesium-aluminium alloy from which the MAGNOX reactor gets its name. This cladding material was selected, in addition to a CO_2 gas coolant, due to their low neutron neutron absorption properties. Thermalisation of fast neutrons was achieved by using a graphite moderator. The high uranium density of the metal in conjunction with the neutron-transparent reactor materials negated the need

for uranium enrichment. Very similar reactor designs have been built in France and North Korea [70]. Nonetheless the low damage tolerance and poor chemical stability of natural metal uranium was not sufficient for the second generation high burnup power reactors, so the world moved towards enriched UO_2 during the 1970s.

The second generation of reactors can generally be split into light water reactors (LWR) and gas-cooled reactors. In virtually all generation II designs UO_2 fuel was adopted due to its chemical stability, high melting point and enhanced radiation damage tolerance, thus, enabling improved thermal efficiency and higher burnups to be achieved [3]. The ability of UO_2 to accommodate high levels of non-stoichiometry [71] is particularly useful as the chemical composition changes during irradiation. The high temperature operation of such reactors means that LWRs can be split into boiling water reactors (BWR) and pressurised water reactors (PWR). The PWR prevents the boiling of the coolant water under normal operation by maintaining a pressure of around 152 atmospheres in the primary loop and uses a heat exchange to generate steam in a lower pressure secondary loop [3]. The BWR design has a lower primary loop pressure and utilises steam generation directly from the reactor core to power the steam turbines. Although efficiency is enhanced in BWRs, activation products and FP release to the turbines creates a radiological hazard during maintenance. Unlike most other LWR designs, the Reaktor Bolshoy Moshchnosti Kanalnyy (RBMK) [3] design uses graphite in addition to water as a moderator [72]. Alternatively, gas-cooled reactors have also been used, particularly in the UK. The UK advanced gas cooled reactor design (AGR) used a CO_2 coolant in conjunction with a separate graphite moderator. The design is a natural evolution from the MAGNOX reactor but the use of enriched UO_2 fuel in conjunction with CO_2 coolant enables high temperature operations for which neither the zircalloy cladding of LWRs nor the MAGNOX cladding are suitable, so stainless steel is used instead. The preferential oxidation of LWR zirconium based clad limits hyper-stoichiometry in the UO_2 matrix [73] but the extent to which this is true for AGRs is not clear, as stainless steel has a highly passive Cr_2O_3 layer.

Although the melting point of UO_2 is much greater than for uranium metal, the thermal

conductivity is relatively poor so the fuel pellet radius is kept very thin to prevent melting. An additional feature of AGRs is a central bore hole in the pellet designed to avoid centre line temperatures exceeding the melting point. For nearly all the generation II designs the UO_2 fuel must be enriched to compensate for its low uranium density, as well as, neutron absorption by either the cladding in AGRs or by the coolant in LWRs. However, one notable exception is the CANDU reactor [3] which uses a pressurised water system but, instead of conventional water, it uses deuterium water (or D_2O). Deuterium can be described as neutron saturated and, therefore, has a low neuron capture cross section making it relatively transparent, however, it still acts as a moderator [3]. Furthermore, the relatively low operating temperature enables transparent Zr cladding to be used. Consequently, natural UO_2 is sufficient to provide the reactivity required to achieve criticality despite the relatively low uranium density of UO_2.

Generation III reactors designs are very similar to generation II reactors but with a focus on increased power output and enhanced passive safety. Fundamentally, the reactor cores are much the same as for previous LWR designs but each plant will operate more primary reactor loops in tandem to maximise the power output of a particular site. This is, in part, due to difficulties in creating a new licensed site for reactor operation. Instead the current UK renaissance will aim to build on existing nuclear sites. A strong focus on passive safety mechanisms for loss of coolant accidents should help mitigate the risks associated with the most prominent disasters of the past, ensuring lessons have been learnt. In particular, the European pressurised reactor (EPR) features an improved core catcher [74] designed to limit the consequences of meltdown, whilst AP1000s feature a passive backup coolant system that uses condensation [75].

1.5 Key features of spent nuclear fuel

The changes that UO_2 pellets undergo during irradiation will be discussed here. Understanding the atomic processes that govern the key features of SNF is important for under-

standing fuel performance in the reactor and its long term stability for the direct disposal in a DGR. The research reported in this thesis contributes to this.

1.5.1 Macroscopic damage

During reactor operation the fuel pellet experiences extreme radial temperature gradients, from around 1400 K at the centre to the reactor operating temperature across just 3 mm. Heating and cooling during refuelling cycles creates additional thermal stresses. Figure 1.7a) shows macroscopic cracks and pores in an irradiated UO_2 pellet following a temperature ramp test [4]. Radial cracking can be observed in the rim region near the cladding and at the central region. In the intermediate region, between the rim and the centre, circumferential cracking dominates.

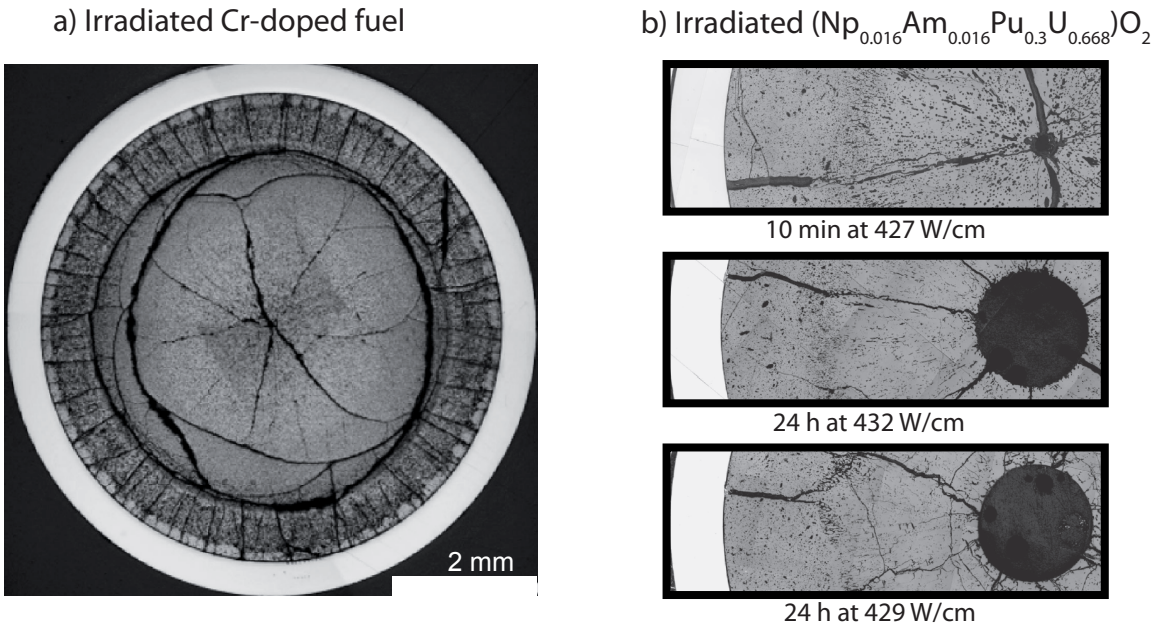


Figure 1.7: a) Ceramographic cross section of UO_2 pellets showing macroscopic cracks and pores following irradiation in a BWR and a subsequent temperature ramp test [4]. b) The macroscopic changes undergone by (Np,Am,Pu,U)O_2 MOX fuel after irradiation in a fast breeder reactor for up to 24 hours [5].

Figure 1.7b) shows very little circumferential cracking in MOX fast breeder reactor fuel that has not undergone temperature ramping [5]. However, the evolution of a large hole can be clearly observed due to the migration of voids up the temperature gradient and their accumulation at the centre. This a common feature for LWR fuels [76].

1.5.2 Fission product distribution

As discussed in section 1.2 a wide range of species are generated as fission products during reactor operation (Figure 1.4). These fission products are to a greater or lesser extent soluble in the UO_2 lattice. Figure 1.8 shows a schematic illustration of the irradiated fuel microstructure throughout which the fission products are distributed.

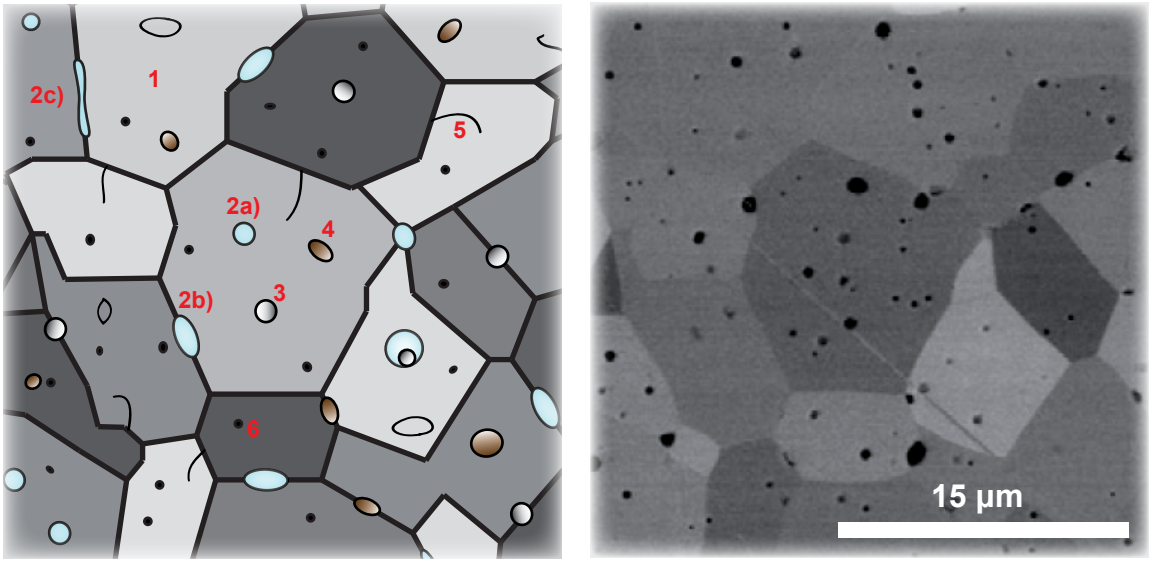


Figure 1.8: Schematic illustration of the key features (1-6) of irradiated UO_2 (left). The grain structure has been mapped onto an undoped SIMFuel micrograph (right) of Hiezl *et al.* [6]. 1) Soluble fission products remain in solution in the grain. 2) Volatile rare gases migrate to form either a) intragranular bubbles or b) intergranular bubbles that grow and eventually interlink (c). Other insoluble fission products precipitate out to form 3) metallic or 4) oxide particles. Extended defects such as 5) dislocations and 6) voids are generated due to radiation damage.

Since fission products vary widely in their chemical and physical interactions with the UO_2

lattice; their relative importance cannot be considered simply in terms of their yields alone. Generally speaking fission products can be split into four categories [2]:

1. **Soluble fission products** - A wide range of fission products exhibit some degree of solubility in UO_2. In particular, Y, Nb and the lanthanides are found in solid solution in UO_2 over a sufficiently large range of stoichiometry and composition [77]. The high solubility of lanthanides in both UO_2 and UO_{2+x} has been shown using atomistic simulation by Middleburgh *et al.* [78]. This is especially true for hyper-stoichiometric UO_{2+x} where oxidation of uranium to the 5+ charge state provides favourable charge compensating defects for accommodation of the lanthanides as trivalent cations. Sr also exhibits solubility in the UO_2 lattice but this is highly dependent on the stoichiometry of the fuel: Kleykamp *et al.* [79] state that Sr solubility increases by an order of magnitude in UO_2 when compared to $UO_{1.94}$. In the latter case, where solution becomes unfavourable, Sr is precipitated into Ba-containing oxide precipitates (see below). Despite the similarity between Ba and Sr, Ba exhibits a much lower solubility as reported by Sari *et al.* [80] and by Lucata *et al.* [9]. Ce exhibits solubility in the UO_2 matrix at concentrations even exceeding those obtained at high burnup [81, 82], whereas, Zr will become insoluble above 0.4 mole % (about 1 % burnup) [83]. In total, soluble fission products represent a yield of around 30-49 % (based on Figure 1.4) depending on the particular conditions of the fuel.

2. **Volatile fission products** - A number of the insoluble fission products are known to be unable to form stable secondary phases. In particular, the rare gases Kr and Xe are highly insoluble in the UO_2 matrix and are unable to react with other fission products to form precipitates due to their inert nature. Nonetheless, they are generated in the UO_2 matrix due to fission and must migrate through the bulk to regions where accumulation may occur, leading to bubble formation. The exact mechanism of bubble formation is not known but it has been suggested that Xe and Kr may form bubbles associated to secondary metal or oxide precipitates, although it is not clear if the bubbles initiate precipitate formation or vice versa (see Figure 1.9a) [7]. Similarly, bubbles

can also pin to dislocations, as shown in Figure 1.9b [8]. The formation and growth of fission gas bubbles strongly influences fuel performance as it degrades the mechanical properties, thermal conductivity and causes fuel swelling. Grain boundary bubbles grow as fission gases migrate through the bulk, leading to bubble interconnection (see Figure 1.9a) and eventual fission gas release from the pellet [84]. The rapid acceleration of this process under very high temperature conditions, such as during a loss of coolant accident (LOCA), is of great importance to operational safety. Xe is thought to migrate within Schottky defects through the bulk grain [85, 86]. I and Br are also highly volatile leading to a significant proportion of their yields being released from the pellet [87–89]. Although atomistic simulations [90–92] suggest I is accommodated at Schottky defects, diffusion may occur via oxygen or uranium vacancies depending on non-stoichiometry. Therefore, limiting the availability these defects could help minimise I concentrations at the fuel-clad gap and limit stress corrosion cracking (SCC) of the cladding. Alternatively, I is said to react with Cs and become trapped in the fuel, however experiments indicate Cs and I are at different places in the fuel making this unlikely [79]. Based on Figure 1.4, the volatile fission products represent 13-25 % of the total fission product yield.

3. **Metallic precipitates** - A wide range of fission products are not readily oxidised to a valence state that would enable easy solid solution in UO_2. Instead Ru, Mo, Tc, Rh, Pd, Ag, Cd, In, Sn and Sb all precipitate to form metallic particles [6, 79, 93, 94]. These secondary phases are composed mainly from the 4d transition metals from which they get their name, the 5-metal particles. Alternatively, these precipitates are referred to as the white phase due to the relative brightness in an SEM image (see Figure 1.9a) or the ϵ-ruthenium phase (due to the large Ru fission product yield). The Mo content is governed by the oxygen potential of the fuel. As fission proceeds and the uranium content is reduced, oxygen is more readily available resulting in the oxidation of Mo to MoO_2 which, although insoluble in the UO_2 lattice, can be accommodated in secondary oxide precipitates [79]. Mo, therefore, acts as a buffer to the hyper-stoichiometry of the fuel and, consequently, may reduce the solubility of

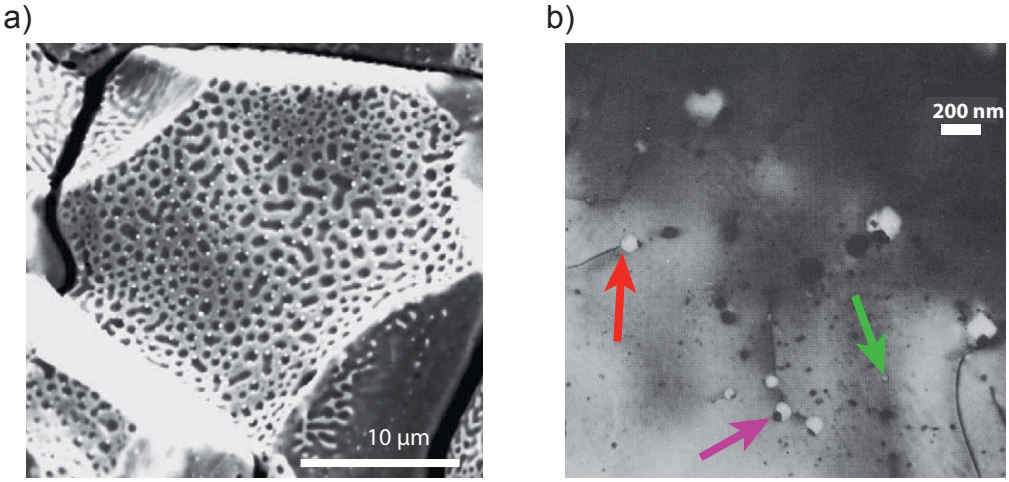


Figure 1.9: a) Micrograph showing the association of bubbles with (white) metallic precipitates at grain boundaries in irradiated UO_2. The early stages of bubble interlinking can also be seen (taken from [7]). b) The formation of small (100-300 Å bubbles) in the UO_2 matrix (green arrow) and larger bubbles at dislocation lines (red arrow). Association of the bubble with solid precipitates is also observed in this example (purple arrow) [8].

many fission products in the host UO_2 matrix [78]. The proportion of fission products that are accounted for in metallic precipitates is around 27 % but this reduces with the oxidation of Mo at higher burnups.

4. **Oxide precipitates** - A range of fission products are insoluble in the UO_2 host matrix and precipitate as secondary oxide phases. Collectively these phases are referred to as the grey phase due to their relative brightness in an SEM compared to the white phase [79]. The exact composition, and even existence, of the grey phase is highly dependent on reactor conditions and history, however the main components are Ba, Zr, U and Pu. Kleykamp *et al.* [79] report the grey phase in high temperature fast breeder reactor fuel as (Ba, Sr, Cs)(U, Pu, Mo, Zr, RE)O_3, where RE indicates unidentified rare earth metals. This can be treated as a substituted $BaZrO_3$ cubic perovskite compound. Similarly, Sari *et al.* [80] report the presence of similar grey phase precipitates in $(U_{0.8},Pu_{0.2})O_3$ simulated fuel whilst Lucata *et al.* [9] also observed $BaZrO_3$ type precipitates in high burnup LWR SIMFuel. It must be pointed out that the presence

of grey phase precipitates in the low temperature PWRs has not been noted. This may indicate that, although the grey phase is the most stable way to accommodate these fission products, there is a significant kinetic barrier preventing precipitation. It is not surprising then that the grey phase has only been observed in the high temperature fast breeder fuel [79] or in simulated fuel that has been sintered at high temperatures whilst containing the fission product species [6, 9]. AGR fuel operates at higher temperatures and the presence of the grey phase has also been noted in AGR SNF [95]. This indicates that the low diffusivity of the main grey phase components, Ba and Zr, is the limiting factor in determining the presence of such secondary phases. Similarly, further substitution of fission products, such as the rare earth metals, may be limited according to their diffusivity following a fission event (discussed further in Chapter 4).

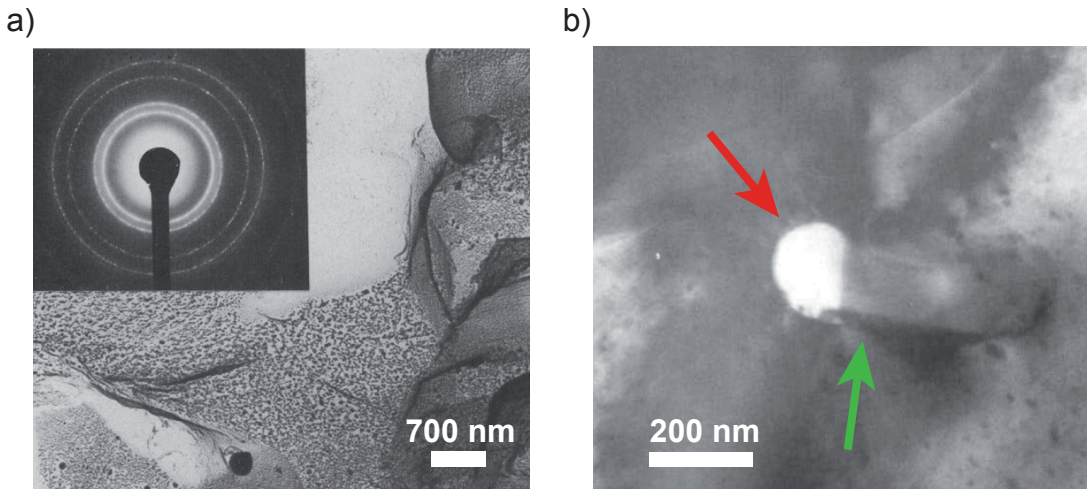


Figure 1.10: a) TEM micrograph and SAED pattern from a grain boundary in SIMFuel showing small perovskite precipitates [9]. b) TEM micrograph of fission gas bubble (red arrow) association with a $BaZrO_3$ precipitate (green arrow) in LWR fuel at 4.5% burnup [10].

1.6 Defects in crystals

Atoms bound by metallic, covalent or ionic interactions can form a regular array that exhibits a high degree of order. The symmetry of this crystal can be described by the periodic

repetition of a unit cell in all directions. The most stable crystal structure depends on the size of the constituent species, the type of bonding, the composition, the entropy, the temperature and the pressure.

Examining the atomic interactions within a crystal enables many perfect crystal properties to be investigated. For example, thermal expansion, elastic constants, thermal conductivity and specific heat. These properties are altered by the formation of point defects or extended defects such as dislocations and grain boundaries. Atomistic studies are useful for calculating the thermodynamics involved in defect formation and the consequences for observable materials properties or defect mobility.

The thermally equilibrated defect concentration, $[D]$, at temperature, T, is dependent on the defect formation energy, E_f and the concentration of possible defect sites, n_D [44]:

$$[D] = n_D \exp\left(-\frac{E_f}{k_B T}\right) \tag{1.1}$$

where k_B is the Boltzmann constant. The crystal structure determines the number of available sites for vacancies, interstitials and larger defect configurations. Atomic scale calculations can be used to determine the defect formation energy (see Chapter 2). Defect calculations must consider the full defect processes, such as oxygen Frenkel pair formation [96]:

$$\mathrm{O}_\mathrm{O}^\times \rightarrow \mathrm{O}_\mathrm{i}'' + \mathrm{V}_\mathrm{O}^{\bullet\bullet} \tag{1.2}$$

where $[\mathrm{O}_\mathrm{i}''] = [\mathrm{V}_\mathrm{O}^{\bullet\bullet}]$ in a closed system. Importantly, defect clustering can alter both the number of sites and the formation energy. Understanding the energy required for the accommodation of fission products as defects in a crystal structure can give insight into the distribution of fission products within the fuel.

Similarly, defect mobility is governed by the energy barrier between two stable defect sites. An Arrhenius relationship can be used to describe the diffusivity, D:

$$D = D_0 \exp\left(-\frac{E_a}{k_B T}\right) \tag{1.3}$$

where D_0 is the pre-exponential term and E_a is the activation energy [159]. Contributions to the activation energy include the energy barrier between two stable sites as well as the formation energy for migration assisting defects. The pre-exponential term is determined by the attempt frequency, dimensional restraints and the correlation effects.

1.7 Thesis objectives

There are range of issues that atomic scale simulation can be used to investigate with regard to nuclear fuel performance. In particular, the fission product solubility in UO_2 is known to be a strong function of non-stoichiometry from both atomistic simulation [78, 97] and experimental observation [79]. Furthermore, the level of non-stoichiometry in the fuel has been identified as a potential difference between UK AGR fuel and LWR fuel due to the different claddings. Previous atomistic simulations do not consider the possibility for preferential fission product solution in secondary oxide phases, as seen by Kleykamp *et al.* for fast breeder fuel [79]. If this behaviour is dependent on the non-stoichiometry of UO_2 possible differences in fission product distribution between AGR SNF and LWR SNF may arise. Similarly, the migration of uranium vacancies as the rate limiting step in Xe and Kr bulk diffusion could be another source of differences between reactor types that exhibit different levels of excess oxygen.

The broad range of temperatures experienced by a nuclear fuel pellet during the fuel cycle underpins the importance of an atomistic model to reproduce the thermophysical properties of fuel materials from 300 K to 3000 K. In Chapter 3 a detailed comparison of the atomistic models reveals the difficulty previous potentials have with accurately describing the elastic constants, thermal expansion and phase stability of UO_2. In order to describe atomic scale behaviour consistently, over all temperatures of interest, an improved potential model must be developed. Therefore, the results of this thesis can be split into a two pronged approach investigating: i) the effect of non-stoichiometry using previous potential models (Chapters 4 and 5) and ii) the effect of temperature using an improved model (Chapters 6 and 7).

- **Chapter 4: Fission product segregation to secondary oxide phases** - Using a previous potential that provides a good description of UO_2, UO_{2+x} and a wide range of fission products, the role of secondary oxide precipitates in fission product distribution will be investigated. Firstly, the precipitation of the (Ba,Sr)ZrO_3 grey phase will be studied as a function of non-stoichiometry in the UO_2 phase. Subsequently, the thermodynamic driving force for soluble fission products (in particular the rare earth elements) to segregate to these precipitates will be investigated. The segregation of fission products to BaO, SrO and ZrO_2 must also be calculated due to their presence in the secondary oxide phases [79]. Additionally, the precipitation of $CrUO_4$ is possible in hyper-stoichiometric Cr-doped fuel [4] and its role in fission product distribution will be similarly identified.

- **Chapter 5: Uranium vacancy migration in UO_2 and UO_{2+x}** - The role of non-stoichiometry on the mobility of uranium vacancies will be studied. In particular, excess oxygen is incorporated in the fuel through oxygen interstitial charge compensated by the oxidation of U^{4+} to U^{5+}. As such, the dominant positive charge compensating species that cluster with uranium vacancies are U^{5+} cations in UO_{2+x} rather than oxygen vacancies in UO_2. Therefore, uranium vacancy migration energies will be calculated within clusters that can form in UO_2 and UO_{2+x}. Furthermore, the change in the energy barrier for uranium vacancy migration is analysed as function of the different cluster configurations. This extends previous DFT studies [98] that only considered the most favourable configuration.

- **Chapter 6: A many-body potential for the description of actinide oxides** - As will be discussed in detail in Chapter 3, current pairwise atomistic models do not describe UO_2 particularly well over the full range of temperatures typical of different reactors. Therefore, a new model is derived in Chapter 6 to improve the description of the temperature dependent properties of the actinide oxide series from 300-3000 K. This is achieved by making actinide-oxygen interactions dependent on the coordination environment and by fitting to a broad experimental data set.

- **Chapter 7: Modelling the behaviour of mixed oxides** - Using the new model (of Chapter 6) the thermal expansion, specific heat capacity, oxygen diffusivity and thermal conductivity of the (U,Th)O_2 and (U,Pu)O_2 systems will be investigated over a wide temperature range. It is important to study the role of a non-uniform cation sublattice on these properties in order to identify the effect of U^{238} transmutation in conventional fuel, whilst also building a data set for the introduction of MOX fuels into the fuel cycle [60].

In addressing these problems a number of issues arrose, which were not addressed. These are described in Chapter 8, future work.

Chapter 2

Methodology

2.1 Static methods

As will be discussed in greater detail in section 2.3, interatomic forces can be determined using empirical potentials and then utilised in atomistic simulations. A number of simulation techniques have been implemented in this thesis, however, they generally fall into two distinct categories: static methods and molecular dynamics. The former will be described here and the latter in section 2.2.

2.1.1 Static energy minimisation

The 3D energy surface, as a function of atomic configuration, is analogous to a 2D landscape containing hills (maxima), valleys (minima) and passes (saddle points). The total energy of a system, U_{Total}, is described as the sum of all individual atom potential energies, E_i:

$$U_{Total}(\mathbf{r_1},...,\mathbf{r_n}) = \sum_i E_i(\mathbf{r_1},...,\mathbf{r_n}) \tag{2.1}$$

where the energy of an individual atom is defined in terms of its separation from all other atoms in the system. As discussed later (see section 2.3), a number of empirical models have been developed to describe the energy of interaction between atoms.

The aim of an energy minimisation algorithm is to adjust the atomic configuration until all atoms sit at the bottom of their potential well. An initial guess can be made in which atoms will be positioned at different locations of the energy surface, some closer to minima and some closer to maxima. The gradient of the energy surface at the location of any given atom (force) is used to identify the direction and distance that the atom is moved during one iteration of the energy minimisation algorithm. The system configuration is adjusted sequentially until it has reached the local energy minimum. Convergence is achieved once the change in $U(\mathbf{r_1},...,\mathbf{r_n})$ between two consecutive minimisation iterations falls below a chosen value. Similarly, a convergence criteria can be applied to the atomic forces such that they must also have fallen below certain value. Furthermore, the Hessian of the system (second derivative matrix) is said to be positive definite if the system is at a local minimum. This ensures that the system is not in an unstable zero force configuration, such as a maxima or saddle point. As the system is in the minimum closest to the initial configuration, it is often necessary to sample a large number of initial guesses so that one may be confident that the global minimum has been correctly identified. This is important when there are several possible crystals structures for a particular system. For example in the MO_2 system there are a number of possible polymorphs (α-PbO_2, Anatase, Baddeleyite etc.) and upon energy minimisation the cell parameters will relax but the symmetry of the system may well remain. All possible structures must be used as a starting point in separate energy minimisation calculations so that metastable polymorphs can be discounted (see Chapter 3). Alternatively, when considering defects in complex systems or large defect clusters, many initial defect configurations must be sampled to ensure the global minimum is attained.

During minimisation various restrictions, such as fixed lattice parameters or an external pressure, can be placed on the system. This is utilised in latter sections to extend energy minimisation calculations beyond the study of defect energies to include the investigation

of defect volumes.

2.1.2 Defect calculations within the Mott-Littleton approach

The Mott-Littleton method [99] enables the investigation of defects at the dilute limit, thus negating the issue of defect self interaction when using periodic boundary conditions in the supercell method (see section 2.1.4). It enables the embedding of a defective lattice within a perfect crystal that extends to infinity. The crystal around the defect is divided into two concentric spherical regions centred around the defect, whereby the inner and outer regions are labelled I and IIa (see Figure 2.1). Region IIb is defined as the remainder of the crystal from the edge of regions IIa to infinity. At this stage there is no difference between regions IIa and IIb so the total energy of the system can be defined in terms of the energy of region I (U_{11}) and regions II (U_{22}), so that:

$$U_{total}(\mathbf{x},\mathbf{y}) = U_{11}(\mathbf{x}) + U_{12}(\mathbf{x},\mathbf{y}) + U_{22}(\mathbf{y}) \tag{2.2}$$

where $\mathbf{x}$ and $\mathbf{y}$ are the ionic coordinates of region I and region II respectively. U_{12} represents the interaction energy between regions I and II.

The configuration in region I, $\mathbf{x}$, is allowed to fully relax as these atoms are the most perturbed by the defect. Conversely, the atoms in region II are weakly perturbed and their atomic displacements are determined by treating it as a polarisable continuum:

$$\mu = \frac{Vqr}{r^3}(1 - \epsilon_0^{-1}) \tag{2.3}$$

where μ is the polarisation per unit cell with volume V and the distance to the defect is r. The polarisation has two contributions; the ionic polarisation (described empirically using the shell model) and the polarisation arising from ionic displacements. The latter is used to determine the displacements of atoms in region II, $\mathbf{y}$. As these displacements are relatively small their relationship with the energy of region II, U_{22}, is approximately harmonic:

$$U_{22} = \frac{1}{2}\mathbf{yAy} \tag{2.4}$$

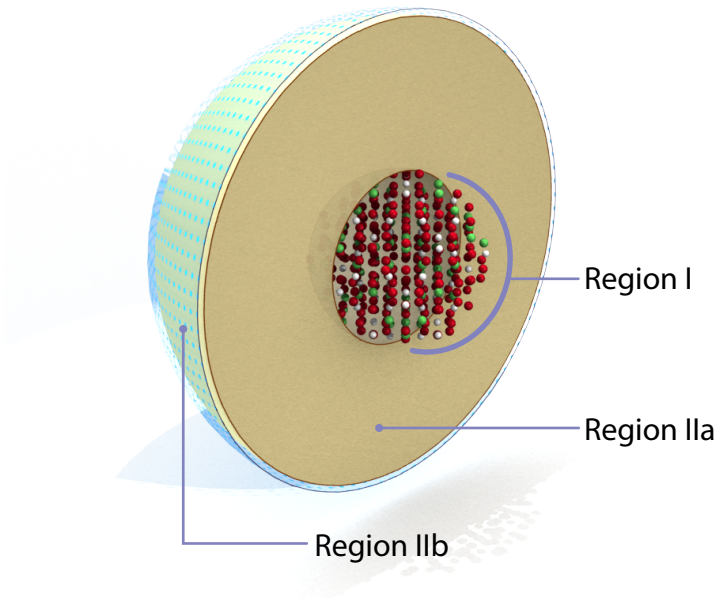


Figure 2.1: Schematic of the Mott-Littleton regions centred around a defect [11].

where **A** is the Hessian force matrix of region II. However, as region II is infinite **A** would have infinite dimensions and could not be evaluated. This issue can be avoided by applying the condition that the displacements of region II are at their equilibrium values, $\mathbf{y_e}$:

$$\left.\frac{\partial U_{total}(\mathbf{x},\mathbf{y})}{\partial \mathbf{y}}\right|_{\mathbf{y}=\mathbf{y_e}} = \left.\frac{\partial U_{12}(\mathbf{x},\mathbf{y})}{\partial \mathbf{y}}\right|_{\mathbf{y}=\mathbf{y_e}} + \mathbf{A}\mathbf{y} = 0 \tag{2.5}$$

$$\left.\frac{\partial U_{12}(\mathbf{x},\mathbf{y})}{\partial \mathbf{y}}\right|_{\mathbf{y}=\mathbf{y_e}} = -\mathbf{A}\mathbf{y} \tag{2.6}$$

This condition simply states that for small deviations from equilibrium positions in region II the forces are equal and opposite to the interaction forces with region I, thus, ensuring that the net force of the whole system remains zero. Therefore, it is possible to eliminate the energy of region II from equation 2.2 by using equation 2.6:

$$U_{total}(\mathbf{x},\mathbf{y}) = U_{11}(\mathbf{x}) + U_{12}(\mathbf{x},\mathbf{y}) - \frac{1}{2}\left(\frac{\partial U_{12}(\mathbf{x},\mathbf{y})}{\partial \mathbf{y}}\right)\mathbf{y} \tag{2.7}$$

Nonetheless, the crystal still extends to infinity and so does the total system energy. However, in the limit very far from the defect the perfect and defective systems converge. There-

fore, a cancellation in terms can be achieved by calculating the defect energy (i.e. the difference in energy between the defective system and the perfect system) which has a finite value:

$$U_{defect}(\mathbf{x},\mathbf{y}) = U^{d}_{total}(\mathbf{x},\mathbf{y}) - U^{p}_{total}(\mathbf{x},\mathbf{y}) \tag{2.8}$$

Now the distinction between regions IIa and IIb must be made. Region IIb only interacts with region I through its polarisation (equation 2.3) due to the net defect charge of region I and can be treated as a continuum, whereas region IIa interacts with region I through Coulombic interactions explicitly but excludes short range interactions. Thus, the difference between the radius of region IIa and region I must be at least the short-range cut off used in the empirical potential definition. This ensures the short range interactions are not artificially cut off by the region IIa radius.

Using the method outlined in section 2.1.1 the defect energy, U_{defect}, can be minimised by adjusting the atomic configurations in regions I and II. Based on an initial guess of the defect configuration, typically by adding or removing atoms at perfect lattice or interstitial sites, the local minimum energy configuration can be found.

2.1.3 Rational functional optimisation within Mott-Littleon

During energy minimisation the system Hessian is used to confirm that the system is indeed at a stable defect configuration. The Hessian can also be used determine that, although the net system forces are zero (stationary), the system is in fact unstable or, alternatively, at a saddle point between two stable configurations. This approach is utilised in the Rational Functional Optimisation (RFO) method in the general utility lattice programme (GULP) [100]. Saddle points are a special case where the system forces are zero but the Hessian has a single negative eigenvalue. In this case all atoms in the system, bar one, have positive second energy derivatives in all directions and are, therefore, at stable positions. However, the one remaining atom has a negative second energy derivative in a particular direction but

has positive second energy derivatives in all orthogonal directions. This is consistent with one atom in the system being at a saddle point between two stable configurations.

When implementing this method an initial guess must be made for the saddle point configuration, typically involving a defect occupying the mid point between two stable arrangements. The system is then iteratively refined until the required criteria have been satisfied. It is important to examine the final atomic configuration to confirm the arrangement makes sense with respect to the corresponding stable end points.

2.1.4 Defects in supercell statics

The lattice can be described by taking a limited number of repeats of the primitive cell and applying periodic boundary conditions to this supercell (see Figure 2.2). As such, the positions of all atoms in the primary supercell are repeated periodically at intervals according to the supercell dimensions. This ensures that atomic forces in the primary cell imitate those expected in the bulk crystal. However, when studying a defective lattice the accuracy of the simulation is limited by the choice of supercell size. By adding a defect to the primary supercell cell you also include defects in all of the repeated cells (i.e. a lattice of defects) and, as such, a defect concentration has been generated, rather than an isolated defect.

If one wishes to study defects in the dilute limit, as can be achieved explicitly with the Mott-Littleton method, the concentration must be sufficiently low that self defect interactions are negligible. As with the Mott-Littleton method the defect energy is the difference between the defective and the perfect lattice. By converging the defect energy with respect to increasing supercell size one can ensure that the defect-defect distance is sufficiently large that the dilute limit is approached. Although this is relatively simple for charge neutral defects for which interactions are only short range and the supercell remains neutral, there are a number of problems when simulating charged defects. The infinite repetition of point charges in a periodic system creates an unphysical net charge that must cancelled out using a neutralising background jellium [101–103]. The electrostatic energy of a periodically re-

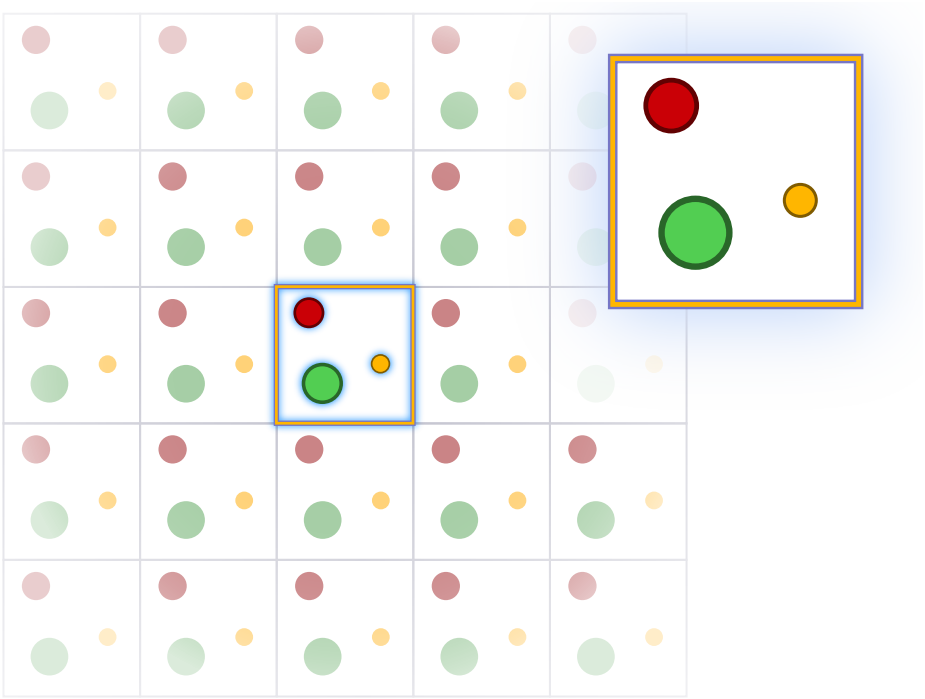


Figure 2.2: Representation of the periodic boundary conditions of the supercell method. The atomistic configuration of the primary cell is repeated to infinity in all directions [11].

peating finite system containing a point charge q and a neutralising background jellium is the Madelung energy [101, 102],

$$E_M = -\frac{q^2\alpha}{2\epsilon L} \tag{2.9}$$

where $\alpha = 2.7393$ for fluorite cubic systems, ϵ is the permittivity of the medium and L is the supercell length. The formation energy of a charged point defect in a supercell of size L can therefore be written as,

$$E_f(L) = E_f^{\infty} - \frac{q^2\alpha}{2\epsilon L} \tag{2.10}$$

where E_f^{∞} is the defect energy in the isolated limit. The defect energies, $E_f(L)$, can be calculated in a number of supercells of varying sizes and plotted as a function of $\frac{1}{L}$. The isolated defect energy, E_f^{∞}, is found by extrapolating this linear function to $\frac{1}{L} = 0$.

2.2 Molecular dynamics simulation

Using a set of forces defined using an interatomic potential (section 2.3), the temporal evolution of the atomic accelerations, velocities and positions can be determined according to Newton's laws of motion [104]. By assigning kinetic energy to the system molecular dynamics (MD) allows the atomic trajectories to be sampled. The gradient of the potential energy of an atom, $\phi_i(\mathbf{r}(t))$, with respect to position is used to determine the direction and magnitude of the atomic acceleration:

$$\ddot{\mathbf{r}}(t) = \frac{\mathbf{F}_i(\mathbf{r}(t))}{m_i} = \frac{-\nabla\phi_i(\mathbf{r}(t))}{m_i} \tag{2.11}$$

where in Cartesian coordinates the force on an atom, $\mathbf{F}_i$, is given by the gradient of the potential energy, $\nabla\phi_i = \hat{\mathbf{x}}\frac{\partial\phi_i}{\partial x} + \hat{\mathbf{y}}\frac{\partial\phi_i}{\partial y} + \hat{\mathbf{z}}\frac{\partial\phi_i}{\partial z}$, where the mass of the atom is m_i and $\ddot{\mathbf{r}}$ is the acceleration.

The atomic configuration is used in conjunction with the interatomic potential, to determine the acceleration of the atoms at a given time t (equation 2.11). Using the velocity Verlet integration method [105, 106] it is possible to determine the atomic position and velocity at time $t + \delta t$ as follows. A second order differential equation can be split into two first order differential equations - i.e. let $\mathbf{a}(t) = \dot{\mathbf{v}}(t) = \ddot{\mathbf{r}}(t)$ and $\mathbf{v}(t) = \dot{\mathbf{r}}(t)$. By Taylor expanding $\mathbf{r}(t + \delta t)$ about $\mathbf{r}(t)$ and $\mathbf{v}(t + \delta t)$ about $\mathbf{v}(t)$ one gets:

$$\mathbf{r}(t + \delta t) = \mathbf{r}(t) + \delta t\dot{\mathbf{r}}(t) + \frac{\delta t^2}{2}\ddot{\mathbf{r}}(t) + O\delta t^3 \tag{2.12}$$

$$\mathbf{v}(t + \delta t) = \mathbf{v}(t) + \delta t\dot{\mathbf{v}}(t) + \frac{\delta t^2}{2}\ddot{\mathbf{v}}(t) + O\delta t^3 \tag{2.13}$$

All of the above terms can defined in terms of known quantities except for $\ddot{\mathbf{v}}$. However, Taylor expansion of $\dot{\mathbf{v}}$ remedies this:

$$\dot{\mathbf{v}}(t + \delta t) = \dot{\mathbf{v}}(t) + \delta t\ddot{\mathbf{v}}(t) + O\delta t^2 \tag{2.14}$$

All terms in equations 2.12-2.14 can then be expressed in terms of $\mathbf{a}(t)$, $\mathbf{v}(t)$ and $\mathbf{r}(t)$

$$\mathbf{r}(t + \delta t) = \mathbf{r}(t) + \delta t\mathbf{v}(t) + \frac{1}{2}\delta t^2\mathbf{a}(t) \tag{2.15}$$

$$\mathbf{v}(t + \delta t) = \mathbf{v}(t) + \frac{1}{2}\delta t\left[\mathbf{a}(t) + \mathbf{a}(t + \delta t)\right] \tag{2.16}$$

where the acceleration of an atom, $\mathbf{a}(t)$ is defined by the gradient of its potential energy, $\mathbf{a}(\mathbf{r}) = -\frac{\nabla\phi_i(\mathbf{r})}{m_i}$. This approch to solving Newton's equations of motion means that information about the position, $\mathbf{r}(t)$, and velocity, $\mathbf{v}(t)$, of atoms at time t is sufficient to determine the atomic trajectories for subsequent steps, that is,

- Calculate new positions, $\mathbf{r}(t+\delta t)$, using equation 2.15
- Determine $\mathbf{a}(t+\delta t)$ using equation 2.11 and the updated positions
- Calculate new velocities, $\mathbf{v}(t+\delta t)$, using equation 2.16 and start again.

By repeatedly solving the velocity Verlet equations the evolution of the system with time can be examined. Despite significant improvements in the computational power available system sizes are still very small (10^3-10^6 atoms) compared to Avogadro's number and simulations times are limited to the order of 10^{-9} s [107]. As such, the MD simulations presented here are limited to nanometer-sized systems and nanosecond timescales. Underlying these system constraints is the need to keep the timestep to only 1 or 2 femtoseconds.

There are numerous issues with using such small system sizes in MD simulation to investigate bulk properties. In particular, a system of only thousands of atoms has a far greater proportion of atoms at the surface compared to even the smallest crystals which are made up of billions upon billions of atoms. In order to imitate the behaviour of the bulk material periodic boundaries are used, such that the simulation box is surrounded by images of itself. Each atom in the primary simulation cell is repeated identically in each of the periodic cells. This has the effect of creating a system that imitates a bulk crystal but, because the atomic positions and velocities in the periodic cells are identical to those in the primary cell, the information must only be recorded once for the atoms in the primary cell. The atoms in the periodic cells are essentially only there to ensure the correct atomic forces in the primary cell. This is particularly important for ionic systems where the superposition of Coulombic forces due to a periodic arrangement of charged species creates a long range electrostatic field. Note that if the trajectory of an atom takes it over the periodic boundary it appears at the opposite side of the cell. As the primary cell size is increased the system becomes

closer to a true representation of the crystal. It is important to select the correct supercell size according to the feature that one is attempting to study: for example a grain boundary requires a much larger supercell size than the perfect crystal.

So far a classical view of the system, with precise equations of motion that map an initial state to all corresponding future states, has been given. However, there is a disconnect between these atomic trajectories and the measurable macroscopic properties. Statistical mechanics provides the link between atomic and macroscopic scales by using the concept of a thermodynamic ensemble. The thermodynamics ensemble represents all possible arrangements and momenta of a system that have a set of common extensive quantities. In molecular dynamics simulations it is implicit that the number of atoms remains the same regardless of the state of the system. It is, therefore, an extensive quantity. Similarly, the volume and energy of the system also remain constant and are also extensive quantities. This is known as the microcanonical ensemble or, more commonly, the NVE (constant number, volume and energy) ensemble.

Bulk properties are calculated by ensemble averages, where an observable value is averaged over all states of a system with a weighting in favour of low energy states (in NVE this corresponds to high entropy states). Weighting towards low energy states essentially ensures the bulk properties are averaged according to the time spent in a given state. In molecular dynamics this is achieved by taking an average of states sampled over a number of timesteps. However, the simulation must be in equilibrium to ensure the MD time average corresponds to the ensemble average and, thus, the true thermodynamic quantity.

2.3 Empirical potential description of crystalline solids

2.3.1 Pairwise potentials

A crucial factor in the ability of atomistic simulations to accurately reproduce the behaviour of a material is the correct description of interatomic forces by a potential set. Typically a

classical Born description of interatomic forces is used, whereby ions are treated as points acting under pair interactions with the other ions in the system. This is a special case of equation 2.1 where the total energy of the system, U_{ij}, is determined by summing independent pairwise contributions, $\phi_{\alpha\beta}(r_{ij})$, over the whole system. In ionic systems these interactions are described by short, $\phi_{short}(r_{ij})$, and long range Coulombic, $\phi_{coul}(r_{ij})$, contributions:

$$U_{ij} = \frac{1}{2}\sum_{i}\sum_{i\neq j}\phi_{\alpha\beta}(r_{ij}) \tag{2.17}$$

$$\phi_{\alpha\beta}(r_{ij}) = \phi_{coul}(r_{ij}) + \phi_{short}(r_{ij}) \tag{2.18}$$

where α and β indicate the species of atoms i and j respectively and r_{ij} is the interionic separation of a given pair.

The Coulombic contribution is inversely proportional to the separation of ions i and j:

$$\phi_{coul}(r_{ij}) = \frac{q_\alpha q_\beta}{4\pi\epsilon_0 r_{ij}} \tag{2.19}$$

where q_α and q_β represent the charges of ions i and j respectively and ϵ_0 is the permittivity of free space. Partial charges can be used such that $q = Z^{eff}|e|$, however they must be proportional to their formal charges ensuring the system remains charge neutral. The use of periodic boundary conditions in conjunction with the long range Coulombic interactions is dealt with by using the Ewald Summation [108].

The short range interactions of ions are approximated by using empirical potentials. Different short range potential forms have been developed depending on the bonding of the system studied. For example, the covalency is often described using the Morse potential [109] and, alternatively, the Buckingham potential [110] has been developed to describe short range repulsion and attractive van der Waals interactions [111]. All such potentials have parameters that underpin their ability to describe the properties of a material. In particular, the lattice parameter, elastic constants and specific heat have been key experimental properties used in the selection of candidate parameter sets. As this thesis is primarily concerned with the simulation of uranium dioxide, example potential forms and parameter

sets are reported below. The vast majority use either Buckingham, 4-range Buckingham, Buckingham-Morse or tabulated potential forms:

- **Buckingham** - Goel-08 [25], Grimes-91 [2], Skomurshki-06 [26], Catlow [15], Arima-1 [27], Busker [16], Lewis_a [28], Lewis_b [28], Lewis_c [28], Meis1 [17], MOX-07 [18, 19], Tharmalingam1 [29] and Walker [30]

$$\phi_{short}(r_{ij}) = A_{\alpha\beta}\exp\left(\frac{-r_{ij}}{\rho_{\alpha\beta}}\right) - \frac{C_{\alpha\beta}}{r^6} \tag{2.20}$$

- **4-range Buckingham** - Jackson1 [20], Jackson2 [20], Karakasidis [31], Meis [21], Morelon [22], Read-10 [23] and Sindzingre [32]

$$\phi_{short}(r_{ij}) = \begin{cases} A_{\alpha\beta}\exp\left(\frac{-r_{ij}}{\rho_{\alpha\beta}}\right) & \text{if } r < r_1 \\ \text{5th-degree polynomial} & \text{if } r_1 < r < r_{min} \\ \text{3rd-degree polynomial} & \text{if } r_{min} < r < r_2 \\ -\frac{C_{\alpha\beta}}{r^6} & r_2 < r \end{cases}$$

- **Buckingham-Morse** - Yakub-09 [14] and Basak [13]

$$\phi_{short}(r_{ij}) = A_{\alpha\beta}\exp\left(\frac{-r_{ij}}{\rho_{\alpha\beta}}\right) - \frac{C_{\alpha\beta}}{r^6} + D_{\alpha\beta}\left[\exp\left(-2\gamma_{\alpha\beta}(r_{ij}-r_0)\right) - 2\exp\left(-\gamma_{\alpha\beta}(r_{ij}-r_0)\right)\right] \tag{2.21}$$

- **Tabulated** - Tiwary-09 [33] and Tiwary-11 [34]

A detailed comparison of these potential sets for the description of uranium dioxide thermophysical properties is given in Chapter 3.

2.3.2 The shell model

Many of the above potentials include atomic polarisability by treating the atoms as massive, charged ionic cores attached to massless, oppositely charged shells where the energy is harmonic with respect to core-shell separation [16, 20, 28, 112, 113]. This enables the correct description of the dielectric properties of the material and is particularly important when

modelling charged defects. This allows Coulombic shielding due to atomic polarisation in addition to ionic displacement. A representation of the shell model for a positively charged ionic core and a negatively charged shell is presented in Figure 2.3 [113].

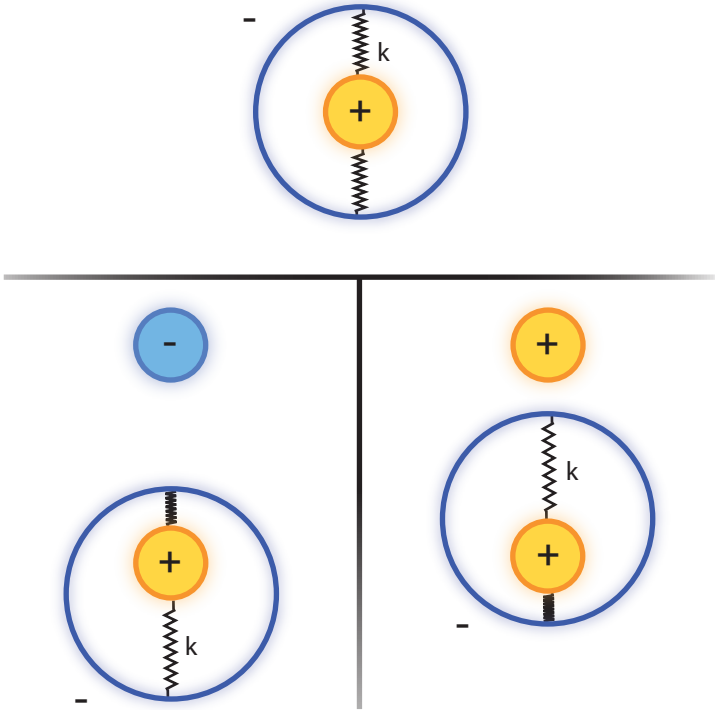


Figure 2.3: Representation of the shell model for a positively charged ionic core attached to a negatively charged shell with a spring of stiffness, k.

In the vicinity of a negatively charged species the negative shell is displaced away from the species, whereas, if the species were positive the shell would be displaced towards the species. This represents the internal relaxation of an ion due to an external electric field and, as such, the addition of the shell model favours lower defect energies compared to a rigid ion that has less degrees of freedom. Similarly, a study by Bishop *et al.* [114] shows that migration barriers are also reduced when using the shell model.

The extent to which one ion is polarised by another depends on the electric field due to all the surrounding charged species. Therefore, the system energy can no longer be split into a simple pairwise description, so that the shell model makes the potential many-body.

However, the implementation of the shell model in an MD simulation poses significant difficulties as one must deal with massless entities. Either an energy minimisation must be carried out on the shells after each timestep to update their positions [115] or nominal but small masses must be assigned to the shells [116]. Both approaches add significant computation time and are even omitted from most mainstream MD codes, such as that used in this thesis: LAMMPS [117].

2.3.3 Embedded atom method potentials

Splitting the energy of the system into a set of independent pair interactions is a simplification of the atomic interactions of a real system. This is most clearly identified by the Cauchy violation ($C_{12} \neq C_{44}$) observed experimentally in a wide range of oxide elastic constants, including UO_2 [118]. If the system energy was truly the sum independent pair interactions then there would be no Cauchy violation [119]. Dawes and Basak [120] developed the embedded atom method (EAM) as a many-body addition to the pairwise description in order to describe metallic systems, so that the energy of the system can be written as:

$$U_{ij} = \frac{1}{2} \sum_{i} \sum_{i \neq j} \phi_{\alpha\beta}(r_{ij}) + \sum_{i} F_{\alpha}(\rho_T) \tag{2.22}$$

where the first term is attributed to the highly repulsive pairwise interactions and the second term is the embedded atom method. ρ_T represents the total electron density at atom i due to all surrounding atoms j and is closely approximated by the sum of the individual atomic densities (i.e. $\rho_T = \sum_{i \neq j} \rho_{\beta}(r_{ij})$). The embedding function, F_{α}, determines the embedding energy of atom i due to the total electron density of the surrounding atoms, ρ_T. The selection of a non linear embedding function, F_{α}, ensures the pairwise density functions, $\rho_{\beta}(r_{ij})$, cannot be separated when describing the total energy of the system, thus making the potential many-bodied. In other words the bonding between two atoms cannot be described without knowledge of the surrounding atomic positions.

Due to the strong analogy between this potential description and the electronic structure of metals, the EAM has primarily been used for modelling metals. Therefore, previous EAM

models are beyond the scope of this thesis, as here only oxides are considered. However, in a later chapter the EAM is used as a perturbation to a more conventional Buckingham-Morse potential, in order to extend the modelling of actinide oxides beyond a pairwise description without needing to use shells (see Chapter 6).

Chapter 3

Comparison of uranium dioxide potentials

Over the last four decades a large number of potentials (equation 2.17) have been developed for the simulation of UO_2 at the atomic scale. Figure 3.1 depicts the time line for most of these potentials and their key features, such as potential form and shell model (see section 2.3). In this chapter the UO_2 properties predicted by these potential models are calculated using the methods described in Chapter 2 and compared to experimental data over a wide range of temperatures, thus highlighting their strengths and weakness. The EAM model developed for this thesis is not included in this comparison but is discussed in detail in Chapter 6.

3.1 MO_2 phases

One of the key criteria for selecting a suitable UO_2 potential is the correct prediction of the fluorite structure as having the lowest lattice energy per formulae unit compared to other common MO_2 polymorphs. Energy minimisation using the General Utility Lattice

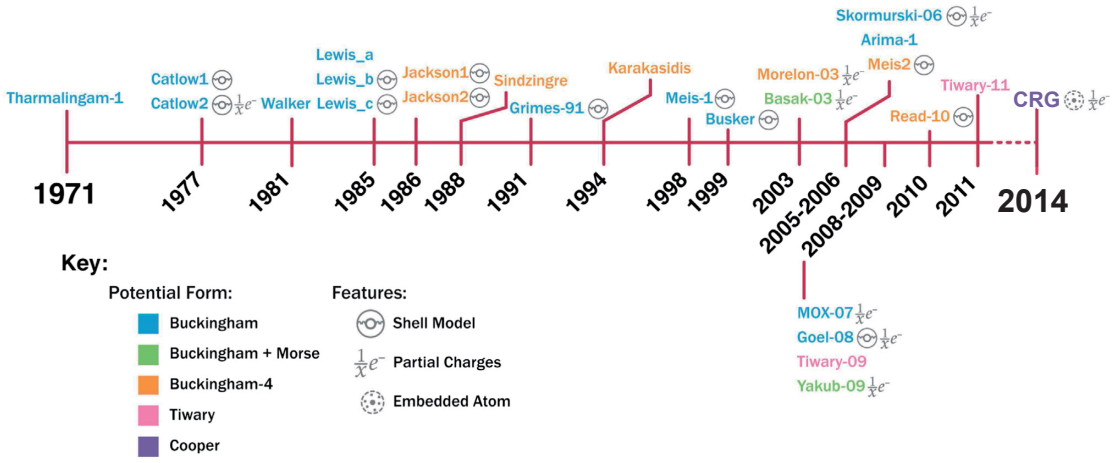


Figure 3.1: Timeline of the UO_2 interatomic potentials through the last four decades taken from Murphy *et al.* [12]. CRG refers to the potential developed in Chapter 6.

Programme (GULP) [100] is carried out to relax both atomic positions and lattice vectors to identify the lattice energy for a given structure. If a particular potential identifies a non-fluorite structure as having a lower lattice energy per formula unit than fluorite it is discounted as a suitable parameter set. Chernatynskiy *et al.* [121] conducted a similar investigation due to the detrimental effect such parasitic non-fluorite structures have on the thermal properties predicted by a potential set.

Table 3.1 shows the difference in lattice energy per formulae unit for a given MO_2 structure and that of the fluorite structure. Negative energy differences identify structures that are more stable than fluorite. The results show that, although most do not, some potentials are unsuitable as they predict non-fluorite structures to be lowest in energy (i.e. Goel-08 [25], Skomurski-06 [26], Arima-1 [27], Meis1 [17], Karakasidis [31], Sindzingre [32], Tiwary-09 [33] and Tiwary-11 [34]). These potentials are, therefore, discounted for further studies. Negative phonons in the fluorite structure are a common feature of potential models that predict another polymorph to be more stable [121].

	Energy Difference per UO_2 Formulae Unit (eV)						
Potential	α-PbO_2	Anatase	Baddeleyite	Cotunnite	Rutile	Brookite	Pyrite
Goel-08 [25]	-0.045	0.061	-0.045	Fluorite	**-0.070**	0.075	Fluorite
Grimes-91 [2]	Fluorite	0.872	Fluorite	Fluorite	0.626	Fluorite	Fluorite
Skomurshki-06 [26]	Fluorite	0.565	Fluorite	Fluorite	**-0.641**	Fluorite	Fluorite
Catlow1 [15]	Fluorite	0.623	Fluorite	Fluorite	0.506	Fluorite	Fluorite
Catlow2 [15]	Fluorite	0.200	Fluorite	Fluorite	0.139	Fluorite	Fluorite
Arima-1 [27]	-0.006	-0.003	-0.006	Fluorite	**-0.039**	0.128	Fluorite
Busker [16]	Fluorite	0.451	Fluorite	Fluorite	0.281	Fluorite	Fluorite
Lewis_a [28]	Fluorite	0.437	Fluorite	Fluorite	0.369	Fluorite	Fluorite
Lewis_b [28]	Fluorite	0.437	Fluorite	Fluorite	0.369	Fluorite	Fluorite
Lewis_c [28]	Fluorite	0.378	Fluorite	Fluorite	0.325	Fluorite	Fluorite
Meis1 [17]	-0.349	**-0.442**	-0.349	-0.009	-0.336	-0.233	-0.001
MOX-07 [18, 19]	Fluorite	0.676	Fluorite	0.325	0.515	Fluorite	Fluorite
Tharmalingam1 [29]	-0.099	-0.212	-0.099	**-0.336**	-0.233	-0.233	-0.001
Walker [30]	-0.044	**-0.126**	-0.044	Fluorite	-0.070	0.072	Fluorite
Jackson1 [20]	Fluorite	0.642	Fluorite	0.631	0.518	Fluorite	Fluorite
Jackson2 [20]	Fluorite	0.944	Fluorite	Fluorite	0.000	Fluorite	Fluorite
Karakasidis [31]	**-0.007**	0.950	**-0.007**	Fluorite	-	0.121	-
Meis2 [21]	Fluorite	0.721	Fluorite	Fluorite	0.626	Fluorite	Fluorite
Morelon-03 [22]	Fluorite	0.388	Fluorite	0.530	0.363	Fluorite	Fluorite
Read-10 [23]	Fluorite	0.489	Fluorite	Fluorite	0.418	Fluorite	Fluorite
Sindzingre [32]	**-0.047**	-	**-0.047**	-	-	0.069	2.906
Basak-03 [13]	0.043	0.494	0.043	Fluorite	0.053	0.303	Fluorite
Yakub-09 [14]	0.237	0.533	0.179	Fluorite	0.239	Fluorite	Fluorite
Tiwary-09 [33]	Fluorite	-1.010	Fluorite	**-1.644**	-0.616	0.291	-1.438
Tiwary-11 [34]	Fluorite	-1.010	Fluorite	**-1.644**	-0.616	0.291	-1.438

Table 3.1: The difference in energy between the lattice energies predicted for common metal dioxide crystal structures and the fluorite structure. Structures that are unstable and minimise to the fluorite structure are labelled as such. Where a non-fluorite structure has the lowest lattice energy it is identified in bold.

3.2 Thermal expansion

For a given potential set a 4×4×4 fluorite supercell of the UO_2 system is heated between 300 K and 3000 K at 75 K intervals with a fixed timestep of 2 fs and at zero pressure. At each temperature the systems were held for 20 ps with the volume averaged over the final 4 ps. The lattice parameter as function of temperature is determined from the volume at each temperature and is shown in Figure 3.2 for a range of UO_2 potentials.

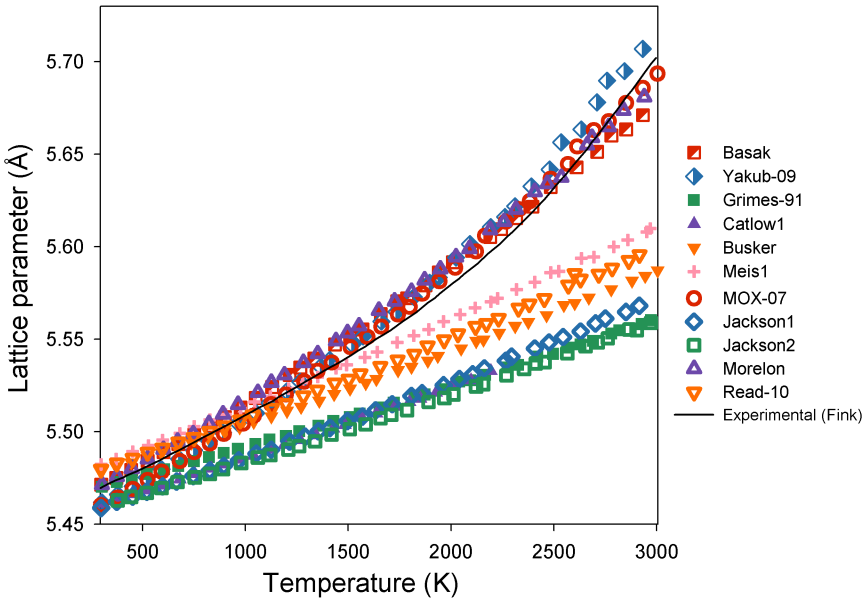


Figure 3.2: Thermal expansion of uranium dioxide as predicted by a range of empirical pair potentials [2, 13–23]. The experimental data of Fink *et al.* [24] is included for comparison.

All of the potentials have a reasonably good agreement with the lattice parameter at 300 K as this is considered a key criteria in potential fitting. Furthermore, the Basak-03 [13], Yakub-09 [14], MOX-07 [18, 19] and Morelon [22] potentials all provide a good description of the thermal expansion up to 3000 K. However, all the other models in Figure 3.2 significantly underestimate thermal expansion and, consequently the high temperature lattice parameter. Therefore, only the potentials that accurately describe thermal expansion are employed for studying properties over a wide temperature range, although the remaining models are

still useful at lower temperatures.

3.3 Elastic properties

The bulk modulus is determined at each temperature interval of the thermal expansion calculations by exerting isotropic compressive and tensile strains on the equilibrated system and examining the derivative of pressure with volume. The bulk modulus is then calculated using equation 6.8.

$$K = -V\frac{dP}{dV} \tag{3.1}$$

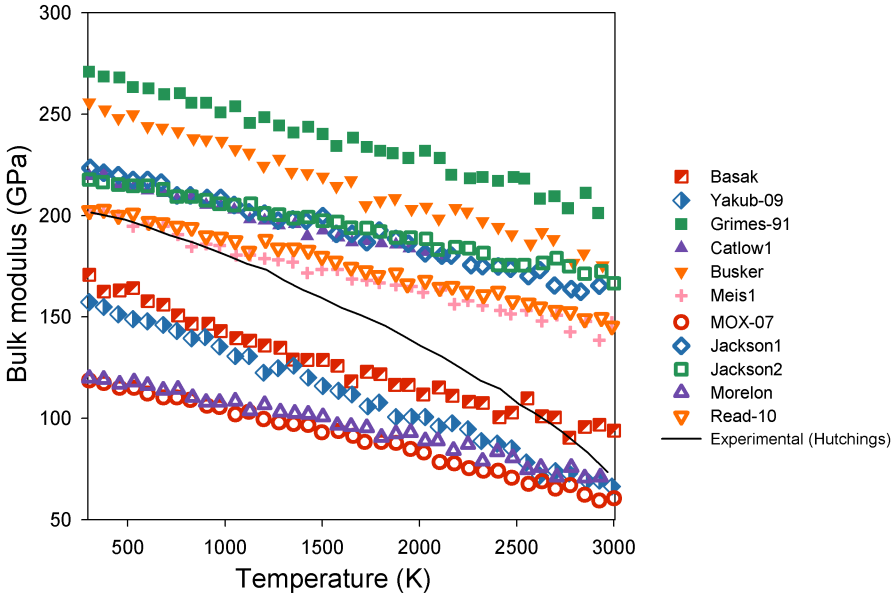


Figure 3.3: Bulk modulus as a function temperature of uranium dioxide as predicted by a range of empirical pair potentials [2, 13–23, 25–34]. The experimental data of Hutchings *et al.* [35] is included for comparison.

Figure 3.3 shows the variation of bulk modulus with temperature for a range of UO_2 potentials. This shows that there are currently no models that can accurately predict the UO_2

bull modulus over the full temperature range. Instead, a parameter set will only reproduce the bulk modulus at either low or high temperatures but not both. In particular, those that describe the thermal expansion well all significantly underestimate the bulk modulus until very high temperatures. Unfortunately this leaves no potential set capable of reproducing both thermal expansion and bulk modulus over the whole temperature range. A significant body of work in this thesis is dedicated to creating a new potential to remedy the apparent compromise that must be made between structural and elastic properties (see Chapter 6).

In addition to the MD calculations of bulk modulus, the single crystal elastic constants have also been determined from energy minimisation calculations in GULP with the atomic positions and lattice parameters relaxed. Table 3.2 shows the elastic constants calculated for a range of UO_2 potentials. It demonstrates that potentials that do not use the shell model are not capable of capturing C_{12} and C_{44} at the same time. This is because without the use of shells the many body effects arising from ionic polarisability cannot be included and the resultant pairwise interactions are incapable of capturing the Cauchy violation observed in UO_2. As they represent massless entities, shells pose a challenge to the standard molecular dynamics (MD) algorithm. Whilst they have been included in MD, either by assigning nominal but small masses to the shells [116] or by updating shell positions through a static energy minimisation, stage performed for each MD time step [115], such methods lead to longer calculation times with the effect of decreasing the time or system size that can be simulated. Consequently, shells are regularly omitted from MD simulations and are not even supported in most of the mainstream MD codes (e.g. LAMMPS [117]). As such, a choice must be made between fitting to C_{12} or to C_{44} leading to the bulk modulus either being overestimated or underestimated (see Figure 3.3). I believe that if it is possible to accurately reproduce all of C_{11}, C_{12} and C_{44} without the shell model so that it can be included in MD simulations it may be possible to reproduce the temperature dependence of bulk modulus between 300 K and 3000 K. This approach motivates the development of a new UO_2 potential (see Chapter 6).

Potential	Elastic Constant (GPa)			
	Bulk Modulus	C_{11}	C_{12}	C_{44}
Expt. [118]	204.0	389.3	118.7	59.7
Basak-03 [13]	176.9	408.1	61.2	59.5
Yakub-09 [14]	162.9	345.3	71.7	66.7
Goel-08 [25]	168.0	371.5	66.3	61.4
Grimes-91 [2]	273.0	524.2	147.4	89.3
Skomurshki-06 [26]	199.0	382.6	107.3	59.4
Catlow1 [15]	223.9	420.0	125.9	66.3
Catlow2 [15]	211.8	434.4	100.5	57.4
Arima-1 [27]	227.9	479.8	101.9	95.5
Busker [16]	258.9	532.1	122.3	118.8
Lewis_a [28]	223.3	427.0	121.5	119.4
Lewis_b [28]	223.2	426.8	121.8	88.5
Lewis_c [28]	221.8	426.9	119.3	49.9
MOX-07 [18, 19]	122.8	217.0	75.7	73.3
Tharmalingam1 [29]	221.9	472.8	96.4	84.3
Walker [30]	225.4	471.0	102.6	89.4
Jackson1 [20]	224.9	421.2	126.5	66.8
Jackson2 [20]	221.0	398.4	132.4	73.8
Karakasidi [31]	181.6	369.3	87.8	70.3
Meis2 [21]	208.8	389.2	118.6	59.6
Morelon-03 [22]	125.0	217.1	79.0	78.4
Read-10 [23]	208.3	391.4	116.7	58.1
Sindzingre [32]	181.1	370.7	86.3	65.6

Table 3.2: The single crystal elastic constants from energy minimisation calculations in GULP [122]. Experimental values are also reported for comparison.

Chapter 4

Fission product segregation to secondary oxide phases

Part of the work presented here appears in:
M.W.D. Cooper, S.C. Middleburgh and R.W. Grimes, *J. Nucl. Mater.* **438**, 238-245 (2013) [123]
M.W.D. Cooper, D.J. Gregg, Y. Zhang, G.J. Thorogood, G.R. Lumpkin, R.W. Grimes and S.C. Middleburgh, *J. Nucl. Mater.* **442**, 236-241 (2013) [124]
M.W.D. Cooper, S.C. Middleburgh and R.W. Grimes, *Prog. Nucl. Energ.* **72**, 33-37 (2014) [125]

4.1 Introduction

As has been discussed extensively in Chapter 1, a wide range of fission products are produced in the reactor. This includes species that are, to a greater or lesser extent, soluble in the parent uranium dioxide lattice. Some are insoluble and gaseous so that they form bubbles (e.g. Xe and Kr [126, 127]) or volatile and able to react with the cladding (e.g. I [95]). Other species precipitate as components in a 5-metal particle (e.g. Pd and Pt [10]) or as a separate oxide phase (e.g. Ba, Sr and Zr [2]). This latter set of elements form the so-called

grey phase, a term used by Kleykamp *et al.* [79] from its relative brightness in SEM micrographs of SNF. Kleykamp *et al.* [79] also found BaO and SrO precipitates in and around the (Ba,Sr)ZrO_3 grey phase. The bonding phase at the cladding-fuel interface has not been very well characterised in light water reactors (LWRs) and may contain significant proportions of ZrO_2 due to oxidation of the zircalloy cladding [128]. Furthermore, the presence of U^{5+} ions in hyper-stoichiometric UO_{2+x} creates the possibility of a $CrUO_4$ bonding layer forming at the AGR fuel-clad interface. Alternatively, in Cr-doped hyper-stoichiometric UO_{2+x} Cr^{3+} and U^{5+} may precipitate to form $CrUO_4$.

The grey phase consists of elements that can be accommodated at two cation sites within the perovskite lattice, the main constituents of which are Ba^{2+} and Zr^{4+}, forming $BaZrO_3$. It is also often termed (Ba,Sr)ZrO_3 to reflect the significant Sr^{2+} component that substitutes at the perovskite A site [79]. More accurately it could be described as (Sr,Ba,Cs)(Zr,U,Mo)O_3 [9, 79, 80] although other elements can also substitute into this oxide lattice. The grey phase is characterised by the cubic perovskite structure of $BaZrO_3$ although pure $SrZrO_3$ is orthorhombic at room temperature [9, 79, 129–131]. Sr, Ba, and Zr are particularly abundant FPs [2], consistent with (Ba,Sr)ZrO_3 being a good model for studying the grey phase. Furthermore, Kleykamp *et al.* [79] identified this composition for grey phase precipitates taken from FBR fuel. They found that as the ratio of oxygen to metal, O/M. of the whole fuel increased, the proportion of perovskite B sites occupied by Mo^{4+} increased [79]. Thus, the increase in oxygen potential led to the oxidation of Mo metal from the five-metal phase and its incorporation into the grey phase.

ZrO_2 assumes a monoclinic structure at room temperature with high temperature phase transitions to tetragonal and fluorite structures [132], which are associated with large volume changes. BaO and SrO are characterised by the simple rock salt structure. $CrUO_4$ exhibits an orthorhombic structure as demonstrated by Felten *et al.* [133] and more recently by researchers at the Australian Nuclear Science and Technology Organisation (ANSTO) [124].

The solubility of Sr, Cs and Xe into SrO, BaO and MgO [134, 135] has been investigated using density functional theory (DFT) calculations and into $UO_{2\pm x}$ [136] using DFT+U, where

electron correlation effects are described by the Hubbard or U parameter. Similarly, Brillant *et al.* [137] studied the solution of He, Kr, Xe, I, Te, Ru, Sr and Ce into $UO_{2\pm x}$. Alternatively, in recent work the stability of a wide range of FPs in UO_2 and UO_{2+x} has been assessed with respect to their relative binary oxides using geometry optimised empirical pair potentials [78]. This followed from earlier work [2] that also considered the possibility that some FPs, especially Ba, Sr, and Zr, could form perovskite ternary oxides rather than binary oxides. This made a considerable difference to the relative solubility of these specific FPs. That earlier study did not, however, consider the possibility that other species might substitute into $CrUO_4$ or (Ba,Sr)ZrO_3 and their associated binary oxides as an alternative to remaining in the UO_2 or UO_{2+x} lattice (as has been observed experimentally [9, 79, 80]).

Here the relative solubility of an extensive range of trivalent and tetravalent cations is considered into $BaZrO_3$ and $SrZrO_3$ (as end members of (Ba,Sr)ZrO_3), BaO, SrO, ZrO_2 and $CrUO_4$, from their equilibrium sites in UO_2 and UO_{2+x} (as recently identified [78]). Importantly, the $BaZrO_3$, $SrZrO_3$, BaO, SrO, and ZrO_2 phases do not exhibit any reported non-stoichiometry in relation to the molar proportion of oxygen and so they provide a clear set of cation solution sites as well as interstitial sites whose energies are independent of oxygen potential (unlike UO_2 which readily oxidises to UO_{2+x}).

The work of Middleburgh *et al.* [78] found that the solubility of FPs into UO_2 and UO_{2+x} was a strong function of hyper-stoichiometry. In particular, small trivalent cations, such as the fuel additive Cr^{3+} [4], were found to be significantly less soluble in UO_2 compared to UO_{2+x}. The lowest energy solution mechanisms in UO_2 and UO_{2+x} were found to involve the creation of charge compensating oxygen vacancies and U^{5+} cations, respectively, so that for trivalent cations occupying U^{4+} sites (T'_U) the most stable charge compensated clusters were (in Kröger-Vink notation [96]) $\{2T'_U : V^{\bullet\bullet}_O\}^\times$ for UO_2 and $\{T'_U : U^{\bullet}_U\}^\times$ for UO_{2+x} [78]. These clusters form the starting point for the partition mechanisms derived in this chapter.

Here the results are presented for the precipitation of secondary oxide phases from uranium dioxide and the partition of fission products into such phases as a function of non-stoichiometry.

4.2 Calculation details

Due to the large variety of fission products investigated in this work, the species-inclusive Busker potential set is employed [16]. Furthermore, this potential set includes a U^{5+}-O^{2-} interaction enabling the simulation of hyper-stoichiometric UO_{2+x}. As discussed in Chapter 3, it provides a reasonable description of the lattice parameter, elastic constants and dielectric properties of the uranium dioxide system at low temperatures making it suitable for the study of defect energies through the geometry optimisation techniques employed in this chapter. Energy minimisation calculations are carried out within the Mott-Littleton regime [99] (described in Chapter 2) where region I and IIa radii are 13.0 Å and 34.0 Å respectively. The radii were chosen to ensure the zirconium vacancy, V''''_{Zr}, defect energy is converged to within 0.1 eV for both the $BaZrO_3$ and $SrZrO_3$ phases (see Figures 4.1 and 4.2). The highly charged zirconium vacancy defect, V''''_{Zr}, is selected for convergence as the long-range Coulombic interactions are the limiting factor in selecting Mott-Littleton region sizes [123]. There was little additional computational demand through the use of a large RII radius. Therefore, setting it to 34.0 Å allowed a degree of conservatism when investigating larger defect clusters.

In order to identify the lowest energy arrangement for a given defect cluster in UO_2, $BaZrO_3$, $SrZrO_3$, BaO, SrO, ZrO_2 and $CrUO_4$, a wide range of possible configurations must be sampled. For example, in UO_2 and ZrO_2 the lowest energy configurations were determined by exploring all possible arrangement of each cluster within a volume of 2×2×2 fluorite unit cells. Similarly, all the configurations of each cluster within a volume of 3×3×3 cubic perovskite unit cells are sampled for the $BaZrO_3$ and $SrZrO_3$ phases. A volume of 3×1×3 orthorhombic unit cells [133] (approximately cubic) is considered for identifying the lowest energy configurations in the $CrUO_4$ system. Finally, a volume of 4×4×4 rock salt unit cells is used for the investigation of cluster configurations in BaO and SrO.

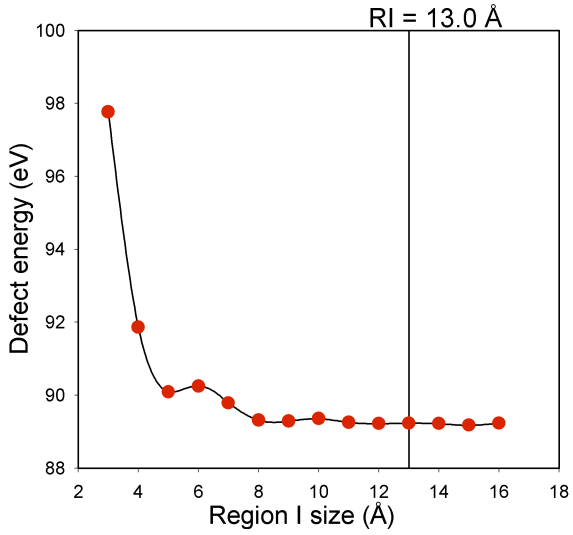


Figure 4.1: Convergence of the zirconium vacancy, V''''_{Zr}, defect energy as function of region I radius. The selection of 13.0 Å for the region IIa radius ensures that the V''''_{Zr} defect energy is converged to within 0.1 eV.

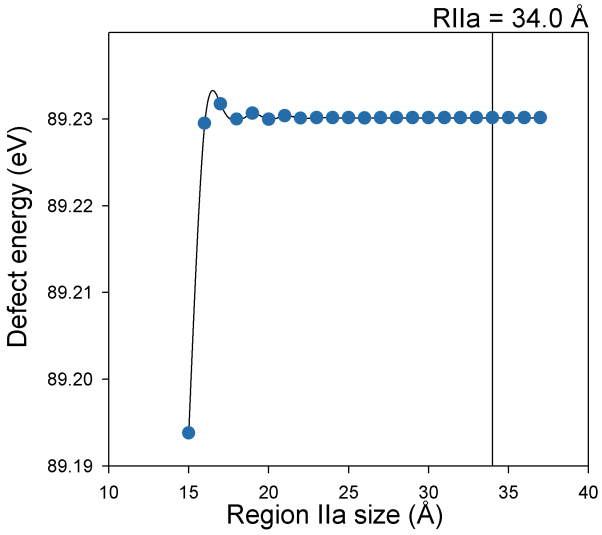


Figure 4.2: Convergence of the zirconium vacancy, V''''_{Zr}, defect energy as function of region IIa radius. The selection of 34.0 Å for the region IIa radius ensures that the V''''_{Zr} defect energy is converged to within 0.01 eV. For all calculations in this figure the region I radius is fixed at 13.0 Å.

4.3 Precipitation energies for the secondary oxide phases

The precipitation of Ba^{2+}, Sr^{2+}, Cr^{3+} and Zr^{4+} from their stable defect clusters in UO_2 and UO_{2+x} to form $BaZrO_3$, $SrZrO_3$, ZrO_2 and $CrUO_4$ determines the availability of this secondary oxide phase for the accommodation of FPs. In the case of ZrO_2 its availability at the fuel-clad interface may be facilitated due to its role as a passive oxide layer on PWR Zircalloy cladding. Similarly, $CrUO_4$ is possibly present in the bonding layer between AGR stainless steel cladding and the fuel pellet. Alternatively, the presence of Cr^{3+} and U^{5+} cations in Cr-doped hyperstoichiometric UO_{2+x} opens the possibility of creating $CrUO_4$ precipitates within the fuel pellet. Following previous work [78], it is assumed that the dominant charge compensating defect for cation solution in stoichiometric UO_2 is the oxygen vacancy $V_O^{\bullet\bullet}$. However, under hyper-stoichiometric conditions the dominant intrinsic defects in UO_{2+x} are oxygen interstitials O_i'' clustered to electron holes at uranium sites $U_U^{\bullet}$ [78]. These charge compensating defects underpin the difference in the solubility of aliovalent fission products in UO_2 compared to UO_{2+x}. For example, Ba^{2+} and Sr^{2+} cations (or more generally A^{2+}) create negatively charged substitutional defects when occupying the U^{4+} cation site. As such, they form different clusters in UO_2 and UO_{2+x} according to the relevant positive charge compensating species. Conversely, Zr^{4+} is accommodated isovalently at the U^{4+} site negating the requirement for charge compensation and consequently there is no distinction between UO_2 and UO_{2+x} [138].

It is, therefore, possible to define mechanisms for $BaZrO_3$ and $SrZrO_3$ precipitation from UO_2 (reaction 4.1) and UO_{2+x} (reaction 4.2). Reactions 4.3 and 4.4 indicate the mechanism for BaO and SrO precipitation from UO_2 and UO_{2+x} respectively. ZrO_2 precipitation mechanisms from UO_2 and UO_{2+x} are indistinguishable and are represented by reaction 4.5. On the other hand, $CrUO_4$ precipitation is only possible in the presence of U^{5+} cations formed in hyper-stoichiometric UO_{2+x} (reaction 4.6).

$$\mathbf{2UO_2} + \{A''_U : V^{\bullet\bullet}_O\}^{\times} + Zr^{\times}_U \rightarrow 2U^{\times}_U + O^{\times}_O + \mathbf{AZrO_3} \quad (4.1)$$

$$\mathbf{2UO_2} + \{A''_U : 2U^{\bullet}_U\}^{\times} + Zr^{\times}_U \rightarrow 2U^{\times}_U + \{O''_i : 2U^{\bullet}_U\}^{\times} + \mathbf{AZrO_3} \quad (4.2)$$

$$\mathbf{UO_2} + \{A''_U : V^{\bullet\bullet}_O\}^{\times} \rightarrow U^{\times}_U + O^{\times}_O + \mathbf{AO} \quad (4.3)$$

$$\mathbf{UO_2} + \{A''_U : 2U^{\bullet}_U\}^{\times} \rightarrow U^{\times}_U + \{O''_i : 2U^{\bullet}_U\}^{\times} + \mathbf{AO} \quad (4.4)$$

$$\mathbf{UO_2} + Zr^{\times}_U \rightarrow U^{\times}_U + \mathbf{ZrO_2} \quad (4.5)$$

$$\mathbf{2UO_2} + \{Cr'_U : U^{\bullet}_U\}^{\times} \rightarrow 2U^{\times}_U + \mathbf{CrUO_4} \quad (4.6)$$

Table 4.1: Precipitation energies are reported for $BaZrO_3$ and $SrZrO_3$ from UO_2 and UO_{2+x} through mechanisms that are analogous to reactions 4.1 and 4.2 respectively, whilst the precipitation of ZrO_2 occurs through reaction 4.5 regardless of non-stoichiometry. The precipitation enthalpies of BaO and SrO from UO_2 and UO_{2+x} are calculated through reactions 4.3 and 4.4 respectively. Under hyper-stoichiometric conditions the precipitation of $CrUO_4$ is also possible via reaction 4.6.

	Precipitation Energy from UO_2 / eV	Precipitation Energy from UO_{2+x} / eV
$BaZrO_3$	-4.74	2.28
$SrZrO_3$	-3.78	3.17
BaO	-3.53	3.50
SrO	-2.58	4.37
ZrO_2	-0.66	-0.66
$CrUO_4$	-	-2.27

Table 4.1 shows that under stoichiometric conditions $BaZrO_3$, $SrZrO_3$, BaO, SrO and ZrO_2 will readily precipitate from their stable defect clusters in UO_2. However, as the precipitation energy for $BaZrO_3$ (or $SrZrO_3$) is lower than for that of ZrO_2 combined with BaO (or SrO), it is expected that Zr^{4+} will preferentially co-precipitate with Ba^{2+} or Sr^{2+} to form the perovskite phases. The relative abundances of Ba, Sr and Zr as fission products will

determine whether ZrO_2 or BaO and SrO will form the residual oxide phases following full precipitation of (Ba,Sr)ZrO_3.

Under hyperstoichiometric UO_{2+x} conditions Table 4.1 shows that precipitation of $BaZrO_2$, $SrZrO_3$ SrO and BaO is no long favourable (reactions 4.2 and 4.4). However, the precipitation of ZrO_2 remains possible as it does not require charge compensation in the UO_2 or UO_{2+x} phases. Despite the lack of stability in UO_{2+x} it is important to consider partition into the grey phase because (i) other FPs may stabilise it with respect to UO_{2+x} and (ii) precipitates formed at lower non-stoichiometry may persist temporarily, especially if the fuel has been cooled before oxidation of the UO_2 phase occurs.

The negative precipitation energy of -2.27 eV indicates that under hyper-stoichiometric conditions Cr^{3+} and U^{5+} readily precipitate from their stable defect clusters in Cr-doped UO_{2+x} to form $CrUO_4$ (reaction 4.6). However, the absence of U^{5+} cations will prevent precipitation from stoichiometric UO_2.

4.4 Segregation between uranium dioxide and the grey phase

4.4.1 Partition energies of tetravalent cations into (Ba,Sr)ZrO_3

Having identified the favourable precipitation of $BaZrO_3$ and $SrZrO_3$, the mechanisms by which other fission products and minor actinides may segregate to these phases from uranium dioxide are identified. The mechanisms by which fission products undergo segregation is determined by their valence state. If accommodated aliovalently, then clustering with charge compensating defects also plays an important role. Tetravalent cations (M^{4+}) were shown by Middleburgh *el al.* [138] to be accommodated isovalently at the U^{4+} site in UO_2, thus, negating the need for charge compensating defects. The most stable sites for the accommodation of tetravalent fission products in $BaZrO_3$ and $SrZrO_3$ must also be identified to complete the partition reaction. All mechanisms considered for the partition of tetravalent cations into $BaZrO_3$ from UO_2 involved substitution at least partly at either the

A^{2+} or Zr^{4+} sites. The former requires negatively charged compensating defects that bind to $M_A^{\bullet\bullet}$ through Couloumbic attraction. All possible tetravalent partition mechanisms are indicated by reactions 4.7-4.11[1] with the associated partition energies reported in Figure 4.3, as function of ionic radius:

$$\overline{M_U^\times} + Zr_{Zr}^\times \rightarrow \overline{Zr_U^\times} + M_{Zr}^\times \tag{4.7}$$

$$\overline{M_U^\times} + \overline{O_O^\times} + A_A^\times \rightarrow \overline{\{A_U'' : V_O^{\bullet\bullet}\}^\times} + \{M_A^{\bullet\bullet} : O_i''\}^\times \tag{4.8}$$

$$\overline{M_U^\times} + A_A^\times + Zr_{Zr}^\times \rightarrow \overline{Zr_U^\times} + \{M_A^{\bullet\bullet} : A_{Zr}''\}^\times \tag{4.9}$$

$$\overline{M_U^\times} + 2A_A^\times \rightarrow \overline{\{A_U'' : A_i^{\bullet\bullet}\}^\times} + \{M_A^{\bullet\bullet} : V_A''\}^\times \tag{4.10}$$

$$\overline{2M_U^\times} + 2A_A^\times + Zr_{Zr}^\times \rightarrow \overline{Zr_U^\times} + \overline{\{A_U'' : A_i^{\bullet\bullet}\}^\times} + \{2M_A^{\bullet\bullet} : V_{Zr}''''\}^\times \tag{4.11}$$

Figure 4.3 shows that for all tetravalent cations the most favourable partition mechanism into $BaZrO_3$ and $SrZrO_3$ occurs via reaction 4.7, and it is clear that there is a strong thermodynamic driving force encouraging the partition of small FP tetravalent cations (Ru^{4+} and Mo^{4+}). This bias towards small cations is not surprising as Zr^{4+} (0.72 Å) is significantly smaller than U^{4+} (0.89 Å) [36]. Conversely, large tetravalent cations (such as the actinides Am^{4+}, Pu^{4+} and Np^{4+} and the fission product Ce^{4+}) will be preferentially accommodated on the larger U^{4+} site. Comparison between the equivalent energies in $BaZrO_3$ and $SrZrO_3$ (see Figures 4.3a and 4.3b) indicates more favourable (more negative) partition energies into $SrZrO_3$ for small tetravalent cations but even less favourable (more positive) for large tetravalent cations. This is due to the smaller lattice parameter of $SrZrO_3$ which favours the accommodation of smaller tetravalent cations. It must be pointed out that Mo and Ru readily form metal precipitates and the proportion of such species in the grey phase will be dependent on the oxygen potential, as seen by Kleykamp *et al.* [79]. Interestingly, the possibility for Mo uptake by the grey phase as a function of oxidising conditions could enable an alternative mechanism by which fuel oxidation may be buffered.

[1] Conventional Kröger-Vink notation does not allow for distinction between oxygen sites in the UO_2 and the secondary phases. As such, from now on we will distinguish all defects in the UO_2 lattice with a line, e.g. $\overline{M_U^\times}$.

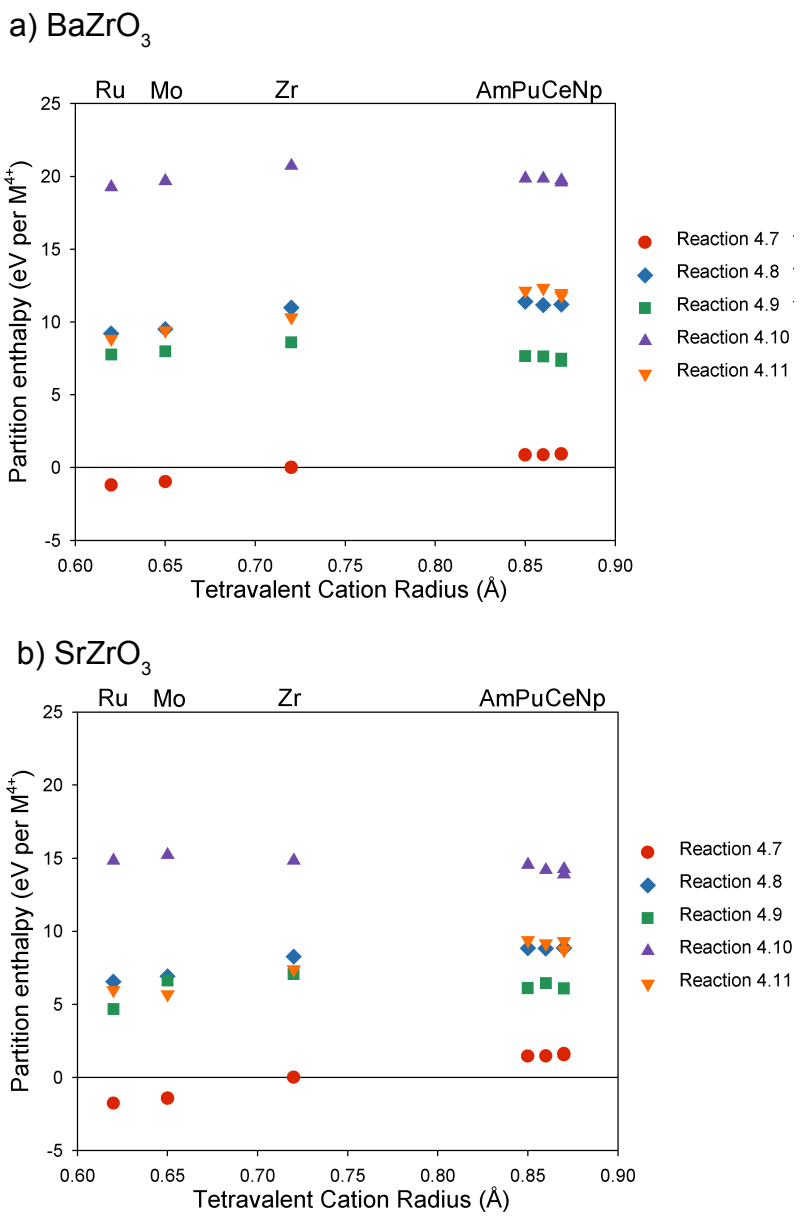


Figure 4.3: Partition enthalpies for tetravalent cations into a) $BaZrO_3$ and b) $SrZrO_4$ from uranium dioxide as a function of ionic radius by substitution at the Zr^{4+} site (reaction 4.7) and substitution at the Ba^{2+} site with charge compensation by an oxygen interstitial (reaction 4.8), an antisite (reaction 4.9), a Ba^{2+} vacancy (reaction 4.10) or a Zr^{4+} vacancy (reaction 4.11).

4.4.2 Change in lattice volumes due to tetravalent cation segregation

Having identified reaction 4.7 as the lowest energy mechanism for tetravalent segregation into the grey phase it is possible to determine the change in lattice volume of the respective phases. The changes in lattice volume due to the substituted defects in $BaZrO_3$ and $SrZrO_3$ (i.e. M_{Zr}^{X}) are shown in Figure 4.4. Tetravalent cations that have negative partition energies are predicted to segregate to the grey phase and all form defects that result in a contraction of $BaZrO_3$ and $SrZrO_3$. Conversely, those that have positive partition energies were all predicted to cause an expansion of $BaZrO_3$ and $SrZrO_3$. However, as they are not predicted to segregate to the grey phase only tetravalent cations with negative volumes will be observed.

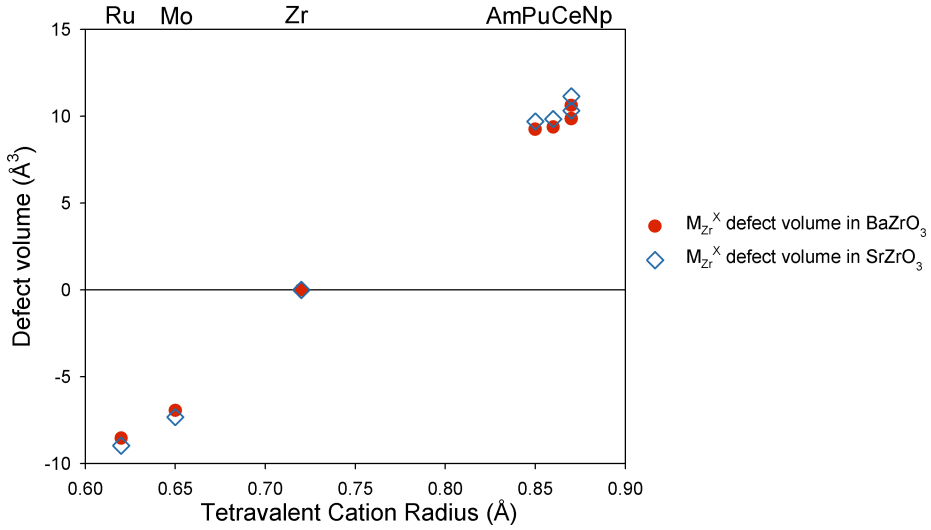


Figure 4.4: Change in lattice volume of $BaZrO_3$ and $SrZrO_3$ for tetravalent cation accommodation on the Zr^{4+} site as a function of ionic radius.

The combined volume change of both phases due to reaction 4.7 is the difference in defect volumes for the cations in UO_2 or UO_{2+x} [138] and in the grey phase. Figure 4.5 shows the net volume change due to tetravalent cation partition into $BaZrO_3$ and $SrZrO_3$. Small tetravalent cations, such as Ru^{4+} and Mo^{4+}, do segregate to (Ba,Sr)ZrO_3, and as a result there is a net contraction of both phases. Conversely, tetravalent cations with ionic radii

greater than that of Zr^{4+} will expand the fuel through reaction 4.7 but, as previously stated, partition is energetically unfavourable for these large tetravalent cations. Thus, segregation of tetravalent cations will result in a combined contraction of the uranium dioxide phase and the grey phase.

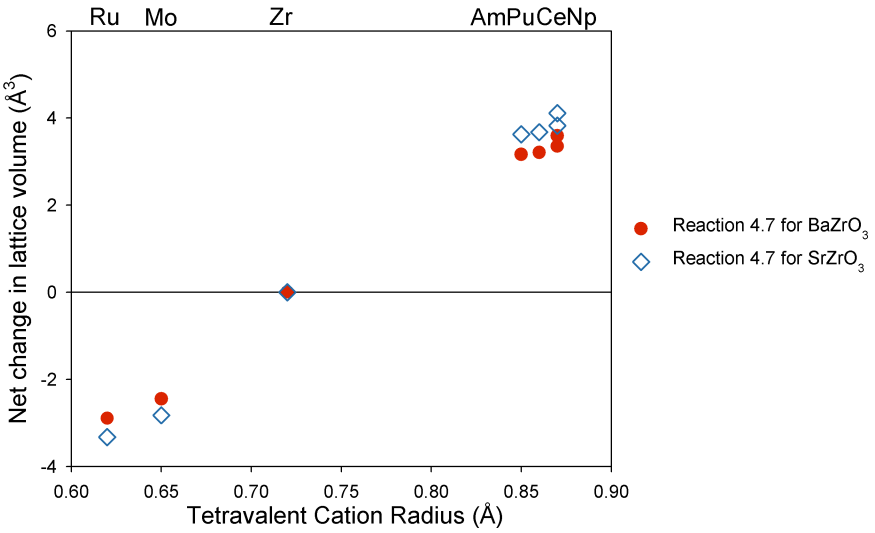


Figure 4.5: Combined change in lattice volume of both the gray phase and the uranium dioxide phases for tetravalent cation segregation by isovalent accommodation at the Zr^{4+} site.

4.4.3 Partition energies of trivalent cations into (Ba,Sr)ZrO_3

From stoichiometric UO_2 into (Ba,Sr)ZrO_3

Unlike the tetravalent cations, accommodation of trivalent cations in uranium dioxide requires charge compensation and, therefore partition is dependent on non-stoichiometry. Furthermore, trivalent cations cannot be accommodated isovalently at either A^{2+} or Zr^{4+} sites so all partition mechanisms require charge compensation in both the uranium dioxide and grey phases. For the case of stoichiometric UO_2 all possible mechanisms are described

by reactions 4.12-4.22:

$$\overline{\{2T'_U : V^{\bullet\bullet}_O\}^\times} + A^\times_A + Zr^\times_{Zr} \rightarrow \overline{Zr^\times_U} + \overline{\{A''_U : V^{\bullet\bullet}_O\}^\times} + \{T^\bullet_A : T'_{Zr}\}^\times \quad (4.12)$$

$$\mathbf{2UO_2} + \overline{\{2T'_U : V^{\bullet\bullet}_O\}^\times} + A^\times_A + Zr^\times_{Zr} \rightarrow \overline{2U^\times_U} + \overline{O^\times_O} + \{T^\bullet_A : T'_{Zr}\}^\times + \mathbf{AZrO_3} \quad (4.13)$$

$$\overline{\{2T'_U : V^{\bullet\bullet}_O\}^\times} + 2Zr^\times_{Zr} + O^\times_O \rightarrow \overline{2Zr^\times_U} + \overline{O^\times_O} + \{2T'_{Zr} : V^{\bullet\bullet}_O\}^\times \quad (4.14)$$

$$\overline{\{2T'_U : V^{\bullet\bullet}_O\}^\times} + A^\times_A + 2Zr^\times_{Zr} \rightarrow \overline{Zr^\times_U} + \overline{\{A''_U : V^{\bullet\bullet}_O\}^\times} + \{2T'_{Zr} : Zr^{\bullet\bullet}_A\}^\times \quad (4.15)$$

$$\mathbf{2UO_2} + \overline{\{2T'_U : V^{\bullet\bullet}_O\}^\times} + A^\times_A + 2Zr^\times_{Zr} \rightarrow \overline{2U^\times_U} + \overline{O^\times_O} + \{2T'_{Zr} : Zr^{\bullet\bullet}_A\}^\times + \mathbf{AZrO_3} \quad (4.16)$$

$$\overline{2\{2T'_U : V^{\bullet\bullet}_O\}^\times} + 3Zr^\times_{Zr} \rightarrow \overline{3Zr^\times_U} + \overline{\{V''''_U : 2V^{\bullet\bullet}_O\}^\times} + \{3T'_{Zr} : T^{\bullet\bullet\bullet}_i\}^\times \quad (4.17)$$

$$\overline{\{2T'_U : V^{\bullet\bullet}_O\}^\times} + \overline{O^\times_O} + 2A^\times_A \rightarrow \overline{2\{A''_U : V^{\bullet\bullet}_O\}^\times} + \{2T^\bullet_A : O''_i\}^\times \quad (4.18)$$

$$\overline{\{2T'_U : V^{\bullet\bullet}_O\}^\times} + 2A^\times_A + Zr^\times_{Zr} \rightarrow \overline{Zr^\times_U} + \overline{\{A''_U : V^{\bullet\bullet}_O\}^\times} + \{2T^\bullet_A : A''_{Zr}\}^\times \quad (4.19)$$

$$\mathbf{2UO_2} + \overline{\{2T'_U : V^{\bullet\bullet}_O\}^\times} + 2A^\times_A + Zr^\times_{Zr} \rightarrow \overline{2U^\times_U} + \overline{O^\times_O} + \{2T^\bullet_A : A''_{Zr}\}^\times + \mathbf{AZrO_3} \quad (4.20)$$

$$\overline{\{2T'_U : V^{\bullet\bullet}_O\}^\times} + 3A^\times_A \rightarrow \overline{\{A''_U : V^{\bullet\bullet}_O\}^\times} + \overline{\{A''_U : A^{\bullet\bullet}_i\}^\times} + \{2T^\bullet_A : V''_A\}^\times \quad (4.21)$$

$$\overline{2\{2T'_U : V^{\bullet\bullet}_O\}^\times} + 4A^\times_A + Zr^\times_{Zr} \rightarrow \overline{Zr^\times_U} + \overline{2\{A''_U : V^{\bullet\bullet}_O\}^\times} + \overline{\{A''_U : A^{\bullet\bullet}_i\}^\times} + \{4T^\bullet_A : V''''_{Zr}\}^\times \quad (4.22)$$

Of all the possible mechanisms considered for the partition of trivalent cations from stoichiometric UO_2 into $BaZrO_3$ the most favourable involved self-charge compensating defects, i.e. reaction 4.13, or oxygen vacancy formation, i.e. reaction 4.14. Self-charge compensating defects were found to either occupy first or fourth nearest neighbour sites depending on ionic radius (see Figure 4.6); Cr^{3+} through to Lu^{3+} occupy first nearest neighbour sites, whereas Er^{3+} through to La^{3+} are in fourth nearest neighbour sites. The oxygen vacancy was found at the first nearest neighbour site with respect to both trivalent cations substituted at Zr^{4+} sites making the $\{2T'_{Zr} : V^{\bullet\bullet}_O\}^\times$ cluster linear for all trivalent cations (see Figure 4.7).

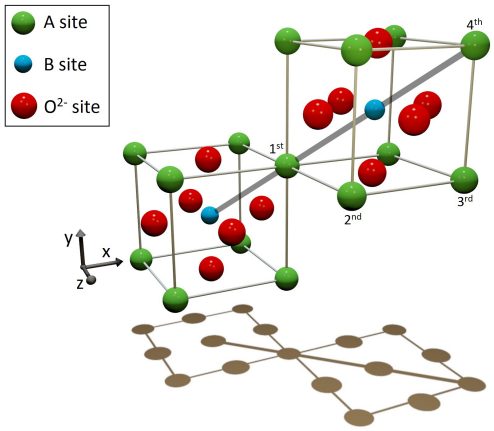


Figure 4.6: The cubic perovskite structure of the grey phase. The A site species, Ba^{2+} or Sr^{2+}, are represented by green spheres, whilst the blue sphere indicate the positions of the B site species, Zr^{4+}, with O^{2-} shown in red. The 4 nearest positions of a divalent cation are identified with respect to a Zr^{4+} ion in the lower cube.

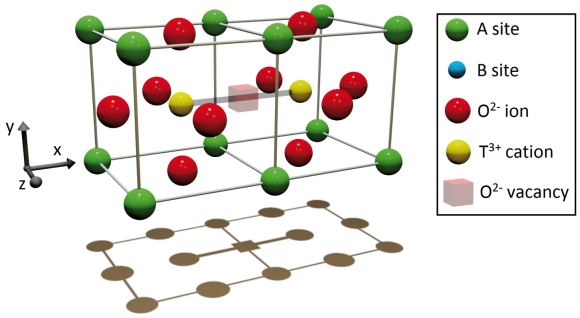


Figure 4.7: The lowest energy configuration for the $\{2T'_{Zr} : V_O^{\bullet\bullet}\}^{\times}$ cluster. The A site species, Ba^{2+} and Sr^{2+}, are represented by green spheres, whilst the yellow spheres indicate the positions of the substitutional trivalent cations occupying B sites, T'_{Zr}, with O^{2-} shown in red and the semi-transparent red cube indicating an oxygen vacancy, $V_O^{\bullet\bullet}$.

Negative partition energies were calculated for Cr^{3+} and Fe^{3+} through reaction 4.14 and for Sm^{3+}, Nd^{3+}, Pr^{3+} and La^{3+} via reaction 4.13, indicating that these trivalent cations will tend to segregate to the $BaZrO_3$ phase, whereas, In^{3+}, Lu^{3+}, Er^{3+}, Y^{3+} and Dy^{3+} will remain in the UO_2 phase (see Figure 4.8a). Although a positive partition energy is also determined for Gd^{3+}, the small energy indicates that entropy will promote accommodation in both phases. These results agree with the work of Kleykamp *et al.* [79] who identified that some rare earth elements are accommodated by the grey phase. However, Kleykamp *et al.* [79] did not identify specific species.

Due to the large computational demand of recalculating the defect energies for all the possible configurations of the larger $\{4T^{\bullet}_{Sr} : V''''_{Zr}\}^{\times}$ and $\{3T'_{Zr} : T_i^{\bullet\bullet\bullet}\}^{\times}$ clusters it was decided to not include these reactions for $SrZrO_3$ (i.e. reaction 4.17 and 4.22). The highly unfavourable energies associated with these mechanisms into $BaZrO_3$ supports this decision. The partition energies for all other mechanisms into $SrZrO_3$ are reported in Figure 4.8b. As was true for $BaZrO_3$, the most favourable mechanisms for the partition of trivalent cations into $SrZrO_3$ from stoichiometric UO_2 are 4.13 and 4.14. However, for $SrZrO_3$ a significant number of different cluster configurations are all of similar energy and there is no need to specify specific configurations. Negative partition energies, indicating a thermodynamic drive for segregation into the $SrZrO_3$ phase, are predicted for Cr^{3+} and Fe^{3+} via substitution at the Zr^{4+} site (reaction 4.14). Conversely, the positive partition energies predicted for In^{3+}, Lu^{3+}, Er^{3+}, Y^{3+}, Dy^{3+}, Gd^{3+}, Sm^{3+}, Nd^{3+}, Pr^{3+} and La^{3+} indicate that they remain in UO_2, in contrast to the situation for $BaZrO_3$ where negative partition energies are calculated for Sm^{3+}, Nd^{3+}, Pr^{3+} and La^{3+}. This behaviour reflects a reduction in solubility exhibited by large trivalent cations in $SrZrO_3$ compared to $BaZrO_3$ (since the Sr^{2+} substitution site is smaller than that of Ba^{2+}). It is, therefore, expected that trivalent fission product segregation is dependent on the Ba:Sr ratio in the grey phase, whereby a high Ba content would encourage segregation.

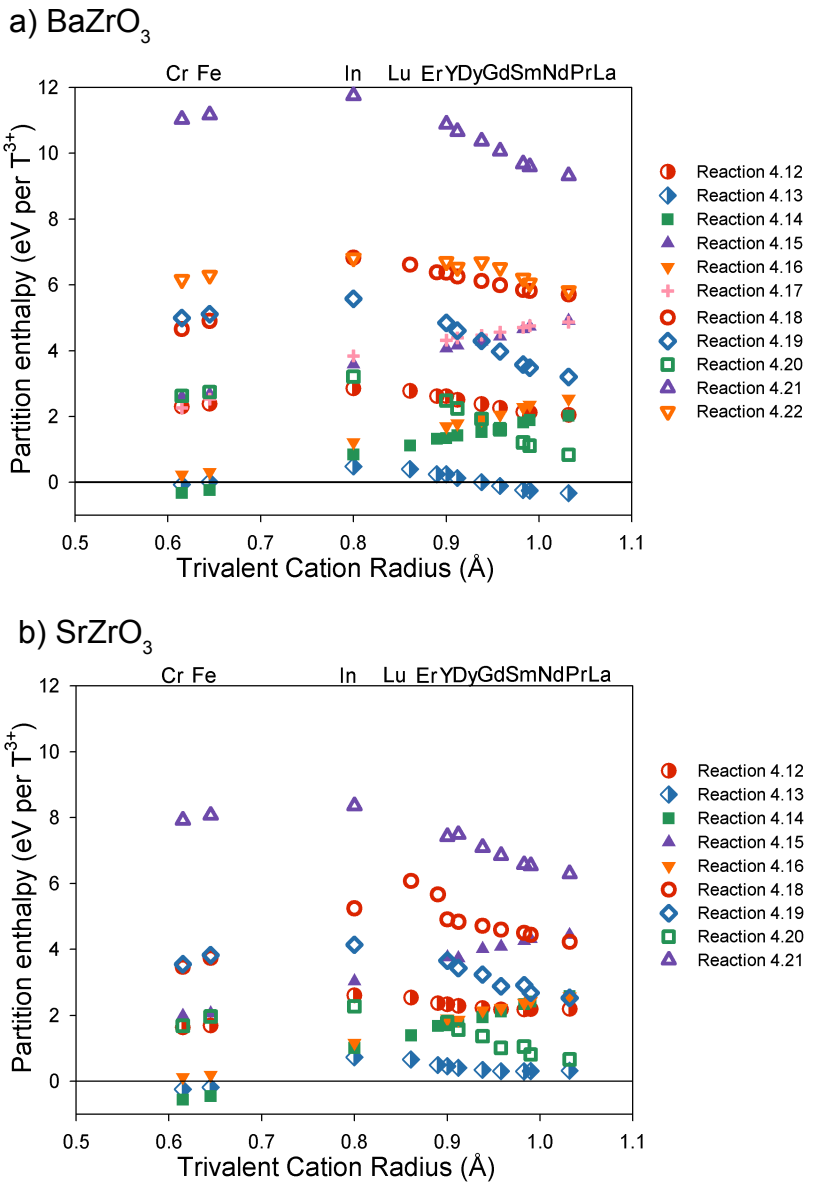


Figure 4.8: Partition enthalpies for trivalent cations into a) $BaZrO_3$ and b) $SrZrO_3$ from stoichiometric UO_2 as a function of ionic radius by reactions 4.12-4.22. Full and open symbols indicate mechanisms that occur via the Zr^{4+} and A^{2+} sites respectively, whilst half symbols identify reactions with accommodation at both $AZrO_3$ cation sites.

From hyper-stoichiometric UO_{2+x} into (Ba,Sr)ZrO_3

As the accommodation of trivalent cations in UO_{2+x} requires charge compensating U^{5+} defects, as opposed to oxygen vacancies in UO_2, it is necessary to derive a new set of partition reactions. All the possible mechanisms for trivalent segregation from hyper-stoichiometric UO_{2+x} to $BaZrO_3$ or $SrZrO_3$ are described by reactions 4.23-4.33:

$$\overline{2\{T'_U : U^{\bullet}_U\}^{\times}} + A^{\times}_A + Zr^{\times}_A \rightarrow \overline{Zr^{\times}_U} + \overline{\{A''_U : 2U^{\bullet}_U\}^{\times}} + \{T^{\bullet}_A : T'_{Zr}\}^{\times} \quad (4.23)$$

$$\mathbf{2UO_2} + \overline{2\{T'_U : U^{\bullet}_U\}^{\times}} + A^{\times}_A + Zr^{\times}_A \rightarrow \overline{2U^{\times}_U} + \overline{\{2U^{\bullet}_U : O''_i\}^{\times}} + \{T^{\bullet}_A : T'_{Zr}\}^{\times} + \mathbf{AZrO_3} \quad (4.24)$$

$$\overline{2\{T'_U : U^{\bullet}_U\}^{\times}} + 2Zr^{\times}_{Zr} + O^{\times}_O \rightarrow \overline{2Zr^{\times}_U} + \overline{\{2U^{\bullet}_U : O''_i\}^{\times}} + \{2T'_{Zr} : V^{\bullet\bullet}_O\}^{\times} \quad (4.25)$$

$$\overline{2\{T'_U : U^{\bullet}_U\}^{\times}} + A^{\times}_A + 2Zr^{\times}_{Zr} \rightarrow \overline{Zr^{\times}_U} + \overline{\{A''_U : 2U^{\bullet}_U\}^{\times}} + \{2T'_{Zr} : Zr^{\bullet\bullet}_A\}^{\times} \quad (4.26)$$

$$\mathbf{2UO_2} + \overline{2\{T'_U : U^{\bullet}_U\}^{\times}} + A^{\times}_A + 2Zr^{\times}_{Zr} \rightarrow \overline{2U^{\times}_U} + \overline{\{2U^{\bullet}_U : O''_i\}^{\times}} + \{2T'_{Zr} : Zr^{\bullet\bullet}_A\}^{\times} + \mathbf{AZrO_3} \quad (4.27)$$

$$\overline{4\{T'_U : U^{\bullet}_U\}^{\times}} + 3Zr^{\times}_{Zr} \rightarrow \overline{3Zr^{\times}_U} + \overline{\{V''''_U : 4U^{\bullet}_U\}^{\times}} + \{3T'_{Zr} : T^{\bullet\bullet\bullet}_i\}^{\times} \quad (4.28)$$

$$\overline{2\{T'_U : U^{\bullet}_U\}^{\times}} + \overline{\{2U^{\bullet}_U : O''_i\}^{\times}} + 2A^{\times}_A \rightarrow \overline{2\{A''_U : 2U^{\bullet}_U\}^{\times}} + \{2T^{\bullet}_A : O''_i\}^{\times} \quad (4.29)$$

$$\overline{2\{T'_U : U^{\bullet}_U\}^{\times}} + 2A^{\times}_A + Zr^{\times}_{Zr} \rightarrow \overline{Zr^{\times}_U} + \overline{\{A''_U : 2U^{\bullet}_U\}^{\times}} + \{2T^{\bullet}_A : A''_{Zr}\}^{\times} \quad (4.30)$$

$$\mathbf{2UO_2} + \overline{2\{T'_U : U^{\bullet}_U\}^{\times}} + 2A^{\times}_A + Zr^{\times}_{Zr} \rightarrow \overline{2U^{\times}_U} + \overline{\{2U^{\bullet}_U : O''_i\}^{\times}} + \{2T^{\bullet}_A : A''_{Zr}\}^{\times} + \mathbf{AZrO_3} \quad (4.31)$$

$$\overline{2\{T'_U : U^{\bullet}_U\}^{\times}} + 3A^{\times}_A \rightarrow \overline{\{A''_U : 2U^{\bullet}_U\}^{\times}} + \overline{\{A''_U : A^{\bullet\bullet}_i\}^{\times}} + \{2T^{\bullet}_A : V''_A\}^{\times} \quad (4.32)$$

$$\overline{4\{T'_U : U^{\bullet}_U\}^{\times}} + 4A^{\times}_A + Zr^{\times}_{Zr} \rightarrow \overline{Zr^{\times}_U} + \overline{2\{A''_U : 2U^{\bullet}_U\}^{\times}} + \overline{\{A''_U : A^{\bullet\bullet}_i\}^{\times}} + \{4T^{\bullet}_A : V''''_{Zr}\}^{\times} \quad (4.33)$$

Figure 4.10 shows that the lowest energy mechanisms for the partition of trivalent cations between hyper-stoichiometric UO_{2+x} and $BaZrO_3$ are found to involve self-charge compensating extrinsic defects (reaction 4.23) or the creation of oxygen interstitials (reaction 4.29). The oxygen interstitial preferentially forms a split interstitial in the $\langle 110 \rangle$ direction at a first nearest neighbour site with respect to both trivalent cations substituted at Ba^{2+} sites (see Figure 4.9).

Regardless of the species studied, all trivalent cations are predicted to remain in UO_{2+x} (see Figure 4.10a). This is in contrast to stoichiometric UO_2 where a number of cations

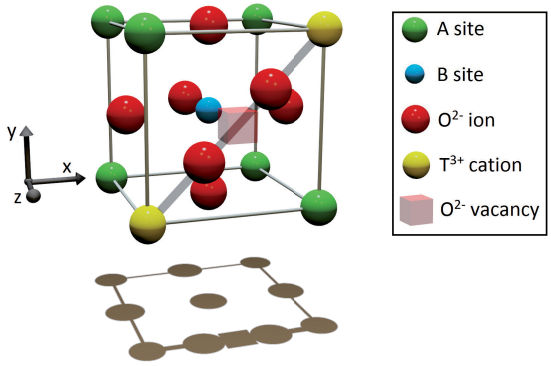


Figure 4.9: The lowest energy configuration for the $\{2T_A^{\bullet} : O_i''\}^{\times}$ cluster. The A site species, Ba^{2+} and Sr^{2+}, are represented by green spheres, whilst the yellow spheres indicate the positions of the substitutional trivalent cations at A sites, $T_A^{\bullet}$. Blue spheres indicate the B site species, Zr^{4+}, with O^{2-} shown in red and the semi-transparent red cube indicating an oxygen vacancy, $V_O^{\bullet\bullet}$. The interstitial oxygen forms a $\langle 110 \rangle$ split interstitial with another oxygen ion.

partition into $BaZrO_3$. The difference is a consequence of the greater solubility of trivalent cations in hyper-stoichiometric UO_{2+x} compared to UO_2, as predicted by Middleburgh *et al.* [78].

The lowest energies for trivalent cation partition from UO_{2+x} into $SrZrO_3$ involve self-charge compensation by extrinsic defects (reaction 4.23). Results shown in Figure 4.10b indicate positive partition energies for all trivalent species considered. Thus, in contrast to the to the situation for UO_2 where Cr^{3+} and Fe^{3+} segregate to the $SrZrO_3$ phase, all trivalent cations will remain in UO_{2+x}. This is, however, the same as with the partition of trivalent cations from hyper-stoichiometric UO_{2+x} into $BaZrO_3$. Thus, overall partition into the grey phase is predicted to be unfavourable from UO_{2+x}.

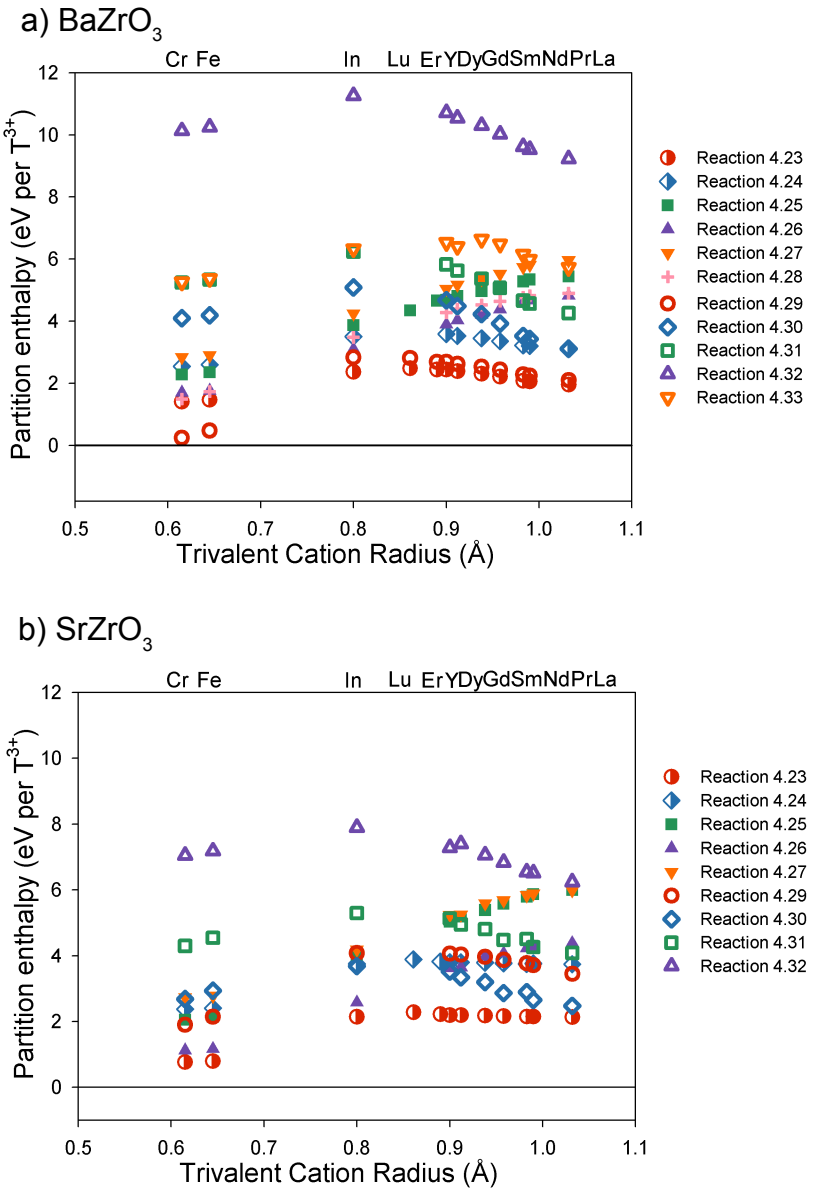


Figure 4.10: Partition enthalpies for trivalent cations into a) $BaZrO_3$ and b) $SrZrO_3$ from hyper-stoichiometric UO_{2+x} as a function of ionic radius by reactions 4.23-4.33. Full and open symbols indicate mechanisms that occur via the Zr^{4+} and A^{2+} sites respectively, whilst half symbols identify reactions with accommodation at both $AZrO_3$ cation sites.

4.4.4 Change in lattice volumes due to trivalent cation segregation

The lowest energy partition mechanisms for a number of trivalent cations from UO_2 and UO_{2+x} into $BaZrO_3$ and $SrZrO_3$ have been identified in the previous sections. No segregation of trivalent cations into $BaZrO_3$ or $SrZrO_3$ is expected from UO_{2+x}; as such only the lowest energy partition mechanisms from UO_2, either by reaction 4.14 for small trivalent cations (such as Cr^{3+} and Fe^{3+}) or via reaction 4.13 for larger trivalent cations will be considered further. The cluster configurations formed have been discussed previously (Figures 4.6-4.9). Here we examine the change in lattice volume of UO_2, $BaZrO_3$ and $SrZrO_3$ involved in these reactions.

Figure 4.11 shows the change in volume of $BaZrO_3$ and $SrZrO_3$ due to the $\{T_A^{\bullet} : T'_{Zr}\}^{\times}$ cluster for In^{3+}, Lu^{3+}, Er^{3+} , Y^{3+}, Dy^{3+}, Gd^{3+}, Sm^{3+}, Nd^{3+}, Pr^{3+} and La^{3+}. The majority of these defect clusters cause an expansion of $BaZrO_3$ or $SrZrO_3$, although many were not predicted to segregate to the grey phase. Those that have negative partition energies are all predicted to form clusters with positive defect volumes in $BaZrO_3$, resulting in an expansion of the $BaZrO_3$ lattice. Conversely, the fuel dopants Cr^{3+} and Fe^{3+} are predicted to partition to both $BaZrO_3$ and $SrZrO_3$ by forming $\{2T'_{Zr} : V_O^{\bullet\bullet}\}^{\times}$ clusters which cause lattice contractions (see Figure 4.11).

The combined volume changes in both phases as a consequence of segregation to grey phases from UO_2 described by reactions 4.13 and 4.14 indicate how the fuel volume may change overall due to trivalent cation partition (see Figure 4.12). The segregation of Cr^{3+} and Fe^{3+} into $BaZrO_3$ and $SrZrO_3$ through reaction 4.14 is expected to result in a net contraction of UO_2 and the grey phase. Conversely, La^{3+} and Pr^{3+} are expected to segregate to $BaZrO_3$ by reaction 4.13 with a net expansion. Nd^{3+}, Sm^{3+} and Gd^{3+}, which also segregate from UO_2, are predicted to contribute to an overall contraction although the contraction due to Nd^{3+} is negligible. All other trivalent cations are not predicted to segregate to the grey phase and as such there is no change.

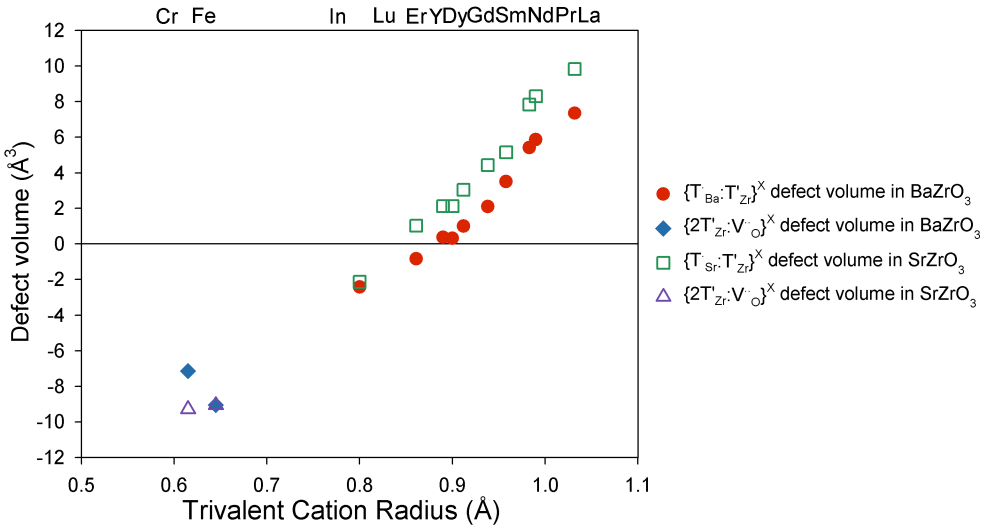


Figure 4.11: Change in lattice volume of $BaZrO_3$ and $SrZrO_3$ as a function of ionic radius for trivalent cations on the Zr^{4+} site with charge compensation by oxygen vacancies for Cr^{3+} and Fe^{3+} and by self charge compensation via accommodation at both cation sites for In^{3+}, Lu^{3+}, Er^{3+}, Y^{3+}, Dy^{3+}, Gd^{3+}, Sm^{3+}, Nd^{3+}, Pr^{3+} and La^{3+}.

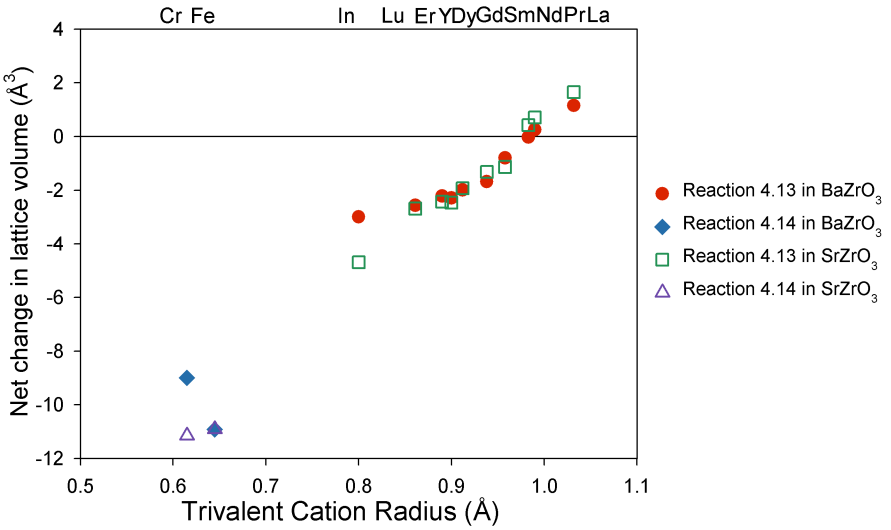


Figure 4.12: Combined lattice volume changes of both the grey phase and the uranium dioxide phase, as function of ionic radius [36], for trivalent cation segregation to the Zr^{4+} site with charge compensation by oxygen vacancies for Cr^{3+} and Fe^{3+} (reaction 4.13) and by self charge compensation via accommodation at both cation sites for In^{3+}, Lu^{3+}, Er^{3+}, Y^{3+}, Dy^{3+}, Gd^{3+}, Sm^{3+}, Nd^{3+}, Pr^{3+} and La^{3+} (reaction 4.14).

4.4.5 Effect of Cr-doping on segregation to the grey phase

Partition into (Ba,Sr)ZrO_3 from UO_2 and UO_{2+x}

Figures 4.3-4.10 show the importance of ion size matching for the favourable partition of FPs into the grey phase. When considering large trivalent FPs it is proposed that a mixed cation mechanism could reduce partition energies further, so that in the presence of excess Cr^{3+} the large trivalent cation can substitute at a large Ba^{2+} site ($T^{\bullet}_{Ba}$) whilst charge compensation is provided by the substitution of Cr^{3+} at the Zr^{4+} site (Cr'_{Zr}), thereby forming the cluster $\{T^{\bullet}_{Ba} : Cr'_{Zr}\}^{\times}$. Similarly to previous sections, the lowest partition energy mechanisms were identified from UO_2 (reaction 4.34) or UO_{2+x} (reaction 4.35) into $BaZrO_3$. These represent modified versions of reactions 4.13 and 4.23 that ensure ideal ion size matching.

$$\mathbf{4UO_2} + \overline{\{2Cr'_U : V^{\bullet\bullet}_O\}^{\times}} + \overline{\{2T'_U : V^{\bullet\bullet}_O\}^{\times}} + 2A^{\times}_A + 2Zr^{\times}_{Zr} \rightarrow \overline{4U^{\times}_U} + \overline{2O^{\times}_O} + 2\{T^{\bullet}_A : Cr'_{Zr}\}^{\times} + \mathbf{2AZrO_3} \tag{4.34}$$

$$\overline{\{Cr'_U : U^{\bullet}_U\}^{\times}} + \overline{\{T'_U : U^{\bullet}_U\}^{\times}} + A^{\times}_A + Zr^{\times}_{Zr} \rightarrow \overline{Zr^{\times}_U} + \overline{\{A''_U : 2U^{\bullet}_U\}^{\times}} + \{T^{\bullet}_A : Cr'_{Zr}\}^{\times} \tag{4.35}$$

Comparison of Figure 4.13 with Figures 4.8 and 4.10 demonstrates that when there is excess Cr^{3+} present it can reduce the partition energy of large trivalent FPs into both $BaZrO_3$ and $SrZrO_3$. Furthermore, Lu^{3+}, Er^{3+}, Y^{3+}, Dy^{3+} and Gd^{3+} now have negative partition energies from UO_2 and are expected to fully segregate to $BaZrO_3$ and $SrZrO_3$ by reaction 4.34.

There is also a reduction in partition energy observed from hyper-stoichiometric UO_{2+x} into $BaZrO_3$ and $SrZrO_3$. However, the energies remain positive. Thus, the presence of excess Cr^{3+} in hyper-stoichiometric fuel is not sufficient to cause segregation to $BaZrO_3$ or $SrZrO_3$. Nonetheless, the presence of excess Cr in UO_{2+x} has been predicted to create $CrUO_4$ precipitates. The role of such precipitates in fission product segregation is examined later (see section 4.6).

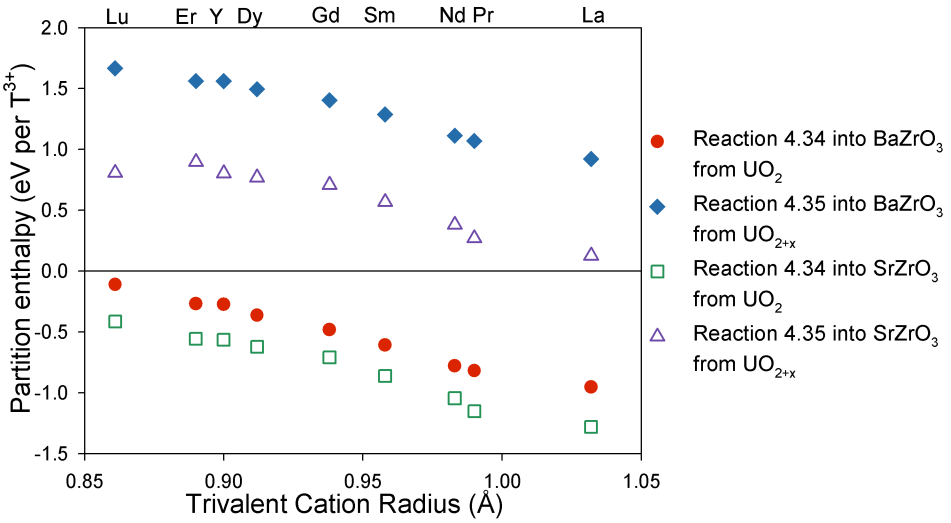


Figure 4.13: Partition enthalpies for trivalent cations into $BaZrO_3$ or $SrZrO_3$ from Cr-doped stoichiometric UO_2 and hyper-stoichiometric UO_{2+x} as a function of ionic radius by accommodation at the Ba site, $T^{\bullet}_{Ba}$, with charge compensation by Cr^{3+} substitution at the Zr^{4+} site, Cr'_{Zr}.

4.4.6 Effect of excess Cr on swelling due to trivalent cation segregation

The presence of excess Cr^{3+} in the fuel and its role in the mixed cation partition mechanism from UO_2 into $BaZrO_3$ or $SrZrO_3$ (reaction 4.34) has been shown to make the partition reactions for trivalent cations significantly more favourable. In fact, all of the large trivalent cations studied are predicted to segregate from UO_2 into $BaZrO_3$ and $SrZrO_3$ in the presence of excess Cr^{3+}. Here the change in lattice volume of UO_2, $BaZrO_3$ and $SrZrO_3$ involved in segregation by reaction 4.34 is investigated.

Figure 4.14 shows that for Lu^{3+}, Er^{3+}, Y^{3+}, Dy^{3+}, Gd^{3+}, Sm^{3+}, Pr^{3+} and La^{3+} the $\{T^{\bullet}_{A} : Cr'_{Zr}\}^{\times}$ clusters, predicted to form in both $BaZrO_3$ and $SrZrO_3$, all result in a contraction of the grey phase lattice. This contraction is most pronounced for small trivalent cations. Furthermore, the changes in lattice volume due to these species in the grey phases are more negative for a given trivalent cation than in the UO_2 phase. Thus, Figure 4.15 shows that there is an overall contraction of both phases due to the partition of trivalent cations with excess Cr^{3+} (reaction 4.34). This contraction is most pronounced for large trivalent cations.

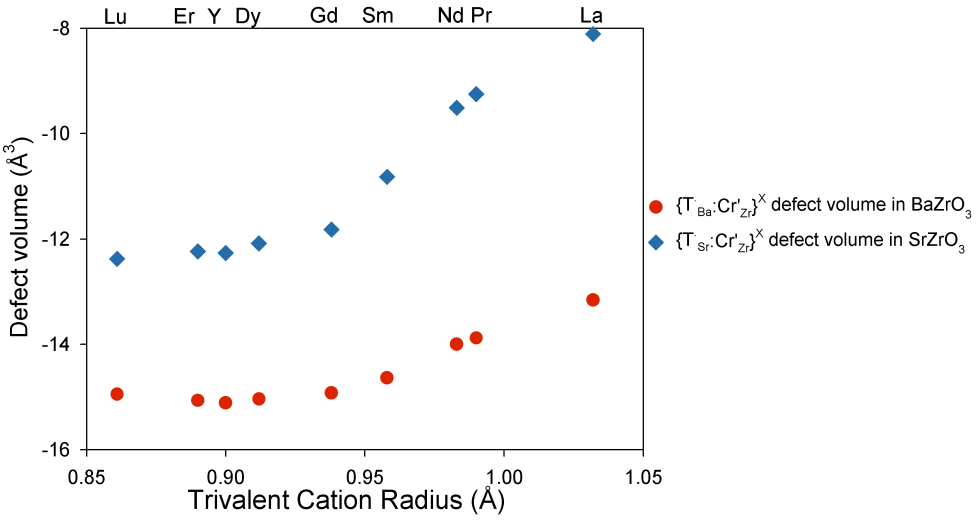


Figure 4.14: Change in lattice volume of $BaZrO_3$ and $SrZrO_3$, as a function of ionic radius, for trivalent cations on the Ba^{2+} site with charge compensation by Cr^{3+} substitution at the Zr^{4+} site. The defects occupy first nearest neighbour sites with respect to each other.

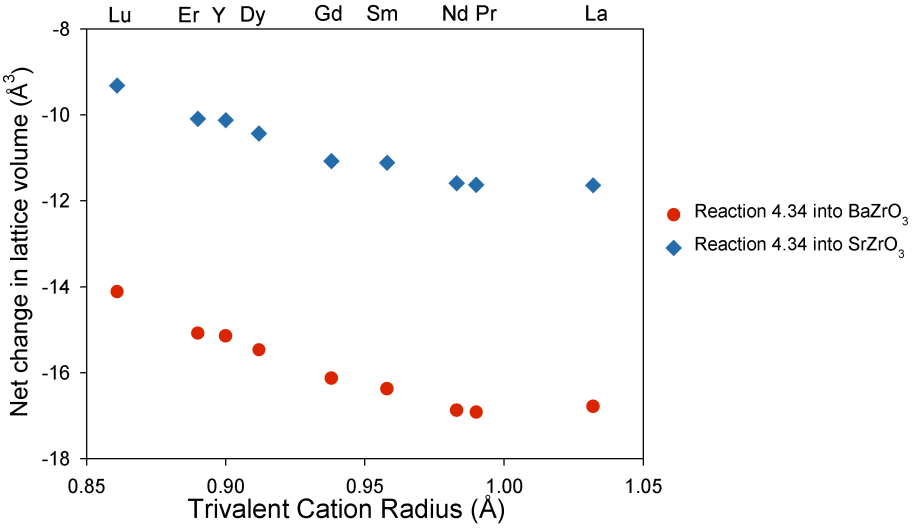


Figure 4.15: Combined change in lattice volume of both the grey phase and the uranium dioxide phase, as a function of ionic radius, for the segregation of trivalent cations at the Ba^{2+} site with charge compensation by Cr^{3+} substitution at the Zr^{4+} site. The defects occupy first nearest neighbour sites with respect to each other.

4.5 Segregation between uranium dioxide and zirconia

4.5.1 Partition energies of tetravalent cations into ZrO_2

A number of mechanisms for the partition of tetravalent cations from their stable isovalent sites in uranium dioxide into the ZrO_2 have been considered of which their isovalent accommodation at Zr^{4+} sites was most favourable (reaction 4.36).

$$\mathbf{UO_2} + \overline{M_U^{\times}} + Zr_{Zr}^{\times} \rightarrow \overline{U_U^{\times}} + M_{Zr}^{\times} + \mathbf{ZrO_2} \tag{4.36}$$

$$\overline{M_U^{\times}} + Zr_{Zr}^{\times} \rightarrow \overline{Zr_U^{\times}} + M_{Zr}^{\times} \tag{4.37}$$

Figure 4.16 reports the partition energy as a function of tetravalent cation radius. It is clear that there is a strong thermodynamic driving force encouraging the partition of small FP tetravalent cations (e.g. Ru^{4+} and Mo^{4+}). This bias towards small cations is not surprising as Zr^{4+} (0.72 Å) is significantly smaller than U^{4+} (0.89 Å) [36], providing better size matching. Conversely, large tetravalent cations (such as the actinides Am^{4+}, Pu^{4+} and Np^{4+} and the fission product Ce^{4+}) will be preferentially accommodated at the larger U^{4+} site. Although the energies are slightly lower, the expected behaviour is similar to that of $BaZrO_3$ and $SrZrO_3$.

4.5.2 Partition energies of trivalent cations into ZrO_2

From stoichiometric UO_2 into ZrO_2

Of all the mechanisms (reactions 4.38-4.41) for the partition of trivalent cations from stoichiometric UO_2 into ZrO_2 the most favourable involves charge compensation by oxygen vacancy formation (reaction 4.38). Trivalent species occupy Zr^{4+} sites either at first nearest neighbour sites (Figure 4.17) or at second nearest neighbour sites (Figures 4.18 and 4.19) with respect to the charge compensating oxygen vacancy, as shown previously by Zacate *et al.* [139]. In this work the specific configurations for the second nearest neighbour clusters

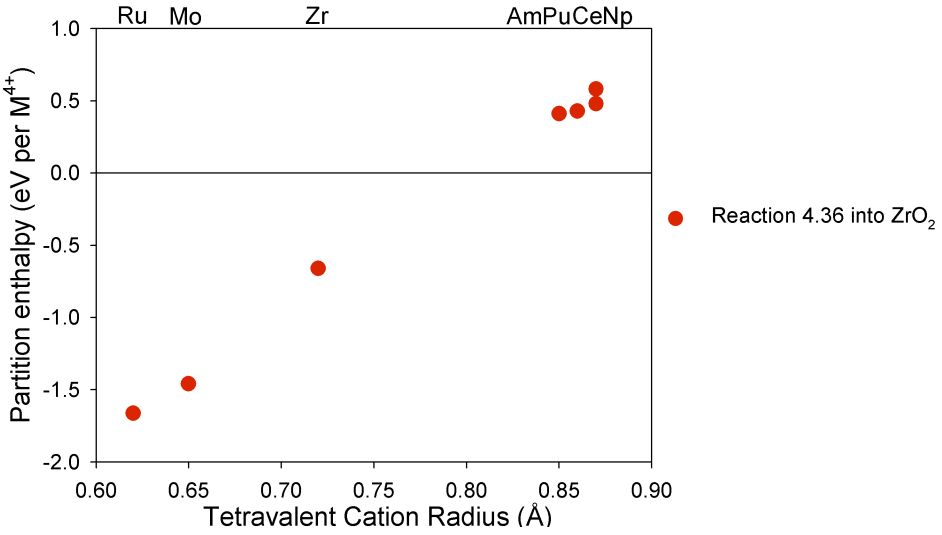


Figure 4.16: Partition enthalpies for tetravalent cation segregation into ZrO_2 from uranium dioxide as a function of ionic radius by isovalent substitution at the Zr^{4+} site.

are also identified; trivalent cations either occupy first nearest neighbour Zr^{4+} sites (Figure 4.18) or second nearest neighbour Zr^{4+} sites (Figure 4.19) with respect to each other. The angles formed by these clusters are 50° and 95° respectively.

$$\mathbf{2UO_2} + \overline{\{2T'_U : V_O^{\bullet\bullet}\}^{\times}} + 2Zr_{Zr}^{\times} + O_O^{\times} \rightarrow \overline{2U_U^{\times}} + \overline{O_O^{\times}} + \{2T'_{Zr} : V_O^{\bullet\bullet}\}^{\times} + \mathbf{2ZrO_2} \tag{4.38}$$

$$\overline{\{2T'_U : V_O^{\bullet\bullet}\}^{\times}} + 2Zr_{Zr}^{\times} + O_O^{\times} \rightarrow \overline{2Zr_U^{\times}} + \overline{O_O^{\times}} + \{2T'_{Zr} : V_O^{\bullet\bullet}\}^{\times} \tag{4.39}$$

$$\mathbf{4UO_2} + \overline{2\{2T'_U : V_O^{\bullet\bullet}\}^{\times}} + 3Zr_{Zr}^{\times} \rightarrow \overline{4U_U^{\times}} + \overline{2O_O^{\times}} + \{3T'_{Zr} : T_i^{\bullet\bullet\bullet}\}^{\times} + \mathbf{3ZrO_2} \tag{4.40}$$

$$\mathbf{UO_2} + \overline{2\{2T'_U : V_O^{\bullet\bullet}\}^{\times}} + 3Zr_{Zr}^{\times} \rightarrow \overline{4Zr_U^{\times}} + \overline{2O_O^{\times}} + \{3T'_{Zr} : T_i^{\bullet\bullet\bullet}\}^{\times} \tag{4.41}$$

Figure 4.20 shows that negative partition energies were calculated for Cr^{3+}, Fe^{3+}, In^{3+}, Lu^{3+}, Er^{3+}, Y^{3+}, Dy^{3+}, Gd^{3+} and Sm^{3+}. As such these trivalent cations are expected to segregate from stoichiometric UO_2 into ZrO_2. However, the positive partition energies calculated for Nd^{3+}, Pr^{3+} and La^{3+} indicate that these species will remain in the stoichiometric UO_2 phase.

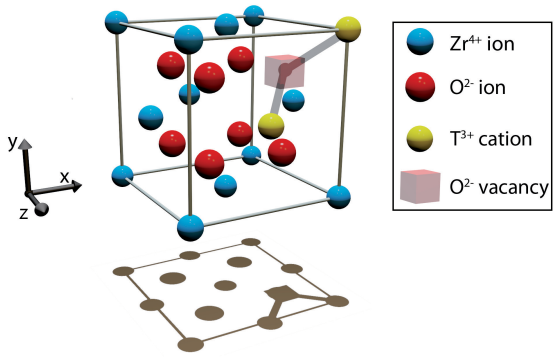


Figure 4.17: The lowest energy configuration of the $\{2T_{Zr} : V_O^{\bullet\bullet}\}^{\times}$ cluster associated with the Cr^{3+} and Fe^{3+} trivalent cations. Blue and red spheres indicate the intrinsic Zr^{4+} and O^{2-} species respectively, with the semi-transparent cube identifying the oxygen vacancy, $V_O^{\bullet\bullet}$. Substitutional trivalent cations at Zr^{4+} sites, T'_{Zr}, are shown by yellow spheres.

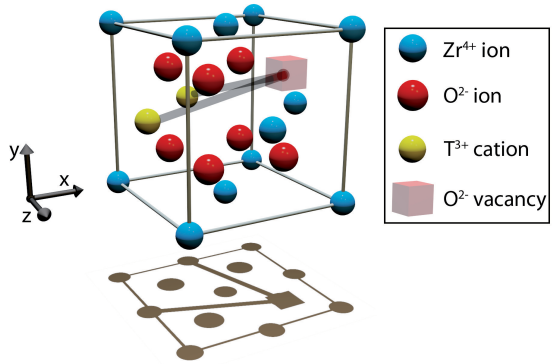


Figure 4.18: The lowest energy configuration of the $\{2T_{Zr} : V_O^{\bullet\bullet}\}^{\times}$ cluster associated with the In^{3+}, Lu^{3+}, Er^{3+}, Y^{3+}, Dy^{3+}, Gd^{3+} and Sm^{3+} trivalent cations. Blue and red spheres indicate the intrinsic Zr^{4+} and O^{2-} species respectively, with the semi-transparent cube identifying the oxygen vacancy, $V_O^{\bullet\bullet}$. Substitutional trivalent cations at Zr^{4+} sites, T'_{Zr}, are shown by yellow spheres.

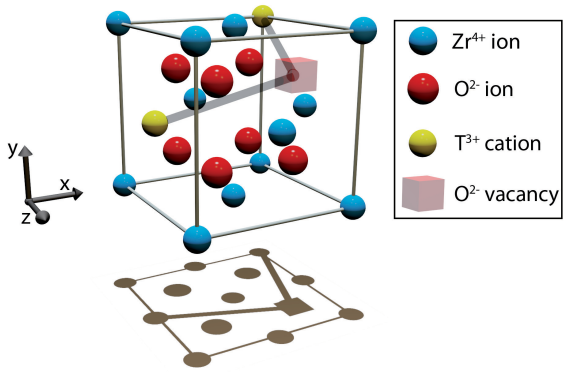


Figure 4.19: The lowest energy configuration of the $\{2T_{Zr} : V_O^{\bullet\bullet}\}^{\times}$ cluster associated with the Nd^{3+}, Pr^{3+} and La^{3+} trivalent cations. Blue and red spheres indicate the intrinsic Zr^{4+} and O^{2-} species respectively, with the semi-transparent cube identifying the oxygen vacancy, $V_O^{\bullet\bullet}$. Substitutional trivalent cations at Zr^{4+} sites, T'_{Zr}, are shown by yellow spheres.

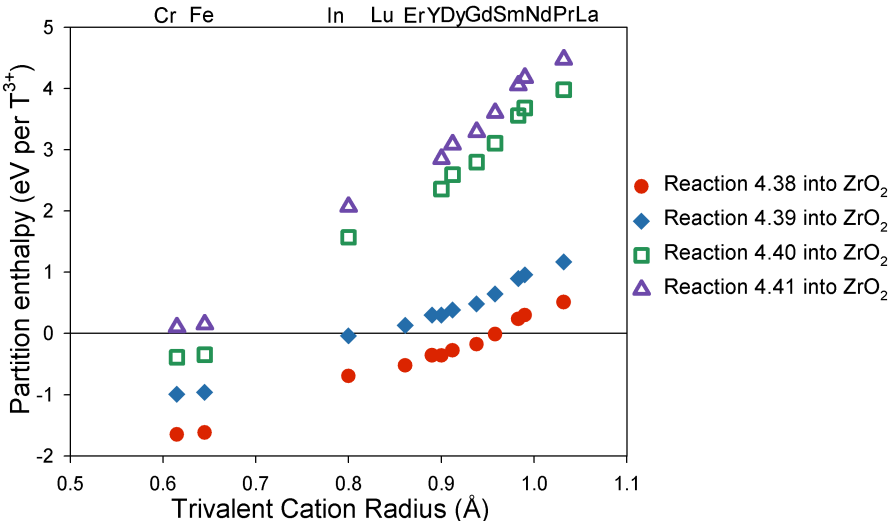


Figure 4.20: Partition enthalpies for trivalent cations into ZrO_2 from stoichiometric UO_2, as a function of ionic radius, by accommodation at the Zr^{4+} site with charge compensation by oxygen vacancies (reactions 4.38 and 4.39) or by self-interstitials (reactions 4.40 and 4.41).

From hyper-stoichiometric UO_{2+x} into ZrO_2

Of all the possible mechanisms (reactions 4.42-4.45) for trivalent cation partition from hyper-stoichiometric UO_{2+x} into ZrO_2, as was the case from UO_2, the lowest energy mechanisms involve the creation of charge compensating oxygen vacancies in the ZrO_2 phase (reaction 4.42). Nevertheless, regardless of the species studied, all trivalent cations have positive partition energies and, therefore, remain in hyper-stoichiometric UO_{2+x} (see Figure 4.21). As for (Ba,Sr)ZrO_3, this is a result of the greater solubility of trivalent cations in hyper-stoichiometric UO_{2+x} compared to stoichiometric UO_2 [78].

$$\mathbf{2UO_2} + \overline{2\{T'_U : U^{\bullet}_U\}^{\times}} + 2Zr^{\times}_{Zr} + O^{\times}_O \rightarrow \overline{2U^{\times}_U} + \overline{\{O''_i : 2U^{\bullet}_U\}^{\times}} + \{2T'_{Zr} : V^{\bullet\bullet}_O\}^{\times} + \mathbf{2ZrO_2} \quad (4.42)$$

$$\overline{2\{T'_U : U^{\bullet}_U\}^{\times}} + 2Zr^{\times}_{Zr} + O^{\times}_O \rightarrow \overline{2Zr^{\times}_U} + \overline{\{O''_i : 2U^{\bullet}_U\}^{\times}} + \{2T'_{Zr} : V^{\bullet\bullet}_O\}^{\times} \quad (4.43)$$

$$\mathbf{4UO_2} + \overline{4\{T'_U : U^{\bullet}_U\}^{\times}} + 3Zr^{\times}_{Zr} \rightarrow \overline{4U^{\times}_U} + \overline{2\{O''_i : 2U^{\bullet}_U\}^{\times}} + \{3T'_{Zr} : T^{\bullet\bullet\bullet}_i\}^{\times} + \mathbf{3ZrO_2} \quad (4.44)$$

$$\mathbf{UO_2} + \overline{4\{T'_U : U^{\bullet}_U\}^{\times}} + 3Zr^{\times}_{Zr} \rightarrow \overline{3Zr^{\times}_U} + \overline{2\{O''_i : 2U^{\bullet}_U\}^{\times}} + \{3T'_{Zr} : T^{\bullet\bullet\bullet}_i\}^{\times} \quad (4.45)$$

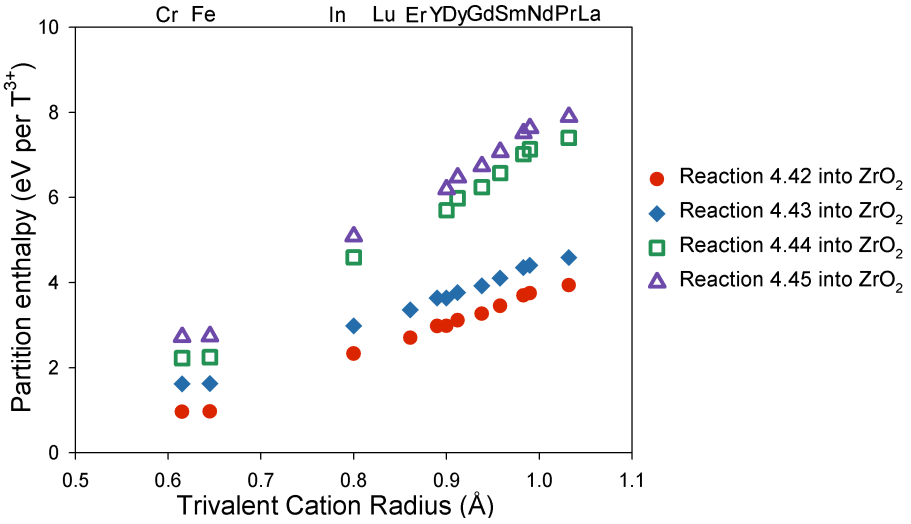


Figure 4.21: Partition enthalpies for trivalent cations into ZrO_2 from hyper-stoichiometric UO_{2+x} as a function of ionic radius by accommodation at the Zr^{4+} site with charge compensation by oxygen vacancies (reactions 4.42 and 4.43) or by self-interstitials (reactions 4.44 and 4.45).

4.6 Segregation between UO_{2+x} and $CrUO_4$

4.6.1 Partition energies of tetravalent cations

As discussed in section 4.3, in Cr-doped hyper-stoichiometric UO_{2+x} the precipitation of $CrUO_4$ is favourable. All possible mechanisms (reactions 4.46-4.54) considered for the partition of tetravalent cations into $CrUO_4$ from UO_{2+x} involved substitution at least partly at either the Cr^{3+} or U^{5+} sites. The most favourable of these involved self-charge compensating defects (reaction 4.46) or oxygen vacancy formation (reaction 4.51).

$$\mathbf{2UO_2} + \overline{2M_U^\times} + Cr_{Cr}^\times + U_U^\times \rightarrow \{M'_U : M^\bullet_{Cr}\}^\times + \overline{2U_U^\times} + \mathbf{CrUO_4} \tag{4.46}$$

$$\mathbf{4UO_2} + \overline{2M_U^\times} + \overline{\{O_i'' : 2U_U^\bullet\}^\times} + 2Cr_{Cr}^\times \rightarrow \{2M^\bullet_{Cr} : O_i''\}^\times + \overline{4U_U^\times} + \mathbf{2CrUO_4} \tag{4.47}$$

$$\mathbf{2UO_2} + \overline{M_U^\times} + Cr_{Cr}^\times + U_U^\times \rightarrow \{M^\bullet_{Cr} : U'_U\}^\times + \overline{U_U^\times} + \mathbf{CrUO_4} \tag{4.48}$$

$$\mathbf{2UO_2} + \overline{2M_U^\times} + 2Cr_{Cr}^\times + U_U^\times \rightarrow \{2M^\bullet_{Cr} : Cr''_U\}^\times + \overline{2U_U^\times} + \mathbf{CrUO_4} \tag{4.49}$$

$$\mathbf{7UO_2} + \overline{3M_U^\times} + \overline{2\{O_i'' : 2U_U^\bullet\}^\times} + 4Cr_{Cr}^\times \rightarrow \{3M^\bullet_{Cr} : V'''_{Cr}\}^\times + \overline{7U_U^\times} + \mathbf{4CrUO_4} \tag{4.50}$$

$$\overline{2M_U^\times} + 2U_U^\times \rightarrow \{2M'_U : V^{\bullet\bullet}_O\}^\times + \overline{\{O_i'' : 2U_U^\bullet\}^\times} \tag{4.51}$$

$$\mathbf{2UO_2} + \overline{M_U^\times} + Cr_{Cr}^\times + U_U^\times \rightarrow \{M'_U : U^\bullet_{Cr}\}^\times + \overline{U_U^\times} + \mathbf{CrUO_4} \tag{4.52}$$

$$\mathbf{2UO_2} + \overline{2M_U^\times} + Cr_{Cr}^\times + 2U_U^\times \rightarrow \{2M'_U : U^{\bullet\bullet}_{Cr}\}^\times + \overline{2U_U^\times} + \mathbf{CrUO_4} \tag{4.53}$$

$$\overline{M_U^\times} + 2U_U^\times \rightarrow \{M'_U : U_U^\bullet\}^\times + \overline{U_U^\times} + U_{i.p.}^{6th} - U_{i.p.}^{5th} \tag{4.54}$$

Figure 4.22 reports the partition energies as a function of tetravalent cation radius. It is clear that there is a strong thermodynamic driving force encouraging the partition of small FP tetravalent cations (such as Ru^{4+} and Mo^{4+}) by reaction 4.46 or by reaction 4.51 for Zr^{4+}. Conversely, large tetravalent cations (such as the actinides Am^{4+}, Pu^{4+} and Np^{4+} and the FP Ce^{4+}) will preferentially remain in the hyper-stoichiometric UO_{2+x} phase. This bias towards small cations is not surprising as both cation sites in the $CrUO_4$ are smaller than the U^{4+} site in UO_{2+x}.

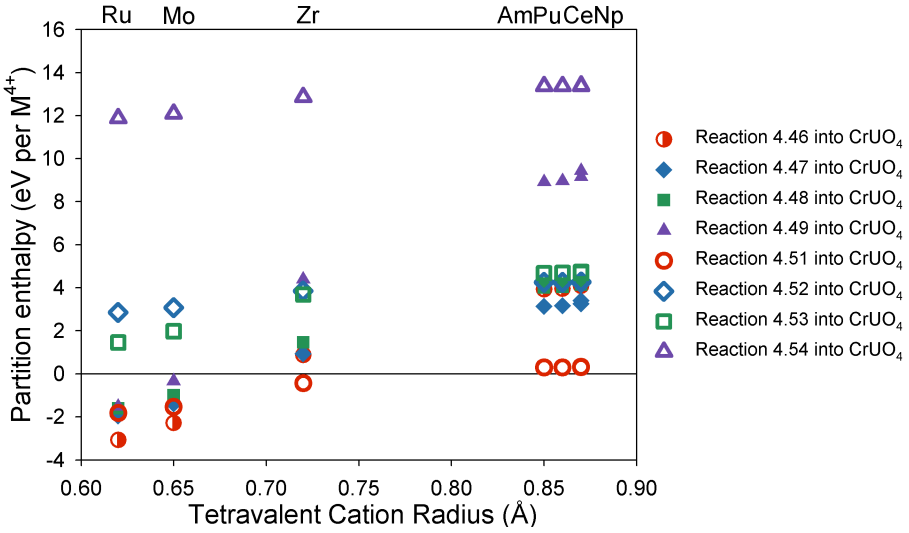


Figure 4.22: Partition enthalpies for tetravalent cations into $CrUO_4$ from hyper-stoichiometric UO_{2+x} as a function of ionic radius by substitution, at least partly, at either Cr^{3+} or U^{5+} via reactions 4.46-4.54.

4.6.2 Partition energies of trivalent cations

Of all the possible mechanisms (reactions 4.55-4.59) considered for the partition of trivalent cations from hyper-stoichiometric UO_{2+x} into $CrUO_4$ the most favourable involved their isovalent substitution at Cr^{3+} sites (reaction 4.55).

$$\mathbf{2UO_2} + \overline{\{T'_U : U^{\bullet}_U\}^{\times}} + Cr^{\times}_{Cr} \rightarrow T^{\times}_{Cr} + \overline{2U^{\times}_U} + \mathbf{CrUO_4} \tag{4.55}$$

$$\overline{\{T'_U : U^{\bullet}_U\}^{\times}} + U^{\times}_U \rightarrow \{T''_U : V^{\bullet\bullet}_O\}^{\times} + \overline{\{O''_i : 2U^{\bullet}_U\}^{\times}} \tag{4.56}$$

$$\mathbf{4UO_2} + \overline{\{T'_U : U^{\bullet}_U\}^{\times}} + U^{\times}_U + 2Cr^{\times}_{Cr} \rightarrow \{T''_U : 2U^{\bullet}_{Cr}\}^{\times} + \overline{2U^{\times}_U} + \mathbf{CrUO_4} \tag{4.57}$$

$$\mathbf{2UO_2} + \overline{\{T'_U : U^{\bullet}_U\}^{\times}} + U^{\times}_U \rightarrow \{T''_U : U^{\bullet\bullet}_{Cr}\}^{\times} + \overline{2U^{\times}_U} + \mathbf{CrUO_4} \tag{4.58}$$

$$\overline{\{T'_U : U^{\bullet}_U\}^{\times}} + 3U^{\times}_U \rightarrow \{T''_U : 2U^{\bullet}_U\}^{\times} + \overline{2U^{\times}_U} + 2U^{6th}_{i.p.} - 2U^{5th}_{i.p.} \tag{4.59}$$

Figure 4.23 shows a negative partition energy was calculated for Fe^{3+} through reaction 4.55, thus Fe^{3+} would be expected to segregated into the $CrUO_4$ phase. However, unfavourable size effects meant that all other trivalent cations studied, In^{3+}, Y^{3+}, Dy^{3+}, Gd^{3+}, Sm^{3+}, Nd^{3+}, Pr^{3+} and La^{3+}, exhibit positive partition energies, indicating that these trivalent cations

exhibit a bias to remain in the UO_{2+x} phase.

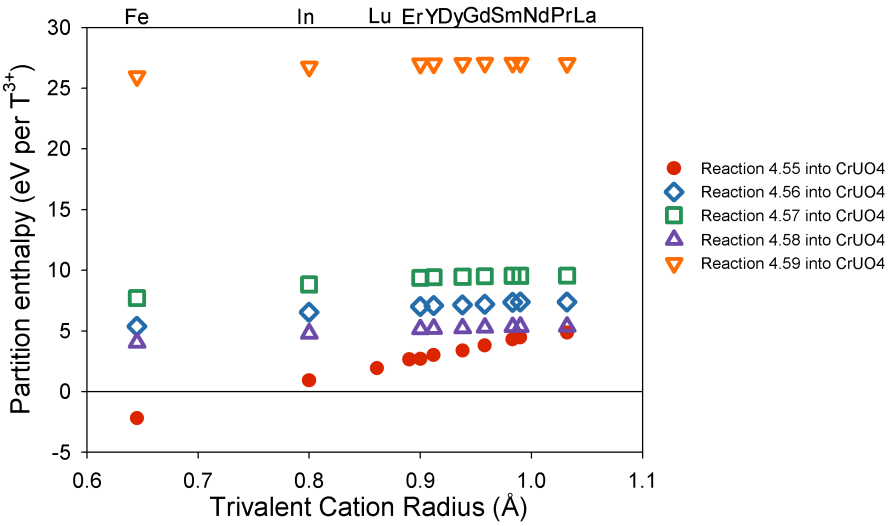


Figure 4.23: Partition enthalpies for trivalent cations into $CrUO_4$ from hyper-stoichiometric UO_{2+x} as a function of ionic radius by isovalent substitution at Cr^{3+} sites (reaction 4.55) or substitution at the U^{5+} (reactions 4.56-4.59).

4.7 Conclusions and further discussion

4.7.1 Tetravalent species

Partition of tetravalent cations is not influenced by uranium dioxide non-stoichiometry as these ions all substitute isovalently at the U^{4+} sites. Mo^{4+} and Ru^{4+} have negative partition energies into both $BaZrO_3$ and $SrZrO_3$ and, therefore, are expected to segregate to $(Ba,Sr)ZrO_3$ from UO_2 or UO_{2+x}, consistent with experimental observations [9, 79, 80]. Furthermore, a net contraction of the uranium dioxide and grey phase is predicted due to such segregation. Consequently, one would expect to observe a greater overall contraction of fuel due to the formation of Ru^{4+} and Mo^{4+} fission products than if they remain in the uranium dioxide, although the precipitation of metallic particles must be included for a more complete analysis (see future work Chapter 8). Mo is known to be a buffer for hyper-

stoichiometric fuel and prevents the further oxidation of the fuel to U_3O_8. It is possible that Mo accommodation in the grey phase could provide an alternative mechanism for buffering the oxidation of UO_2. Similarly, Mo and Ru are also predicted to segregate to $CrUO_4$ precipitates in hyper-stoichiometric Cr-doped fuels (e.g. ADOPT [4]) or, alternatively, at the AGR the fuel-clad interface. Under both hyper-stoichiometric and stoichiometric conditions ZrO_2 precipitates are also predicted to exist and the segregation of Ru^{4+} and Mo^{4+} to such precipitates is favourable. These results are also applicable to the PWR fuel-clad interface where ZrO_2 exists as the passivating layer of the Zircaloy cladding.

The larger tetravalent cations, Am^{4+}, Pu^{4+}, Ce^{4+} and Np^{4+}, have positive partition energies from UO_2 or UO_{2+x} into $BaZrO_3$, $SrZrO_3$, ZrO_2 and $CrUO_4$. These tetravalent cations are, therefore, expected to always remain in UO_2 or UO_{2+x}. This is not unexpected due to the similar chemistry and ionic radii of these species and the uranium cation.

4.7.2 Trivalent species

In undoped stoichiometric UO_2 (but not UO_{2+x}) the segregation of the large trivalent cations Sm^{3+}, Nd^{3+}, Pr^{3+} and La^{3+} into $BaZrO_3$ is expected, although not into $SrZrO_3$: so it is predicted that these fission products will be preferentially accommodated in grey phase precipitates that have a high Ba:Sr ratio. On the other hand, the smaller ions In^{3+}, Lu^{3+}, Er^{3+}, Y^{3+}, Dy^{3+} and Gd^{3+}, all exhibit positive partition energies into $BaZrO_3$ and $SrZrO_3$ from UO_2 and are not expected to segregate. Alternatively, the presence of excess Cr [4] in the fuel enables favourable segregation of all trivalent cations into $BaZrO_3$ and $SrZrO_3$ from UO_2, thus enhancing segregation to the grey phase and removing the dependence of the Ba:Sr ratio. This may be important because grey phase precipitates could act as fission gas nucleation sites [10]. Furthermore, the enhanced removal of fission products from uranium dioxide may be deleterious because some grey phase compositions are known experimentally to have markedly lower thermal conductivities than UO_2 [140]. On the other hand, removal of fission product defects from the UO_2 lattice may enhance the conductivity of the UO_2 fraction. Despite Cr-doping not being sufficient to enable segregation to (Ba,Sr)ZrO_3

from hyper-stoichiometric UO_{2+x}, it does enable the precipitation of the $CrUO_4$ phase; however the calculations suggest that trivalent cations will remain in solution in UO_{2+x} rather than segregate to $CrUO_4$.

Trivalent cations can also be accommodated in ZrO_2 instead of remaining in stoichiometric UO_2, and this is predicted for In^{3+}, Lu^{3+}, Er^{3+}, Y^{3+}, Dy^{3+}, Gd^{3+} and Sm^{3+}. A number of elements, particularly trivalent cations such as Y^{3+}, act to stabilise the cubic fluorite structure of ZrO_2 to much lower temperatures, even down to room temperature [141]. If sufficient segregation were to have occurred (presumably requiring higher burn-up and longer fuel residence times) the coherency between uranium dioxide and zirconia at the fuel-cladding interface could be greatly increased over an extended temperature range. This could help explain why fracture between the fuel and cladding is sometimes observed within the UO_2 rather than at the cladding-fuel interface [128]. Conversely, no trivalent cation segregation to ZrO_2 is predicted from UO_{2+x}.

Chapter 5

Uranium vacancy migration in UO_2 and UO_{2+x}

This work is published in:
M. W. D. Cooper, S. C. Middleburgh and R. W. Grimes, *Solid State Ionics* **266**, 68-72 (2014) [142]

5.1 Introduction

The migration of uranium ions in uranium dioxide is an important factor in determining the mobility and release of fission gases from nuclear fuel pellets [84, 143–145] (see Chapter 1 for a more detailed discussion). Xe, Kr and other fission products migrate via the uranium sublattice where vacancy mediated diffusion controls the species release. The transport of intrinsic point defects is also a key parameter in the recovery from radiation damage. By understanding the mechanisms underpinning uranium vacancy migration, fuel performance predictions can be improved.

Experiments by Matzke [146] estimated the Arrhenius activation enthalpy for uranium vacancy migration to be 5.6 eV in UO_2 and 2.6 eV in UO_{2+x}. The migration enthalpies were

computed by measuring the diffusion of ^{238}Pu in uranium dioxide and were, therefore, not strictly indicative of uranium cation transport, especially considering the possibility that Pu can be in the 3+ rather than 4+ charge state in the stoichiometric case [73]. Reimann and Lundy [147], for example, calculated the Arrhenius activation enthalpy value to be 4.3 eV in UO_2. Although other experimental work has been carried out, it often focused on mixed oxides such as (U,Pu)$O_{2\pm x}$ [148]. Thus, despite efforts to understand the effect of non-stoichiometry and temperature on the contribution of uranium vacancies, the underlying migration mechanisms in UO_2 and UO_{2+x} are still not sufficiently well understood.

Difficulties with experimental studies have meant that a great deal of theoretical work has been carried out to understand the transport of cations in UO_2. Early work by Catlow [15] used empirical potentials to estimate the vacancy migration enthalpy in $UO_{2\pm x}$ for transport with and without charge balancing oxygen vacancies, but it did not consider charge compensation by U^{5+} cations. The results agreed with the UO_2 and UO_{2+x} experimental values, especially that the peak in activation enthalpy occurred at the stoichiometric composition. The activation enthalpy was calculated to be ~5.3 eV. Jackson *et al.* [20], using the same modelling technique, included the migration of U^{3+} and U^{5+} cations in UO_2 as well as U^{4+} cations. They predicted the migration enthalpy to increase as a function of U ion charge, so that, U^{3+}, U^{4+} and U^{5+} cations exhibited migration enthalpies of 3.32 eV, 4.85 eV and 7.32 eV respectively.

More recently, 19 different empirical potentials have been compared by Govers *et al.* [145] and validated against density functional theory (DFT) or experimental data where available. Depending on the empirical model, uranium vacancy (V_U'''' in Kröger-Vink notation [96]) migration was computed to proceed with an enthalpy ranging from 0.6 eV to 8.2 eV, quite an extra-ordinary spread. There was no obvious correlation between those models that employed formal charges (i.e. the uranium and oxygen charges set to +4*e* and -2*e*, respectively) and those models that use partial charge models. Notably, the calculations presented by Govers *et al.* [145] did not consider cluster configurations using charge compensating defects, due to computational restraints, lack of information and that it was not the main

focus of the study.

The DFT calculations of Dorado *et al.* [149] investigated uranium vacancy migration enthalpy using a form of occupational control to ensure the lowest enthalpy arrangement was attained. During electronic structure optimisation of a uranium vacancy within a charge neutral supercell, the charge compensating U^{5+} defects can be investigated. However, Dorado *et al.* [149] used a 4+ background charged supercell negating the necessity for charge balancing U^{5+} defects. The reported migration enthalpies were dependent on the oxygen displacement and exchange correlation used; the lowest enthalpy barrier of 3.6 eV employed GGA exchange correlation with a Hubbard correction. Although nudged elastic band methods implemented in DFT would be capable of capturing the behaviour of the small polaron rearrangement of the U^{5+} cation (as the electronic structure is optimised separately in each step of the uranium vacancy migration) it is not possible to identify multiple U^{5+} arrangements that have migration enthalpies very close to the lowest enthalpy pathway and could also contribute to diffusion. Due to the high computational cost and large number of cluster configurations needed, DFT is not yet suitable for studying the effect of oxygen vacancy reconfiguration during uranium vacancy migration within Schottky clusters. Furthermore, DFT studies are usually limited to a 2×2×2 supercell containing 96 lattice sites [97, 149–151]. Conversely, the use of fully dilute techniques such as the Mott-Littleton method are possible with empirical potentials.

Here the role of uranium vacancies in uranium ion transport in stoichiometric and hyper-stoichiometric uranium dioxide is considered. Unlike previous empirical studies, charge compensating defects in UO_2 and in UO_{2+x} are included. As shown previously, the dominant positive charge compensating species in stoichiometric UO_2 is the oxygen vacancy ($V_O^{\bullet\bullet}$) [78]. In hyper-stoichiometric UO_{2+x}, accommodation of excess oxygen by the formation of oxygen interstitials will annihilate any remaining oxygen vacancies and then oxidises U^{4+} to form U^{5+} defects ($U_U^{\bullet}$). U^{5+} cations will, therefore, be the dominant positively charged species compensating the negatively charged uranium vacancies in UO_{2+x}. Thus, vacancy mediated uranium migration enthalpy is investigated in $\{V_U'''' : 2V_O^{\bullet\bullet}\}^{\times}$ and

$\{V_U'''' : 4U_U^\bullet\}^\times$ defect clusters, representing UO_2 and UO_{2+x} respectively. Rather than only considering the most stable arrangement, as has previously been the case [149, 152], the uranium vacancy migration enthalpy is also calculated for a large number of configurations to understand whether a metastable arrangement of the defect cluster may dominate, or at least contribute, to the migration mechanism despite the enthalpy penalty for reconfiguration.

5.2 Calculation details

Atomistic simulations have been carried out using the General Utility Lattice Program (GULP) [100]. The energy of interaction between two ions, i and j, were described by the short range Buckingham potential [110] type potential (see section 2.3.1), using the parameters derived by Busker *et al.* [16, 153]. This potential set was chosen due its ability to describe the properties of UO_2 accurately at the low temperature limit (see Chapter 3) that is applicable to the static methods employed in this Chapter.

Defect cluster enthalpies were determined using energy minimisation calculations within the Mott-Littleton approach [99], as described in Chapter 2, with region I and IIa radii of 13.0 Å and 34.0 Å respectively (as used with this potential set previously [78, 154]). Defect enthalpies were determined for all possible configurations of the $\{V_U'''' : 2V_O^{\bullet\bullet}\}^\times$ and $\{V_U'''' : V_O^{\bullet\bullet}\}''$ clusters that fit within a 2×2×2 cubic fluorite unit cell volume. By including the isolated oxygen vacancy defect enthalpy, the latter cluster is considered as a partially bound version of the former (note the change in cluster charge). As discussed in section 5.1, this cluster, which incorporates oxygen vacancies, establishes the state in stoichiometric UO_2. Equivalently, hyper-stoichiometric UO_{2+x} was investigated by determining the defect enthalpies of the $\{V_U'''' : 4U_U^\bullet\}^\times$, $\{V_U'''' : 3U_U^\bullet\}'$, $\{V_U'''' : 2U_U^\bullet\}''$ and $\{V_U'''' : U_U^\bullet\}'''$ clusters again for all configurations it is possible to form within the 2×2×2 fluorite supercell volume, but this time the charged clusters are partly bound leaving additional isolated U^{5+} ions.

For each cluster configuration, a rational functional optimisation (RFO) [155] calculation

was used to determine the system enthalpy at the saddle point for the migration of a U^{4+} ion into a first nearest neighbour uranium vacancy in the $\langle 110 \rangle$ direction. The enthalpy barrier was determined by subtracting the saddle point enthalpy from the associated defect cluster enthalpy in a similar manner to the previous study of vacancy migration in UO_2 carried out by Govers *et al.* [145]. Care was taken to include only saddle points that would facilitate migration of the species into the vacancy as the RFO method may find other points that fulfil the stopping criterion of the saddle point finder.

The possibility that during vacancy migration reconfiguration of the cluster from its most stable configuration into a metastable arrangement reduces the enthalpy barrier is studied. If the reduction in the enthalpy barrier is greater than the change in enthalpy of the cluster due to reconfiguration (reconfiguration enthalpy), a lower overall uranium vacancy migration enthalpy has been identified. Thus, from now on migration enthalpy refers to the combination of reconfiguration enthalpy and the enthalpy barrier for a given cluster configuration. A number of approximations have been made, in particular, that the oxygen sub-lattice is able to move far more rapidly than the uranium vacancy, which allows a metastable arrangement of the $\{V_U'''' : 2V_O^{\bullet\bullet}\}^{\times}$ cluster to exist for the migration event. This is acceptable given experimental and modelling studies report oxygen migration to be orders of magnitude faster than for uranium [15, 20, 156]. Similarly, it is assumed that the hole on the uranium sub-lattice (which is responsible for U^{5+} being 5+) is very mobile compared to uranium vacancies - a sensible approximation given the small-polaron behaviour of U^{5+} in the lattice [157].

Migration of the U^{3+} cation and U^{5+} cation into a vacancy were also considered as these species may exist due to variations in stoichiometry or via the endothermic reaction $U^{4+} \rightarrow \frac{1}{2}U^{3+} + \frac{1}{2}U^{5+}$ (the Catlow-MacInnes process [158]) with an enthalpy of ~1.7 eV (obtained using DFT methods [149]) or ~1.9 eV (using empirical and experimental methods [20]).

5.3 Isolated uranium vacancy migration

From its initial position at a uranium site, the uranium vacancy can migrate to one of the 12 surrounding first nearest neighbour uranium sites located in the ⟨110⟩ (and orthogonal) directions. Alternatively, it is possible for the uranium vacancy to migrate directly to one of the 6 second nearest neighbour uranium positions located in the ⟨100⟩ (and orthogonal) directions. Figure 5.1a illustrates the two possible uranium vacancy migration mechanisms.

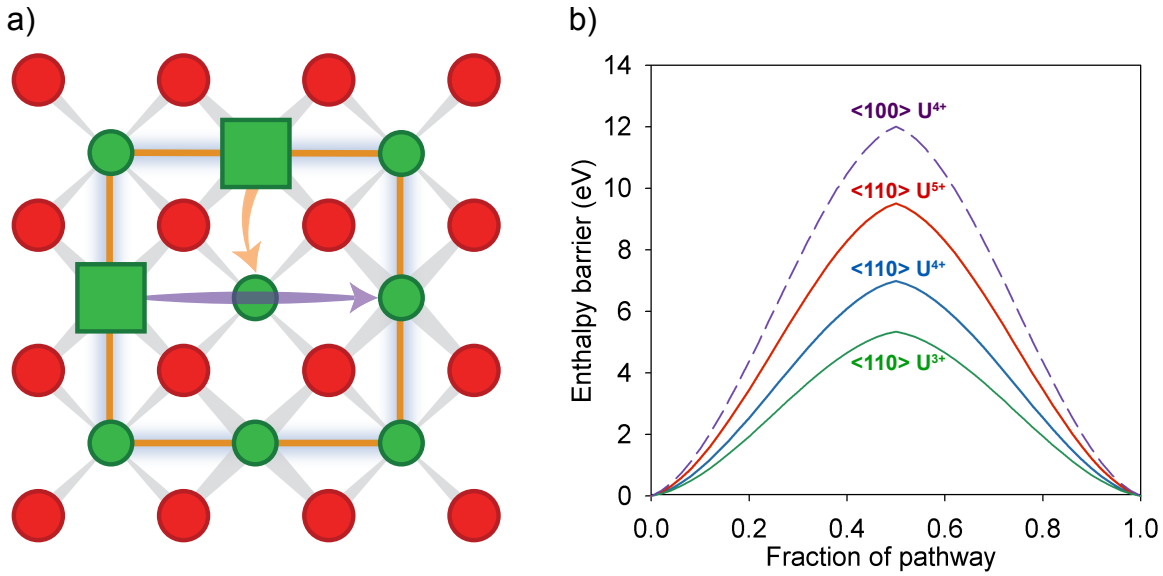


Figure 5.1: a) Schematic illustration of the fluorite structure of UO_2 projected in the ⟨100⟩ direction. Uranium and oxygen ions are indicated by green and red spheres respectively. Note that uranium cations are located on two parallel planes. The fluorite unit cell is identified by the orange box. ⟨100⟩-type and ⟨110⟩-type uranium vacancy mediated uranium migration mechanisms are shown by purple and orange arrows respectively. Uranium-oxygen bonds are shown in light grey. b) The enthalpy barriers without charge compensating defects for ⟨100⟩-type and ⟨110⟩-type U^{4+} migration as well as ⟨110⟩-type migration for U^{3+} and U^{5+}.

Due to the large computational demand of investigating the enthalpy barriers within all possible configurations of the $\{V_U : 2V_O^{\bullet\bullet}\}^{\times}$ and $\{V_U'''' : 4U_U^{\bullet}\}^{\times}$ clusters, highly unfavourable

migration mechanisms must be ruled out. The enthalpy barrier for U^{4+} migration via the vacancy mechanism is calculated to be 12.01 eV and 6.99 eV in the ⟨100⟩ and ⟨110⟩ directions respectively (see Figure 5.1b). As the barrier for migration for ⟨100⟩-type migration is so large, migration between second nearest neighbour sites can be ruled out. Alternatively, a U^{3+} and U^{5+} can form with an enthalpy of ∼1.7 eV or ∼1.9 eV (according to [20, 149]). As such, the migrating species may not be a U^{4+} but either U^{5+} or U^{3+}. The enthalpy barriers for each of these species into a vacancy (without any charge compensating defects) is predicted to proceed with energies of 9.51 eV and 5.34 eV for U^{5+} and U^{3+}, respectively. The former barrier is significantly larger than for U^{4+} and the possibilty of U^{5+} migration is subsequently discounted. Conversely, the U^{3+} barrier is 1.57 eV lower than for the migration of U^{4+} into the uranium vacancy. Nonetheless, the uranium vacancy and U^{3+} ion, being similarly charged defects, Coulombically repel with an energy of 1.82 eV. This combined with the enthalpy required to form the U^{3+} defect (1.7-1.9 eV) makes this migration mechanism also unlikely. Therefore, the remainder of this study is restricted to ⟨110⟩-type migration within charge compensating clusters.

5.4 Uranium vacancy migration in stoichiometric UO_2

Using the RFO technique, the enthalpy barrier for U^{4+} migration via a vacancy mechanism in the ⟨110⟩ direction has been calculated for the fully charge compensated $\{V_U'''' : 2V_O^{\bullet\bullet}\}^{\times}$ cluster (of which there are 4032 configurations) as well as the partially bound $\{V_U'''' : V_O^{\bullet\bullet}\}''$ cluster (64 configurations) and the isolated vacancy, V_U''''. The reconfiguration enthalpy for a given metastable cluster is defined as the enthalpy required to go from most stable $\{V_U'''' : 2V_O^{\bullet\bullet}\}^{\times}$ cluster to the metastable configuration. As such, all $\{V_U'''' : V_O^{\bullet\bullet}\}''$ reconfiguration enthalpies also include the isolated oxygen vacancy defect enthalpy in a manner that permits them to be considered as a subset of the $\{V_U'''' : 2V_O^{\bullet\bullet}\}^{\times}$ cluster (with one unbound oxygen vacancy). In agreement with the work of Dorado *et al.* [156], the association of oxygen vacancies to form the partially bound and then fully bound clusters (reactions 5.1 and 5.2) was calculated to be preferable with binding enthalpies of 4.24 eV and 3.67 eV associ-

ated with the lowest energy cluster configurations.

$$V_U'''' + V_O^{\bullet\bullet} \xrightarrow{-4.24\ \text{eV}} \{V_U'''' : V_O^{\bullet\bullet}\}'' \tag{5.1}$$

$$\{V_U'''' : V_O^{\bullet\bullet}\}'' + V_O^{\bullet\bullet} \xrightarrow{-3.67\ \text{eV}} \{V_U'''' : 2V_O^{\bullet\bullet}\}^{\times} \tag{5.2}$$

Interestingly, the lowest enthalpy fully charge balanced cluster does not involve the oxygen vacancies in a first nearest neighbour position to the cation vacancy. The lowest enthalpy cluster is illustrated in Figure 5.3. Using this ground state, we can now proceed to understand whether there is a metastable cluster that produces an overall reduction in migration enthalpy.

Figure 5.2 reports total migration enthalpies (enthalpy barrier + reconfiguration enthalpy) for a U^{4+} ion migrating into the uranium vacancy as a function of the reconfiguration enthalpy for a given $\{V_U'''' : 2V_O^{\bullet\bullet}\}^{\times}$ cluster configuration. The enthalpy barrier associated with the most stable $\{V_U'''' : 2V_O^{\bullet\bullet}\}^{\times}$ cluster is 6.60 eV and is highlighted in Figure 5.3a. Interestingly, there are 17 metastable cluster configurations with a lower total migration enthalpy than 6.60 eV. The lowest total migration enthalpy of just 6.41 eV occurs via a metastable cluster with a reconfiguration enthalpy of 2.44 eV and an enthalpy barrier of just 3.97 eV. The arrangement of this cluster and the migration of the U^{4+} into the vacancy is illustrated in Figure 5.3b.

Although one cannot be certain that the absolute migration enthalpy is correct, the existence of alternative migration pathways via metastable cluster configurations has been demonstrated for stoichiometric UO_2.

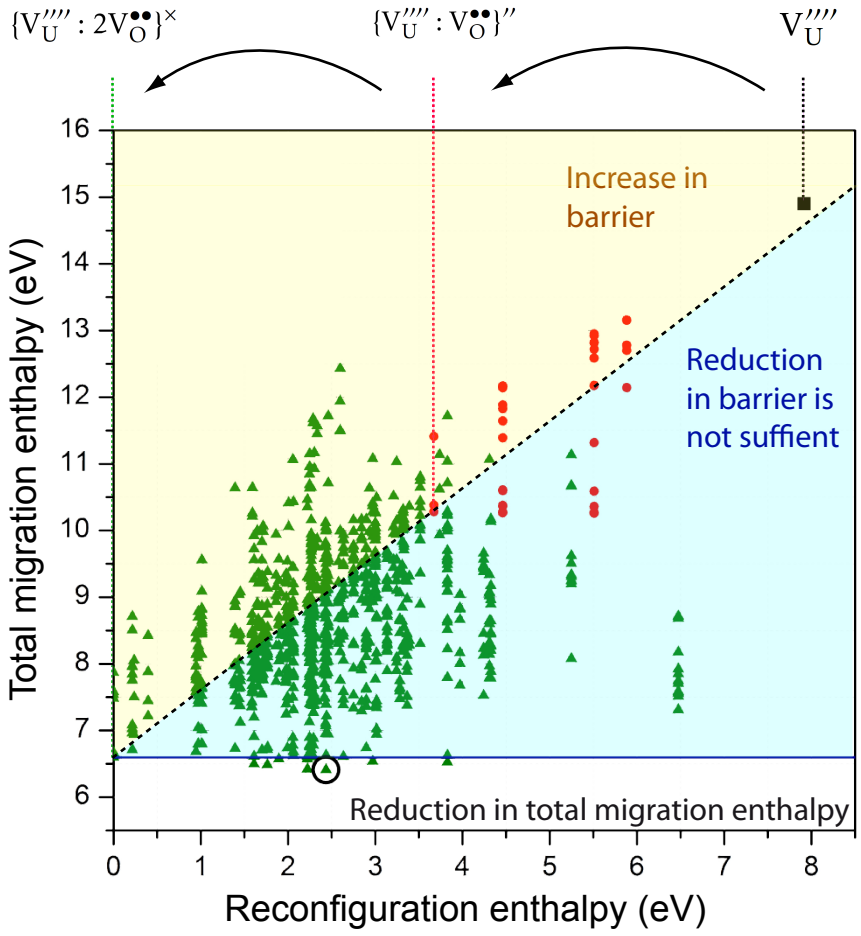


Figure 5.2: Uranium vacancy migration enthalpy as a function of metastable cluster enthalpy relative to the most stable cluster $\{V_U'''' : 2V_O^{\bullet\bullet}\}^{\times}$ cluster. Green triangles represent configurations of the $\{V_U'''' : 2V_O^{\bullet\bullet}\}^{\times}$ cluster where both charge compensating oxygen vacancies are within 9.5 Å of the migrating uranium vacancy. Configurations where only one oxygen vacancy is bound are shown by red circles. The migration when all constituent defects are in the dilute limit is shown by the black square. The blue horizontal line represents the migration enthalpy for the most stable $\{V_U'''' : 2V_O^{\bullet\bullet}\}^{\times}$ cluster configuration (6.60 eV). The cluster with the lowest total migration enthalpy (6.41 eV) is circled.

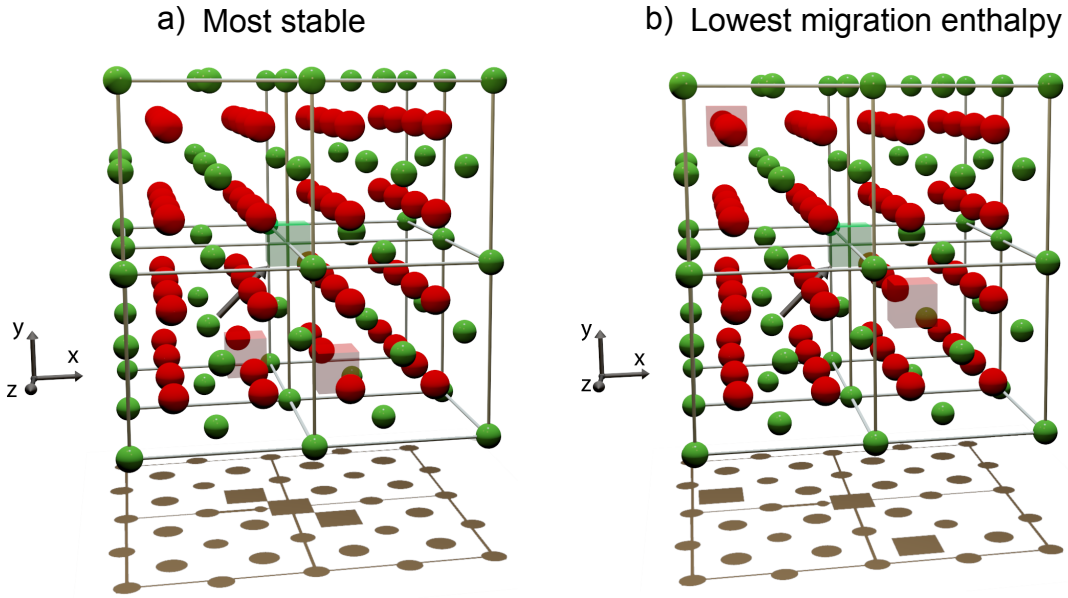


Figure 5.3: a) The most stable and b) lowest total migration enthalpy configurations of the $\{V_U'''' : 2V_O^{\bullet\bullet}\}^{\times}$ cluster for stoichiometric UO_2. U^{4+} and O^{2-} ions are represented by green and red spheres respectively. Similarly, uranium and oxygen vacancies are indicated by green and red semi-transparent cubes respectively. The migration pathway of the U^{4+} cation into the the uranium vacancy is shown by the black arrow.

5.5 Uranium vacancy migration in hyper-stoichiometric UO_{2+x}

The dominant positive charge compensating species in hyper-stoichiometric UO_{2+x} is the U^{5+} ion occupying the U^{4+} lattice site (i.e. $U_U^{\bullet}$). As such, the migration of uranium via a vacancy mechanism must be investigated for the fully charge balanced $\{V_U^{''''}:4U_U^{\bullet}\}^{\times}$ cluster (755,160 configurations) as well as the partially charge balanced $\{V_U^{''''}:3U_U^{\bullet}\}'$ (26,970 configurations), $\{V_U^{''''}:2U_U^{\bullet}\}''$ (930 configurations) and $\{V_U^{''''}:U_U^{\bullet}\}'''$ clusters (31 configurations). The reconfiguration enthalpy for a given metastable configuration is again defined as the enthalpy required to transition from the most stable $\{V_U^{''''}:4U_U^{\bullet}\}^{\times}$ arrangement to the metastable configuration. Therefore, all $\{V_U^{''''}:3U_U^{\bullet}\}'$, $\{V_U^{''''}:2U_U^{\bullet}\}''$ and $\{V_U^{''''}:U_U^{\bullet}\}'''$ clusters energies also include one or more isolated $U_U^{\bullet}$ defect energies such that they can be considered as a subset of the $\{V_U^{''''}:4U_U^{\bullet}\}^{\times}$ cluster. However, the binding of U^{5+} defects to the uranium vacancy to form the fully bound configuration is calculated to be favourable with progressive binding energies for each partly compensated cluster shown in reactions 5.3-5.6.

$$V_U^{''''} + U_U^{\bullet} \xrightarrow{-1.60\ \text{eV}} \{V_U^{''''}:U_U^{\bullet}\}''' \tag{5.3}$$

$$\{V_U^{''''}:U_U^{\bullet}\}''' + U_U^{\bullet} \xrightarrow{-1.43\ \text{eV}} \{V_U^{''''}:2U_U^{\bullet}\}'' \tag{5.4}$$

$$\{V_U^{''''}:2U_U^{\bullet}\}'' + U_U^{\bullet} \xrightarrow{-1.08\ \text{eV}} \{V_U^{''''}:3U_U^{\bullet}\}' \tag{5.5}$$

$$\{V_U^{''''}:3U_U^{\bullet}\}' + U_U^{\bullet} \xrightarrow{-1.33\ \text{eV}} \{V_U^{''''}:4U_U^{\bullet}\}^{\times} \tag{5.6}$$

Figure 5.4 reports total migration enthalpies (enthalpy barrier + reconfiguration enthalpy) for a U^{4+} ion migrating into the uranium vacancy as a function of the reconfiguration enthalpy for a given $\{V_U^{''''}:4U_U^{\bullet}\}^{\times}$ cluster configuration. The enthalpy barrier associated with the most stable $\{V_U^{''''}:4U_U^{\bullet}\}^{\times}$ cluster is 7.23 eV and the configuration is given in Figure 5.5a. There is, however, a metastable cluster that is 0.52 eV less stable but has a migration enthalpy barrier of just 6.32 eV. This represents a total migration enthalpy of 6.84 eV, which is 0.39 eV lower than vacancy migration in the most stable cluster. In a similar manner to the situation in stoichiometric UO_2, the reduction in the enthalpy barrier outweighs the enthalpy penalty to reconfigure the cluster and, as such, this migration process is more

favourable. The arrangement of this cluster and the migration of the U^{4+} into the vacancy is illustrated in Figure 5.5b. There are 358 other metastable clusters that also exhibit lower enthalpy migration pathways; these are shown in Figure 5.4 as points below the parity line.

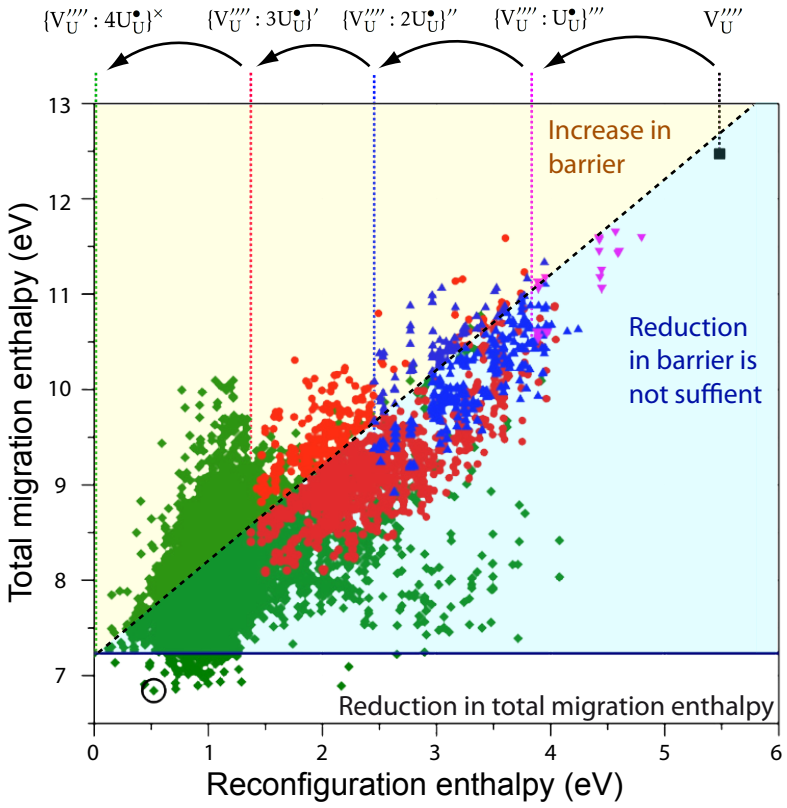


Figure 5.4: Uranium vacancy migration enthalpy as a function of metastable cluster enthalpy relative to the most stable $\{V_U'''' : 4U_U^\bullet\}^\times$ cluster. Green diamonds represent configurations of the $\{V_U'''' : 4U_U^\bullet\}^\times$ cluster where all U^{5+} ions are within 9.5 Å of the migrating uranium vacancy. Configurations where one, two or three U^{5+} ions are bound are represented by pink triangles, blue triangles and red circles respectively. Finally, the case where all constituent defects are in the dilute limit is shown by the black square. The blue horizontal line represents the migration enthalpy for the most stable $\{V_U'''' : 4U_U^\bullet\}^\times$ cluster (7.23 eV). The configuration with the lowest total migration enthalpy (6.82 eV) is circled.

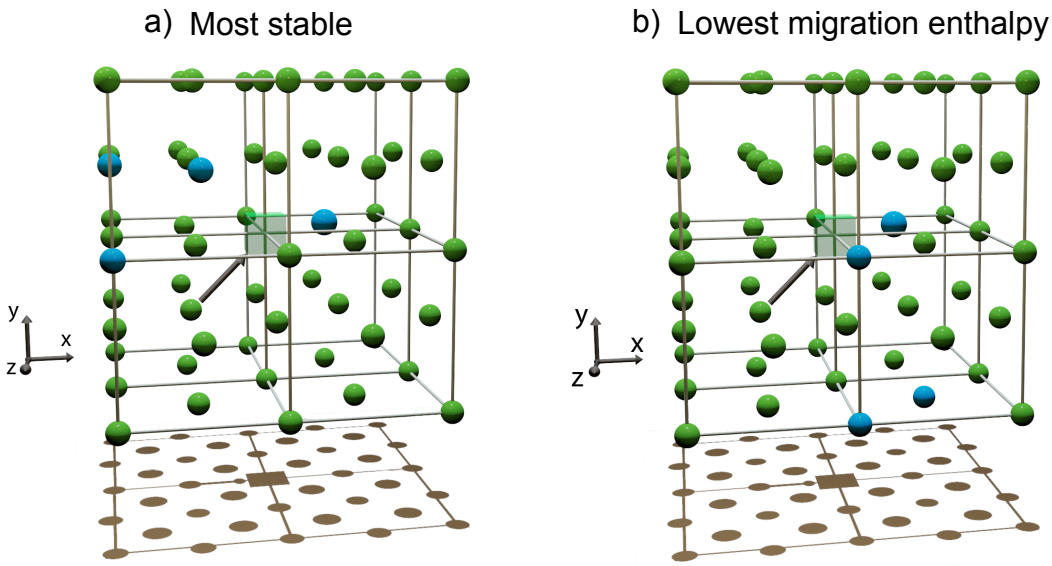


Figure 5.5: a) The most stable and b) lowest total migration enthalpy configurations of the $\{V_U'''' : 4U_U^{\bullet}\}^{\times}$ cluster for hyperstoichiometric UO_{2+x}. U^{4+} and U^{5+} cations are represented by green and blue spheres respectively. For clarity the oxygen sublattice is omitted. The migration pathway of the U^{4+} cation into the the uranium vacancy is shown by the black arrow.

5.6 Conclusions

These results demonstrate that the lowest enthalpy cluster arrangement will not necessarily provide the lowest overall migration enthalpy for U^{4+} transport via a vacancy mechanism. Reconfiguration of the cluster to a metastable arrangement enables alternative diffusion mechanisms with lower migration enthalpies than that of the most stable cluster. In the case of stoichiometric UO_2 the lowest overall migration enthalpy was 6.41 eV (0.19 eV lower than the migration involving the most stable defect cluster arrangement). A further 17 mechanisms were also found to be more favourable than the most stable configuration. Similarly, in hyper-stoichiometric UO_{2+x}, 358 metastable configurations were identified as having lower overall migrations enthalpies than the most stable configuration, the lowest of which was 6.89 eV (0.64 eV more favourable than in the most stable cluster).

Although hyper-stoichiometric UO_{2+x} has been predicted to exhibit a slightly higher overall

migration enthalpy than that for stoichiometric UO_2, the prediction that there are so many more possible diffusion pathways of similar enthalpy in UO_{2+x} is significant. By treating the migration enthalpies as approximately the same (i.e. $E_1^m \approx E_2^m \approx ... \approx E_n^m$) the following simplification of the Arrhenius relationship can be made,

$$\begin{aligned} D =& D_1 exp\left(\frac{-E_1^m}{k_B T}\right) + D_2 exp\left(\frac{-E_2^m}{k_B T}\right) + ... + D_n exp\left(\frac{-E_n^m}{k_B T}\right) \\ \approx& (D_1 + D_2 + ... + D_n) exp\left(\frac{-E^m}{k_B T}\right) \end{aligned} \tag{5.7}$$

As the number of similar migration pathways, n, is one order of magnitude greater in UO_{2+x} than for UO_2 this will make a proportionate contribution to the pre-exponential term in the Arrhenius relationship. This will enhance diffusivity in hyper-stoichiometric UO_{2+x}, especially at higher temperatures where the pre-exponential term is most significant. Nevertheless to be definitive further work must be undertaken to calculate other contributions to the pre-exponential term, such as the correlation factor and attempt frequency [159] that may be configuration dependent.

This work suggests techniques that do not include charge balancing defects or only include them in the lowest enthalpy arrangement only will not accurately capture the lowest possible migration barrier in the UO_2-UO_{2+x} system. This is potentially relevant in other ionic systems. Furthermore, it is necessary to identify the possibly large number of related migration mechanisms that occur with similar migration enthalpies via metastable clusters.

Chapter 6

A many-body potential for the description of actinide oxides

Part of this work is published in:

M.W.D. Cooper, M.J.D. Rushton, R.W. Grimes, *J. Phys.: Condens. Matter* **26**, 105401 (2014) [160]

M.W.D. Cooper, S.T. Murphy, M.J.D. Rushton, R.W. Grimes, *J. Nucl. Mater.* **461**, 206-214 (2015) [181]

S.T. Murphy, M.W.D. Cooper, R.W. Grimes, *Solid State Ionics* **267**, 80-87 (2014) [44]

The developers of DP_POLY now support this model as of version 4.06.1

Support for the potential model is provided at:

abulafia.mt.ic.ac.uk/potentials/actinides/

6.1 Introduction

UO_2 has been studied widely as it is the basis of conventional reactor fuels. It can be blended with other actinide oxide powders, in particular PuO_2, to form what is commonly called mixed oxide fuel (MOX). As such, it is important to better understand the thermomechanical properties of both component phases in order to understand the performance of these fuels.

A detailed comparison of potential models and their ability to reproduce the experimentally observed properties of uranium dioxide was given in Chapter 3; here these models are briefly revisited. Atomistic modelling techniques have been used for many years to provide information on the elementary mechanisms that govern the observable behaviour of actinide oxides [2, 13, 14, 16, 20, 22, 23, 27, 28, 30–34, 107, 112, 161–163]. The complex chemistry associated with these systems has meant that, ideally, the interatomic forces governing their properties have been better described using quantum mechanical (QM) based methods. Due to the large computational demands QM methods impose, however, system sizes are restricted. For this reason, methods employing classical pair potentials are often used, allowing properties associated with larger length and time scales to be studied, for example the multi-grain simulations of Govers *et al.* [107].

As discussed out in Chapter 3, over the years ionic interactions within UO_2 models have been described using a number of different potential forms. Several employ the Buckingham potential [2, 16, 27, 28, 30, 112, 161–163] whilst some augment this with the Morse potential for anion-cation interactions [13, 14]; others employ the four-range Buckingham form [20, 22, 23, 31, 32] whilst it is even possible to dispense with a simple analytical form entirely, in favour of splines combined to describe a quantum mechanically derived energy surface [33, 34]. Nevertheless, Govers *et al.* [152, 164] have shown that while a specific potential may reproduce a subset of thermomechanical properties well, none are able to reproduce an extensive set of properties. Also there is no single consistent set of potentials for all of AmO_2, CeO_2, CmO_2, NpO_2, PuO_2, ThO_2 and UO_2. Although a number of models

exist, (see the reviews of Govers *et al.* [152, 164], Chernatynskiy *et al.* [121], Potashnikov *et al.* [19] and Murphy *et al.* [12]), those of Basak [13], Morelon [22] and Yakub [14] have been identified as describing the thermal expansion of UO_2 particularly well [19]. Nonetheless, all three fail to reproduce all elastic constants correctly. Importantly, the bulk modulus is in poor agreement with experimental data over a broad temperature range [19, 164].

A number of potential models include polarisability by splitting ions into positively charged cores associated with massless, negatively charged shells such that the internal energy is harmonic with respect to core-shell displacement [113]. The shell model accounts for some many-body effects by making the interactions coordination dependent. This is important because a simple pairwise description of the interactions is not capable of reproducing the Cauchy violation observed in actinide oxides with the fluorite structure (i.e. $C_{12} \neq C_{44}$) [152]. As they represent massless entities, shells pose a challenge to the standard MD algorithm. Whilst they have been included in MD, either by assigning nominal but small masses to the shells [116] or by updating shell positions through a static energy minimisation stage performed for each MD time step [115], such methods lead to longer calculation times with the effect of decreasing the time or system size that can be simulated. Therefore, rigid ion potentials tend to be favoured for MD simulations and the shell model is even omitted from the majority of mainstream MD codes, such as the one used here (i.e. LAMMPS [117]).

For the first time, an alternative potential form is applied here to consistently model actinide oxides. In particular it includes many-body effects using the embedded atom method (EAM) [120]. An empirical fitting procedure is employed, where material properties calculated using the model are compared with experimental values. Over a series of fitting rounds, the parameters are adjusted to improve the quality of this match. During the initial phase, static energy minimisation simulations (see section 6.2.2 for details) are used to fit against lattice parameter, bulk modulus and individual elastic tensor constants (where available) until a reasonable set of parameters is obtained. The next phase of the fitting procedure additionally includes MD calculations (see section 6.2.2) to allow the temperature dependence of lattice parameter (i.e. thermal expansion) to be captured by the model. By

fitting parameters for AmO_2, CeO_2, CmO_2, NpO_2, PuO_2, ThO_2 and UO_2 simultaneously, with common oxygen-oxygen interactions, a better description of the experimentally determined elastic constants (including the Cauchy violation) and thermal expansion for all actinide oxides is achieved. CeO_2 is included as it is produced in large quantities as a fission product [2] and is often used as an experimental surrogate for PuO_2 [165].

Using the new potential, the bulk modulus is examined over a wide temperature range and compared to experimental data. This property was not included in the fitting procedure and as such provides one test of the approach. Similarly, the temperature dependence of the specific heat for UO_2, PuO_2 and ThO_2 was determined and compared to experimental data. The melting point of UO_2, PuO_2 and ThO_2 was also predicted and validated against experimental data, providing another aspect of mode validation. Finally, Schottky and Frenkel defect process energies, calculated using static energy minimisation, are also reported, however given the range of values previously reported [151, 166–172] it is less useful in terms of validation.

6.2 Calculation details

6.2.1 Description of the potential form

In an attempt to increase both the range of reproducible properties and move beyond the pairwise description of actinide oxides used in the past, the model combines a pair potential description of each system with the many-body EAM description of Daw and Baskes [120]. Unusually for an EAM type model, ions are assigned charges. Coulombic interactions were calculated using the Ewald method [108]. Further, the Particle-Particle Particle-Mesh (PPPM) version of the Ewald summation was used for the MD calculations within LAMMPS in order to improve computational efficiency [117, 173]. As such, the potential energy, E_i,

of an atom i with respect to all other atoms can be written as follows,

$$E_i = \frac{1}{2}\sum_j \phi_{\alpha\beta}(r_{ij}) - G_\alpha\left(\sum_j \sigma_\beta(r_{ij})\right)^{\frac{1}{2}} \tag{6.1}$$

The potential has two distinct components, one that is pairwise and the other many-bodied. The pairwise interaction between two atoms i and j, separated by r_{ij}, is given by $\phi_{\alpha\beta}(r_{ij})$. This has both long range electrostatic, $\phi_C(r_{ij})$, and short range contributions. The latter are described using Morse, $\phi_M(r_{ij})$, and Buckingham, $\phi_B(r_{ij})$, potential forms [109, 110]. α and β are used to label the species of atom i and atom j respectively.

$$\phi_{\alpha\beta}(r_{ij}) = \phi_C(r_{ij}) + \phi_B(r_{ij}) + \phi_M(r_{ij}) \tag{6.2}$$

$$\phi_C(r_{ij}) = \frac{q_\alpha q_\beta}{4\pi\epsilon_0 r_{ij}} \tag{6.3}$$

$$\phi_M(r_{ij}) = D_{\alpha\beta}[\exp(-2\gamma_{\alpha\beta}(r_{ij} - r^0_{\alpha\beta})) - 2\exp(-\gamma_{\alpha\beta}(r_{ij} - r^0_{\alpha\beta}))] \tag{6.4}$$

$$\phi_B(r_{ij}) = A_{\alpha\beta}\exp\left(\frac{-r_{ij}}{\rho_{\alpha\beta}}\right) - \frac{C_{\alpha\beta}}{r_{ij}^6} \tag{6.5}$$

where $A_{\alpha\beta}$, $\rho_{\alpha\beta}$, $C_{\alpha\beta}$, $D_{\alpha\beta}$, $\gamma_{\alpha\beta}$ and r^0_{ij} are empirical parameters that describe the Buckingham and Morse potentials between atom i and atom j. The fitting of these parameters is described in section 6.2.2.

$\phi_C(r_{ij})$, $\phi_M(r_{ij})$ and $\phi_B(r_{ij})$ potentials are all included for cation-oxygen interactions. $\phi_M(r_{ij})$ is used to include a degree of covalency in cation-oxygen bonding, however it is not necessary in the short-range potential description of oxygen-oxygen or cation-cation interactions which are described using $\phi_C(r_{ij})$ and $\phi_B(r_{ij})$ only (i.e. if $\alpha = \beta$, $D_{\alpha\beta} = 0$). An 11.0 Å cut-off is used for the short ranged pairwise interactions (equations 6.4 and 6.5).

For the Coulombic contribution the total charges of the ions are non-formal such that $q_\alpha = Z^{eff}_\alpha|e|$, however they are proportional to their formal charges ensuring the system is charge neutral ($Z^{eff}_\alpha = 2.2208$ for tetravalent cations and $Z^{eff}_\alpha = -1.1104$ for oxygen anions). In contrast to the variable charge approach used in potentials for other systems [174, 175], the partial charges used here are fixed.

The second term in equation 6.1 uses the EAM to introduce a subtle many-body perturbation to the more dominant pairwise interactions. It achieves this many-body dependency by summing a set of pairwise functions, $\sigma_\beta(\mathrm{r_{ij}})$, between atom i and its surrounding atoms. $\Sigma\sigma_\beta(\mathrm{r_{ij}})$ is then passed through a non linear embedding function (note that if the embedding function were linear this would reduce to a pairwise description). $\sigma_\beta(\mathrm{r_{ij}})$ is inversely proportional to the 8^{th} power of the inter-ionic separation with n_β being the constant of proportionality (equation 6.6) that must be empirically fitted to experimental data.

$$\sigma_\beta(r_{ij}) = \left(\frac{n_\beta}{r_{ij}^8}\right)\frac{1}{2}(1 + \mathrm{erf}(20(r - 1.5))) \tag{6.6}$$

The embedding function used means the many-body energy perturbation is proportional to the square root of the $\Sigma\sigma_\beta(\mathrm{r_{ij}})$ with G_α being the constant of proportionality (equation 6.1). As such, the total energy of atom i (E_i) is given by the sum of its pairwise interactions with the many-body perturbation due to the EAM term (equation 6.1). An error function is included in equation 6.6 as a soft short range cut-off below 1.5 to prevent forces due to the embedded atom term overcoming the short range pair repulsion in MD simulations. An upper limit cut-off of 11.0 Å, similar to that on equations 6.4 and 6.5, was also used for equation 6.6. The selection of the EAM potential forms ensure that atomic interactions become progressively weaker with increasing coordination. This will be discussed in greater detail once the potential parameters have been fitted (section 6.2.2).

6.2.2 Fitting procedure

The charges and initial parameter selection of Yakub *et al.* [14] was used for UO_2 because it has been shown to predict thermal expansion well [19].

Parameters for equations 6.1-6.6 are derived for AmO_2, CeO_2, CmO_2, NpO_2, PuO_2, ThO_2 and UO_2 by fitting to experimentally observed data of lattice parameters, bulk elastic constants [118, 176–179] and thermal expansion data [24, 37–42]. The Nelder-Mead simplex algorithm [180] is used to minimise a merit function, comparing data from energy minimised structures and MD calculations with experimental data. In the interests of efficiency

the individual GULP [100] and LAMMPS [117] (for MD) runs used to evaluate the merit function for each iteration of a fitting run were performed in parallel using a fitting system developed for this study by Rushton [160]. This greatly reduced the time taken to minimise the objective function.

Since the parameters specific to oxygen (i.e. the oxygen embedding function and oxygen-oxygen pair interactions) are common between the systems it is necessary to fit to all oxides simultaneously in order to identify the optimum oxygen parameter set. This is important because it facilitates the modelling of oxide solid solutions, although mixed cation interactions (e.g. U-Th) must also be fitted. The implementation of the potential for mixed oxides will be the focus of Chapter 7.

From geometry optimisation calculations within GULP [100] the individual components of the elastic constant tensor and bulk modulus can be calculated for a given set of interatomic potentials. This allows fitting to the experimental elastic data. Fitting to single crystal elastic data is preferable where it is available, as is the case for CeO_2, ThO_2 and UO_2 [118, 177, 179], because it enables fitting to the C_{11}, C_{12} and C_{44} constants. There is, however, a lack of single crystal data for the AmO_2, CmO_2, NpO_2 and PuO_2 systems; in these cases fitting was performed against experimental bulk modulus values [176, 178]. Following the recommendation of Chernatynskiy *et al.* [121] candidate parameter sets were discounted throughout fitting if they did not predict a fluorite lattice energy that was lower than for the other common MO_2 polymorphs (i.e. the α-PbO_2, anatase, baddeleyite, brookite, cotunnite, pyrite and rutile structures).

MD simulations allowed temperature effects to be included in the fitting procedure, with the variation in lattice parameter as a function of T being considered, starting at 300 K. The upper temperature range for available experimental data varied and was 1200 K, 900 K, 700 K, 1300 K, 1300K, 2000 K and 3000 K for AmO_2, CeO_2, CmO_2, NpO_2, PuO_2, ThO_2 and UO_2 respectively [24, 37–42]. These calculations were carried out in the NPT ensemble with Nosé-Hoover thermostat and barostat relaxation times of 0.1 ps and 0.5 ps respectively with a 4×4×4 fluorite unit supercell (768 atoms). The fitting process is concerned mainly with

reproducing thermal expansion so MD simulations were carried out on a 4×4×4 fluorite unit supercell (768 atoms) with a fixed timestep of 2 fs. This is a small supercell for an MD calculation, and was chosen in order to maintain a reasonable balance between accuracy and necessary simulation time as a result of the need to perform several MD runs at each iteration of the fitting run. Given the number of free parameters, convergence of the fitting procedure could take many steps, therefore in order for the process to remain tractable this system size was determined to be appropriate. Each simulation was carried out for 10 ps over a range of temperatures from 300 K to 3000 K with the volume sampled every time step before being averaged over the last 2 ps, thereby, ensuring enough time for the system to reach equilibrium.

Bulk properties were not sufficiently sensitive to changes in the cation-cation interactions and therefore these were not included in the fitting procedure. Nonetheless, they must be specified to ensure cation-cation repulsion at short distances during future irradiation damage or high temperature simulations. Therefore, the Buckingham A_{UU} term (18600 eV), based on simple electron gas calculations, due to Grimes *et al.* [2] was used for all cation-cation interactions. The Buckingham ρ_{UU} term of Grimes *et al.* [2] was also used for U-U interactions but scaled to ionic radius for all other cation-cation interactions (see Figure 6.1).

The final parameter set derived by this fitting process is summarised in tables 6.1 and 6.2 for pairwise and many-body interactions respectively. A number of these parameters exhibit a linear relationship with certain physical properties of the oxide systems, for example $\rho_{\alpha\beta}$, $\gamma_{\alpha\beta}$ and r_{ij}^0 terms scale linearly with cation radius, oxide bulk modulus and lattice parameter respectively (similar relationships have been noted previously for rare earth oxide pyrochlore materials [182]). Although this aids selection of all initial parameters when new actinide oxide systems are added to the potential set, similar relationships for the $A_{\alpha\beta}$, $D_{\alpha\beta}$, G_α and n_β parameters are not apparent and, as such, one must be careful not to bias parameter selection by assumed relationships.

As discussed earlier, the EAM component in equation 6.1 enables the development of a co-

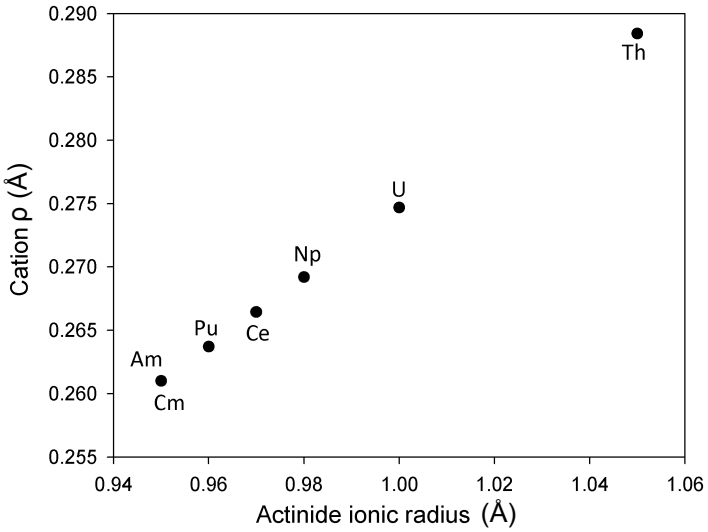


Figure 6.1: Scaling of cation-cation ρ terms as a function of cation radius (coordination number VIII) [36]. The value of ρ_{UU} = 0.275, from Grimes *et al.* [2], is the reference point.

ordination dependent potential. By selecting a density term that increases with decreasing separation in conjunction with a negative embedding function, the EAM is attractive. However, the negative square root form of the embedding function means that it contributes sequentially less to interatomic binding as the coordination of a given ion is increased. For example, this is shown using red lines in Figure 6.2 for a uranium cation embedded by one, two or three oxygen anions all at a separation of 2 Å. Similarly, the total potential energy per uranium-oxygen pair (including Coulombic, Buckingham and Morse terms) is reported in Figure 6.3.a for a uranium cation coordinated by one, two and three equidistant oxygen anions (N.B. O-O interactions are omitted). The same information is also shown for Pu-O and Th-O interactions alongside the corresponding forces (first derivative of energy) in Figure 6.3.b. These results show that actinide-oxygen binding gets sequentially lower for Pu-O, U-O and Th-O interactions. In particular, Figure 6.3.b shows that the lowest energy separation (zero force) is greater for Th-O than for U-O than for Pu-O and corresponds to the relative lattice parameters of ThO_2, UO_2 and PuO_2. Similarly, for all actinides, bonding is reduced as the actinide coordination is increased, thereby demonstrating the many-body nature of this potential set. This is indicative of the EAM potential forms selected in equa-

Table 6.1: Parameters for the pairwise interactions described by equations 6.2-6.5. The Pu-O potential was adjusted compared to the original published work [160] and then submitted to *J. Phys. Mater* [181]. The modified parameters are identified with an asterisk.

Interaction	$\phi_B(r_{ij})$			$\phi_M(r_{ij})$		
$\alpha-\beta$	$A_{\alpha\beta}$ / eV	$\rho_{\alpha\beta}$ / Å	$C_{\alpha\beta}$ / eV.Å^6	$D_{\alpha\beta}$ / eV	$\gamma_{\alpha\beta}$ / Å^{-1}	$r^0_{\alpha\beta}$ / Å
Ce-Ce	18600	0.266400	0.0	-	-	-
Th-Th	18600	0.288400	0.0	-	-	-
U-U	18600	0.274700	0.0	-	-	-
Np-Np	18600	0.269200	0.0	-	-	-
Pu-Pu	18600	0.263700	0.0	-	-	-
Am-Am	18600	0.260900	0.0	-	-	-
Cm-Cm	18600	0.260900	0.0	-	-	-
Ce-O	351.341	0.380517	0.0	0.71925	1.86875	2.35604
Th-O	315.544	0.395903	0.0	0.62614	1.85960	2.49788
U-O	448.779	0.387758	0.0	0.66080	2.05815	2.38051
Np-O	360.436	0.383047	0.0	0.76382	1.84020	2.36838
Pu-O	527.516*	0.379344	0.0	0.70185	1.98008	2.34591
Am-O	364.546	0.377388	0.0	0.74668	1.95534	2.32486
Cm-O	356.083	0.377488	0.0	0.76128	2.08061	2.31107
O-O	830.283	0.352856	3.884372	-	-	-

tion 6.1 (see Figure 6.2). The strong coordination dependence of Pu-O interactions arises due to the particularly high EAM n_{Pu} and G_{Pu} parameters of this system. Conversely, low EAM parameters for ThO_2 reduced the effect of coordination on Th-O interactions.

6.2.3 Defect calculation details

Although not used in fitting, defect formation energies were calculated for isolated charged point defects and charge neutral defect clusters using the supercell approach. This approach is necessary due to the incompatibility of the EAM with the Mott-Littleton method. However, one issue with using this approach for charged defects is the unphysical system

Table 6.2: Parameters for the many-body interactions described by equations 6.1 and 6.6. The Pu potential was adjusted compared to the original published work [160] and then reported separately [181]. The modified parameters are identified with an asterisk.

Species	G_α (eV.Å$^{1.5}$)	n_β (Å^5)
Ce	0.308	1556.803
Th	1.185	1742.622
U	1.806	3450.995
Np	0.343	1796.945
Pu	2.168*	3980.058*
Am	0.333	1631.091
Cm	0.494	1503.704
O	0.690	106.856

charge that arises due to periodic boundary conditions. Therefore, a charge neutralising jellium is required and the interaction of the defect with this background charge must be accounted for [101–103]. The correction used to determine the defect energy in the dilute limit is described in section 2.1.4 on the supercell method (see Chapter 2). The defect energies, $E_f(L)$, were calculated in 3×3×3, 4×4×4 and 5×5×5 supercells and plotted as a function of $\frac{1}{L}$. The isolated defect energy, E_f^∞, is found by extrapolating this linear function to $\frac{1}{L} = 0$. When considering bound charge neutral clusters $q = 0$ and the Madelung correction no longer applies, as a result the defect energies are converged to within 0.1 eV for the 5×5×5 supercell. A more detailed description of these cluster configurations can be found in section 6.3.3.

6.2.4 Thermophysical properties validation

Having derived a parameter set, the ability of the potential to describe thermophysical properties of the actinide oxide systems must be validated. 10×10×10 fluorite supercells of the CeO_2, ThO_2, UO_2, NpO_2, PuO_2, AmO_2 and CmO_2 systems are heated sequentially from 300 K to 3000 K at 25 K intervals with a fixed timestep of 2 fs and at zero pressure. At each

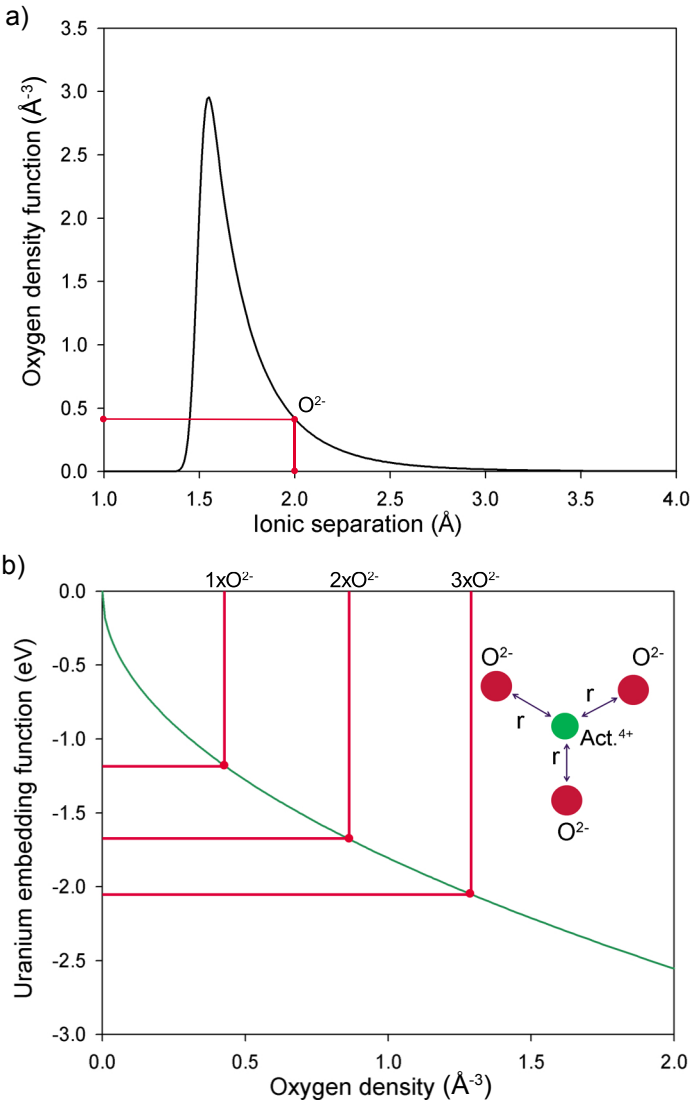


Figure 6.2: Example a) oxygen density and b) uranium embedding functions derived using the new potential. Red lines indicate the effect of embedding a uranium cation potential within the densities of one, two and three oxygen densities at 2 Å. The interaction per uranium-oxygen pair is sequentially less negative (i.e. less favourable) as the coordination of uranium increases.

temperature the systems were held for 20 ps with the volume and enthalpy, H(T), averaged over the final 4 ps. The lattice parameter as function of temperature is determined from the volume at each temperature. In previous experimental work, the specific heat capacity of PuO_2, ThO_2 and UO_2 [39, 43] were determined by fitting a polynomial to the enthalpy

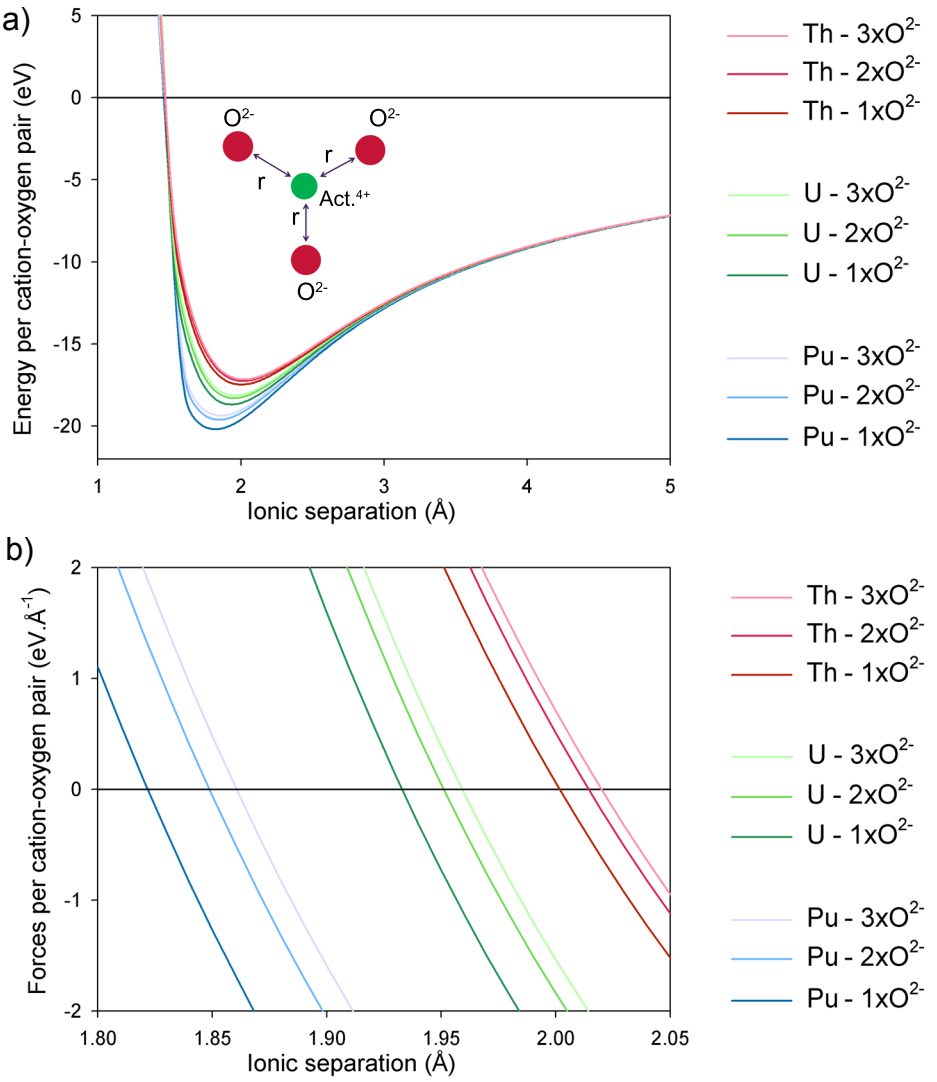


Figure 6.3: a) The potential energy between an actinide cation and one, two or three equidistant oxygen anions as a function of separation per actinide-oxygen pair. The difference in potential shape depends on the coordination environment of the actinide cation and demonstrates the many-body nature of this potential set. b) The interactomic forces as given by the first derivative of potential energy (a) with respect to separation.

increment (increase in enthalpy with respect to STP) as a function of temperature increase, $H(T) - H(298\ K)$, and then using the first derivative of this function, $\frac{\partial H}{\partial T}$, in equation 6.7. The same polynomial form used in analysing the experimental data of enthalpy increment

was then fitted to the equivalent simulation data and its derivative used to calculate specific heat capacity, c_p:

$$c_p = \frac{1}{n}\left(\frac{\partial H}{\partial T}\right)_P \tag{6.7}$$

The bulk modulus was determined at each temperature interval by exerting isotropic compressive and tensile strains (0.95-1.05) on the equilibrated system and examining the derivative of pressure with volume. Bulk modulus was then calculated using equation 6.8.

$$K = -V\frac{dP}{dV} \tag{6.8}$$

The melting points of PuO_2, UO_2 and ThO_2 were determined using a moving interface method similar to that deployed by Govers *et al.* [164]. Two 24×5×5 supercells, one containing PuO_2, UO_2 or ThO_2 with an atomic configuration consistent with the liquid phase and the other consisting of the solid fluorite crystal structure, were equilibrated at the target temperature for 50 ps. The liquid and solid supercells were combined to create a 48×5×5 supercell containing a solid-liquid interface at its centre. By monitoring the position of this interface over the course of a 1 ns MD run it was possible to determine if the temperature of the system was above or below the melting point predicted by the potential model. The growth of either the liquid or crystal phase identified if the calculation had been carried out above or below the melting point respectively. This method was carried out between 2600 K and 3400 K with 50 K intervals for PuO_2, UO_2 and ThO_2.

Although the melting points were not used as fitting data for the original potential set [160], in later work on oxygen diffusivity in (U,Pu)O_2 (Chapter 7), it was shown that the original potential set gave a particularly poor prediction of 3600 K for the PuO_2 melting point. As such, the parameters published originally [160] have been modified (see Tables 6.1 and 6.2) [181] to give the much improved value reported later.

6.3 Results and discussion

6.3.1 Agreement of model with fitting data

Figure 6.4 shows experimental data [37–42] for lattice parameters as a function of temperature alongside MD predictions for the current model. Fitting was carried out to these experimental lattice parameter data over the range of available temperatures. Despite keeping oxygen specific parameters common across all systems, this close agreement with experimental data was achieved.

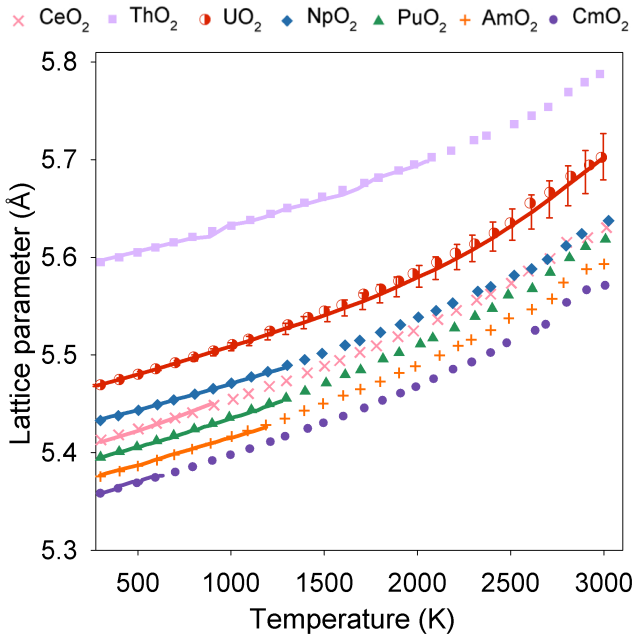


Figure 6.4: Comparison of experimental data (solid lines) for CeO_2 [37], ThO_2 [38], UO_2[39], NpO_2 [40], PuO_2 [40], AmO_2 [41] and CmO_2 [42] with the data points from MD simulations using the new potential.

A number of potentials reported previously exhibit non-fluorite lowest energy structures (refer to Chapter 3), that is, the internal energy of MO_2 structures other than fluorite were predicted to be most stable. Here this error has been avoided by ensuring that, throughout fitting, the fluorite structure has a lower lattice energy than the α-PbO_2, anatase, badde-

leyite, brookite, cotunnite, pyrite and rutile structures. Table 6.3 shows the lattice energy of these structures relative to the fluorite lattice energy per MO_2 formula unit. These results confirm the model's correct identification of fluorite as the lowest energy structure.

Table 6.3: The lattice energy of different phases of MO_2 relative to that of the fluorite structure. F indicates phases that on energy minimization relaxed to fluorite.

	Lattice energy (relative to fluorite) (eV)						
Structure	CeO_2	ThO_2	UO_2	NpO_2	PuO_2	AmO_2	CmO_2
α-PbO_2	F	F	F	F	F	F	F
Anatase	0.566	0.914	0.456	0.729	0.468	0.477	0.436
Baddeleyite	0.154	0.305	0.135	0.201	0.138	0.140	0.155
Brookite	0.403	0.333	0.345	0.229	0.340	0.342	0.333
Cotunnite	0.224	0.148	0.225	0.170	0.259	0.276	0.344
Pyrite	0.121	F	0.183	0.183	0.142	0.126	0.181
Rutile	0.207	0.541	0.202	0.331	0.170	0.161	0.170

Elastic data obtained from static lattice calculations are summarized in table 6.4 alongside the experimental data used in the fitting process. All calculated values lie within 10 % of the experimental data, with the majority within 3.5 %, representing very good agreement across all actinide oxides. Of particular significance is the reproduction of the Cauchy violation, which demonstrates the efficacy of the many-body potential approach.

6.3.2 Validation of model against other experimental data

Having shown good agreement between the model and the experimental data used in parameterising this model, it is important to validate the model against perfect crystal data not used in the fitting procedure.

Since fitting was carried out to elastic constant results from energy minimization calculations, this static approach is not able to capture the temperature dependence of these properties. Thus, using the methodology described in section 6.2.4, the bulk modulus was deter-

Table 6.4: Summary of elastic data calculated in this work and experimental data used for fitting shown in brackets. Fitting for UO_2, ThO_2 and CeO_2 was carried out using C_{11}, C_{12} and C_{44}. However, fitting for the minor actinides was done to bulk modulus only, due to a lack of single crystal data. Virtually no weight was put on the fitting of PuO_2 due to large discrepancy between reported values; ranging from 178.0 GPa to 379.0 GPa [176].

	Elastic Constants / GPa			
	C_{11}	C_{11}	C_{11}	Bulk. Mod.
CeO_2 [177]	405.2 (403.0)	100.5 (105.0)	66.8 (60.0)	202.0 (204.0)
ThO_2 [179]	352.3 (367.0)	113.4 (106.0)	71.7 (79.0)	193.0 (193.0)
UO_2[118]	406.3 (389.3)	71.7 (79.0)	63.89 (59.7)	218.6 (208.9)
NpO_2 [178]	399.6	106.5	69.5	204.2 (200.5)
PuO_2	423.6	125.9	53.5	225.16
AmO_2 [176]	430.7	107.5	71.0	215.2 (205.0)
CmO_2 [176]	455.2	120.4	80.72	232.0 (218.0)

mined between 300 and 3000 K for all actinide oxides. Comparison of the results for UO_2 with the experimental data of Hutchings *et al.* [35] is shown in Figure 6.5, and represents a significant improvement on the predictions reported for the existing empirical potential of Yakub *et al.* [14]. Further, comparison with the results of Chapter 3 demonstrates that the compromise between thermal expansion and bulk modulus that must be made when using pairwise models is negated when using the new many-body model. Although experimental data are not available for the other actinide oxides, values calculated using the new potential are reported in Figure 6.6. All the oxides show roughly linear dependence of bulk modulus with temperature, reflecting the decrease in bulk modulus with increasing lattice parameter. This linear dependence is described by:

$$B(T) = \epsilon T + B_0 \tag{6.9}$$

where B_0 is the bulk modulus extrapolated to 0 K and ϵ is the temperature coefficient. Values for B_0 and ϵ are given in table 6.5.

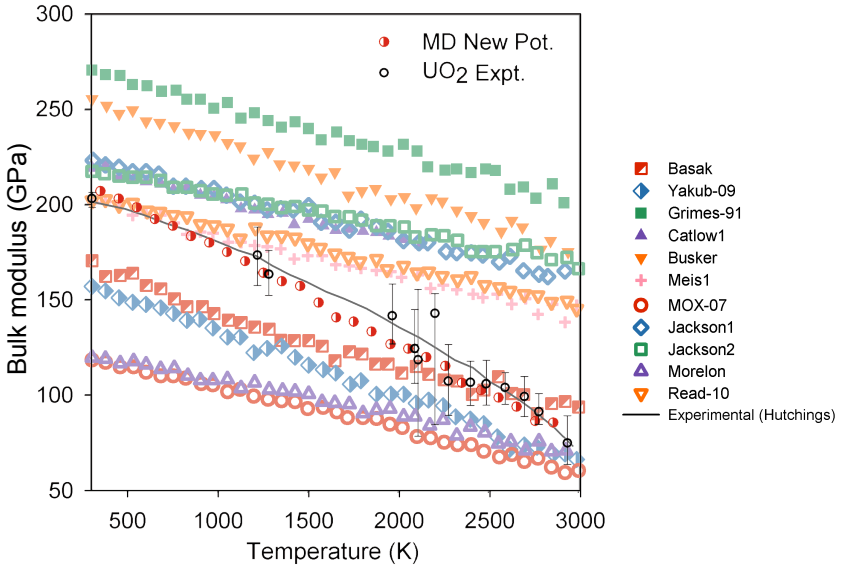


Figure 6.5: Comparison of the new many-body potential potential with experimental data for the temperature dependence of bulk modulus for UO_2 [35]. Figure 3.3 is included for comparison with previous pair potentials (see Chapter 3).

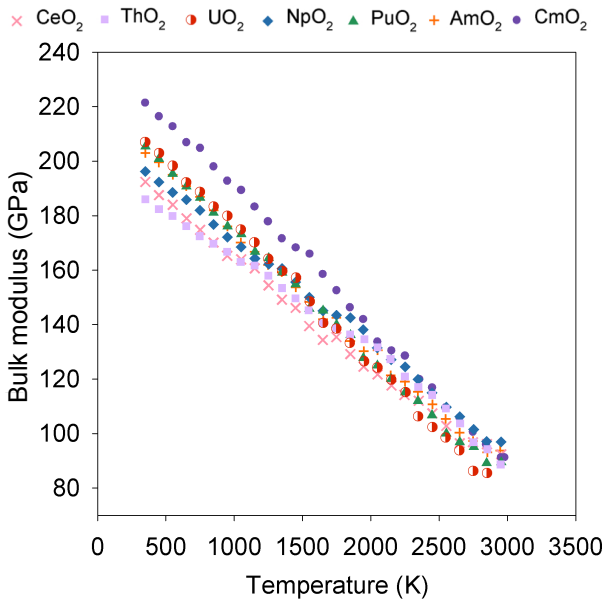


Figure 6.6: Bulk modulus as a function of temperature calculated using the new potential for CeO_2, ThO_2, UO_2, NpO_2, PuO_2, AmO_2 and CmO_2. Although not plotted here, equation 6.9 has been fitted to these data with the coefficients B_0 and ϵ summarized in table 6.6.

Table 6.5: Summary of coefficients obtained by fitting equation 6.9 to the results for bulk modulus as a function of temperature for AmO_2, CeO_2, CmO_2, NpO_2, PuO_2, ThO_2 and UO_2 (Figure 6.6).

	B_0 / GPa	ϵ / GPa.K^{-1}
CeO_2	203.86	-0.0394
ThO_2	201.19	-0.0363
UO_2	226.01	-0.0500
NpO_2	210.59	-0.0389
PuO_2	220.80	-0.0463
AmO_2	217.96	-0.0439
CmO_2	241.03	-0.0509

Figure 6.7 shows the enthalpy increment with respect to STP as a function of temperature for PuO_2, ThO_2 and UO_2 (the three most common fuel cadidates). The polynomials fitted to the MD results are kept consistent with those used previously to describe experimental data [39, 43] to ensure fair comparison of modelling and experiment (note: that the parameters reported in equations 6.10-6.12 are those fitted to the modelling data).

UO_2 [39]:

$$H(T) - H(298K) = -21.18 + 58.11t + 34.14t^2 - 22.79t^3 + 6.43t^4 - 0.45t^5 + 0.54t^{-1} \quad (6.10)$$

ThO_2 [43]:

$$H(T) - H(298K) = -20.58 + 51.68t + 39.77t^2 - 21.63t^3 + 4.15t^4 + 1.00t^{-1} \quad (6.11)$$

PuO_2 [39]:

$$H(T) - H(298K) = -34.92 + 83.84t + 0.89t^3 + 2.27t^{-1} \quad (6.12)$$

where $t = T/1000$, T is the temperature in K and the enthalpy increment, $H(T)-H(298\ K)$, is given in kJ.mol^{-1}. The derivative of the enthalpy increment is used to calculate the specific heat using equation 6.7. Figure 6.7 shows the calculated and experimental results for the enthalpy increment. There is good agreement between experimental and model data for both the enthalpy increment and specific heat of PuO_2, ThO_2 and UO_2 between 300 and 2500 K, typically within 10%. Whilst fitting the polynomial it became apparent that there

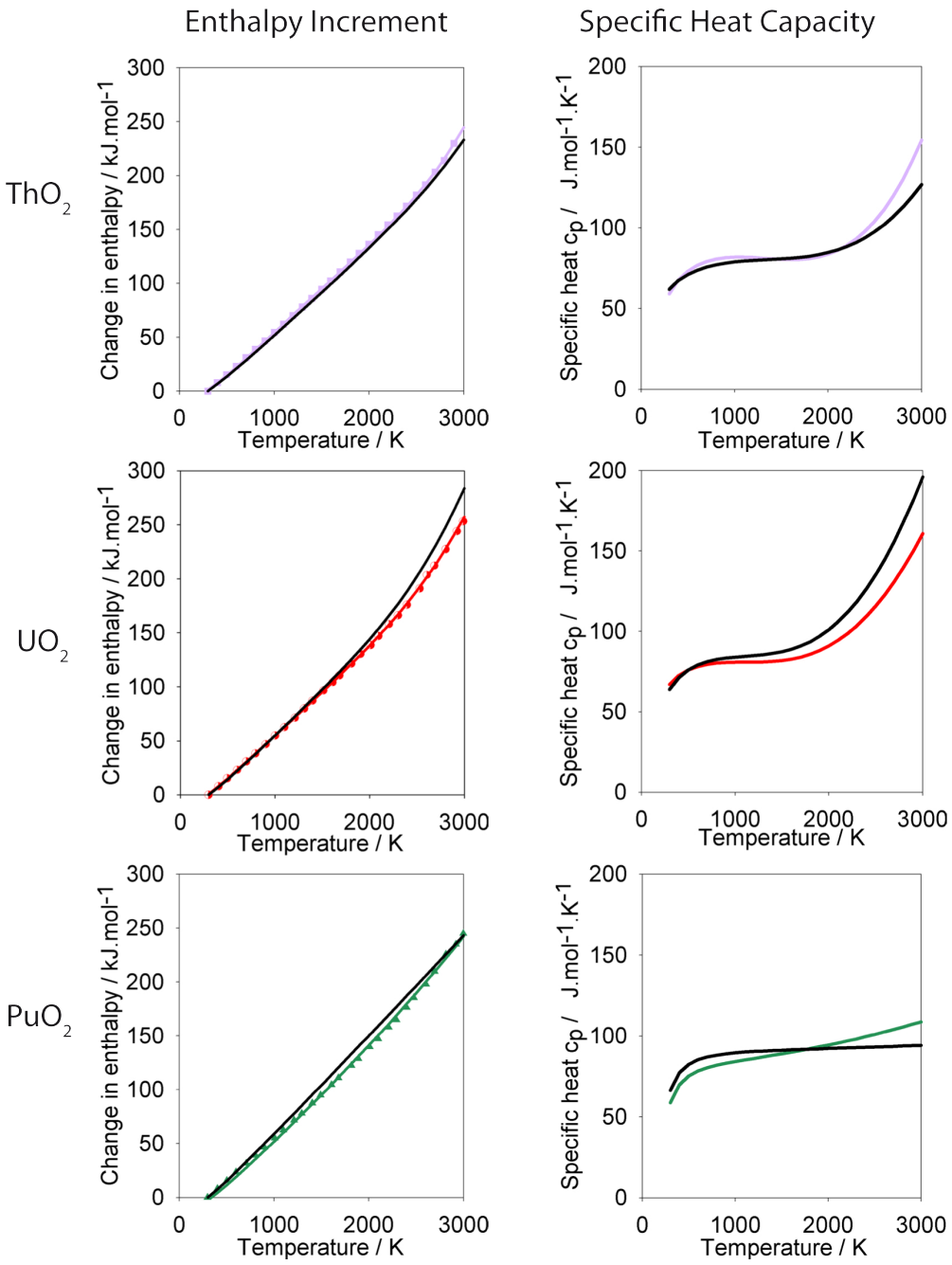


Figure 6.7: Change in enthalpy relative to 300 K as a function of temperature, calculated using the new potential with polynomial fitting for PuO_2 (equation 6.12), ThO_2 (equation 6.11) and UO_2 (equation 6.10) shown in green, purple and red, respectively. The specific heat is calculated from the derivative of these fitted polynomials and reported alongside experimental results shown by a solid black line [39, 43].

was a strong dependence on the particular form of polynomial used. Here the primary concern is comparison with the experimental data, however in Chapter 7 the specific heat is derived directly from the enthalpy increment in order to give an exact prediction by the potential.

Finally, using the moving interface methodology described in section 6.2.4 it is found that at 3000 K and 3100 K the UO_2 structure is dominated by the solid and liquid phases respectively. At 3050 K both phases coexisted. As such, the melting point of UO_2 is predicted to be within the bounds 3000-3100 K, which is in good agreement with the experimental value of 3150 K [39]. Similarly, the ThO_2 and PuO_2 melting points are predicted to be 3600-3700 K and 2700-2900 K respectively, in line with the experimental values of 3665 K [39] and 2700 K [183] respectively. The poor prediction of the PuO_2 melting point using the original potential set [160] of ≈3600 K has been significantly improved by using the modified PuO_2 parameters in Tables 6.1 and 6.2 (as discussed in section 6.2.4).

Figure 6.8 shows atomic positions sampled every 1 fs over 200 fs during the moving interface calculation for UO_2. This simulation was carried out at 3000 K (i.e. below the melting point of UO_2) so the interface moved to the right.

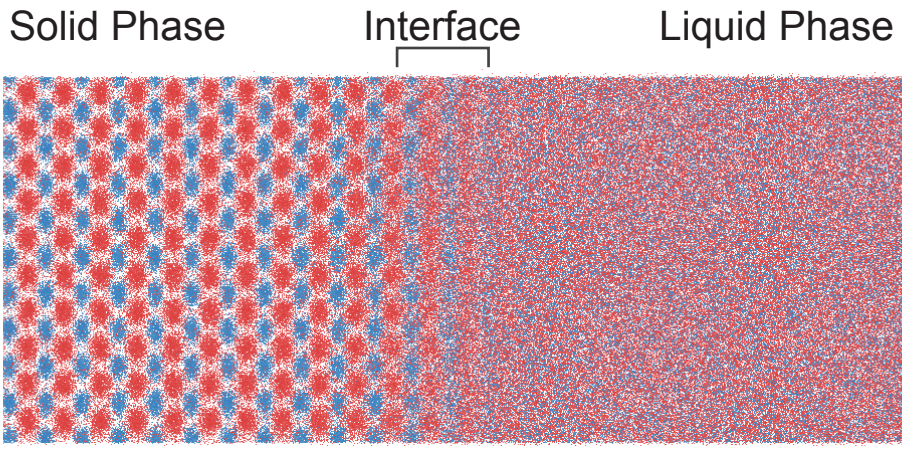


Figure 6.8: The superposition of atomic positions sample every 1 fs over 200 fs during the moving interface method for UO_2 at 3000 K. Uranium and oxygen positions are represented by red and blue dots respectively.

6.3.3 Prediction of defect energies and comparison with DFT

Having validated the potential for the description of the perfect crystal over a large temperature range for both fitting and non fitting data, the model is tested against its ability to describe defective structures. Schottky (reaction 6.13) and Frenkel (reactions 6.14-6.15) energies are calculated for CeO_2, ThO_2, UO_2, NpO_2, PuO_2, AmO_2 and CmO_2. For all defect reactions, both bound and isolated defects are considered,

$$M_M^{\times} + 2O_O^{\times} \rightarrow \{V_M'''' : 2V_O^{\bullet\bullet}\}^{\times} + MO_2 \tag{6.13}$$

$$M_M^{\times} \rightarrow \{M_i^{\bullet\bullet\bullet\bullet} : V_M''''\}^{\times} \tag{6.14}$$

$$O_O^{\times} \rightarrow \{O_i'' : V_O^{\bullet\bullet}\}^{\times} \tag{6.15}$$

where cations are represented by M and oxygen by O [96].

The Schottky reaction (reaction 6.13) involves two oxygen vacancies in first nearest neighbour sites with respect to a uranium vacancy, the oxygen vacancies can occupy first, second or third nearest neighbour sites with respect to each other. These clusters are denoted as SD1, SD2 and SD3 respectively (see Figure 6.9).

When considering bound Frenkel pairs (reactions 6.14-6.15) it was not possible to consider first nearest neighbour sites due to spontaneous recombination during the relaxation of cell geometry. Therefore bound cation Frenkel pair defect energies were calculated for the second nearest neighbour configuration in the $\langle 111 \rangle$ direction with the cation interstitial and vacancy separated by an oxygen anion. Similarly, the constituent point defects in the bound oxygen Frenkel pair are separated by a cation. As in the previous study of Govers *et al.* [152], two configurations of this latter cluster are considered; in both the interstitial occupies the $(-\frac{1}{2},-\frac{1}{2},-\frac{1}{2})$ site, the separating cation is in the (0,0,0) position but the oxygen vacancy either occupies the $(-\frac{1}{4},-\frac{1}{4},-\frac{1}{4})$ or the $(-\frac{1}{4},-\frac{1}{4},\frac{1}{4})$ sites hereby referred to as the OFP1 and OFP2 clusters respectively.

Table 6.6 reports the defect energies of reactions 6.13-6.15 for the intrinsic clusters described above as well as the isolated point defect case. It is the first consistent set of data for

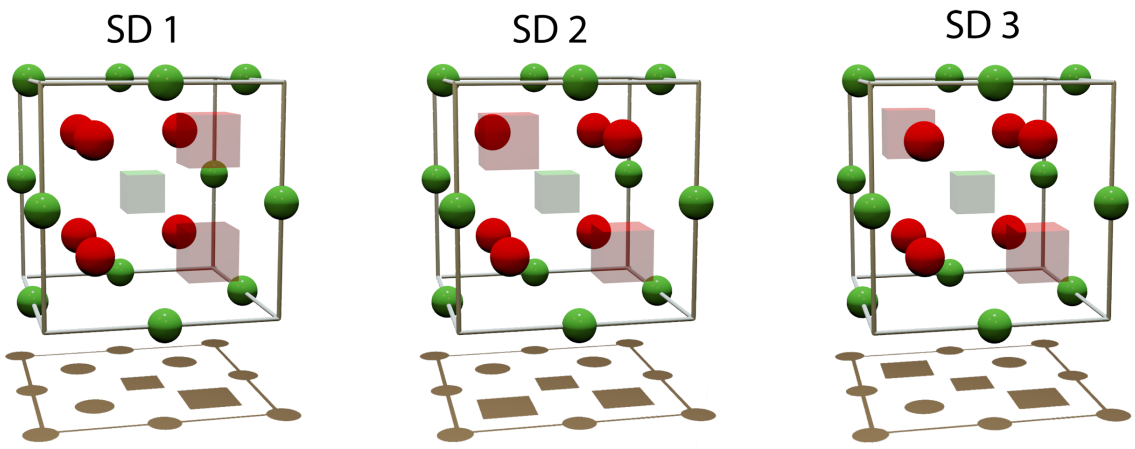


Figure 6.9: The different configurations of the Schottky defect investigated using the EAM model. The oxygen vacancies (red cubes) are in a first nearest neighbour configuration with respect to the actinide vacancy (green cube). The oxygen vacancies are occupy first (SD1), second (SD2) or third (SD3) nearest neighbour sites with respect to each other. Actinide and oxygen ions are represented by green and red spheres respectively.

all these defects for all actinide oxides. For all systems studied the SD3 defect was found to be the lowest Schottky defect energy in the 5×5×5 supercells. This represents a linear arrangement of the Schottky defect in the ⟨111⟩ direction, whereby the distance between the oppositely charge oxygen vacancies is maximised. Conversely, Crocombette *et al.* [166] predicted the lowest energy cluster to have the SD2 configuration, although this may be an artefact of the relatively small 2×2×2 supercell size these authors used. In fact, Figure 6.10 illustrates that even when using the EAM model the lowest energy cluster is indeed the SD2 configuration in the 2×2×2 supercell. The same ordering of lowest energy Schottky defect configurations was identified for all other actinide oxides except ThO_2 (for which SD3 was always the most stable) [44]. The OFP2 configuration has the lowest energy for oxygen Frenkel pair formation. This is the same preference as identified by others previously for a range of UO_2 empirical potentials [152].

There have been extensive DFT studies concerning the formation of point defects in UO_2 [151, 166–172]. From these calculations the predicted isolated Schottky energies range from

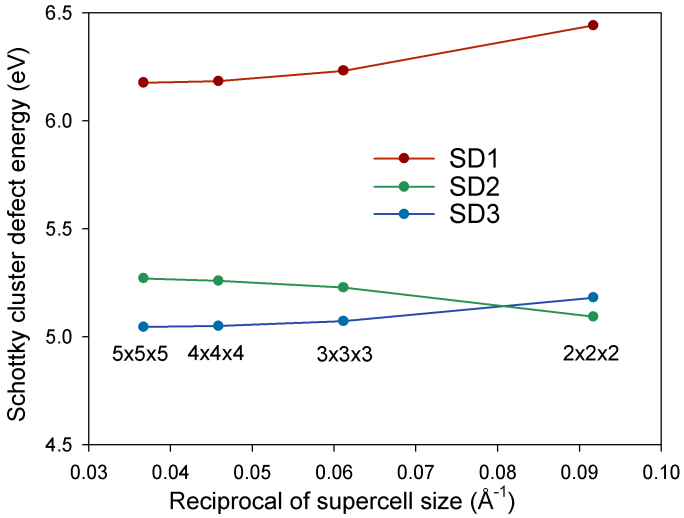


Figure 6.10: The variation of Schottky defect energy for different cluster configurations as a function of supercell size in UO_2 [44].

5.6 eV [167] to 10.6 eV [168], unbound oxygen Frenkel energies between 2.6 eV [151] and 5.77 eV [170] and unbound uranium Frenkel energies of 10.6 eV [166] to 17.2 eV [168]. The isolated Frenkel and Schottky energies calculated here (Table 6.6) all lie within the energy ranges predicted by earlier studies.

6.4 Conclusions

The application of the EAM, in conjunction with Buckingham-Morse pairwise interactions, has been shown to improve the prediction of experimentally determined thermophysical properties of the actinide oxides. Moreover, this provides an alternative to the shell model for including many-body effects in atomic scale simulations of actinide oxides that is robust at high temperatures or for high energy events, such as damage cascades.

The potential has been parametrised against thermal expansion from 300 K to 3000 K via MD and to elastic properties (including the Cauchy violation) via static calculations, using a fitting system developed for the present thesis. During the fitting process pairwise param-

Table 6.6: Schottky (SD), and Frenkel pair (FP) defect energies calculated with the new potential. Lowest energy cluster configurations for a particular cluster are indicated in bold. DFT data for UO_2 [151, 166–172] and ThO_2 [144] have been included in parentheses.

Defect Energy / eV	CeO_2	ThO_2	UO_2	NpO_2	PuO_2	AmO_2	CmO_2
$SD_{isolated}$	10.18	12.89	10.64	11.27	10.38	10.28	11.14
(ab-initio)		*(11.9-20.6)*	*(5.6-10.6)*				
SD_1	6.33	7.51	6.18	6.93	6.22	6.24	6.45
SD_2	5.44	6.62	5.27	6.03	5.31	5.33	5.49
SD_3	**5.23**	**6.39**	**5.05**	**5.82**	**5.09**	**5.11**	**5.25**
Cat-$FP_{isolated}$	16.53	18.23	15.47	17.14	16.33	16.72	17.66
(ab-initio)			*(10.6-17.2)*				
Cat-FP1	**12.55**	**13.65**	**11.09**	**12.98**	**12.07**	**12.53**	**13.00**
O-$FP_{isolated}$	5.47	5.89	5.73	5.64	5.75	5.76	6.34
(ab-initio)		*(6.1-9.8)*	*(2.6-5.77)*				
O-FP1	5.22	5.38	5.37	5.31	5.44	5.48	5.94
O-FP2	**4.83**	**5.03**	**4.94**	**4.94**	**5.02**	**5.06**	**5.49**

eters with a physical interpretation are scaled with associated physical properties, such as the linear relationship between $\rho_{\alpha\beta}$ and ionic radius. This aids sensible parameter selection when experimental data is limited or unreliable whilst indicating how parameters required for oxides not yet included in the potential series may be derived. Fixed oxygen-oxygen interactions across the series have been employed in order to de-convolute these interactions from the cation-oxygen interactions and supports the opportunity to simulate mixed oxide fuels.

Predictions of the thermophysical properties that did not contribute to the fitting process have been used to validate the potential models. The values predicted by the potential are in excellent agreement with the experimental data for the enthalpy increments and the specific heat of PuO_2, ThO_2 and UO_2. Furthermore, a very significant improvement in the temperature dependence of the bulk modulus of UO_2 between 300 K and 3000 K is attained. This particular property had been identified previously (Chapter 3) as one of the

most poorly reproduced when using conventional pairwise potentials [19, 164]. Similarly, predictions for the temperature dependence of bulk modulus have been made for the other actinide oxides and temperature coefficients identified. The melting point of UO_2 is also estimated in agreement with experimental data.

Finally, the potential has been used to predict Schottky and Frenkel energies. These energies and the predicted defect cluster configurations are consistent with previous modelling studies for UO_2.

Going forward, greater confidence can be placed in the predictions of this potential set given the better description of the temperature dependence of actinide oxide thermophysical properties. Although Rushton and Chroneos [184] have recently added a number of rare earth metals to this potential set that are also present in nuclear fuel as fission products, further work is required to include other important fission products such as Cs, Ba, Sr and Xe.

Chapter 7

Modelling the behaviour of mixed oxides

Part of this work is published in:
M.W.D. Cooper, S.T. Murphy, P.C.M. Fossati, M.J.D. Rushton, R.W. Grimes, *Proc. R. Soc. A* **470**, 20140427 (2014) [185]
M.W.D. Cooper, S.T. Murphy, M.J.D. Rushton, R.W. Grimes, *J. Nucl. Mater.* [181]
M.J. Qin, M.W.D. Cooper, E.Y. Kuo, M.J.D. Rushton, R.W. Grimes, G.R. Lumpkin, S.C. Middleburgh, *J. Phys.: Condens. Matter* **26**, 495401 (2014) [186]

Support for modifications to the potential model to enable mixed oxide simulation:
abulafia.mt.ic.ac.uk/potentials/actinides/

7.1 Introduction

As discussed in Chapter 6, the motivation behind the development of a new consistent actinide oxide potential set is, in part, to investigate UO_2 fuel blended with ThO_2 [62] and PuO_2 [183, 187], to form mixed oxide (MOX) fuels. Alternatively, long lived minor actinides can be separated from nuclear waste and blended with UO_2 or MOX for transmutation in a reactor [63] or accelerator driven system [65, 66]. Due to the relative abundance of thorium, ThO_2 is considered as an strong candidate for MOX, whereby Th^{232} transmutates in reactor to U^{233} which can then undergo fission. Similarly, U^{238} undergoes transmutation to Pu^{239} creating an in situ mixed oxide even in conventional fuel at high burnup. As such, it is important to understand the underlying mechanisms that govern the thermophysical and diffusion properties in mixed oxides, due a non-uniform cation sublattice.

For UO_2 there is a deviation from linear thermal expansion and a classical Debye description of the constant pressure specific heat above 1300 K [24, 188–196]. At 2670 K ($0.85T_m$) there is a peak in the specific heat due to the Bredig [197] or superionic transition as seen in other fluorite structures [188]. Below the transition it is not yet clear to what extent the excess specific heat and thermal expansion is driven by oxygen disorder versus electronic defect contributions, or over what temperature ranges these effects may dominate. The high oxygen disorder during the superionic transition is only possible due to the difference in the anion and cation Frenkel energies. There is a temperature regime where, although the anion sublattice is saturated with defects, the stability of the cation sublattice prevents the system from melting.

Potashnikov *et al.* [198] compared the ability of a number of interatomic potentials to predict oxygen diffusivity in UO_2 using MD. However, experimental data for oxygen diffusion will be influenced by the presence of point defects arising due to materials processing conditions, and it is not necessarily comparable with the perfect crystal calculations of Potashnikov *et al.* [198]. For example, the enhancement of oxygen diffusivity due to non-stoichiometry in UO_2 has been demonstrated recently by Govers *et al.* [199] and shown ex-

perimentally by Belle [200]. Similarly, enhanced diffusivity due to Schottky defects was also identified by Potashnikov *et al.* [198]. Therefore, it is not surprising that many simulations on perfect crystals predict lower oxygen diffusivity than experiment.

The potential set derived in Chapter 6 accurately reproduces a wide range of thermomechanical and thermophysical properties for AmO_2, CeO_2, CmO_2, NpO_2, PuO_2, ThO_2 and UO_2, between 300 and 3000 K. In particular, this potential accurately represents the individual elastic constants of the actinide oxides and reproduces the Cauchy violation (that is $C_{12} \neq C_{44}$) by introducing many-body interactions using the embedded atom method (EAM) [120] without the necessity for the shell model [113]. As a result, a significant improvement in the ability of empirical interatomic potentials to reproduce the bulk modulus over a large range of temperatures has been achieved. Importantly, this potential set employs the same description for oxygen-oxygen interactions throughout, enabling the simulation of actinide oxide solid solutions. Furthermore, it accurately reproduces the melting points of UO_2, ThO_2 and PuO_2 making it particularly suitable for investigating $(U_xTh_{1-x})O_2$ and $(U_xPu_{1-x})O_2$ solid solutions.

Thermal conductivity has been another key area for the application of atomistic simulations [121, 201]. In particular the role of crystal defects [202] or grain boundaries [203] in the degradation of thermal conductivity have been studied. Similarly, the non-uniform cation lattice in $(U_xTh_{1-x})O_2$ and $(U_xPu_{1-x})O_2$ solid solutions can be considered as a defective crystal that may inhibit the thermal conductivity of MOX fuels. The classical description of thermal conductivity is dependent on the phonon group velocity [204] where the longitudinal and transverse components of group velocity are dependent on the C_{11} and C_{44} elactic constants respectively. Thus, in order to reproduce both the bulk modulus and thermal conductivity one must accurately describe all single crystal elastic constants C_{11}, C_{12} and C_{44}. As laid out in Chapters 3 and 6, pair potentials alone cannot reproduce all three elastic constants.

Here we investigate, using atomistic simulation, the lattice parameter, linear coefficient of thermal expansion, enthalpy, specific heat at constant pressure and thermal conductivity

for $(U_xTh_{1-x})O_2$ and $(U_xPu_{1-x})O_2$ between 300 and 3600 K for x = 0.00, 0.25, 0.50, 0.75 1.00. Furthermore, the influence of solid solution composition on oxygen defect formation, oxygen diffusivity and the superionic transition is reported.

7.2 Calculation details

MD simulations are carried out using LAMMPS [117] and the set of interatomic potentials derived previously (refer to Chapter 6 and [160]). The model combines a pair potential description of each system with the many-body EAM description of Daw and Baskes [120]. A detailed description of the derivation and validation of this potential form was given in Chapter 6 for AmO_2, CeO_2, CmO_2, NpO_2, PuO_2, ThO_2 and UO_2 [160]. For the study of solid solutions further mixed cation-cation pair interactions (e.g. ϕ_{U-Th}) must also be defined. As was the case for the self cation-cation pair interactions, the mixed cation-cation interactions are dominated by Coulomb interactions at the separations exhibited by the fluorite structure. Hence, it is not possible to fit these parameters to experimental bulk properties. Instead the assumptions made previously for self cation interactions are extended to mixed cation-cation pair potentials. The description of covalency predicted by the Morse potential is not required for cation-cation pairs and is, therefore, excluded for these interactions (e.g. D_{U-Th} = 0 eV). The pre-exponential term of the Buckingham potential is the same for all cation-cation pairs and is based on the parameter reported by Grimes and Catlow [2] (e.g. A_{U-Th} = 18600 eV). However, the reported self cation-cation $\rho_{\alpha\alpha}$ parameters are scaled to cation radius [160]. The following equation [205] is used to determine $\rho_{\alpha\beta}$ parameters for mixed cation-cation pairs whose values are reported in Table 7.1,

$$\rho_{\alpha\beta} = \sqrt{\rho_{\alpha\alpha} \cdot \rho_{\beta\beta}} \tag{7.1}$$

The thermal expansion, specific heat and oxygen diffusivity are investigated for the pure UO_2, ThO_2 and PuO_2 systems as well as for a range of compositions of the $(U_xTh_{1-x})O_2$ and $(U_xPu_{1-x})O_2$ solid solutions. Solid solution crystal structures are created by randomly dis-

Table 7.1: $\rho_{\alpha\beta}$ parameters for the pairwise interactions of mixed cation-cation pairs determined using equation 7.1. As the table is symmetric (i.e. $\rho_{\alpha\beta} = \rho_{\beta\alpha}$) values are only reported once.

(Å)	Ce	Th	U	Np	Pu	Am	Cm
Ce	0.2664	0.2772	0.2705	0.2678	0.2651	0.2637	0.2637
Th	-	0.2884	0.2815	0.2786	0.2758	0.2743	0.2743
U	-	-	0.2747	0.2719	0.2691	0.2677	0.2677
Np	-	-	-	0.2692	0.2664	0.2650	0.2650
Pu	-	-	-	-	0.2637	0.2623	0.2623
Am	-	-	-	-	-	0.2609	0.2609
Cm	-	-	-	-	-	-	0.2609

tributing U^{4+}, Pu^{4+} or Th^{4+} cations on the 4a Wyckoff sites (fluorite actinide sites) throughout a supercell of $10 \times 10 \times 10$ fluorite unit cells. These structures are equilibrated for 40 ps for temperatures between 300 K and 3600 K at 25 K intervals with the thermophysical properties (lattice parameter and enthalpy) obtained from averages taken over the final 2 ps of the simulation. A 2 fs timestep is used in the NPT ensemble with Nosé-Hoover thermostat and barostat times of 0.1 ps and 0.5 ps respectively. For each composition this is repeated for 10 randomly generated structures.

The equilibrated solid solution structures are also used to determine oxygen diffusivity. The oxygen mean squared displacement (MSD) is calculated for 1 ns with a 1 fs timestep for a range of temperatures from 2000 K to 3600 K at 100 K intervals. From this the diffusivity, D, is calculated using the following equation [159],

$$D = \frac{\langle R_O^2 \rangle}{6t} \tag{7.2}$$

where $\langle R_O^2 \rangle$ is the total oxygen MSD and t is the simulation time. Care must be taken to discount the MSD during the first 10-20 fs during which the atoms are adjusting their positions within their initial potential well and random walk diffusion has not commenced.

MD simulations are also carried out on a range of the $(U_xPu_{1-x})O_2$ and $(U_xTh_{1-x})O_2$ solid solution compositions to investigate the degradation in thermal conductivity due to a non-

uniform cation sublattice. Using the non-equilibrium method (NEQM), as implemented in LAMMPS [117], kinetic energy can be transferred between atoms in one region of the supercell to another. For example, a rectangular supercell (e.g. 5×5×30 fluorite unit cells) can be split into slabs along the $\hat{\mathbf{z}}$ direction. By swapping the velocity of the fastest atom in the slab nearest the periodic boundary conditions with that of the slowest atom in the central slab, heat is transferred across the supercell. This kinetic energy exchange gradually creates a temperature gradient between the edge and centre of the supercell (see Figure 7.1). This in turn induces a heat flux, J_Z, from the hot region to the cold region. Eventually a steady state is reached where J_Z is equal and opposite to the kinetic energy exchange so that the temperature profile remains constant. Equation 7.3 is used to determine the thermal conductivity, k, of the supercell from J_Z and the temperature gradient, $\frac{2(T_2-T_1)}{L_Z}$.

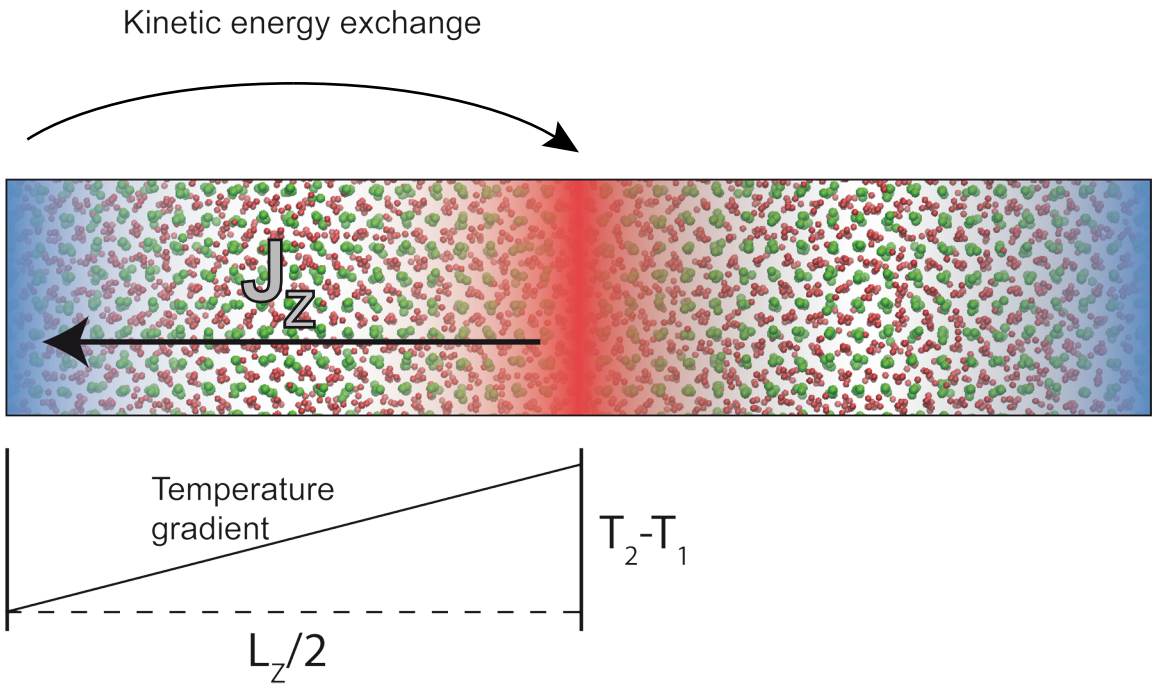


Figure 7.1: A schematic illustration of the NEQM used here to study the thermal conductivity in MD. Uranium and oxygen atoms are shown by green and red spheres respectively.

$$k = \frac{L_Z . J_Z}{2(T_2 - T_1)} \tag{7.3}$$

As discussed in greater detail later (section 7.4.1), the supercell dimensions can impact the thermal conductivity. Although thermal conductivity has been shown previously [204] to be independent of the dimensions perpendicular to heat transport, x and y, it is necessary to determine the variation of conductivity as a function of supercell length in the z-direction. As such, the NEQM was carried out on supercells of 5×5×15, 5×5×20, 5×5×25, 5×5×30 and 10×10×60 fluorite unit cells. The bulk value being determined by extrapolation to a supercell of infinite length. Calculations carried out in the NVE ensemble for 1 ns with a timestep of 2 fs proved sufficient for steady state to be achieved.

For the energy minimisation calculations of isolated oxygen vacancy and interstitial defect enthalpies, carried out by Murphy [185], the same supercells described above are employed. Given the complex structures of these solid solutions, the perfect supercells are subjected to a rigorous energy minimisation procedure to ensure they are fully relaxed. This consists of an initial minimisation under constant volume conditions using a damped dynamics algorithm [206] followed by a constant pressure step using a conjugate gradient method before a final optimization step employing a steepest descent procedure with fixed lattice parameters. Once the solid solution supercells are fully optimised, point defects were introduced into the simulation supercells by either removing (vacancy) or adding (interstitial) oxygen atoms into the supercell. The defective supercells are energy minimised with the lattice parameters fixed in order to represent the dilute limit with the defect enthalpy, ΔH, calculated using:

$$\Delta H = H_{\text{defect}} - H_{\text{perfect}} \tag{7.4}$$

where H_{perfect} and H_{defect} are the total enthalpies of the perfect and defective cells respectively. The oxygen Frenkel enthalpies for UO_2, ThO_2 and PuO_2 are converged to within 0.1 eV for the 10×10×10 supercell compared to the fully isolated enthalpies given previously (refer to Chapter 6 and [160]), therefore, the defect enthalpies are considered to be converged with respect to system size.

For the oxygen vacancy calculations a single oxygen is removed one at a time from each of the oxygen lattice sites in all 10 of the 10×10×10 simulation supercells for each composition, resulting in a total of 80,000 defect simulations. Similarly, the oxygen interstitial defect enthalpy is calculated at every possible interstitial site in all of the supercells, leading to a total of 40,000 defect simulations. This large number of simulations allows us to access the statistical distribution of the defect enthalpies arising from the random arrangement of cations on the 4a Wyckoff sites. As this approach generates a very large number of unique defect enthalpies the data set has been grouped into bins of width 0.01 eV for ease of manipulation and to enable useful presentation of these results.

7.3 Thermophysical and oxygen diffusivity properties

7.3.1 $(U_xTh_{1-x})O_2$

Thermal Expansion

Figure 7.2 shows the increase in the lattice parameter for $(U_xTh_{1-x})O_2$ as a function of temperature for a given composition averaged over 10 randomly generated structures. Below 2000 K the lattice parameter as a function of composition scales linearly between the end member UO_2 and ThO_2 systems. Figure 7.2b shows that the deviation from Vegard's law [207] never exceeds 0.03 % when below 2000 K. However, above these temperatures there is a significant deviation from Vegard's law associated with a 'bump' in the lattice parameter. As will be shown later, this is caused by the onset of the superionic transition.

The increased thermal expansion at high temperature is most clearly seen when considering the linear coefficient of thermal expansion:

$$\alpha_P(L) = \frac{1}{L}\left(\frac{\partial L}{\partial T}\right)_P \tag{7.5}$$

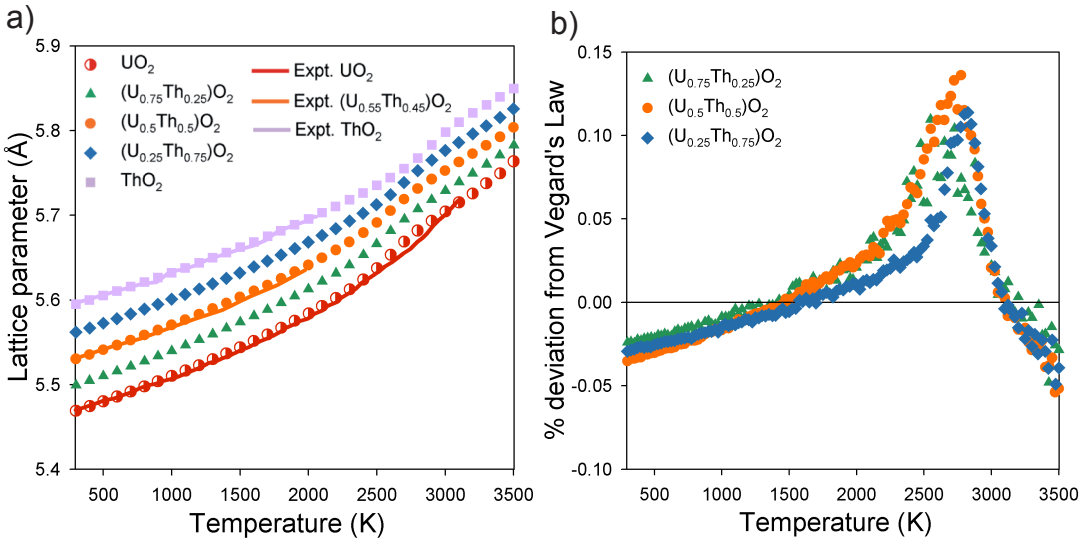


Figure 7.2: a) The variation of lattice parameter as a function of temperature for UO_2, ThO_2 and three $(U_xTh_{1-x})O_2$ compositions. Experimental data has been included for UO_2 [24], ThO_2 [38] and $(U_{55}Th_{45})O_2$ [45]. b) The deviation of the MD lattice parameter calculated from that predicted by Vegard's Law.

where L is the lattice parameter and $\left(\frac{\partial L}{\partial T}\right)_P$ is the first derivative of lattice parameter as a function of temperature. Figure 7.3 shows that for UO_2 the peak in the linear thermal expansion coefficient is at around 2600 K, in close agreement with the experimental value of 2670 K for the UO_2 superionic transition [188]. For ThO_2 the peak is at approximately 2950 K. Interestingly, addition of Th to UO_2 has relatively little effect on the peak in the linear thermal expansion coefficient for $(U_{75}Th_{25})O_2$ and $(U_{50}Th_{50})O_2$, for which the peaks also occur at around 2670 K. However, for $(U_{25}Th_{75})O_2$ the peak is increased to 2700 K. This represents a skew in the superionic transition temperatures towards UO_2.

Enthalpy increment and specific heat

In addition to the volume change as function of temperature, the enthalpy has been investigated from 300 to 3600 K. Figure 7.4 reports the enthalpy increment (increase in enthalpy with respect to standard conditions) as a function of temperature (i.e. $H(T)-H(298\,K)$) aver-

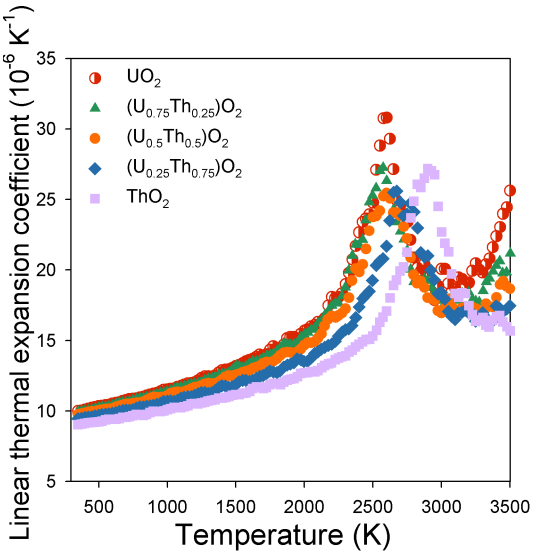


Figure 7.3: The variation of the linear thermal expansion coefficient as a function of temperature for UO_2, ThO_2 and three $(U_xTh_{1-x})O_2$ compositions.

aged over the same 10 randomly generated structures used previously for each solid solution composition. The enthalpy increment increases linearly below 2000 K for all compositions, however there is a high temperature 'bump' in the enthalpy increment. Alternatively, one may consider the variation of specific heat as a function of temperature as described by equation 7.6:

$$c_p = \frac{1}{n}\left(\frac{\partial H}{\partial T}\right)_P \tag{7.6}$$

where n is the number of moles in the supercell and the first derivative of enthalpy, $\left(\frac{\partial H}{\partial T}\right)_P$, has been calculated by fitting a straight line to the enthalpy at a given temperature and the data points ±25 K either side. Figure 7.5 indicates a gradual rise in the specific heat with temperature until around 2000 K at which point it begins to rise more rapidly. For a given composition, the temperature for the peak in specific heat corresponds to the peak in the linear thermal expansion coefficient. Comparison between the MD and experimental data for UO_2 shows a good agreement between 500 K and 1700 K and at the high temperature peak, however between 1700 K and 2400 K the experimental specific heat is in excess of

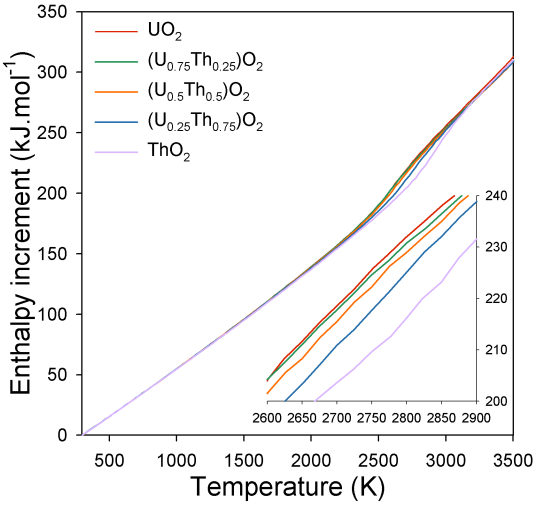


Figure 7.4: The variation of the enthalpy increment as a function of temperature for UO_2, ThO_2 and three $(U_xTh_{1-x})O_2$ compositions.

the MD values. This may be due to the choice of polynomial that was fitted to the experimental enthalpy data, resulting in a smoothing of the peak. Comparison with the specific heat in Chapter 6, where the same polynomial form was also fitted to modelling data, indicates that this may be the case. Alternatively, there are a number of reasons that oxygen disorder may occur at lower temperatures experimentally than in our perfect crystal simulations. For example, lower oxygen defect formation enthalpies may cause the superionic transition to occur at grain boundaries earlier than in the bulk. Similarly, oxygen disorder may occur at lower temperatures around dislocations. Both of these effects could contribute to broadening of the peak in specific heat towards lower temperatures and may account for the discrepancy between experiment and modelling.

Oxygen diffusivity

By assuming an Arrhenius relationship D is plotted logarithmically as a function of $\frac{1}{T}$, so that the gradient is proportional to the activation enthalpy of oxygen diffusion, H_a:

$$D = D_0 \exp\left(\frac{-H_a}{k_B T}\right) \tag{7.7}$$

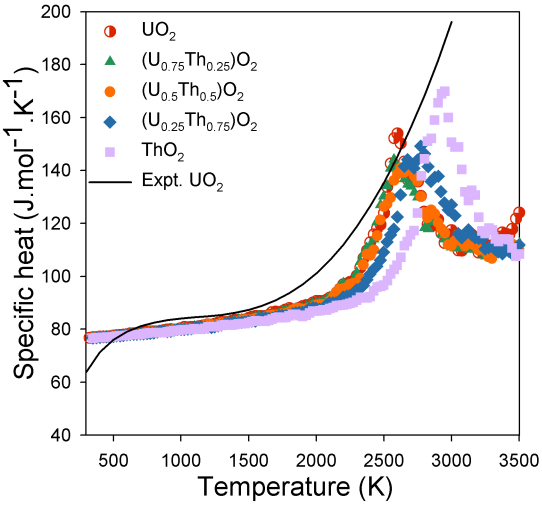


Figure 7.5: The variation of the specific heat capacity at constant pressure as a function of temperature for UO_2, ThO_2 and three $(U_xTh_{1-x})O_2$ compositions. Experimental data for UO_2 is included for comparison [39].

where D_0 is the pre-exponential term, k_B is the Boltzmann constant and T is the temperature. For each composition, D is averaged over all 10 random structures used previously and plotted in Figures 7.6a) and 7.6b) as a function of $\frac{1}{T}$ and composition respectively.

Regions in Figure 7.6a) of constant gradient, and thus activation enthalpy, indicate temperature regimes with a common diffusion mechanism. As in previous studies [198], it is shown that the transition between the fully crystalline low temperature and superionic high temperature behaviour occurs over a range of temperatures specific to each composition. Using the gradient of Figure 7.6a), Figure 7.7 indicates that there is a decrease in activation enthalpy for oxygen diffusion as the system undergoes the superionic transition. Beyond the superionic transition the oxygen sublattice exhibits a near liquid structure, thus, accounting for the change in diffusion regime. There is a clear skew in superionic transition temperature for solid solutions towards the UO_2 composition. Furthermore, $(U_{75}Th_{25})O_2$ and $(U_{50}Th_{50})O_2$ have the same superionic transition temperature as UO_2; corresponding to the peaks in the thermophysical properties. Although this does not yet prove they are due to the same structural changes, it does indicate there may be a link.

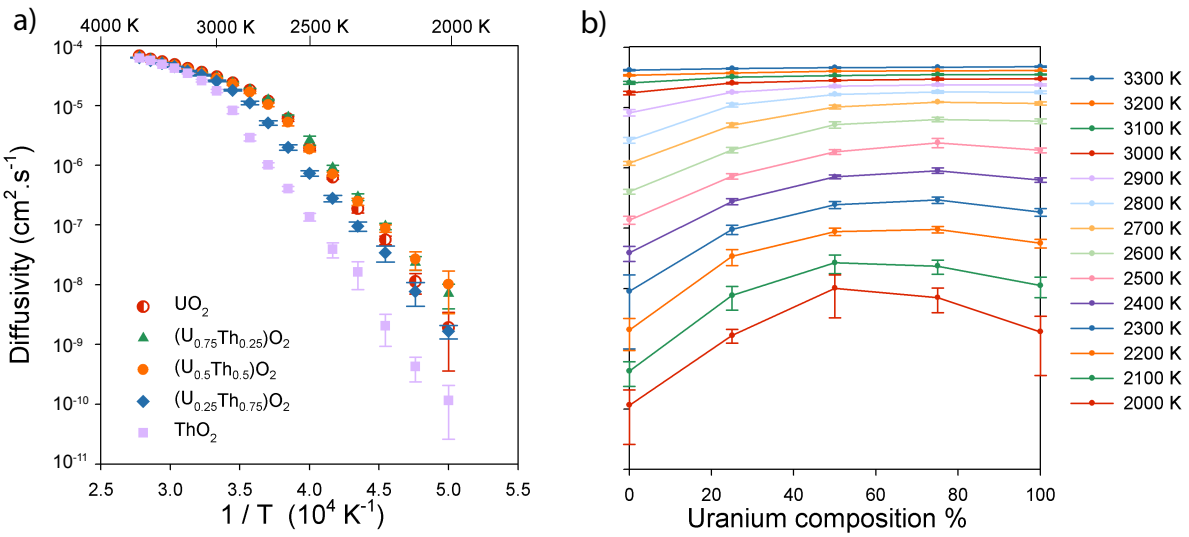


Figure 7.6: The variation of oxygen diffusivity as a function of a) temperature and b) composition for UO_2, ThO_2 and three $(U_xTh_{1-x})O_2$ compositions.

Below the superionic transition Figures 7.6a and 7.6b indicates that, rather than decreasing oxygen diffusivity, addition of Th to UO_2 actually enhances oxygen mobility. Of the compositions studied here $(U_{50}Th_{50})O_2$ has the highest oxygen diffusivity between 2000 K and 2200 K, whilst $(U_{75}Th_{25})O_2$ has the highest oxygen diffusivity between 2200 K and 2600 K. Furthermore, the trends in Figures 7.6a) and 7.6b) suggests that oxygen diffusivity may be further enhanced at lower temperatures in the mixed oxides.

Defect enthalpies

Disorder on the oxygen sublattice, and the resultant oxygen mobility, is underpinned by the enthalpy required to create oxygen vacancies and interstitials. Unlike UO_2 and ThO_2, for which all oxygen sites are identical, the mixed oxides have a large variety of oxygen sites with differing environments according to the surrounding cations species. Depending on the ratio of U:Th the likelihood of a particular defect coordination environment changes.

Figure 7.8 shows the fraction of oxygen sites that lie within 0.005 eV (i.e. half the bin width

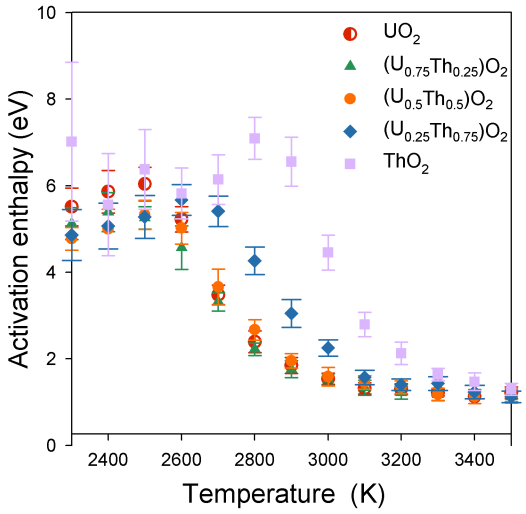


Figure 7.7: The variation of oxygen activation enthalpy as a function of temperature for UO_2, ThO_2 and three $(U_xTh_{1-x})O_2$ compositions.

selected for graph plotting) of a given oxygen vacancy formation enthalpy. For each composition there are 5 distinct peaks. These correspond to the 5 possible first nearest neighbour coordination environments experienced by oxygen anions, that is coordinated by 0, 1, 2, 3 and 4 uranium cations (or 4, 3, 2, 1 and 0 thorium cations). The lowest enthalpy peaks correspond to higher coordination by uranium cations and lower coordination by thorium cations. This is unsurprising given the lower oxygen vacancy formation enthalpy of UO_2, which indicates coordination by uranium cations favours low oxygen vacancy enthalpies. However, based on this analysis one may expect the $(U_xTh_{1-x})O_2$ oxygen diffusivity to be a simple interpolation between the end members, yet clearly for some compositions oxygen diffusivity in $(U_xTh_{1-x})O_2$ exceeds that in UO_2. This is explained in terms of the change in lattice parameter and the oxygen vacancy defect volume. Solid solutions with a smaller U:Th ratio have a greater lattice parameter, which results in a downward shift in vacancy defect enthalpies. This is consistent with oxygen vacancies having positive defect volumes. Oxygen sites that are fully coordinated by uranium cations and in a system with a greater lattice parameter than UO_2 have lower oxygen vacancy formation enthalpies than in the pure UO_2 system. The $(U_{0.25}Th_{0.75})O_2$ system, therefore, has the lowest enthalpy peak

given that it has the largest lattice parameter. However, the peak is small reflecting the small proportion of uranium cations.

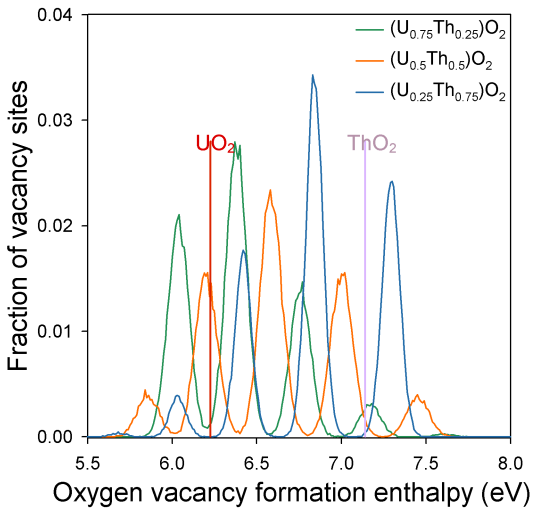


Figure 7.8: The fraction of oxygen sites that lie within 0.005 eV of the corresponding oxygen vacancy formation enthalpy for UO_2, ThO_2 and three $(U_xTh_{1-x})O_2$ compositions. From left to right, the peaks correspond to sites coordinated by 4, 3, 2, 1 and 0 uranium cations (or 0, 1, 2, 3 and 4 thorium cations). There is only one value for UO_2 and ThO_2 as represented by vertical lines.

Similarly to Figure 7.8 for oxygen vacancies, Figure 7.9 shows the fraction of oxygen interstitial sites that lie with 0.005 eV of a given oxygen interstitial formation enthalpy. Regardless of composition there are a significant number of interstitial sites that are lower in enthalpy than for those of either of the end members. As such, when considering the full oxygen Frenkel enthalpies ($O_i'' + V_O^{\bullet\bullet}$) a strong case is made that enhanced diffusion arises from a significant fraction of low enthalpy oxygen defect processes due to a non-uniform cation sublattice in MOX (see Chapter 8 for further discussion).

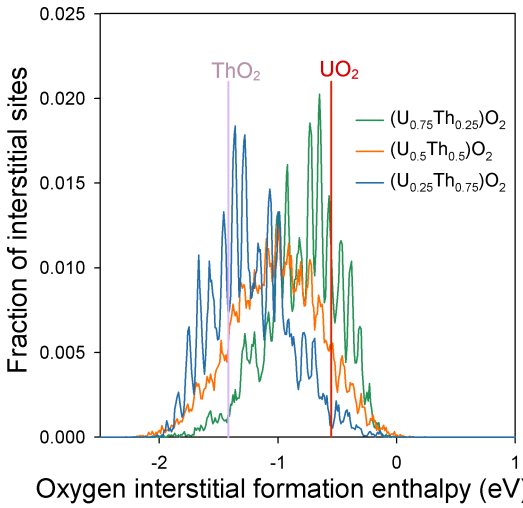


Figure 7.9: The fraction of oxygen interstitial sites that lie within 0.005 eV of the corresponding oxygen interstitial formation enthalpy for UO_2, ThO_2 and three $(U_xTh_{1-x})O_2$ compositions. There is only one value for UO_2 and ThO_2 as represented by vertical lines.

7.3.2 $(U_xPu_{1-x})O_2$

The role of the mixed U-Pu cation sublattice on the superionic transition temperature and the effect on the thermophysical properties of $(U_xPu_{1-x})O_2$ will now be discussed with comparison to the $(U_xTh_{1-x})O_2$ system. Figure 7.10 shows the increase in the lattice parameter for $(U_xPu_{1-x})O_2$ as a function of temperature for a given composition averaged over 10 randomly generated structures. Experimental data for UO_2 [24] and PuO_2 [208] are included, showing a good agreement with the model. Similarly to $(U_xTh_{1-x})O_2$, below 2000 K the lattice parameter of a given solid solution scales linearly between the end member UO_2 and PuO_2 systems with the deviation from Vegard's law [207] remaining below 0.03 %. Deviations from Vegard's law occur above 2000 K but, unlike $(U_xTh_{1-x})O_2$, there is a 'dip' in the deviation before the eventual 'bump' due to high temperature oxygen disorder that has an associated volume change. As will be shown later, the initial dip is due to the onset of the superionic transition in PuO_2 before the solid solutions. This is in contrast to $(U_xTh_{1-x})O_2$ where UO_2, $(U_{0.75}Th_{0.25})O_2$ and $(U_{0.5}Th_{0.5})O_2$ compositions all exhibit the same transition temperatures.

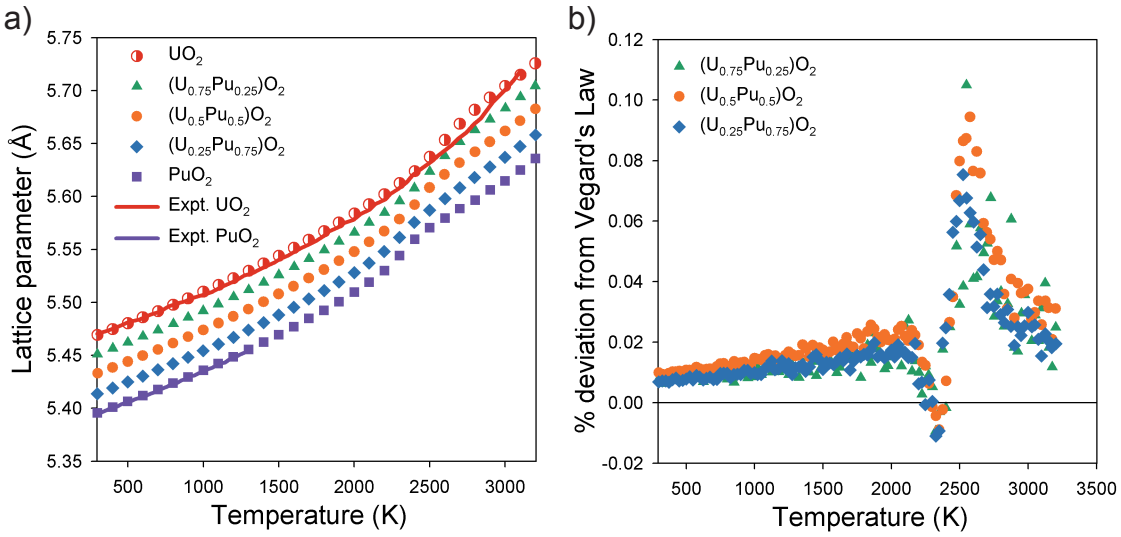


Figure 7.10: a) The variation of lattice parameter as a function of temperature for UO_2, PuO_2 and three $(U_xPu_{1-x})O_2$ compositions. Experimental data has been included for UO_2 [24], PuO_2 [40]. b) The deviation of the MD lattice parameter calculated from that predicted by Vegard's Law.

The 'bump' in the thermal expansion can most clearly be seen by considering the linear thermal expansion coefficient, as calculated using equation 7.5. Figure 7.11 shows the change in linear thermal expansion coefficient for $(U_xPu_{1-x})O_2$ as a function of temperature. The high temperature peaks associated with the superionic transition are no longer skewed to one particular end member, rather the temperatures at which they occur are approximately a linear interpolation between the end members. This is in contrast to the case for $(U_xTh_{1-x})O_2$, where a skew was seen towards the low temperature peak of UO_2. Note that the superionic transition occurs at a lower temperature for PuO_2 than for UO_2 than for ThO_2, which is consistent with ordering of their respective melting points, T_m, and the relationship for fluorite systems that the transition should occur at around $0.85T_m$ [197]. This underpins the importance of a potential's ability to predict melting points. However, this has not been validated for the AmO_2, CmO_2, CeO_2 and NpO_2 parameter set given in Chapter 6 and should be the topic of future work to improve this parameter set (see Chapter 8).

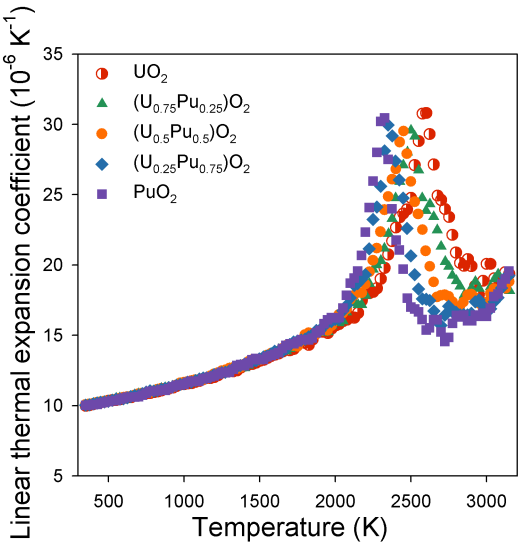


Figure 7.11: The variation of the linear thermal expansion coefficient as a function of temperature for UO_2, PuO_2 and three $(U_xPu_{1-x})O_2$ compositions.

Enthalpy increment and specific heat

During the thermal expansion simulations used to determine the lattice parameter as a function of temperature the enthalpy at each temperature was also calculated from 300 to 3200 K. Figure 7.12 reports the enthalpy increment (increase in enthalpy with respect to standard conditions) as a function of temperature (i.e. $H(T) - H(298\ K)$) averaged over the same 10 randomly generated structures used previously for each solid solution composition. Similarly to $(U_xTh_{1-x})O_2$, there is a linear increase in the enthalpy increment below about 2000 K regardless of the $(U_xPu_{1-x})O_2$ composition. However, above 2000 K there is a 'bump' in the enthalpy increment that is commensurate with the superionic transition and the 'bump' in lattice parameter shown in Figure 7.10. Alternatively, one may consider the

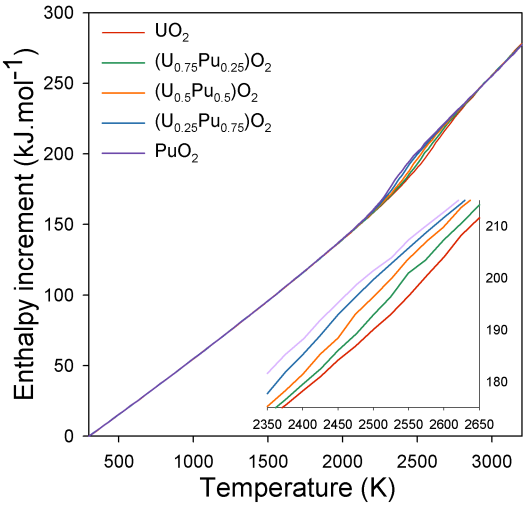


Figure 7.12: The variation of the enthalpy increment as a function of temperature for UO_2, PuO_2 and three $(U_xPu_{1-x})O_2$ compositions.

variation of specific heat as a function of temperature, as described by equation 7.6, where the first derivative of enthalpy, $\left(\frac{\partial H}{\partial T}\right)_P$, has been calculated by fitting a straight line to the enthalpy at a given temperature and the data points ±25 K either side. Figure 7.13 indicates a gradual rise in the specific heat with temperature until around 2000 K at which point it begins to rise more rapidly. For a given composition, the peak in specific heat coincides

with the peak in the linear thermal expansion coefficient. As for the linear thermal expansion coefficient, the temperatures at which the peaks in specific heat occur also follow a linear interpolation between the end members. This is in contrast to the $(U_xTh_{1-x})O_2$ system for which there is a skew towards the low temperature UO_2 peak. This indicates that the enhancement of oxygen diffusivity due to a mixed cation sublattice is somewhat less for $(U_xPu_{1-x})O_2$ compared to $(U_xTh_{1-x})O_2$.

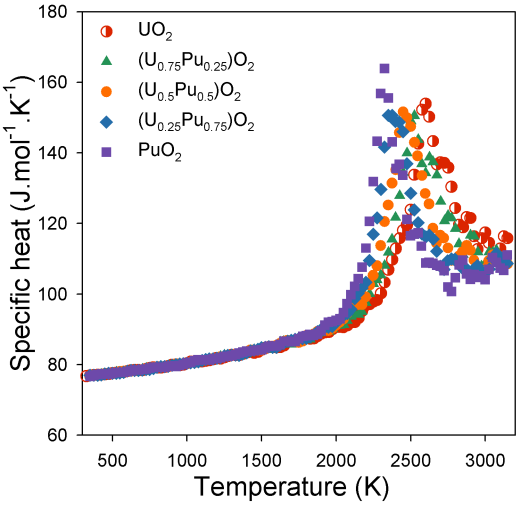


Figure 7.13: The variation of the specific heat capacity at constant pressure as a function of temperature for UO_2, PuO_2 and three $(U_xPu_{1-x})O_2$ compositions.

Oxygen diffusivity

By assuming an Arrhenius relationship, D is plotted logarithmically as a function of $\frac{1}{T}$, so that the gradient is proportional to the activation enthalpy, H_a (equation 7.7). For each composition, D is averaged over all 10 random structures used previously and plotted in Figures 7.14a and 7.14b as a function of $\frac{1}{T}$ and composition respectively.

Regions of Figure 7.14a that have a constant gradient, and therefore constant activation enthalpy, would be consistent with temperature regimes that have a common diffusion mechanism. As such, it can clearly be seen from Figure 7.14a) that there is a high temperature

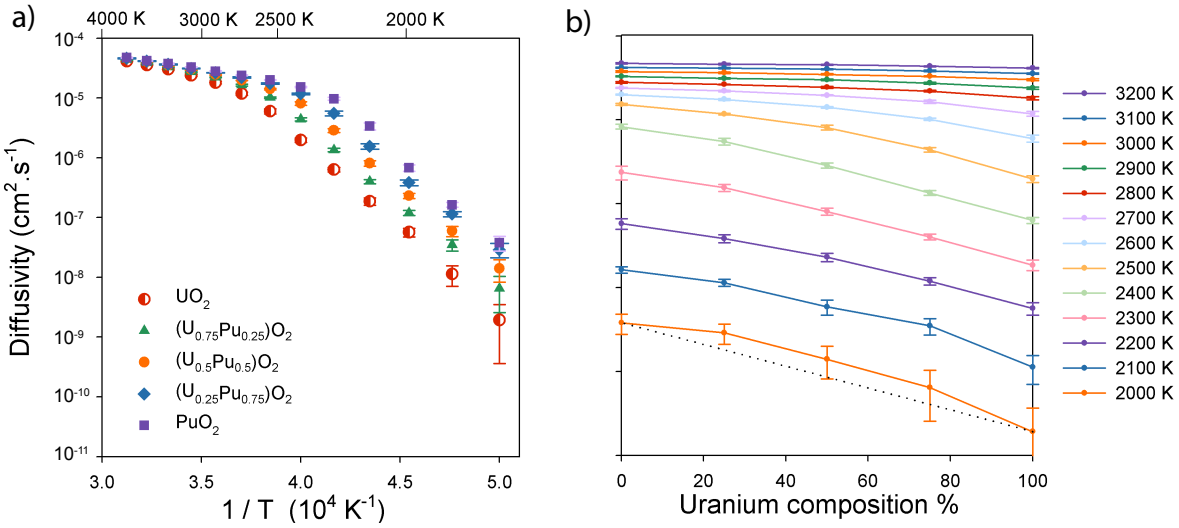


Figure 7.14: The variation of oxygen diffusivity as a function of a) temperature and b) composition for UO_2, PuO_2 and three $(U_xPu_{1-x})O_2$ compositions.

change in the diffusion mechanism that occurs after the superionic transition. Similarly, Figure 7.15 shows the activation enthalpy for oxygen diffusion as calculated from the gradient of the data in Figure 7.14a. As the systems undergo the superionic transition over a range of temperatures, there is a significant reduction in the activation enthalpy. It demonstrates that there is no skew in the superionic transition to low temperatures for the $(U_xPu_{1-x})O_2$ system, especially in comparison to $(U_xTh_{1-x})O_2$ where addition of Th to UO_2 was found to have a limited effect on the superionic transition temperature. In contrast, additions of U to PuO_2 are found to raise the superionic transition temperature even for small additions.

Below the superionic transition temperature, Figures 7.14a and 7.14b indicate that additions of U to PuO_2 reduce oxygen mobility. For all temperatures and compositions studied here, oxygen mobility is always greater for PuO_2 than for $(U_xPu_{1-x})O_2$. This is in contrast to $(U_xTh_{1-x})O_2$ where additions of Th to UO_2 increase, rather than reduce, oxygen diffusivity. Nonetheless, oxygen diffusivity is greater in $(U_xPu_{1-x})O_2$ than would be expected from a linear interpolation of the values for UO_2 and PuO_2.

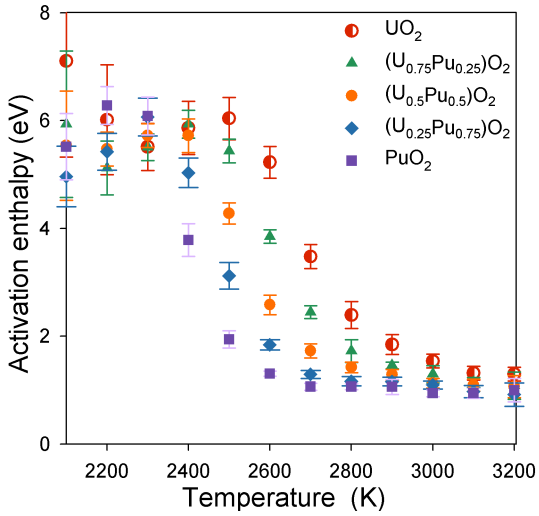


Figure 7.15: The variation of oxygen activation enthalpy as a function of temperature for UO_2, PuO_2 and three $(U_xPu_{1-x})O_2$ compositions.

Defect enthalpy

Disorder on the oxygen sublattice, and the resultant oxygen mobility, is underpinned by the enthalpy required to create oxygen vacancies and interstitials. Unlike UO_2 and PuO_2, for which all oxygen sites are identical, the mixed oxides have a large variety of oxygen sites with differing environments dictated by the surrounding cations species. Depending on the ratio of U:Pu the likelihood of a particular defect coordination environment changes. Of particular interest is the question - how does the defect enthalpy distribution differ in $(U_xPu_{1-x})O_2$ compared to $(U_xTh_{1-x})O_2$ and can this be used to explain why the enhancement of oxygen mobility is less significant?

Figure 7.16 shows the fraction of oxygen sites that lie within 0.005 eV of a given oxygen vacancy formation enthalpy. For each composition there are 5 distinct peaks. These correspond to the 5 possible first nearest neighbour coordination environments experienced by oxygen anions, that is, coordinated by 0, 1, 2, 3 and 4 plutonium cations (or 4, 3, 2, 1 and 0 uranium cations). The lowest enthalpy peaks correspond to higher coordination by plutonium cations and lower coordination by uranium cations. This is unsurprising given

that the oxygen vacancy formation enthalpy is lower in PuO_2 than in UO_2. However, based on this analysis one would expect the $(U_xPu_{1-x})O_2$ oxygen diffusivity to be a simple interpolation between the end members, yet clearly for some compositions oxygen diffusivity in $(U_xPu_{1-x})O_2$ exceeds the linear interpolation. As for $(U_xTh_{1-x})O_2$, this is explained in terms of the change in lattice parameter. Solid solutions with a higher U:Pu ratio have a greater lattice parameter, which results in a shift in vacancy defect enthalpies to lower enthalpies, as is consistent with oxygen vacancies having positive defect volumes. Therefore the presence of oxygen sites that are fully coordinated by plutonium cations, but in a system with a greater lattice parameter, results in a significant proportion of oxygen vacancy formation enthalpies that are lower than for pure PuO_2. However, the effect of the lattice parameter on the $(U_xPu_{1-x})O_2$ vacancy enthalpies is far lower than for $(U_xTh_{1-x})O_2$ because the difference in lattice parameter between PuO_2 and UO_2 is much smaller than between ThO_2 and UO_2. Consequently, the lowest enthalpy peaks for all solid solution compositions lie approximately on top of each other and although this is sufficient to enhance oxygen diffusivity above the linear interpolation of the end members it is not sufficient to cause oxygen diffusivity that exceeds that of PuO_2.

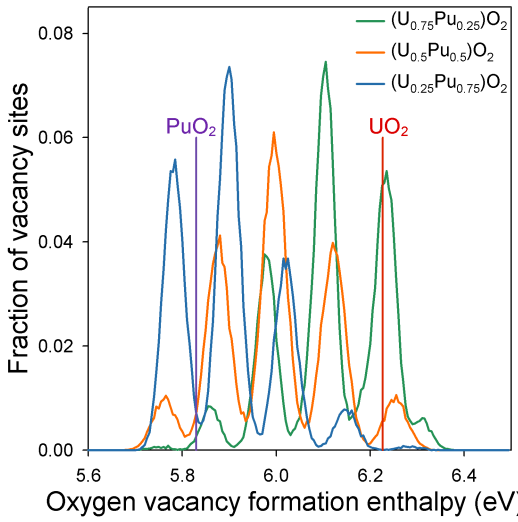


Figure 7.16: The fraction of oxygen sites that lie within 0.005 eV of the corresponding oxygen vacancy formation enthalpy for UO_2, PuO_2 and three $(U_xPu_{1-x})O_2$ compositions. From left to right, the peaks correspond to sites coordinated by 4, 3, 2, 1 and 0 plutonium cations (or 0, 1, 2, 3 and 4 uranium cations). There is only one value for UO_2 and PuO_2 as represented by vertical lines.

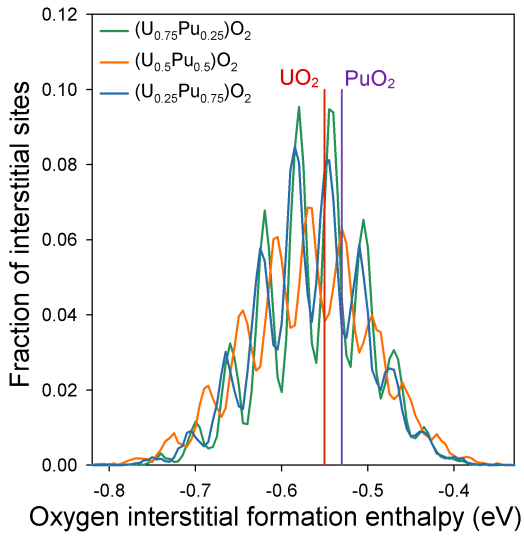


Figure 7.17: The fraction of oxygen interstitial sites that lie within 0.005 eV of the corresponding oxygen interstitial formation enthalpy for UO_2, PuO_2 and three $(U_xPu_{1-x})O_2$ compositions. There is only one value for UO_2 and PuO_2 as represented by vertical lines.

7.4 Degradation of fuel thermal conductivity

7.4.1 $(U_xTh_{1-x})O_2$

The effect of a non-uniform cation sublattice on oxygen defect enthalpies in $(U_xTh_{1-x})O_2$ and the consequences for the thermophysical properties has been discussed in section 7.3.1. However, the non-uniform cation sublattice can also be considered an imperfect lattice. As has been shown experimentally [209], this deviation from a 'clean' lattice can generate phonon scattering centres that degrade heat transport mechanisms. For example, if $x > 0.5$ Th atoms can be treated as substitutional defects in a UO_2 lattice. Similarly, if $x < 0.5$ the U atoms can be treated as substitutional defects in a ThO_2 lattice. Here the degradation of thermal conductivity due to the non-uniform cation lattice in the $(U_xTh_{1-x})O_2$ system is studied with respect to the end member thermal conductivities.

The finite supercell size limits the effective phonon mean free path causing an underestimate of thermal conductivity compared to the bulk value. Nonetheless, the thermal conductivity of a finite system, as calculated using the non-equilibrium method, can be examined as a function of the supercell size to determine the bulk value. Using Matthiessen's rule for relaxation time [204], the effective phonon mean free path, l_{eff}, in a finite system can be written as:

$$\frac{1}{l_{eff}} = \frac{1}{l_{\infty}} + \frac{1}{l_{BC}} \tag{7.8}$$

where l_{∞} is the mean free path in an infinite medium due to both phonon-phonon scattering and, if they are present, scattering from defects. l_{BC} is the mean free path associated with phonon scattering due to boundary conditions. It has been shown previously [203] that the supercell dimensions perpendicular to the direction of heat transfer (L_x and L_y) have little effect of the thermal conductivity, so the supercell cross section was kept fixed at 5×5 unit cells. l_{BC} can be defined as the average distance travelled by a phonon in the $\hat{\mathbf{z}}$ direction between scattering events. This is taken as half the distance between the hot region and the

cold region of our system so that:

$$\frac{1}{l_{BC}} = \frac{4}{L_z} \tag{7.9}$$

where L_z is the supercell length in the direction of heat propagation.

The definition of the thermal conductivity from kinetic theory is given as [204]:

$$k = \frac{1}{3} c v l_{eff} \tag{7.10}$$

where c is the specific heat due to the phonons and v is the group velocity of an acoustic branch. The specific heat above the Debye temperature is given by the Dulong-Petit value, such that $c = \frac{3}{2} k_B n$, so that combining equations 7.8-7.10 gives:

$$\frac{1}{k} = \frac{2a^3}{k_B N_c v} \left(\frac{1}{l_\infty} + \frac{4}{L_z} \right) \tag{7.11}$$

where N_c is the number of atoms in the unit cell, a is the lattice parameter and k_B is the Boltzmann constant. An interesting point is that the group velocity of the phonon branch can be approximated as $v = (v_L + 2v_T)/3$, where v_L and v_T are the longitudinal and transverse group velocities. They are given by $v_L = \sqrt{\frac{C_{11}}{\rho}}$ and $v_T = \sqrt{\frac{C_{44}}{\rho}}$ [204]. Note that for pairwise interactions C_{12}=C_{44}, so they are not able to reproduce the correct UO_2 phonon behaviour without underestimating the bulk modulus, $K = \frac{1}{3}(C_{11} + 2C_{12})$. This provides further credence to the choice of the many-body approach used here.

Equation 7.11 shows that the inverse of conductivity is a linear function of the inverse of supercell length. By the extrapolation to $\frac{4}{L_z} = 0$ (i.e. $L_z \to 0$) equation 7.11 becomes,

$$\frac{1}{k} = \frac{2a^3}{k_B N_c v} \frac{1}{l_\infty} \tag{7.12}$$

so that the only contribution to conductivity is from the mean free path due to phonon-phonon scattering and defect-phonon scattering.

Figure 7.18 shows the variation of $\frac{1}{k}$ as function of $\frac{1}{L_z}$ for perfect UO_2 for a number of temperatures with supercell sizes of 5×5×15, 5×5×20, 5×5×25, 5×5×30 and 10×10×60. The largest supercell was only used for the perfect UO_2 and ThO_2 crystals which are more dependent on the finite box size.

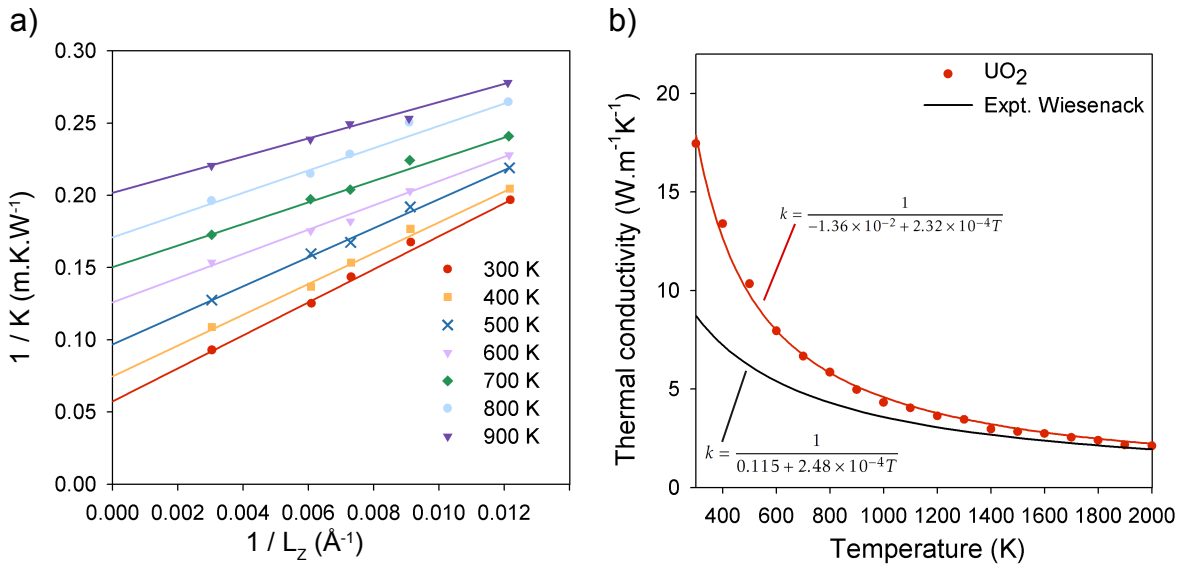


Figure 7.18: a) The variation of the reciprocal of thermal conductivity as a function of the reciprocal of supercell length for perfect UO_2 at a range of temperatures. The y-intercepts indicate the reciprocal of bulk thermal conductivity. b) Shows the bulk values as a function of temperature for unirradiated UO_2 with comparison to the phonon contribution to thermal conductivity of Wiesenack *et al.* [46] as recommended by the IAEA [39].

The linear relationship described by equation 7.11 is shown in Figure 7.18 and the y-intercept is used to determine the thermal conductivity in the bulk. This approach has been repeated for ThO_2 and a range of $(U_xTh_{1-x})O_2$ solid solution compositions. The results of bulk thermal conductivity for UO_2, $(U_{0.95}Th_{0.05})O_2$, $(U_{0.90}Th_{0.10})O_2$, $(U_{0.75}Th_{0.25})O_2$ and $(U_{0.5}Th_{0.5})O_2$ are shown in Figure 7.19 as a function of temperature. This indicates a sharp reduction the thermal conductivity, particularly at low temperatures, due to a reduction in the phonon mean free path, due to scattering associated with a non-uniform cation sublattice. Similarly, Figure 7.20 shows that although ThO_2 has a higher thermal conductivity than UO_2 there is a very significant reduction at low temperatures due to substitutional uranium additions. However, at higher temperatures, as phonon-phonon interactions become the limiting factor in determining the phonon mean free path, the proportionate effect of the non-uniform cation sublattice is far less. It is important, therefore, to consider the temperature at which the fuel will operate. For example, high temperature reactors, such

as the AGR or molten salt designs, operate at temperatures up to 900-1000 K [3] where the thermal conductivity of $(U_{0.5}Th_{0.5})O_2$ is 21 % lower than that of UO_2, whereas the degradation at PWR operating temperatures is 31 %. Similarly, at the peak centre line temperature (typically ~1650 K) the conductivity degradation for $(U_{0.5}Th_{0.5})O_2$ is about 12 % relative to pure UO_2.

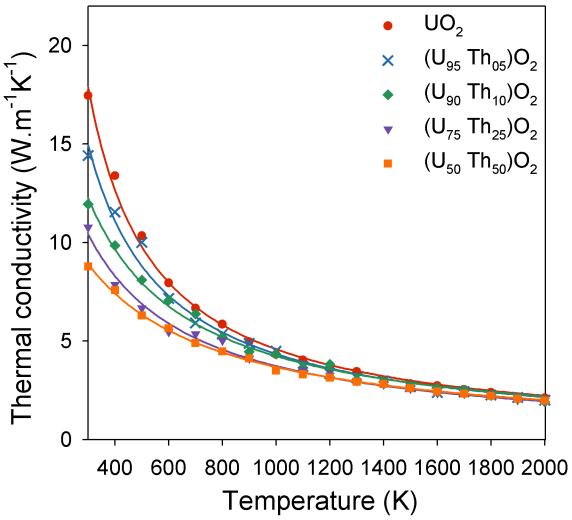


Figure 7.19: The effect of the addition of thorium to UO_2 up to the $(U_{50}Th_{50})O_2$ solid solution composition, as predicted using the non-equilibrium method. Equation 7.13 has been fitted to the data points from MD and is shown using solid lines.

For each composition shown in Figures 7.19 and 7.20, the change in thermal conductivity due to phonon-phonon scattering (influence of temperature) can be described by:

$$k = \frac{1}{a + bT} \tag{7.13}$$

where a and b are parameters that are fitted to experimental or, in this case, MD data. Note that this is the same fitting function as recommended by the IAEA [39] for experimental data except with the omission of the small polaron ambipolar contribution that is not captured by the classical empirical potential approach used here. Having fitted equation 7.13 to the temperature dependence of thermal conductivity for each composition separately, these fitted forms are shown in Figure 7.21 as a function of composition. These results clearly show a stark decrease in thermal conductivity even for compositions relatively close to the

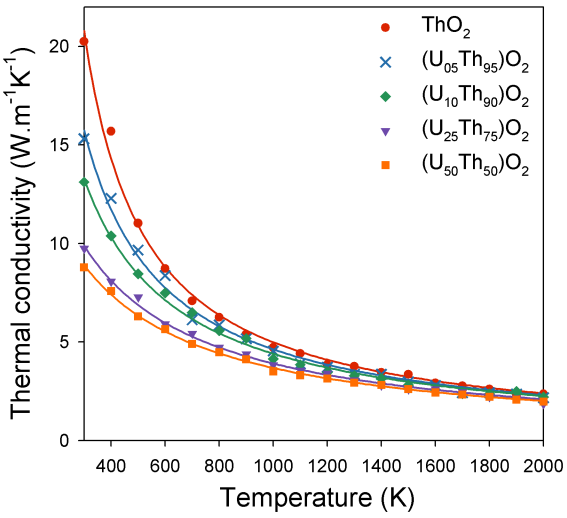


Figure 7.20: The degradation of ThO_2 thermal conductivity by the addition of uranium at thorium sites, as predicted using the non-equilibrium method. Equation 7.13 has been fitted to the data points from MD and is shown using solid lines.

end members. Unsurprisingly the minimum occurs at the 50-50 composition where the distance between dissimilar cation sites is smallest and has the greatest effect in limiting the phonon mean free path.

Clearly it is not optimal to have a vast set of different versions of equation 7.13, one for every possible composition of $(U_xTh_{1-x})O_2$. Rather, it is far more useful to accommodate the effect of defect concentration on conductivity as a modification to equation 7.13. Hence, the l_∞ term in equation 7.8 can be split into a temperature dependent term, $\frac{1}{l_T}$, and a defect scattering term, $\frac{1}{l_{defect}}$:

$$\frac{1}{l_{eff}} = \frac{1}{l_T} + \frac{1}{l_{defect}} + \frac{1}{l_{BC}} \tag{7.14}$$

Having already extrapolated our thermal conductivity values to the bulk value, the effect of the boundary conditions on the phonon mean free path can be omitted and equation 7.12 can be modified to obtain:

$$\frac{1}{k} \propto \frac{1}{l_T} + \frac{1}{l_{defect}} \tag{7.15}$$

The temperature dependent component of phonon mean free path is already accounted for

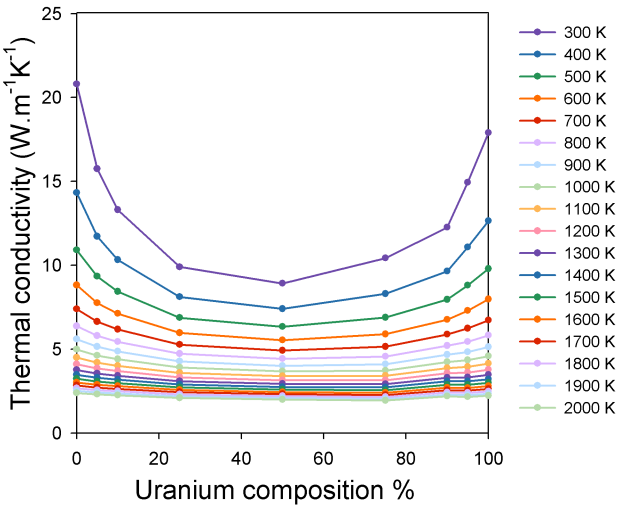


Figure 7.21: The variation of thermal conductivity as a function of uranium composition for the $(U_xTh_{1-x})O_2$ solid solution for a range of temperatures. This data is based on the fitting of equation 7.13 to the MD data in Figures 7.19 and 7.20.

by equation 7.13. However, an additional term must be included to account for the effect of defects on the phonon mean free path.

Using scattering theory (see Figure 7.22) the probability of a phonon being scattered by a defect as it travels through a thin slab of crystal of thickness dx and area A by the ratio of the total scattering cross section of the defects to the slab area:

$$P = \frac{Area_{defects}}{Area_{slab}} = \frac{\sigma n_D A dx}{A} = \sigma n_D dx \tag{7.16}$$

where n_D is the defect concentration. Therefore, the rate at which phonons are scattered by defects can be expressed as:

$$\frac{dI}{dx} = -I\sigma n_D = -\frac{I}{l_{defect}} \tag{7.17}$$

where I is the phonon flux through the slab and l_{defect} is the phonon mean free path due to defect scattering, therefore:

$$\frac{1}{l_{defect}} = \sigma n_D \tag{7.18}$$

This relationship holds true as long as the defects can be treated as isolated (i.e. no cross section overlap). Therefore, a more generalised power law is used to account for the possibility

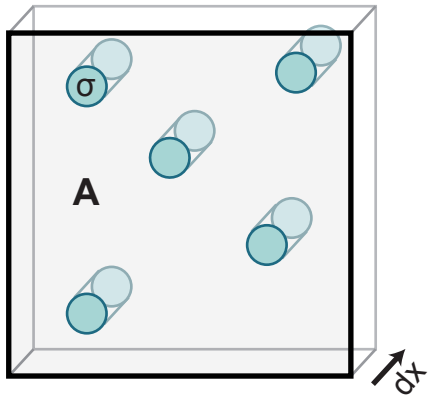


Figure 7.22: Schematic of a slab of area A and thickness dx cut through a medium containing scattering defects with cross sectional area σ.

that phonon-defect interactions change at particularly high concentrations.

$$k = \frac{1}{a + bT + cn_D^d} \tag{7.19}$$

where a, b, c and d are a full set of parameters than enable the description of both the thermal dependence and the defect concentration dependence of the thermal conductivity of a defective lattice. If one considers the scattering cross section of the defects to be independent of the defect concentration then D should equal 1. However, this is not necessarily the case for large or highly charged defects or at very high defect concentrations. Therefore, if a reasonable fit cannot be achieved over this very broad range of concentrations D will be allowed to vary.

Although equation 7.19 is suitable for describing a single defective lattice over a range of temperatures and defect concentrations, it is not suitable for describing the behaviour of a mixed oxide system over the full compositional range. To resolve this, one may consider the thermal conductivity of $(U_xTh_{1-x})O_2$ as having two contributions: i) from a UO_2 lattice that has a certain concentration of Th_U substitutional defects and ii) from a ThO_2 lattice that has a certain concentration of U_{Th} substitutional defects. The contribution of the UO_2 lattice is proportional to x but the Th_U defect concentration is proportional to $(1-x)$. Conversely, the contribution of the ThO_2 lattice is proportional to $(1-x)$ but the U_{Th} defect concentration

is proportional to x. Therefore, equation 7.19 can be modified to enable the description of the thermal conductivity of $(U_xTh_{1-x})O_2$ as a function of both temperature, T, and uranium composition, x:

$$k = k_{UO_2} + k_{ThO_2} \tag{7.20}$$

$$k = \frac{x}{A + BT + C(1-x)^D} + \frac{1-x}{a + bT + cx^d} \tag{7.21}$$

Note that if $x = 1$ this reduces to just the temperature dependent terms for UO_2 (A and B) and, conversely, if $x = 0$ it becomes the temperature dependent equation for ThO_2. Using CurveExpert Pro [210], which enables multivariable fitting, all of the parameters (A, B, C, D, a, b, c and d) were fitted simultaneously to the MD data reported in Figures 7.19 and 7.20 and are shown in Table 7.2. Figure 7.23 shows the thermal conductivity described by the fitted equation alongside the raw MD data, revealing a very strong agreement (r^2=0.997) that reaffirms the suitability of the equation 7.21 to describe the $(U_xTh_{1-x})O_2$.

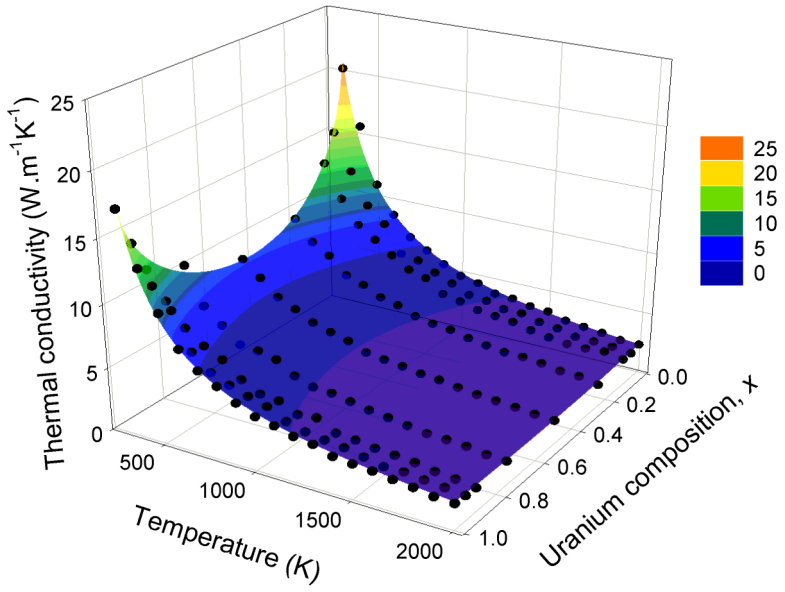


Figure 7.23: The variation of thermal conductivity as a function of uranium composition and temperature for the $(U_xTh_{1-x})O_2$ solid solution. MD data are shown with black spheres whilst the result of fitting equation 7.21 to this data is indicated by the surface.

Table 7.2: The parameters that describe equation 7.21 when fitted to the thermal conductivity data of $(U_xTh_{1-x})O_2$ as predicted from MD. The result of fitting is shown alongside the MD data in Figures 7.23.

UO_2 contribution	ThO_2 contribution
A = -1.36×10^{-2} m.K.W^{-1}	a = -1.73×10^{-2} m.K.W^{-1}
B = 2.32×10^{-4} m.W^{-1}	b = 2.18×10^{-4} m.W^{-1}
C = 7.84×10^{-2} m.K.W^{-1}	c = 1.30×10^{-1} m.K.W^{-1}
D = 6.68×10^{-1}	d = 7.47×10^{-1}

7.4.2 $(U_xPu_{1-x})O_2$

The plutonia-urania solid solution is a candidate fuel for reactors designed to utilise the waste streams from reprocessing facilities. The effect of a non-uniform cation sublattice on oxygen defect enthalpies in $(U_xPu_{1-x})O_2$ and the consequences for the thermophysical properties has been discussed in section 7.3.2. However, the non-uniform cation sublattice can also be considered as a set of substitutional defects as for $(U_x,Th_{1-x})O_2$. For example, if $x > 0.5$ Pu atoms can be treated as substitutional defects in a UO_2 lattice. Similarly, if $x < 0.5$ the U atoms can be treated as substitutional defects in a PuO_2 lattice. The mismatch in ionic radius between U and Pu limits the effective phonon mean free path relative to the pure end members. Here the degradation of thermal conductivity due to the non-uniform cation lattice in the $(U_xPu_{1-x})O_2$ system with respect to the end member thermal conductivities is considered.

The factors contributing to the phonon mean free path of $(U_xTh_{1-x})O_2$ discussed previously are still applicable for $(U_xPu_{1-x})O_2$: i) boundary conditions, ii) phonon-phonon scattering and iii) defect-phonon scattering. Therefore, the equations developed and fitted to the MD data for thermal conductivity previously (i.e. equation 7.21) are used again here. Treatment of the effect of boundary conditions that arise from the supercell method is identical to that used before (see Figure 7.18).

The results for the bulk thermal conductivity for PuO_2, $(U_{0.25}Pu_{0.75})O_2$, $(U_{0.5}Pu_{0.5})O_2$ and

$(U_{0.75}Pu_{0.25})O_2$ are shown in Figure 7.24 as a function of temperature. This indicates only a small reduction the thermal conductivity, even at low temperatures, due to a reduction in the phonon mean free path from scattering associated with a non-uniform cation sublattice. Similarly, Figure 7.25 shows that the degradation of the UO_2 thermal conductivity due to Pu substitutional defects is relatively small compared to the addition of Th defects (see Figure 7.19). In fact, the thermal conductivity of $(U_{0.5}Pu_{0.5})O_2$ is higher than that of $(U_{0.75}Pu_{0.25})O_2$, as the higher conductivity of pure PuO_2 begins to outweigh the relatively small effect of phonon-defect scattering. As for the $(U_xTh_{1-x})O_2$ system, the effect of phonon scattering due to the non-uniform cation lattice becomes progressively weaker as phonon-phonon scattering dominates at higher temperatures.

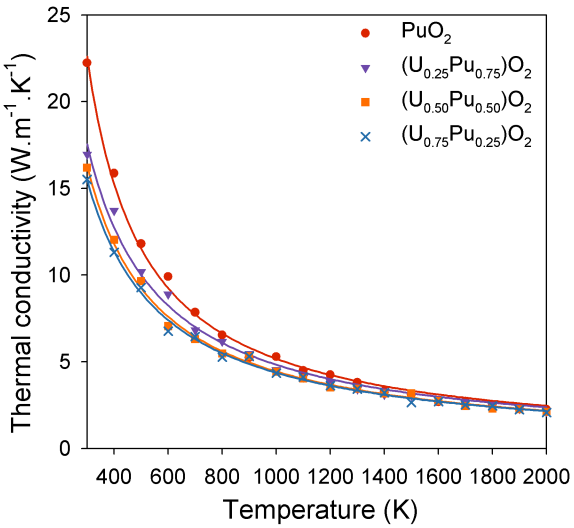


Figure 7.24: The effect of the addition of uranium to PuO_2 up to the $(U_{75}Pu_{25})O_2$ solid solution composition, as predicted using the non-equilibrium method. Equation 7.13 has been fitted to the data points from MD and is shown using solid lines.

For each composition shown in Figures 7.24 and 7.25, equation 7.13 can be fitted to the variation of thermal conductivity due to phonon-phonon scattering (influence of temperature). The thermal conductivity at a number of temperatures from these fitted functions are then shown as a function of composition in Figure 7.26. The results clearly show only a small reduction in thermal conductivity in the mixed oxides compared to the end

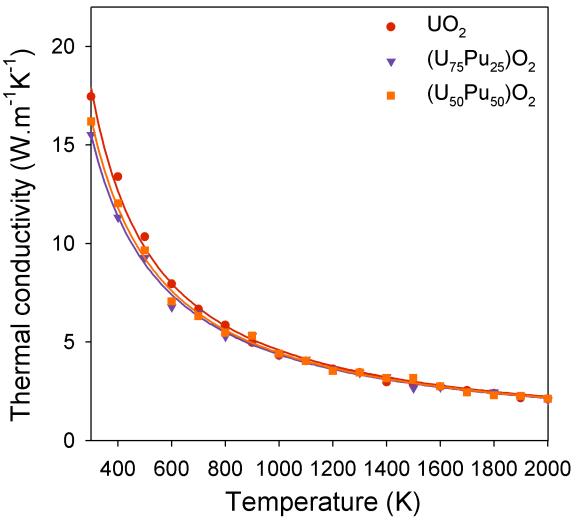


Figure 7.25: The effect of the addition of plutonium to UO_2 up to the $(U_{50}Pu_{50})O_2$ solid solution composition, as predicted using the non-equilibrium method. Equation 7.13 has been fitted to the data points from MD and is shown using solid lines.

members. The degradation of thermal conductivity in $(U_xPu_{1-x})O_2$ is far less significant compared the $(U_xTh_{1-x})O_2$ system. Furthermore, the lowest thermal conductivity occurs at $(U_{0.75}Pu_{0.25})O_2$ rather than at the 50-50 composition where the distance between non-uniform cation sites is smallest and would be expected to have the greatest effect in limiting the phonon mean free path. Apparently, this is because of the limited effect of defect scattering in $(U_xPu_{1-x})O_2$ so that the lower conductivity in pure UO_2 compared to PuO_2 begins to dominate.

Table 7.3: The parameters that describe equation 7.21 when fitted to the thermal conductivity data of $(U_xPu_{1-x})O_2$ as predicted from MD. The result of fitting is shown alongside the MD data in Figure 7.26.

UO_2 contribution	PuO_2 contribution
A = -1.36×10^{-2} m.K.W^{-1}	a = -1.96×10^{-2} m.K.W^{-1}
B = 2.32×10^{-4} m.W^{-1}	b = 2.13×10^{-4} m.W^{-1}
C = 2.61×10^{-2} m.K.W^{-1}	c = 3.02×10^{-2} m.K.W^{-1}
D = 1.00	d = 1.00

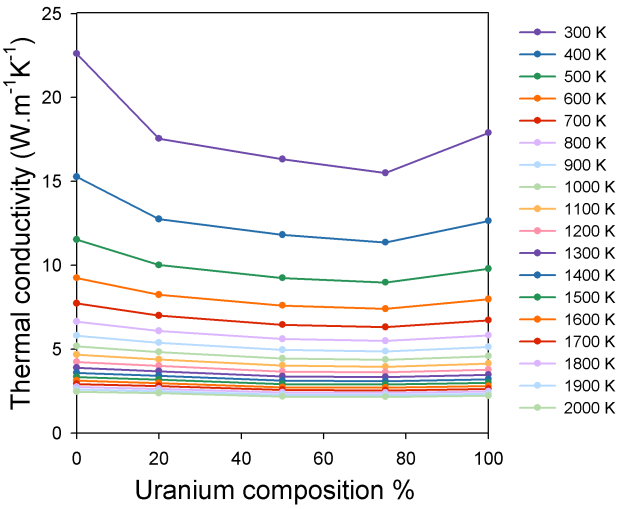


Figure 7.26: The variation of thermal conductivity as a function of uranium composition for the $(U_xPu_{1-x})O_2$ solid solution for a range of temperatures. This data is based on the fitting of equation 7.13 to the MD data in Figures 7.24 and 7.25.

The reduced effect of defect-phonon scattering in $(U_xPu_{1-x})O_2$ compared to $(U_xTh_{1-x})O_2$ can be explained in terms of the mismatch of the end member lattice parameters and the mass difference of the actinides involved. The difference in the lattice parameter of PuO_2 and UO_2 is only 0.074 Å compared to 0.126 Å for UO_2 and ThO_2 (Figures 7.2 and 7.10). Consequently the strain field arround substitutional defects in $(U_xPu_{1-x})O_2$ ought to be smaller compared to $(U_xTh_{1-x})O_2$. Furthermore, the masses of U^{238} and Pu^{239} are more similar compared to those of U^{238} and Th^{232}. As one considers the role of U^{235} in enriched fuels this may change. It is hypothesised that these two effects are what contribute to the far smaller reduction in thermal conductivity seen for $(U_xPu_{1-x})O_2$. In order to separate the mass effect from the lattice parameter effect it would be useful to investigate a system that only exhibits the effect of mass, such as enriched UO_2 (see further work in Chapter 8).

The reduced effect of defects in $(U_xPu_{1-x})O_2$ is demonstrated by the low C and c terms when fitting equation 7.21 to the MD data. Furthermore, it was not necessary to allow the D and d terms to vary, rather they were fixed at 1 in line with scattering theory (equation 7.18) for small defects that do not overlap significantly even at high concentrations.

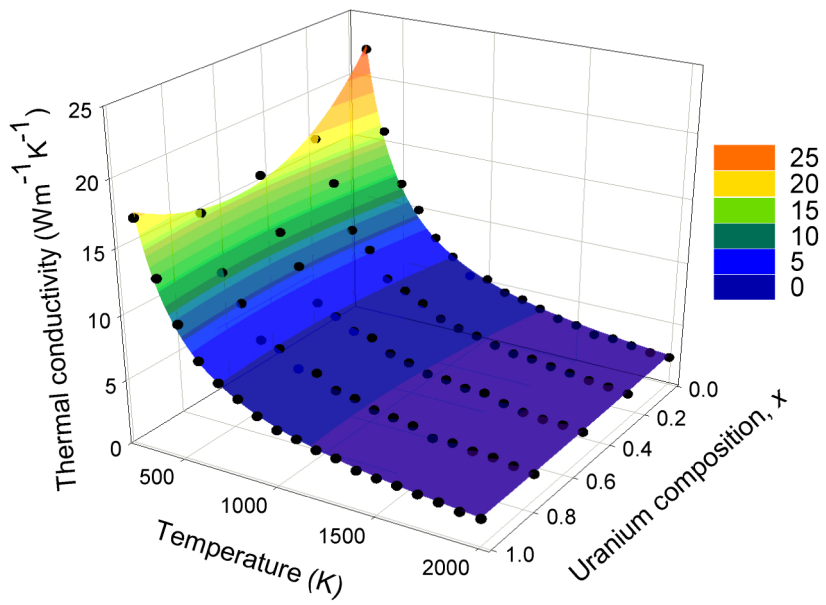


Figure 7.27: The variation of thermal conductivity as a function of uranium composition and temperature for the $(U_xPu_{1-x})O_2$ solid solution. MD data are shown with black spheres whilst the result of fitting equation 7.21 to this data is indicated by the surface.

Figure 7.27 shows the thermal conductivity described by the fitted equation alongside the raw MD data, revealing a very strong agreement (r^2=0.992) that reaffirms the suitability of the equation 7.21 to describe $(U_xPu_{1-x})O_2$.

7.4.3 Degradation of UO_2 due to oxygen Frenkel pairs

MD simulations have been carried out by collaborators at ANSTO to investigate the defect concentrations that arise from radiation damage by 1 keV damage cascades averaged over many primary knock on atom (PKA) directions [186]. Using the EAM potential developed in Chapter 6, Meng *et al.* [186] determined the thermal conductivity of a 5×5×200 supercell as a function of oxygen Frenkel pair concentration (the dominant residual defects). Here equation 7.19 (with d = 1) is fitted to that data using a least mean square approach, achieving a very good agreement (r^2=0.979). The surface predicted by equation 7.19 in conjunction with the fitted parameters (see Table 7.4) is shown in Figure 7.28. Meng *et al.* [186] only

predicted the dependence of thermal conductivity on oxygen Frenkel pair concentration for a 200×5×5 supercell and the finite system correction could thus not be employed. However, as the defect, temperature and finite size terms are treated separately in equation 7.14, the defect parameters c and d are independent of the temperature terms, a and b. Therefore, the c and d terms reported in table 7.4 can be used in conjunction with the A and B terms reported in table 7.3 for bulk UO_2.

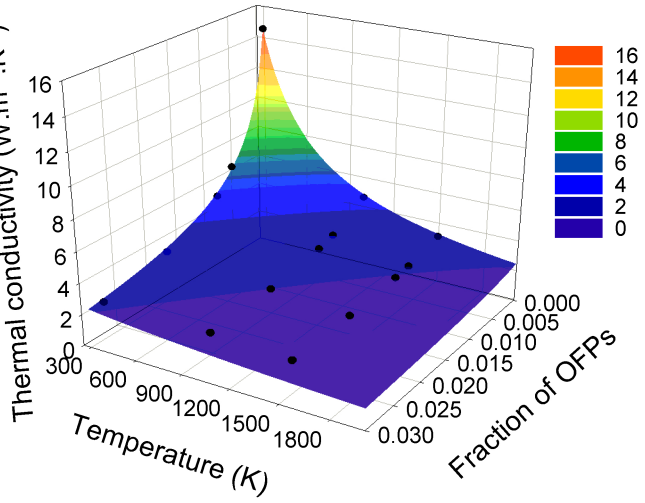


Figure 7.28: The variation of thermal conductivity as a function of oxygen defect concentration and temperature for a 5×5×200 UO_2 supercell. MD data are shown with black spheres whilst the result of fitting equation 7.19 to this data is indicated by the surface.

Table 7.4: The parameters that describe equation 7.19 when fitted to the thermal conductivity of UO_2 as a function of oxygen Frenkel pair concentration as predicted from MD. The result of fitting is shown alongside the MD data in Figure 7.28.

UO_2 200×5×5
a = 1.05×10^{-2} m.K.W^{-1}
b = 1.95×10^{-4} m.W^{-1}
c = 13.00 m.K.W^{-1}
d = 1.00

7.5 Conclusions

The lattice parameter, thermal expansion coefficient, enthalpy increment, specific heat capacity, oxygen diffusivity, oxygen defect formation enthalpies and thermal conductivity of $(U_xTh_{1-x})O_2$ and $(U_xPu_{1-x})O_2$ have been calculated using MD simulations in combination with the potential developed in Chapter 6, which has been modified here to enable mixed oxide simulations.

Below 2000 K the lattice parameter of both $(U_xTh_{1-x})O_2$ and $(U_xPu_{1-x})O_2$ were shown to closely follow a linear interpolation between the lattice parameters of the end members. The MD values only deviate from Vegard's mixing rule by a maximum of 0.03 % below 2000 K [207]. Above this temperature there is a 'bump' in the lattice parameter and the linear thermal expansion coefficient. Similarly, a 'bump' is seen in the enthalpy and specific heat at constant pressure calculated from MD simulations, which is commensurate with the 'bump' in thermal expansion. This peak is associated with the creation of oxygen Frenkel defects at high temperatures and the superionic transition that the oxygen sublattice undergoes as this disorder proceeds. There is an enthalpy of formation required to undergo this transition that is evident in the peak in specific heat capacity. Simultaneously, the lattice swelling due to this disorder results in a peak in the thermal expansion coefficient. The temperature at which this transition occurs is lowest in PuO_2 and highest in ThO_2 with UO_2 in between. This is in line with the transition occurring at $0.85T_m$. The transition temperature is concentration dependent in the solid solution of these end members. Although the transition temperature of $(U_xPu_{1-x})O_2$ linearly interpolates between that of PuO_2 and UO_2, there is a skew towards lower temperatures for the onset of the transition in $(U_xTh_{1-x})O_2$. In fact, it is only for $(U_{0.25}Th_{0.75})O_2$ that there is any significant increase the superionic transition temperature due to the addition of Th in UO_2.

Underpinning the superionic transition is the generation and mobility of oxygen defects. In both systems there is enhanced oxygen mobility below the superionic transition with respect to a linear interpolation of the end member oxygen diffusivities. However, only in

the $(U_xTh_{1-x})O_2$ system does the enhanced oxygen diffusivity actually exceed that of the end members. Furthermore, despite ThO_2 having the lowest oxygen diffusivity and PuO_2 having the highest, additions of Th to UO_2 actually increases the oxygen mobility more significantly than additions of Pu, as shown in Figure 7.29. This counter intuitive result may be important when understanding the behaviour of candidate MOX fuels or the change in oxygen mobility with burnup.

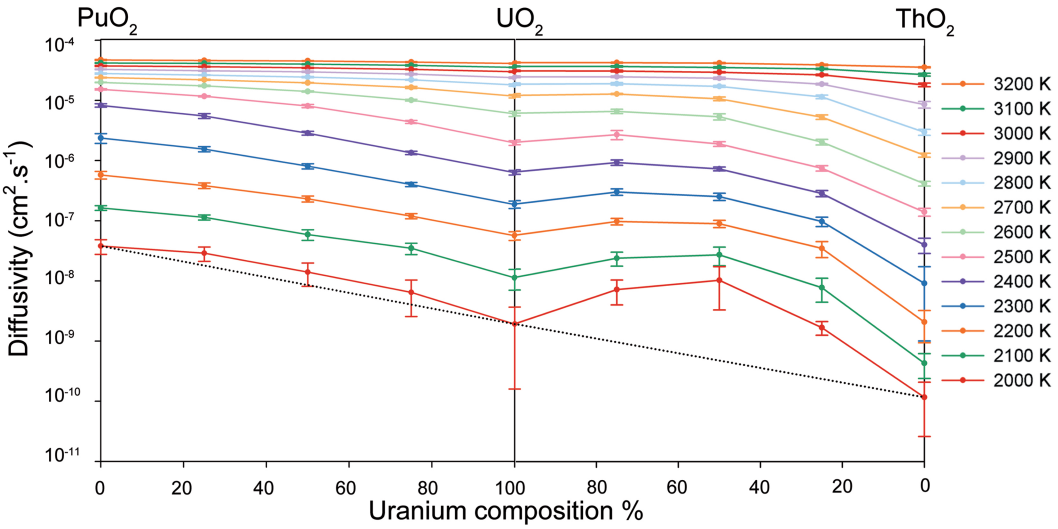


Figure 7.29: The variation of oxygen diffusivity as a function of uranium composition, x, for $(U_xPu_{1-x})O_2$ (left) and $(U_xTh_{1-x})O_2$ (right).

The enhanced oxygen diffusivity of $(U_xTh_{1-x})O_2$ compared to $(U_xPu_{1-x})O_2$ can be explained partly by considering the oxygen defect formation enthalpies. Figure 7.30a shows the distribution of vacancy formation enthalpies and indicates that for both $(U_{0.5}Th_{0.5})O_2$ and $(U_{0.5}Pu_{0.5})O_2$ there are a number of vacancies that exhibit lower formation enthalpies than the end members. Similarly, the solid solution systems have a large number of interstitial formation enthalpies that are below those of the end members, see Figure 7.30a. In order to consider the full isolated Frenkel pair enthalpies, the vacancy and interstitial distributions must be combined. The fraction of Frenkel pairs, N, with a given formation enthalpy, E_F, can be determined by identifying all interstitial-vacancy pairs that combine to give E_F and then multiplying their fractions from Figures 7.30a and 7.30b. The sum of these mixed pair

fractions gives the total fraction of Frenkel pairs with that formation enthalpy:

$$N(E_F) = \sum_{E_i+E_v=E_F} n(E_i).n(E_v) \tag{7.22}$$

where $n(E_i)$ and $n(E_v)$ represent the fraction of interstitial sites and vacancy sites with a given formation enthalpy respectively. Figure 7.30c demonstrates that the lowest enthalpy Frenkel enthalpies are in the $(U_{0.5}Th_{0.5})O_2$ system. This contributes to higher oxygen disorder and the higher diffusivity in $(U_xTh_{1-x})O_2$ compared to $(U_xPu_{1-x})O_2$, shown in Figure 7.29; a trend that is not apparent by considering just the end member Frenkel enthalpies. Furthermore, by comparing just the end member Frenkel pairs one would expect there to be a wider variety of enthalpies present in $(U_xPu_{1-x})O_2$, however this is not the case as demonstrated in Figure 7.30c.

The results on the thermal conductivity of $(U_xTh_{1-x})O_2$ and $(U_xPu_{1-x})O_2$ also exhibit behaviour that deviates from a linear interpolation of the end member thermal conductivities. In this case the non-uniform cation sublattice contributes to phonon scattering due to substitutional defects. Figure 7.31 demonstrates this behaviour is more significant in $(U_xTh_{1-x})O_2$ than $(U_xPu_{1-x})O_2$.

Similar to oxygen mobility, the degradation of thermal conductivity can be explained in terms of the difference between the end member lattice parameters. This is more significant in $(U_xTh_{1-x})O_2$ and results in stronger phonon scattering by the non-uniform cation sublattice compared to that of $(U_xPu_{1-x})O_2$. Additionally, uranium and plutonium have more similar masses, which minimises the degradation of the thermal conductivity in $(U_xPu_{1-x})O_2$. For both systems equations have been developed to describe thermal conductivity as a function of temperature and composition.

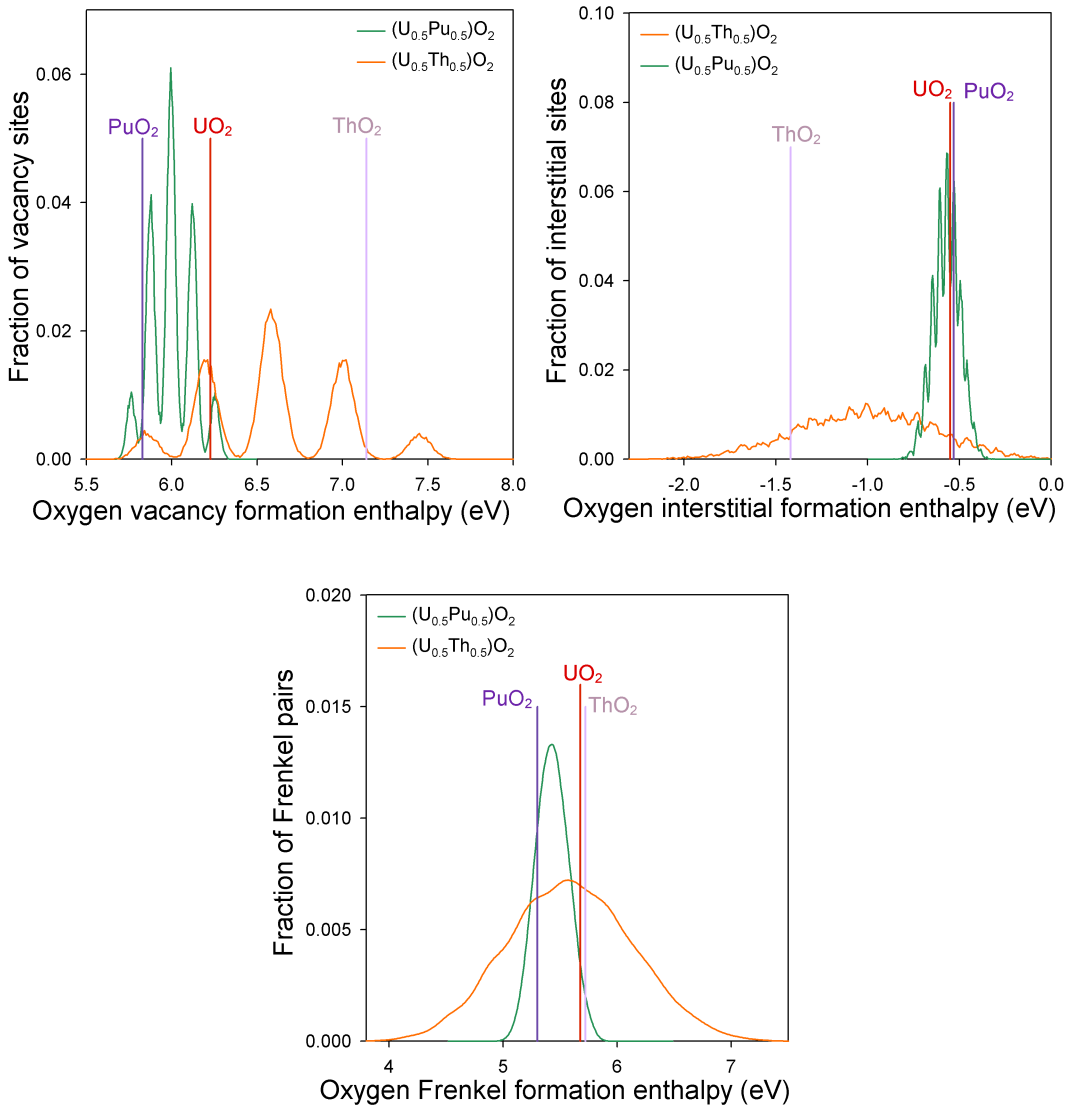


Figure 7.30: The fraction of defect sites that lie within 0.005 eV of a given defect enthalpy. The distribution of a) vacancy and b) interstitial enthalpies for $(U_{0.5}Th_{0.5})O_2$ compared to $(U_{0.5}Pu_{0.5})O_2$. The distribution of isolated oxygen Frenkel enthalpies is shown in c) by combining every possible combination vacancy-interstitial pair. For the end member systems there are only single values as represented by vertical lines.

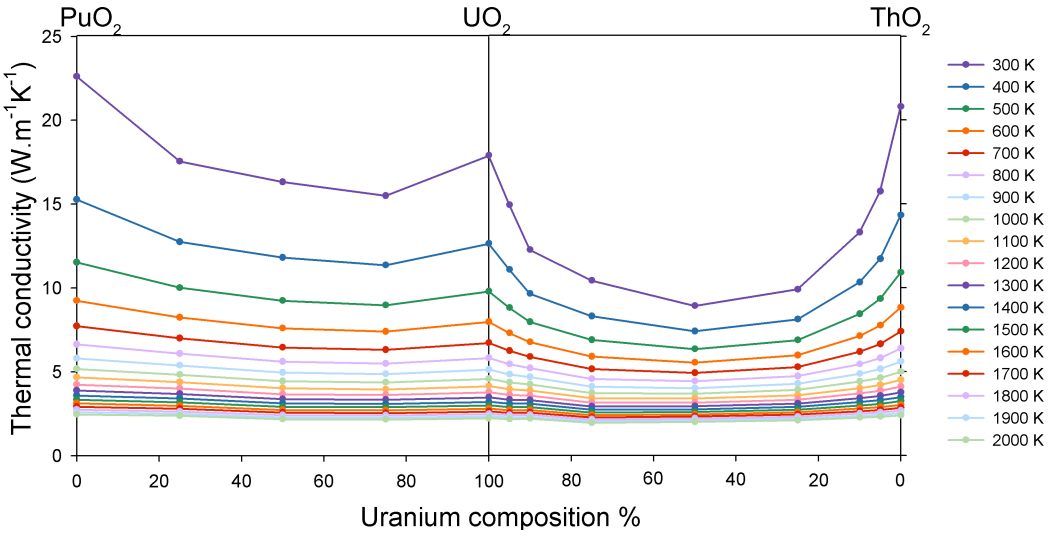


Figure 7.31: The thermal conductivity of $(U_xPu_{1-x})O_2$ (left) and $(U_xTh_{1-x})O_2$ (right) at a number of temperatures as a function of uranium composition, x.

Chapter 8

Future work

8.1 Fission product distribution

Although the thermodynamic drive for fission products to segregate to the secondary oxide phases has been established, further work must be carried out to identify the rate at which this occurs. For example Kleykamp *et al.* [79] observed rare earth fission product accommodation in the grey phase in high temperature fast breeder reactor fuel, in line with the predictions of Chapter 4. However, such grey phase precipitates are not reported for low temperature PWR fuel, thereby indicating that there may be a significant kinetic barrier for fission products to migrate, accumulate and form precipitates. Furthermore, grey phase precipitates are also observed in SIMFuel [9], where dopants are blended and sintered with the UO_2 powder, such that it is not necessary for fission products to diffuse through the UO_2 matrix in order to form the grey phase. Therefore, further work (similar to that of Chapter 5) is proposed that would study the migration of the relevant fission products through UO_2 and UO_{2+x} to form the secondary oxide precipitates. The migration barrier should also be investigated for trivalent and tetravalent cation species that were predicted to segregate to secondary oxide precipitates. This would give a greater insight into the reactor operating temperatures necessary to enable fission product segregation to their most

stable locations.

It is also possible that fission products will be accommodated at the interface between UO_2 and the grey phase. The very small size of such precipitates (1-5 nm) makes it possible to incorporate full (Ba,Sr)ZrO_3 particles in MD simulations. In that case, the association of fission gas bubbles to grey phase particles could also be studied. To facilitate this, additional potential fitting work must be carried out to establish Ba^{2+}, Sr^{2+}, Zr^{4+} and U^{5+} parameter sets (see section 8.3).

A possible benefit of fission product segregation to secondary phases is that phonon scattering defects are removed from the UO_2 matrix. A similar study to that of Chapter 7 could be carried out on the degradation of the thermal conductivity of $BaZrO_3$, $SrZrO_3$, UO_2 and UO_{2+x} due to the accommodation of fission products as defects. This will provide an indication of whether or not fission product segregation is advantageous for maintaining thermal conductivity as burnup proceeds. Similarly, the grey phase can be considered as a (Ba,Sr)ZrO_3 solid solution leading to degradation of the thermal conductivity due to a mixed cation sublattice. Furthermore, the defect enthalpies calculated for the accommodation of fission products in a (Ba,Sr)ZrO_3 solid solution will probably be better described by a full defect enthalpy distribution, like that of the solid solutions in Chapter 7.

The work on the segregation of tetravalent cations should be expanded to include the Mo and Ru containing secondary metallic precipitates in order to understand fully how their distribution can affect the issue of fuel swelling. In fact, it would be of great interest to undertake a density function theory (DFT) based investigation to study the possibility of the oxidation of Mo and Ru from the secondary metallic precipitates and their resultant accommodation in the grey phase. Currently Mo is known to oxidise directly to MoO_2 buffering excess oxygen in UO_{2+x} [87]. Interestingly the accommodation of Mo in the grey phase provides an alternative oxygen buffering mechanism, which since it has been observed by Kleykamp *et al.* [79] should be a component of further atomic scale studies.

8.2 Uranium vacancy migration

The importance of examining a wide range of cluster configurations in order to determine the lowest enthalpy migration pathway for uranium vacancy mediated migration within a charge compensating cluster has been shown. However, this work must be extended to divalent and trivalent fission product migration, as these species are also accommodated via similar charge compensated clusters. This will give further insight into the kinetic barrier to fission product diffusion that may explain the role of temperature in the likelyhood that fission products will segregate to secondary oxide phases (see section 8.1).

In order to examine such a large number of defect configurations each calculation must be relatively short for the problem to remain tractable. However, it would be useful to examine the most important cluster configurations in more detail using DFT. Therefore, an interesting study would be to take the empirical potential approach, which samples a large number of configurations and eliminates the least favourable, and couple it to a DFT approach that examines the most favourable configurations in greater detail. This would provide the benefits of the more accurate DFT calculations, whilst enabling a very large number of metastable cluster configurations to be tested.

This generalised approach to studying diffusion of defects with larger clusters should be applied to other systems. It is likely that metastable clusters will also be important for other ionic systems where strong defect clustering occurs for oppositely charged species. This includes obvious systems such as Y:ZrO_2 and Gd:CeO_2 but also more exotic battery systems.

Although this work focused on the migration enthalpy, an investigation should undertaken into the configuration dependence of terms that contribute to the pre-exponential, such as the correlation factor and attempt frequency [159].

8.3 EAM Potential

In Chapter 7 the importance of predicting the melting point (T_m) of actinide oxides was discussed. The potential parameters for ThO_2, UO_2 and PuO_2 have been validated against melting point, thus ensuring a reasonable description of the superionic transition, which occurs at $0.85T_m$. It would, therefore, be very useful to go back to the CeO_2, NpO_2, AmO_2 and CmO_2 parameters sets to validate, and where appropriate readjust, them against melting point. This would improve the fidelity of the potential set and ensure the parameters remain consistent.

Work is currently ongoing to develop parameter sets for the Zr^{4+}-O^{2-}, Ba^{2+}-O^{2-}, Sr^{2+}-O^{2-} and U^{5+}-O^{2-} interactions that are consistent with the new EAM potential (preliminary results in Appendix). This will allow investigations of (Ba,Sr)ZrO_3 and hyper-stoichiometric UO_{2+x} using the new EAM potential set.

More generally, other fission products need to be added to this potential set to allow a greater range of nuclear fuel problems to be tackled. Rushton and Chroneos [184] have already added a range of trivalent cations by fitting to doped CeO_2 data, however there are further trivalent fission products to be included and validated for use with the UO_2 potential. Ongoing work is being carried out to include parameters for Xe and Kr by fitting to interatomic forces calculated by DFT methods. This would allow the investigation of fission gas diffusion through the bulk, accumulation in bubbles and even the association of bubbles to grey phase precipitates or dislocations. Cs and I potentials must also be developed as these fission products play an important role in fuel-clad interactions due their reactive nature. Limiting their release from the UO_2 matrix could be a key factor in limiting the corrosion of the cladding.

8.4 Mixed oxides

The isolated oxygen vacancy and interstitial enthalpies have been calculated for $(U_xTh_{1-x})O_2$ and $(U_xPu_{1-x})O_2$, however, future work is required to extend this to clustered Frenkel defects and the migration barriers associated with oxygen diffusion. Additionally, there is the possibility of a percolation limit occurring at compositions close to the end members, whereby, regions of high diffusion are not interconnected over long ranges, thus limiting extended diffusion. The possibility that the percolation limit extends over the periodic boundary condition must be kept in mind and avoided.

A key conclusion of Chapter 7 was that oxygen diffusion is most significantly enhanced for solid solutions with the greatest difference in end member lattice parameter. If this is true one would expect to see more enhanced diffusion in $(Th_xPu_{1-x})O_2$ and future work should be carried out to confirm if this is true. Similarly, the lattice parameter mismatch was also identified as the most important factor in the degradation of the thermal conductivity of these solid solutions, providing additional motivation for the extension of these models to $(Th_xPu_{1-x})O_2$.

Having examined all three ternary systems, additional calculations must be carried out to study the quaternary $(U_xTh_yPu_{1-x-y})O_2$ system. Ideally the analytical equations used to describe defect-phonon scattering in the ternary systems will be transferable to the quaternary systems, so that predictions can begin to be made for any combination of actinide oxides. This would be a significant step towards understanding the effect of a non-uniform lattice in the degradation of the thermal conductivity of mixed oxides and high burnup fuel.

As additional fission products are added to the potential set (see section 8.3) their effect on thermal conductivity and oxygen diffusivity can be investigated. In particular, the trivalent fission products are expected to have a strong effect on oxygen diffusion in UO_2 as they introduce oxygen vacancies through charge compensation. The eventual aim is to have a full potential set that would enable simulations with real life fuel compositions to be investigated.

Finally, given the quality of this model at high temperatures, the potentials can be used to predict properties pertinent to severe accidents. For example, the density of actinide oxide melts and mixed oxide melts. This would include liquid densities but also mechanical properties as a function of temperature. A more ambitious challenge would be to predict the depression of melting point as a function of actinide content for mixed actinide oxides. The challenge comes from there being both solid and liquid in equilibrium with different compositions.

Chapter 9

Summary

This thesis presents the results of atomic scale calculations aimed at investigating irradiated fuel behaviour; understanding the atomistic mechanisms that underpin changes in the thermophysical and chemical properties of nuclear fuel during the fuel cycle. For example, dopants introduced to the fuel at the beginning of life (such as Cr^{3+} or Gd^{3+}) can impact the distribution of fission products during irradiation, affect the accommodation of excess oxygen or degrade the thermal conductivity of the uranium dioxide lattice through defect-phonon scattering processes. Alternatively, the migration of fission gas through bulk UO_2 and its accumulation at either dislocations or grain boundaries is important for fuel performance during normal reactor operations, during accident conditions and during fuel storage or disposal. In order to close the fuel cycle and utilise Pu and minor actinide stockpiles contained in SNF, the performance of mixed oxide fuels must be well understood.

A wide variety of fission products are present in irradiated nuclear fuel. The accommodation of these fission products in various positions of the fuel depends on the reactor conditions. In particular, fission product solubility in uranium dioxide was found to be strongly dependent on non-stoichiometry in previous studies [78, 79]. Similarly, the mobility of uranium vacancies, which is a key parameter for fission gas release, is known to be dependent of uranium dioxide non-stoichiometry [15].

It was also identified in Chapter 1 that atomistic phenomena ought to be examined over the broad range of temperatures experienced by fuel during the fuel cycle. Furthermore, the comparison of previous empirical potentials in Chapter 3 revealed the difficulty pairwise descriptions of interatomic forces have in accurately describing the thermophysical properties of UO_2 over the full range of temperatures.

The work in the thesis can, therefore, be partitioned into two sections, one that aimed to use a suitable previous potential to gain insight into the role of non-stoichiometry, and a second that developed a new potential form enabling the study of mixed actinide oxide systems from 300 to 3000 K.

9.1 Non-stoichiometry

9.1.1 Fission product distribution

During irradiation a reduction in the uranium content of the fuel through fission leads to the presence of excess oxygen. The solubility of fission products in UO_{2+x} has been shown to be greatly enhanced relative to their solubility in UO_2 [78]. It is important, therefore, to identify how the distribution of fission products changes as a consequence. As such, the precipitation of secondary oxide phases and the subsequent segregation of additional fission products to these phases has been investigated. This work used a potential that enables the simulation of UO_{2+x} [16] through the inclusion of a U^{5+} potential. Furthermore, it performs reasonably well in the low temperature regime, which is consistent with the static calculations implemented here and understanding spent fuel after it has been removed from the reactor.

All grey phase constituent phases studied here ($BaZrO_3$, $SrZrO_3$, BaO, SrO and ZrO_2) were predicted to precipitate from their stable defect sites in stoichiometric UO_2. However, the lowest precipitation energies were predicted for $BaZrO_3$ and $SrZrO_3$ indicating that Ba^{2+}, Sr^{2+} and Zr^{4+} will preferentially co-precipitate to form the perovskite phase,

in line with experimental observation [9, 79]. Some of the binary oxides may remain depending on the relative abundance of the Ba, Sr and Zr fission products. Furthermore, ZrO_2 is also present in LWR fuel at the interface with the zircalloy cladding. Under hyperstoichiometric conditions the perovskite grey phase, (Ba,Sr)ZrO_3, is no longer predicted to precipitate, whereas ZrO_2 was predicted to precipitate regardless of uranium dioxide non-stoichiometry. The presence of U^{5+} and Cr^{3+} cations in Cr-doped UO_{2+x} enables the precipitation of $CrUO_4$.

A number of fission products (Ru^{4+}, Mo^{4+}, Zr^{4+} and Ce^{4+}) and the minor actinides (Am^{4+}, Np^{4+} and Pu^{4+}) exist in the 4+ charge state and are, therefore, accommodated isovalently at the uranium site in UO_2 and UO_{2+x}. This negates the need for charge compensating defects, thus removing the dependence of tetravalent cation solubility on the non-stoichiometry of the uranium dioxide phase. The small tetravalent cations (Ru^{4+} and Mo^{4+}) were found to preferentially segregate to $BaZrO_3$, $SrZrO_3$ and ZrO_2 rather than remain in UO_2 or UO_{2+x} by isovalent accommodation at the Zr^{4+} site. The segregation of Ru^{4+} and Mo^{4+} to both cation sites in $CrUO_4$ was also predicted to be favourable, whilst Zr^{4+} is expected to partition to the U^{5+} site. In particular, the accommodation of Mo^{4+} in secondary oxide phases presents a possible mechanism for buffering the excess oxygen in the UO_{2+x} phase as burnup proceeds. Large tetravalent cations (Ce^{4+}, Am^{4+}, Np^{4+} and Pu^{4+}) were not predicted to segregate to any of the secondary due to the similar chemistry and ionic radius between these species and to U^{4+} and that their radii are much larger that that of Zr^{4+}.

The accommodation of trivalent cations in uranium dioxide requires charge compensating intrinsic defects to balance the aliovalent T'_U defects. Therefore, the solubility of trivalent cations in uranium dioxide is different for UO_2 and UO_{2+x}. It was predicted that Sm^{3+}, Nd^{3+}, Pr^{3+} and La^{3+} will segregate to $BaZrO_3$ rather than remain in stoichiometric UO_2. The availability of both divalent (Ba^{2+}) and tetravalent (Zr^{4+}) cation sites enables the accommodation of trivalent cations at both sites simultaneously, thus self charge compensation occurs through the creation of $\{T^{\bullet}_{Ba} : T'_{Zr}\}^{\times}$ clusters. However, the equivalent mechanism is not favourable for segregation to $SrZrO_3$. Therefore, the segregation of Sm^{3+}, Nd^{3+}, Pr^{3+}

and La^{3+} to (Ba,Sr)ZrO_3 was predicted to be dependent on the Ba:Sr ratio. Cr^{3+} and Fe^{3+}, on the other hand, were predicted to segregate to (Ba,Sr)ZrO_3 regardless of the Ba:Sr ratio. A strong dependence of segregation on non-stoichiometry was also identified, with all trivalent cations preferentially remaining in the UO_{2+x} phase. Therefore, reactor designs with different Ba and Sr fission product yields or different levels of non-stoichiometry are predicted to exhibit different levels of trivalent fission product segregation to the grey phase. This may have important consequences for fuel performance. For example, the thermal conductivity of the UO_2 phase may be maintained at higher burnup by removing fission products that are accommodated at substitutional sites and encouraging their segregation to the secondary oxide grey phase. Alternatively, if fission products are accommodated at more stable sites in the grey phase it may limit their release from the fuel matrix under accident conditions.

The self charge compensating mechanism for segregation of trivalent cations at both A and B cation perovskite sites also opens the possibility that large trivalent fission products can interact with small trivalent cation dopants, such as those in Cr-doped ADOPT fuels [4]. In fact, the presence of excess Cr in the fuel has been predicted to reduce the partition enthalpies for large trivalent cations to the extent that Lu^{3+}, Er^{3+}, Y^{3+}, Dy^{3+}, Gd^{3+}, Sm^{3+}, Nd^{3+}, Pr^{3+} and La^{3+} are all predicted to segregate from UO_2 to $BaZrO_3$ and $SrZrO_3$. So if one deems it favourable to encourage fission product segregation it may be possible to engineer this behaviour into the fuel design through the use of suitable dopants. However, the reduction in partition enthalpy due to excess Cr is not sufficient to enable segregation from UO_{2+x}. Nonetheless, $CrUO_4$ precipitates were predicted to form in hyper-stoichiometric Cr-doped fuel, to which Ru^{4+}, Mo^{4+} and Zr^{4+} are expected to segregate. Very low, but positive, partition energies were calculated for the Am^{4+}, Pu^{4+}, Ce^{4+} and Np^{4+} species, indicating that although they are predicted here to remain in the UO_2 phase, entropy may drive them into the $CrUO_4$ at higher temperatures.

BaO and SrO were also expected to precipitate from stoichiometric UO_2. However, none of the trivalent or tetravalent cations were predicted to segregate. Segregation to ZrO_2 from

UO_2 was predicted to be favourable for Cr^{3+}, Fe^{3+}, Lu^{3+}, Er^{3+}, Y^{3+}, Dy^{3+}, Gd^{3+} and Sm^{3+}. This poses an interesting possibility that fission product accommodation at the fuel-clad interface in LWR fuels may stabilise the tetragonal or cubic zirconia structures, with important implications for pellet clad interactions. Although the precipitation of ZrO_2 from UO_{2+x} was predicted to be favourable, all species studied here were calculated to remain dissolved in UO_{2+x} rather than segregate.

9.1.2 Uranium vacancy migration

The role of hyper-stoichiometry in the transport of uranium vacancies has been studied as it is an important parameter in the migration of fission gases, Kr and Xe, through the bulk uranium dioxide. Uranium vacancy migration is also important due to its role in the recovery phase of a damage cascade. Hence the work presented here contributes to a clearer understanding of how non-stoichiometry effects important mechanisms that underpin fuel performance. Uranium vacancies are highly negatively charged and thus bind strongly to positive intrinsic defects, be that $V_O^{\bullet\bullet}$ defects in UO_2 or $U_U^{\bullet}$ defects in UO_{2+x}. The enthalpy barrier for migration of a U^{4+} cation into the vacancy varies depending on the configuration of the cluster. Therefore the work of this thesis builds on the previous work, which focused only on the most stable cluster configurations, by investigating the enthalpy barrier in every possible configuration of the $\{V_U'''' : 2V_O^{\bullet\bullet}\}^{\times}$ and $\{V_U'''' : 4U_U^{\bullet}\}^{\times}$ clusters within a volume of $2 \times 2 \times 2$ fluorite cubic cells.

In stoichiometric UO_2 a large number of configurations were found that exhibited a reduction the enthalpy barrier. However, for most of these configurations the enthalpy required to rearrange the cluster from the most stable arrangement (reconfiguration enthalpy) outweighed the reduction in the enthalpy barrier, such that the total migration enthalpy (reconfiguration enthalpy + enthalpy barrier) was not lower than for the most stable clusters. Nonetheless, 17 cluster configurations were identified that had a lower total migration enthalpy than that for the most stable configuration. The lowest total migration enthalpy in

stoichiometric UO_2 was 6.41 eV (0.19 eV lower than migration involving the most stable cluster).

For hyper-stoichiometric UO_{2+x} there were a very large number of configurations for the $\{V_U'''' : 4U_U^{\bullet}\}^{\times}$ cluster. Furthermore, 358 were identified as having a lower total migration enthalpy than that of the most stable cluster. The lowest overall migration enthalpy was 6.89 eV (0.64 eV than for the most stable cluster).

So it has been clearly demonstrated that to study migration of uranium via a vacancy mediated mechanism in UO_2 and UO_{2+x} one must go beyond a discussion of just the most stable cluster configuration. This is necessary not only to determine the lowest migration enthalpy, but also to identify the broad range of similar enthalpy pathways. This is important for understanding both the temperature dependent and independent term in Arrhenius diffusion. The computational demand of DFT calculations means that studying such a large number of configurations is not currently feasible.

9.2 Temperature effects

Another key factor identified in Chapter 1 is the wide range of temperatures nuclear fuels experience within a nuclear reactor (up to 600-1500 K). Therefore, in order to investigate phenomena at different positions in the fuel pellet, or in different reactor designs, a potential model must accurately reproduce well known materials properties over this wide temperature range.

In Chapter 3 a detailed comparison of existing UO_2 pair potential was reported. Although all potentials gave a good description of the low temperature lattice parameter, it became clear that many exhibit deficiencies in several ways. For example, some incorrectly predicted a non-fluorite lowest enthalpy crystal structure for UO_2 and were discounted from further comparison. Generally speaking the remaining potentials can be split into two categories:

- Those that give a good description of the low temperature properties (lattice parameter and elastic constants) but are not able to capture the thermal expansion or the high temperature bulk modulus. Frequently these potentials implement the shell model, enabling the Cauchy violation ($C_{12} \neq C_{44}$) to be reproduced. However, due to the difficulties with implementing massless shells in MD, shells are frequently omitted.

- Other potentials do not use the shell model for ease of use in MD. Instead they focus on reproducing the thermal expansion. Unfortunately in doing so the bulk modulus is invariably underestimated at low temperatures. Furthermore, the Cauchy violation ($C_{12} \neq C_{44}$) is not reproduced in static calculations.

Most properties were well described by at least one potential so that by careful selection, most phenomena can be investigated, although not over large temperature ranges. One clear exception to this was the temperature dependence of bulk modulus, with could not be describe by any of the potentials.

In Chapter 6, a new potential form has been developed with the aim of capturing the bulk modulus as a function of temperature without having to compromise on any of the other properties. Importantly, for the first time a manybody EAM potential was included in addition to a more conventional pair potential (Buckingham [110] + Morse [109]). This departure from a pairwise description enabled coordination dependent actinide-oxygen interactions to be developed that became less tightly bound as the coordination of a given atom increased. The parameters were successfully fitted to the thermal expansion and elastic constants (including Cauchy violation) of CeO_2, ThO_2, UO_2, NpO_2, PuO_2, AmO_2 and CmO_2. Oxygen-oxygen parameters were kept consistent throughout, thereby, allowing the simulation of mixed oxides. Predictions of the thermophyscial properties that did not contribute to the fitting process were used to validate the new potential model. The values predicted were in excellent agreement with the enthalpy increment, specific heat and melting points of UO_2, PuO_2 and ThO_2. A very significant improvement in the prediction of the temperature dependence of bulk modulus was achieved for UO_2. The temperature dependence of bulk modulus was also investigated for the other actinide oxides for which experimental

data does not seem to be available in the open literature. Agreement with DFT was shown for the most stable Schottky defect cluster configuration in UO_2 when using a 2×2×2 fluorite supercell. However, by examining larger supercell sizes, that are not possible with DFT due to computational demand, a different lowest energy cluster configuration was predicted in the dilute limit. In summary, the potential developed represents a significant improvement on previous models. It captures a very broad range of thermophysical properties from 300 to 3000 K, enabling a wide range of phenomena to be studied over all temperatures experienced by the fuel. Furthermore, to help other groups use this potential, and contribute to a consistent body of simulation work, support for implementation in popular atomistic simulation codes is provided at http://abulafia.mt.ic.ac.uk/potentials/actinides/.

By fixing the oxygen-oxygen interactions across the actinide series the simulation of mixed oxides was possible using the new potential. In Chapter 7, structures for different compositions of the $(U_xTh_{1-x})O_2$ and $(U_xPu_{1-x})O_2$ solid solutions were created by randomly assigning U^{4+}, Th^{4+} and Pu^{4+} cations to the 4a wyckoff sites of a 10×10×10 fluorite supercell. Using these structures the lattice parameter, linear coefficient of thermal expansion, enthalpy increment, specific heat capacity at constant pressure, oxygen diffusivity, oxygen defect enthalpies and thermal conductivity were examined as a function of composition and temperature. Below the superionic transition temperature the lattice parameter of all solid solutions is well described by a linear interpolation of the end member values. However, as the system undergoes the superionic transition there was a 'bump' in the thermal expansion associated with swelling due to oxygen disorder. Similarly, there is a commensurate 'bump' in the specific heat capacity due to the enthalpy required to create oxygen defects during the transition. Below the superionic transition temperature oxygen diffusivity in the solid solutions exceeded that expected from a linear interpolation of the end member oxygen diffusivities. This was very clear for $(U_xTh_{1-x})O_2$ where oxygen diffusivity even exceeded that of both end members. This was explained in terms of the oxygen defect enthalpies, which contribute to the activation enthalpies for diffusion. Lower oxygen Frenkel enthalpies were found in $(U_{0.5}Th_{0.5})O_2$ compared to $(U_{0.5}Pu_{0.5})O_2$, contributing to higher oxygen disorder and diffusion in $(U_xTh_{1-x})O_2$. This is not expected from the end member diffusivities and

defect enthalpies. Further work must be done to study the migration barriers in addition to the clustered defect enthalpies (see future work Chapter 8).

The thermal conductivity of the $(U_xTh_{1-x})O_2$ and $(U_xPu_{1-x})O_2$ solid solutions was found to be highly non linear as a function of composition. Deviations from the perfect end member compositions introduced phonon scattering due to the non-uniform cation sublattice, thereby reducing the phonon mean free path and the thermal conductivity of the system. The concentration and scattering strength of defects governs the extent to which the phonon mean free path is reduced. The degradation of thermal conductivity was more significant for $(U_xTh_{1-x})O_2$ than $(U_xPu_{1-x})O_2$ due to the large lattice parameter mismatch of the end members. Equations were developed and fitted to the MD data that were able to describe $(U_xTh_{1-x})O_2$ and $(U_xPu_{1-x})O_2$ thermal conductivity from 300 to 2000 K and from x=0 to x=1. Understanding how the non-uniform cation lattice suppresses thermal conductivity in these systems is useful for the development of mixed oxide fuels. For example, to ensure a high conductivity to what extent is it preferable to develop a two phase fuel, rather than a $(U_xTh_{1-x})O_2$ solid solution? However, as the breeding of U^{233} from Th^{232} is the primary reason for incorporating Th into the fuel cycle the fuel conductivity would be expected to degrade as transmutation proceeds. Being able to predict the rate and extent of this degradation would be useful to aid in optimising core performance.

Bibliography

[1] Kraushaar, J. J. and Ristinen, R. A. (1993) *"Energy and problems of a technical society"*, John Wiley and Sons Inc., New York.

[2] Grimes, R. W. and Catlow, C. R. A. (1991) *Phil. Trans. R. Soc. Lond. A* **335**, 609.

[3] *"Nuclear Reactor Types"* (2005) The Institution of Electrical Engineers Technical report, London.

[4] Arborelius, J., Backman, K., Hallstadius, L., Limbäck, M., Rebensdorff, B., Zhou, G., Kitano, K. and Löfström, R. (2006) *J. Nucl. Sci. Technol.* **43**, 967.

[5] Kato, M., Maeda, K., Ozawa, T., Kashimura, M. and Kihara, Y. (2011) *J. Nucl. Sci. Technol.* **48**, 646.

[6] Hiezl, Z., Hambley, D. I., Padovani, C. and Lee, W. E. (2015) *J. Nucl. Mater.* **456**, 74.

[7] White, R. (2004) *J. Nucl. Mater.* **325**, 61.

[8] Whapham, A. D. (1966) *Nucl. Technol. Appl.* **2**, 123.

[9] Lucuta, P. G., Verrall, R. A., Matzke, Hj. and Palmer, B. J. (1991) *J. Nucl. Mater.* **178**, 48.

[10] Ray, I. L. F., Thiele, H., and Matzke, H. (1992) *J. Nucl. Mat.* **188**, 90.

[11] Rushton, M. J. D. (2006) *"Simulations of Glass and Ceramic Systems for Nuclear Waste Applications"*, PhD thesis.

[12] Murphy, S. T., Rushton, M. J. D. and Grimes, R. W. (2013) *Prog. Nucl. Energy* **72**, 27.

[13] Basak, C. B., Sengupta, A. K. and Kamath, H. S. (2003) *J. Alloy. Compd.* **360**, 210.

[14] Yakub, E., Ronchi, C. and Staicu, D. (2009) *J. Nucl. Mater.* **389**, 119.

[15] Catlow, C. R. A. (1977) *Proc. R. Soc. Lond. A* **353**, 533.

[16] Busker, G., Chroneos, A., Grimes, R. W. and Chen, I-W. (1999) *J. Am. Ceram. Soc.* **82**, 1553.

[17] Meis, C. and Gale, J. D. (1998) *Mater. Sci. Eng.* **57**, 52.

[18] Potashnikov, S. I., Boyarchenkov, A. S., Nekrasov, K. A. and Kupryazhkin, A. Ya. (2007) *ISJAEE* **8**, 43.

[19] Potashnikov, S. I., Boyarchenkov, A. S., Nekrasov, K. A. and Kupryazhkin, A. Ya. (2011) *J. Nucl. Mater.* **419**, 217.

[20] Jackson, R. A., Murray, A. D., Harding, J. H. and Catlow, C. R. (1986) *Philos. Mag. A* **53**, 27.

[21] Meis, C. and Chartier, A. (2005) *J. Nucl. Mater.* **341**, 25.

[22] Morelon, N.-D., Ghaleb, D., Delaye, J.-M. and Van Brutzel, L. (2003) *Philos. Mag.* **83**, 1533.

[23] Read, M. S. and Jackson, R. A. (2010) *J. Nucl. Mater.* **406**, 293.

[24] Fink, J. (2000) *J. Nucl. Mater.* **279**, 1.

[25] Goel, P., Choudhury, N. and Chaplot, S. L. (2008) *J. Nucl. Mater.* **377**, 438.

[26] Skomurski, F. N., Ewing, R. C., Rohl, A. L., Gale, J. D. and Becker, U. (2006) *Am. Mineral.* **91**, 1761.

[27] Arima, T., Yamasaki, S., Inagaki, Y., and Idemitsu, K. (2005) *J. Alloys Compd.* **400**, 43.

[28] Lewis, G. V. and Catlow, C. R. A. (1985) *J. Phys. C: Solid State Phys.* **18**, 1149.

[29] Tharmalingam, K. (1971) *Philos. Mag.* **23**, 199.

[30] Walker, J. R. and Catlow, C. R. A. (1981) *J. Phys. C: Solid State Phys.* **14**, 979.

[31] Karakasidis, T. and Lindan, P. J. D. (1994) *J. Phys. C: Solid State Phys.* **6**, 2965.

[32] Sindzingre, P. and Gillan, M. J. (1988) *J. Phys. C: Solid State Phys.* **21**, 4017.

[33] Tiwary, P. and van de Walle, A. (2009) *Phys. Rev. B* **80**, 174302.

[34] Tiwary, P., van de Walle, A., Jeon, B. and Grønbech-Jensen, N. (2011) *Phys. Rev. B* **83**, 094104.

[35] Hutchings, M. T. (1987) *J. Chem. Soc., Faraday Trans. 2* **83**, 1083.

[36] Shannon, R. D. (1976) *Acta Cryst.* **A32**, 751.

[37] Hayashi, H., Kanoh, M., Quan, C., Inaba, H., Wang, S., Dokiya, M. and Tagawa, H. (2000) *Solid Sate Ionics* **132**, 227.

[38] Hirata, K., Moriya, K., and Waseda, Y. (1977) *J. Mater. Sci.* **12**, 838.

[39] *"Thermophysical properties database of materials for light water reactors and heavy water reactors"* (2006) IAEA Technical Report, Vienna.

[40] Yamashita, T., Nitani, N., Tsuji, T. and Inagaki, H. (1997) *J. Nucl. Mater.* **245**, 72.

[41] Taylor, D. (1984) *Brit. Ceram. Trans. J.* **83**, 32.

[42] Noé, M. and Peterson, J. R. (1972) *Inorg. Nucl. Chem. Lett.* **8**, 897.

[43] Oetting, F. L. (1982) *J. Nucl. Mater.* **105**, 257.

[44] Murphy, S. T., Cooper, M. W. D. and Grimes, R. W. (2014) *Solid State Ionics* **267**, 80.

[45] Anthonysamy, S., Panneerselvam, G., Bera, S., Narasimhan, S. V., and Vasudeva Rao, P. R. (2000) *J. Nucl. Mater.* **281**, 15.

[46] Wiesenack, W. (1997) *Nucl. Eng. Des.* **172**, 83.

[47] Bondars, B., Heidemane, G., Grabis, J., Laschke, K., Boysen, H., Schneider, J., and Frey, F. (1995) *J. Mater. Sci.* **30**, 1621.

[48] Aldebert, P. and Traverse, J.-P. (1985) *J. Am. Ceram. Soc.* **68**, 34.

[49] Teufer, G. (1962) *Acta Cryst.* **15**, 1187.

[50] Einstein, A. (1905) *Ann. Phys.* **18**, 639.

[51] Heyn, F. A., Aten, A. H. W., and Bakker, C. J. (1939) *Nature* **142**, 516.

[52] Bruno, J. and Ewing, R. C. (2006) *Elements* **2**, 343.

[53] Glaser, A. (2008) *Sci. Glob. Secur.* **16**, 1.

[54] *"Calder Hall Power Station"* (1956) *The Engineer* **1**, 464.

[55] Cowan, R. (1990) *J. Econ. Hist.* **50**, 541.

[56] Amaya, M., Hirai, M., Sakurai, H., Ito, K., Sasaki, M., Nomata, T., Kamimura, K., and Iwasaki, R. (2002) *J. Nucl. Mater.* **300**, 57.

[57] Bagger, C., Mogensen, M., and Walker, C. T. (1994) *J. Nucl. Mater.* **211**, 11.

[58] *"Storage of Spent Nuclear Fuel"* (2014) U.S.NRC website, www.nrc.gov/waste/spent-fuel-storage.html.

[59] Ojovan, M. I. and Lee, W. E. (2013) *"An introduction to nuclear waste immobilisation"*, Elsevier Science Ltd, Amsterdam.

[60] Lung, M. and Gremm, O. (2000) *Nucl. Eng. Des.* **180**, 133.

[61] *"Oxide Fuels - Preferred Options"* (2012) NDA Technical Report.

[62] *"Thorium fuel cycles - potential benefits and challenges"* (2005) IAEA Technical report, Vienna.

[63] Chang, Y. I., Finck, P. J. and Grandy, C. *"Advanced Burner Test Reactor Preconceptual Design Report"* (2006) ANL Technical report, Argonne.

[64] Tsujimoto, K., Sasa, T., Nishihara, K., Takizuka, T. and Takano, H. (2000) *Prog. Nucl. Energ.* **37**, 339.

[65] Bowman, C. D. (1998) *Annu. Rev. Nucl. Part. Sci.* **48**, 505.

[66] Grimes, R. W. and Nuttall, W. J. (2010) *Science* **329**, 799.

[67] Sowerby, M. G. *"Nuclear fission"*, NPL website, www.kayelaby.npl.co.uk.

[68] *"Advances in Applications of Burnup Credit to Enhance Spent Nuclear Fuel Transportation, Storage, Reprocessing and Disposition"* (2005) IAEA Technical Report, Vienna.

[69] Wynne, B. (1982) *"Rationality and ritual: The Windscale inquiry and nuclear decisions in Britain"*, Chalfont St Giles, Bucks. : British Society for the History of Science, .

[70] Fischer, D. *"History of the International Atomic Energy Agency"* (1997) IAEA Technical report, Vienna.

[71] Guéneau, C., Baichi, M., Labroche, D., Chatillon, C. and Sundman, B. (2002) *J. Nucl. Mater.* **304**, 161.

[72] *"RBMK Reactors"* (2010) WNO website, www.world-nuclear.org.

[73] Fullarton, M. L., Qin, M. J., Robinson, M., Marks, N. a., King, D. J. M., Kuo, E. Y., Lumpkin, G. R. and Middleburgh, S. C. (2013) *J. Mater. Chem. A*, **1**, 14633.

[74] *"EPR: How It Works?"* (2014) AREVA website, www.areva.com.

[75] Jordan, D. *"Generic design assessment AP1000 nuclear power plant design by Westinghouse Electric Company LLC Decision document"* (2011) Environment Agency Technical report, Bristol.

[76] Nichols, F. A. (1967) *J. Nucl. Mater.* **22**, 214.

[77] Alleluia, I. B. D., Hoshi, M., Jocher, W. G. and Keller, C. (1981) *J. Inorg. Nucl. Chem* **43**, 1831.

[78] Middleburgh, S. C., Parfitt, D. C., Grimes, R., Dorado, B., Bertolus, M., Blair, P., Hallstadius, L. and Backman, K. (2012) *J. Nucl. Mater.* **420**, 258.

[79] Kleykamp, H., Pashoal, J. O., Pejsa, R. and Thommler, F. (1985) *J. Nucl. Mater.* **130**, 426.

[80] Sari, C., Walker, C. T. and Schumacher, G. (1979) *J. Nucl. Mater.* **79**, 255.

[81] Markin, T. L. and Crouch, E. C. (1970) *J. Inorg. Nucl. Chem.* **32**, 77.

[82] Markin, T. L., Street, R. S. and Crouch, E. C. (1970) *J. Inorg. Nucl. Chem.* **32**, 59.

[83] Romberger, K. A., Baes, C. F. and Stone, H. H. (1967) *J. Inorg. Nucl. Chem.* **29**, 1619.

[84] Turnbull, J. A. and Friskney, C. A. (1982) *J. Nucl. Mater.* **107**, 168.

[85] Matzke, Hj. (1980) *Radiat. Eff.* **53**, 219.

[86] Andersson, D., Garcia, P., Liu, X.-Y., Pastore, G., Tonks, M., Millett, P., Dorado, B., Gaston, D. R., Andrs, D., Williamson, R. L., Martineau, R. C., Uberuaga, B. P., and Stanek, C. R. (2014) *J. Nucl. Mater.* **451**, 225.

[87] Rudling, P., Patterson, C., Adamson, R., and Strasser, A. *"IZNA12 SPECIAL TOPIC REPORT High Burnup Fuel Design Issues and Consequences"* (2012) ANT International Technical report, Mölnlycke.

[88] Childs, B. G. (1963) *J. Nucl. Mater.* **9**, 217.

[89] Cottrell, W. B., Culver, H. N., Scott, J. L., and Yarosh, M. M. *"Fission product release from UO2"* Oak Ridge National Laboratory Technical report.

[90] Busker, G., Grimes, R. W., and Bradford, M. R. (2000) *J. Nucl. Mater.* **279**, 46.

[91] Grimes, R. W., Balls, R. G. J., and Catlow, C. R. A. (1992) *J. Phys. Chem. Solids* **53**, 475.

[92] Dorado, B., Freyss, M., and Martin, G. (2009) *Eur. Phys. J. B* **69**, 203–209.

[93] Thomas, L. E., Einziger, R. E., and Woodley, R. E. (1989) *J. Nucl. Mater.* **166**, 243.

[94] Ewart, F. T., Taylor, R. G., Horspool, J. M., and James, G. (1976) *J. Nucl. Mater.* **61**, 254.

[95] Mignanelli, M. A. and Shaw, T. L. *"Information on phase chemistry in UK spent AGR fuels"* (2009) NNL Technical Report.

[96] Kroger, F. and Vink, H. J. (1956) *J. Solid State Phys.* **3**, 307.

[97] Nerikar, P. V., Liu, X.-Y., Uberuaga, B. P., Stanek, C. R., Phillpot, S. R., and Sinnott, S. B. (2009) *J. Phys.: Condens. Matter* **21**, 435602.

[98] Dorado, B., Durinck, J., Garcia, P., Freyss, M., and Bertolus, M. (2010) *J. Nucl. Mater.* **400**, 103.

[99] Mott, N. F. and Littleton, M. J. (1938) *Trans. Faraday Soc.* **34**, 485.

[100] Gale, J. D. (1997) *J. Chem. Soc.* **93**, 629.

[101] Leslie, M. and Gillan, M. J. (1985) *J. Phys. C: Solid State Phys.* **18**, 973.

[102] Makov, G. and Payne, M. C. (1995) *Phys. Rev. B* **51**, 4014.

[103] Murphy, S. T. and Hine, N. D. M. (2013) *Phys. Rev. B* **87**, 094111.

[104] Newton, I. and Machin, J. (1729) *"The mathematical principles of natural philosophy"*, Benjamin Motte, London.

[105] Swope, W. C. (1982) *J. Chem. Phys.* **76**, 637.

[106] Verlet, L. (1967) *Phys. Rev.* **159**, 98.

[107] Govers, K. and Verwerft, M. (2013) *J. Nucl. Mater.* **438**, 134.

[108] Ewald, P. P. (1921) *Ann. Phys.* **64**, 253.

[109] Morse, P. M. (1929) *Phys. Rev.* **34**, 57.

[110] Buckingham, R. A. (1938) *Proc. R. Soc. Lond. Ser.-A* **168**, 264.

[111] Hamaker, H. C. (1937) *Physica* **4**, 1058.

[112] Catlow, C. R. A., Diller, K. M., and Norgett, M. J. (1977) *J. Phys. C: Solid State Phys.* **10**, 1395.

[113] Dick, B. G. and Overhauser, A. W. (1958) *Phys. Rev.* **112**, 90.

[114] Bishop, C. L., Murphy, S. T., Rushton, M. J. D. and Grimes, R. W. (2012) *Nucl. Instrum. Meth. B* **274**, 195.

[115] Lindan, P. J. D. and Gillan, M. J. (1993) *J. Phys. Condens. Mater.* **5**, 1019.

[116] Mitchell, P. J. and Fincham, D. (1993) *J. Phys. Con. Mat.* **5**, 1031.

[117] Plimpton, S. (1995) *J. Comp. Phys.* **117**, 1.

[118] Fritz, I. J. (1976) *J. Appl. Phys.* **47**, 4353.

[119] Daw, M. S., Foiles, S. M., and Baskes, M. I. (1993) *Mater. Sci. Reports* **9**, 251.

[120] Daw, M. S. and Baskes, M. I. (1984) *Phys. Rev. B* **29**, 6443.

[121] Chernatynskiy, A., Flint, C., Sinnott, S. B., and Phillpot, S. R. (2012) *J. Mater. Sci.* **47**, 7693.

[122] Gale, J. D., Catlow, C. R. A., and Mackrodt, W. C. (1992) *Model. Simul. Mater. Sci. Eng.* **1**, 73.

[123] Cooper, M., Middleburgh, S., and Grimes, R. (2013) *J. Nucl. Mater.* **438**, 238.

[124] Cooper, M. W. D., Gregg, D. J., Zhang, Y., Thorogood, G. J., Lumpkin, G. R., Grimes, R. W., and Middleburgh, S. C. (2013) *J. Nucl. Mater.* **442**, 236.

[125] Cooper, M. W. D., Middleburgh, S. C., and Grimes, R. W. (2013) *Prog. Nucl. Energy* **72**, 33.

[126] Shirsat, A. N., Ali (Basu), M., Kolay, S., Datta, A., and Das, D. (2009) *J. Nucl. Mater.* **392**, 16.

[127] Palmer, I. *"ENIGMA predictions of radial profiles in spent AGR fuel"* (2011) NNL Technical report, Preston.

[128] Malen, K., Micski, A., Schrire, D., and Nilsson, B. *"PIE of high burnup BWR fuel rod IFA-597.3 rod 8"* (2001) Halden enlarged group meeting, Nyköping.

[129] Kennedy, B. J., Howard, C. J., and Chakoumakos, B. C. (1999) *Phys. Rev. B* **59**, 6.

[130] Matsuda, T., Yamanaka, S., Kurosaki, K., and Kobayashi, S. (2003) *J. Alloy. Compd.* **351**, 43.

[131] Kleykamp, H. (1993) *J. Nucl. Mater.* **206**, 82.

[132] Leger, J. M., Tomaszewski, P. E., Atouf, A., and Pereira, A. S. (1993) *Phys. Rev. B* **47**, 14075.

[133] Felten, E. J., Juenke, E. F., and Bartram, S. F. (1962) *J. Inorg. Nucl. Chem* **24**, 839.

[134] Liu, X.-Y., Uberuaga, B. P., and Sickafus, K. E. (2009) *J. Phys. Condens. Matter* **21**, 045403.

[135] Liu, X.-Y., Uberuaga, B. P., Nerikar, P., Stanek, C. R., and Sickafus, K. E. (2010) *Nucl. Nucl. Instrum. Meth. B* **268**, 3014.

[136] Nerikar, P. V., Parfitt, D. C., Casillas Trujillo, L. A., Andersson, D. A., Unal, C., Sinnott, S. B., Grimes, R. W., Uberuaga, B. P., and Stanek, C. R. (2011) *Phys. Rev. B* **84**, 1.

[137] Brillant, G., Gupta, F., and Pasturel, A. (2011) *J. Nucl. Mater.* **412**, 170.

[138] Middleburgh, S. C., Grimes, R. W., Desai, K. H., Blair, P. R., Hallstadius, L., Backman, K., and Van Uffelen, P. (2012) *J. Nucl. Mater.* **427**, 359.

[139] Zacate, M. O., Minervini, L., Bradfield, D. J., Grimes, R. W., and Sickafus, K. E. (2000) *Solid State Ionics* **128**, 243.

[140] Yamanaka, S., Kurosaki, K., Maekawa, T., Matsuda, T., Kobayashi, S., and Uno, M. (2005) *J. Nucl. Mater.* **344**, 61.

[141] Feighery, A. J. and Irvine, J. T. S. (1999) *Solid State Ionics* **121**, 209.

[142] Cooper, M. W. D., Middleburgh, S., and Grimes, R. (2014) *Solid State Ionics* **266**, 68.

[143] Ball, R. G. J. and Grimes, R. W. (1990) *J. Chem. Soc. Faraday Trans.* **86**, 1257.

[144] Yun, Y., Oppeneer, P. M., Kim, H., and Park, K. (2009) *Acta Mater.* **57**, 1655.

[145] Govers, K., Lemehov, S., and Verwerft, M. (2010) *J. Nucl. Mater.* **405**, 252.

[146] Matzke, Hj. (1983) *J. Nuc. Mater.* **114**, 121.

[147] Reimann, D. K. and Lundy, T. S. (1969) *J. Am. Ceram. Soc.* **22**, 511.

[148] Ando, K. and Oishi, Y. (1983) *J. Nucl. Sci. Technol.* **20**, 973.

[149] Dorado, B., Andersson, D. a., Stanek, C. R., Bertolus, M., Uberuaga, B. P., Martin, G., Freyss, M., and Garcia, P. (2012) *Phys. Rev. B* **86**, 035110.

[150] Middleburgh, S. C., Lumpkin, G. R., and Grimes, R. W. (2013) *Solid State Ionics* **253**, 119.

[151] Yu, J., Devanathan, R., and Weber, W. J. (2009) *J. Phys. Condens. Matter* **21**, 435401.

[152] Govers, K., Lemehov, S., Hou, M., and Verwerft, M. (2007) *J. Nucl. Mat.* **366**, 161.

[153] Hanken, B. E., Stanek, C. R., Grönbech-Jensen, N., and Asta, M. (2011) *Phys. Rev. B* **84**, 1.

[154] Cooper, M. W. D., Middleburgh, S. C., and Grimes, R. W. (2013) *J. Nucl. Mater.* **438**, 238.

[155] Banerjee, A., Adams, N., Simons, J., and Shepard, R. (1985) *Am. Chem. Soc.* **89**, 52.

[156] Dorado, B., Garcia, P., Davoisne, C., Fraczkiewicz, M., Pasquet, B., Freyss, M., Valot, C., Baldinozzi, G., Sim, D., and Bertolus, M. (2011) *Phys. Rev. B* **83**, 035126.

[157] Casado, J. M., Harding, J. H., and Hyland, G. J. (1994) *J. Phys.: Condens. Mater.* **6**, 4685.

[158] MacInnes, D. A. and Catlow, C. R. A. (1980) *J. Nucl. Mater.* **89**, 354.

[159] Mehrer, H. (2007) *"Diffusion in Solids"*, Springer-Verlag, Heidelberg.

[160] Cooper, M. W. D., Rushton, M. J. D., and Grimes, R. W. (2014) *J. Phys.: Condens. Mater.* **26**, 105401.

[161] Tan, A. H. H., Grimes, R. W., and Owens, S. (2005) *J. Nucl. Mater.* **344**, 13.

[162] Vyas, S., Grimes, R. W., Gaya, D. H., and Rohlc, A. L. (1998) *J. Chem. Soc. Trans.* **94**, 427.

[163] Minervini, L., Zacate, M. O., and Grimes, R. W. (1999) *Solid State Ionics* **116**, 339.

[164] Govers, K., Lemehov, S., Hou, M., and Verwerft, M. (2008) *J. Nucl. Mat.* **376**, 66.

[165] Tyagi, A. K., Ambekar, B. R., and Mathews, M. D. (2002) *J. Alloy. Comp.* **337**, 277.

[166] Crocombette, J., Jollet, F., Nga, L., and Petit, T. (2001) *Phys. Rev. B* **64**, 104107.

[167] Freyss, M., Petit, T., and Crocombette, J.-P. (2005) *J. Nucl. Mater.* **347**, 44.

[168] Geng, H., Chen, Y., Kaneta, Y., Iwasawa, M., Ohnuma, T., and Kinoshita, M. (2008) *Phys. Rev. B* **77)**, 104120.

[169] Nerikar, P., Watanabe, T., Tulenko, J. S., Phillpot, S. R., and Sinnott, S. B. (2009) *J. Nucl. Mater.* **384**, 61.

[170] Dorado, B., Jomard, G., Freyss, M., and Bertolus, M. (2010) *Phys. Rev. B* **82**, 035114.

[171] Crocombette, J.-P., Torumba, D., and Chartier, A. (2011) *Phys. Rev. B* **83**, 184107.

[172] Crocombette, J.-P. (2012) *Phys. Rev. B* **85**, 144101.

[173] Hockney, R. W. and Eastwood, J. W. (1988) *"Computer Simulation Using Particles"*, McGraw-Hill, New York.

[174] van Duin, A. C. T., Dasgupta, S., Lorant, F., and Goddard III, W. A. (2001) *J. Phys. Chem. A* **105**, 9396.

[175] Yu, J., Sinnott, S. B., and Phillpot, S. R. (2007) *Phys. Rev. B* **75**, 085311.

[176] Idiri, M., Le Bihan, T., Heathman, S., and Rebizant, J. (2004) *Phys. Rev. B* **70**, 014113.

[177] Nakajima, A., Yoshihara, A., and Ishigame, M. (1994) *Phys. Rev. B* **50**, 13297.

[178] Benedict, U., Dabos, S., Dufour, C., Spirlet, J. C. and Pagès, M. (1986) *J. Less-Common Met.* **121**, 461.

[179] Macedo, P. M., Capps, W., and Wachtman, J. B. (1964) *J. Am. Ceram. Soc.* **46**, 651.

[180] Nelder, J. A. and Mead, R. (1965) *Comput. J.* **7**, 308.

[181] Cooper, M. W. D., Murphy, S. T., Rushton, M. J. D., and Grimes, R. W. (2015) *J. Nucl. Mater.* **461**, 206-214.

[182] Minervini, L., Grimes, R. W., and Sickafus, K. E. (2000) *J. Am. Ceram. Soc.* **83**, 1873.

[183] Popov, S. G., Carbajo, J. J., Ivanov, V. K., and Yoder, G. L. *"Thermophysical Properties of MOX and UO_2 Fuels Including the Effects of Irradiation"* (2000) ORNL Technical report.

[184] Rushton, M. J. D. and Chroneos, A. (2014) *Sci. Rep.* **4**, 2.

[185] Cooper, M. W. D., Murphy, S. T., Fossati, P. C. M., Rushton, M. J. D., and Grimes, R. W. (2014) *Proc. Roy. Soc. A* **470**, 20140427.

[186] Qin, M. J., Cooper, M. W. D., Kuo, E. Y., Rushton, M. J. D., Grimes, R. W., Lumpkin, G. R., and Middleburgh, S. C. (2014) *J. Phys.: Condens. Matter* **26**, 495401.

[187] Lee, W. E., Gilbert, M., Murphy, S. T., and Grimes, R. W. (2013) *J. Am. Ceram. Soc.* **96**, 2005.

[188] Hiernaut, J. P., Hyland, G. J., and Ronchi, C. (1993) *Int. J. Thermophys.* **14**, 259.

[189] Gronvold, F., Kveseth, N. J., Sveen, A., and Tichy, J. (1970) *J. Chem. Thermodyn.* **2**, 665.

[190] Fink, J. K., Chasanov, M. G., and Leibowitz, L. (1981) *J. Nucl. Mater.* **102**, 17.

[191] Fink, J. K. (1982) *Int. J. Thermophys.* **3**, 165.

[192] Hein, R. A., Flagella, P. N., and Conway, J. B. (1968) *J. Am. Ceram. Soc.* **51**, 291.

[193] Ruello, P., Desgranges, L., Baldinozzi, G., Calvarin, G., Hansen, T., Petot-Ervas, G., and Petot, C. (2005) *J. Phys. Chem. Solids* **66**, 823.

[194] Chasanov, M., Leibowitz, L., and Gabelnick, S. D. (1973) *J. Nucl. Mater.* **49**, 129.

[195] Szwarc, R. (1969) *J. Phys. Chem. Solids* **30**, 705.

[196] Kerrisk, J. F. and Clifton, D. G. (1972) *Nucl. Tech.* **16**, 531.

[197] Bredig, M. A. (1971) *Colloq. Int. Cent. Nat. Rech. Sci.* **205**, 183.

[198] Potashnikov, S. I., Boyarchenkov, A. S., Nekrasov, K. A., and Kupryazhkin, A.Ya. (2013) *J. Nucl. Mater.* **433**, 215.

[199] Govers, K., Lemehov, S., Hou, M., and Verwerft, M. (2009) *J. Nucl. Mater.* **395**, 131.

[200] Belle, J. (1969) *J. Nucl. Mater.* **30**, 3.

[201] Phillpot, S. R., El-azab, A., Chernatynskiy, A., and Tulenko, J. S. (2011) *J. Mater.* **63**, 73.

[202] Nichenko, S. and Staicu, D. (2013) *J. Nucl. Mater.* **433**, 297.

[203] Watanabe, T., Sinnott, S. B., Tulenko, J. S., Grimes, R. W., Schelling, P. K., and Phillpot, S. R. (2008) *J. Nucl. Mater.* **375**, 388.

[204] Schelling, P. K., Phillpot, S. R., and Keblinski, P. (2002) *Phys. Rev. B* **65**, 144306.

[205] Grimes, R. *"Quantum-Mechanical and Classical Modelling of Defects in Metal Oxides"* (1988) UKAEA Technical report.

[206] Bitzek, E., Koskinen, P., Gähler, F., Moseler, M., and Gumbsch, P. (2006) *Phys. Rev. Lett.* **97**, 170201.

[207] Vegard, L. (1921) *J. Phys.* **5**, 17.

[208] Yamashita, T., Nitani, N., Tsuji, T., and Kato, T. (1997) *J. Nucl. Mater.* **247**, 90.

[209] Gibby, R. L. (1971) *J. Nucl. Mater.* **38**, 163.

[210] Hyams, D. G. (2014) CurveExpert Pro 2.2.0 website, www.curveexpert.net/.

[211] Bell, B. D. C., Murphy, S. T., Burr, P. A., Grimes, R. W., and Wenman, M. R. (2015) *J. Appl. Phys.* **[In Press]**.

[212] Kisi, E. H. and Howard, C. J. (1998) *J. Am. Ceram. Soc.* **84**, 1682.

[213] Zhao, Y. and Weidner, D. J. (1991) *Phys. Chem. Miner.* **18**, 294.

[214] Yamanaka, S., Fujikane, M., Hamaguchi, T., Muta, H., Oyama, T., Matsuda, T., Kobayashi, S., and Kurosaki, K. (2003) *J. Alloy. Comp.* **359**, 109.

[215] Scott, H. G. (1975) *J. Mater. Sci.* **10**, 1527.

Appendix A

Preliminary fitting results for ZrO_2 and $BaZrO_2$

A.1 Fitting ZrO_2

Like previous centrosymmetric potentials, such as pair potentials, the EAM potential form of Chapter 6 could not stabilise the monoclinic ZrO_2 crystal structure. Therefore, fitting was carried out to the tetragonal elastic constants from DFT [211] and experimental lattice parameters using the same method outlined in Chapter 6 for the actinide oxides:

- Elastic constants predicted by the potential from energy minimisation in GULP [100] were fitted to the DFT elastic constants. DFT usually underestimates this, hence the weighting was very low: a factor of 10 lower than for the thermal expansion.
- The temperature dependence of the tetragonal ZrO_2 lattice constants predicted by the potential in LAMMPS were fit to the room temperature data of Bondars *et al.* [47] and high temperature XRD data from Aldebert and Traverse [48] and Teufer [49].

A.1.1 Parameter set

The final parameter set derived by the fitting process is summarised in table A.1. The Zr-Zr parameters are kept consistent with the actinide oxide potential set, such that, A_{Zr-Zr} is fixed at 18600 and ρ_{Zr-Zr} is scaled as a function of ionic radius in line with Figure 6.1.

Table A.1: Potential parameters for ZrO_2 using the same potential form reported in equations 6.1-6.6. O-O parameters are kept the same as for the actinide oxide potential set of Chapter 6.

Pair Parameters		
	Zr-Zr	Zr-O
$A_{\alpha\beta}$ (eV)	18600	1147.471
$\rho_{\alpha\beta}$ (Å)	0.2307	0.3224
$C_{\alpha\beta}$ (eV.Å^6)	0.0	0.0
$D_{\alpha\beta}$ (eV)	-	1.2269
$\gamma_{\alpha\beta}$ (Å^{-1})	-	1.4482
$r^0_{\alpha\beta}$ (Å)	-	1.998
EAM Parameters		
G_{Zr} (eV.Å$^{1.5}$)	1.597	
n_{Zr} (Å^5)	1188.786	

A.1.2 Agreement with DFT

Tables A.2 and A.3 report the elastic constants and lattice parameters predicted by the EAM potential. The DFT predictions of Bell *et al.* [211] are included for comparison. A reasonable agreement is achieved for all single crystal elastic constants with the exception of C_{33}. However, this relates to strain in line with the c lattice parameter, which as can be seen in table A.3 is significantly over estimated by DFT compared to the experimental data used to fit the potential. It is important to note that fitting was not done to the DFT lattice parameters.

Although not used in the fitting procedure, the experimental values for the elastic constants of Ce-doped ZrO_2 by Kisi and Howard [212] are also included in table A.2. For a real comparison Ce-doped ZrO_2 should be simulated using this potential in conjunction with the potential reported for CeO_2 in Chapter 6.

Table A.2: Elastic constants and comparison with DFT [211] used in fitting with low weighting.

(GPa)	EAM Potential	DFT [211]	Expt. (Ce-doped) [212]
C_{11}	338.16	334.25	327
C_{33}	313.04	250.67	264
C_{44}	41.67	9.37	59
C_{66}	166.19	152.69	64
C_{12}	228.93	207.25	100
C_{13}	94.16	48.85	62

Table A.3: Static lattice constants and comparison with DFT [211] not used in fitting.

(Å)	EAM Potential	DFT [211]
a	3.60	3.62
c	5.19	5.28

A.1.3 Agreement with experiment

Figure A.1 shows thermal expansion of the *a* and *b* lattice parameters as predicted using the new potential; there is a good agreement with the experimental value at room temperature. Similarly, the agreement for lattice parameter *c* at room temperature is also good at room temperature (Figure A.2).

The sudden change in behaviour at ≈2000 K in figures A.1 and A.2 seems to indicate a phase transition. If this is due to the high temperature fluorite phase of ZrO_2 (lattice parameter =

a_{cubic}) then the following relationship should be true:

$$a_{cubic} = c = \sqrt{a^2 + b^2} = a\sqrt{2}$$
$$\frac{a}{c} = \frac{\sqrt{2}}{2} = 0.7071 \tag{A.1}$$

It can be seen in figure A.3 that the tetragonal to fluorite phase change occurs at 2000 K. This is a long way off the value of 2650 K shown in the phase diagram [215]. This may, however, be explained in terms of the polycrystalline samples used in experiment, where internal stresses between the grains may oppose the transition to cubic symmetry. This could account for a higher tetragonal to cubic phase transition in experiment compared to the perfect single crystal simulations presented here. It should, however, be noted that in Figure A.3 the experimental results seem to indicated that phase transition is beginning to occur. Future work should be carried out on polycrystalline supercells to examine the effect on the phase transition.

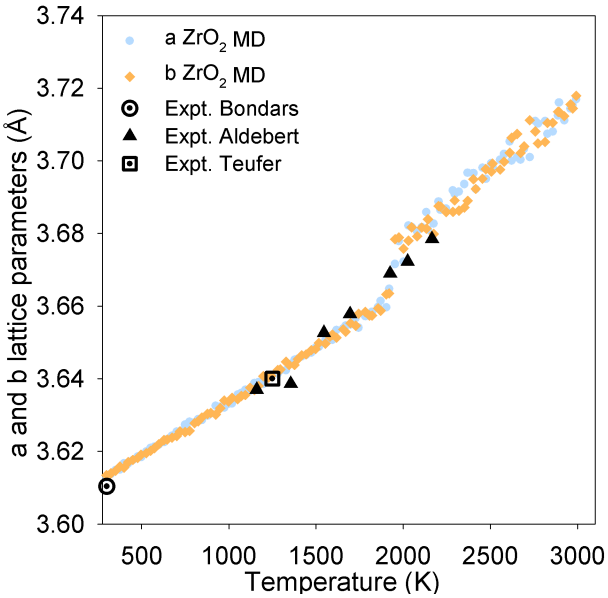


Figure A.1: The variation of the a and b lattice parameters of tetragonal ZrO_2 as a function of temperature using the new potential with comparison to experimental data [47–49].

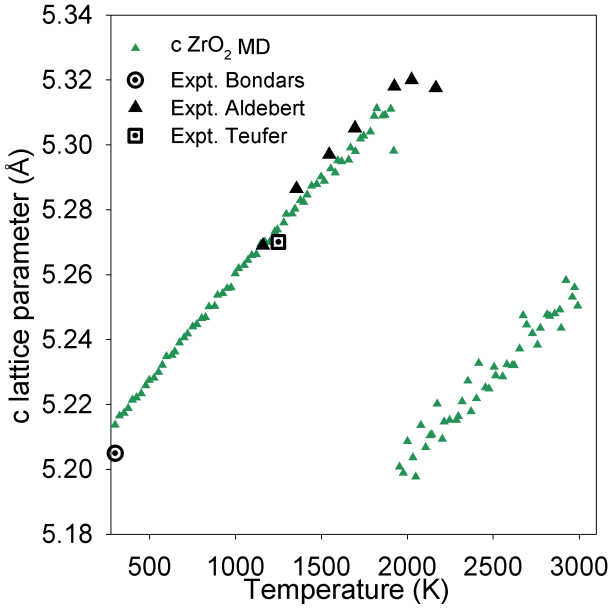


Figure A.2: The variation of the c lattice parameter of tetragonal ZrO_2 as a function of temperature using the new potential with comparison to experimental data [47–49].

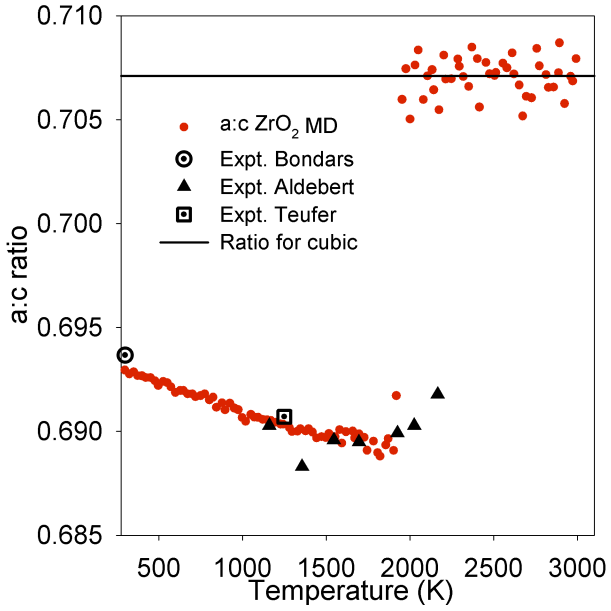


Figure A.3: The variation of the a:c ratio of tetragonal ZrO_2 as a function of temperature using the new potential with comparison to experimental data [47–49]. When $\frac{a}{c} = 0.7071$ the tetragonal structure has changed to the fluorite structure (i.e. above 2000 K).